Burning plasma
Experimental
Superconducting
Tokamak

BEST Research Plan

'From vision to action: BEST missions and pathways to realisation'

ASIPP and EUROfusion

1st Edition

November 2025

Version 1.1
Release date: 27 November 2025

Foreword

This first edition of the BEST Research Plan has been jointly prepared by a dedicated team of ASIPP and EUROfusion researchers, with valuable contributions from UKAEA experts. The work commenced on 26 November 2024 at the 1st Joint BEST Research Plan Meeting at the CRAFT campus in Hefei. The aim of the Research Plan is to establish the foundational framework and facilitate active collaboration among Chinese, European, and other international partners for the development, operation and full exploitation of BEST.

As a living document, the Research Plan will continue to evolve, incorporating additional topics and detailed studies in future editions. We hope that this effort will strengthen the culture of international collaboration on the path towards realizing magnetic confinement fusion as a sustainable energy source. We anticipate that this collaboration will advance toward the joint utilization of this cutting-edge D-T tokamak, playing a critical role in supporting future ITER operations and significantly contributing to the design, development and licensing of CFEDR and next-generation fusion power plants.

Group photo from the 1st Joint BEST Research Plan Meeting held on 26-29 November 2024 in Hefei, China, marking the official commencement of this collaborative activity.

Acknowledgments

ASIPP contributors would like to acknowledge the Chinese Academy of Sciences (CAS) and the Fusion Energy Technology Co., Ltd† for their strong support in the construction of BEST and in the development of the BEST Research Plan.

The work of EUROfusion researchers on the BEST Research Plan was supported within the framework of the EUROfusion Consortium, funded by the European Union via the Euratom Research and Training Programme (Grant Agreement No 101052200 – EUROfusion). Views and opinions expressed are however those of the author(s) only and do not necessarily reflect those of the European Union or the European Commission. Neither the European Union nor the European Commission can be held responsible for them.

The work of UKAEA researchers has been (part-) funded by the UKAEA/EPSRC Fusion Grant 2022/27 (EP/W006839/1).

† Web-site:
http://jbxnah.com

聚变新能(安徽)有限公司
FUSION ENERGY TECHNOLOGY CO.,LTD

Executive summary

As part of its national commitment to modernizing the energy system and achieving a low-carbon future, China has identified nuclear fusion as an essential component of its long-term energy strategy and is accelerating the development of fusion science, technology, and engineering capabilities. The Institute of Plasma Physics, Chinese Academy of Sciences (ASIPP), stands at the core of this effort. With more than four decades of leadership in tokamak research – ranging from HT-series devices to the world-leading EAST superconducting tokamak – ASIPP has built a comprehensive capability, spanning plasma physics, superconducting engineering, cryogenics, power supplies, plasma heating systems, diagnostics, fuel cycle technologies, and nuclear-grade component development.

To transition from present-day experimental devices towards future fusion reactors, ASIPP has defined a stepwise development strategy centered on the China Fusion Engineering Demonstration Reactor (CFEDR). CFEDR's mission is to achieve high fusion gain (Q = 10-30), generate net electricity, demonstrate tritium self-sufficiency, and validate reactor-relevant materials under significant neutron flux and fluence. To supply the required scientific foundations and mature the enabling technologies, ASIPP is constructing a complementary suite of large-scale facilities, including the CRAFT technology campus and the new superconducting tokamak BEST (Burning Plasma Experimental Superconducting Tokamak).

BEST is a pivotal step in this integrated strategy. When completed, it will be the world's largest operating D-T tokamak prior to ITER. With a major radius of 3.6 m, central magnetic field of 6.15 T, a full-tungsten first wall and divertor, and 50 MW of auxiliary heating, BEST is explicitly designed to explore high-performance plasmas, long-pulse operation, and burning-plasma-relevant physics. Its role is two-fold: (1) to act as an advanced physics and technology testbed that accelerates readiness for CFEDR, and (2) to serve the international program by generating D-T data in support of preparing and optimizing future ITER operations.

The missions of BEST span three principal domains:

1) Plasma physics. BEST will explore high-performance D-T scenarios, achieve scientific breakeven ($Q \geq 1$), study confinement in a full-W environment, investigate alpha-particle and fast-ion dynamics, and develop advanced operational regimes capable of approaching burning-plasma conditions ($Q \approx 5$).

2) Fusion technology and engineering. In support of CFEDR, BEST will validate high-field superconducting magnets, high-heat-flux tungsten divertor concepts, heating and current drive systems, plasma-facing components, remote handling, and real-time control systems. BEST will also demonstrate an integrated tritium fuel cycle, including direct internal recycling.

3) Fusion nuclear safety and tritium breeding. BEST will operate with an initially licensed tritium inventory of 110 g and provide a platform for testing tritium accountancy, detritiation systems, and confinement barrier performance. It includes three dedicated ports for Test Blanket Modules (TBMs), enabling early validation of breeding blanket concepts under realistic tokamak conditions.

Construction of BEST is scheduled for completion by the end of 2027, with first plasma expected in late 2027. The operational campaign is structured in multiple stages. Initial hydrogen and deuterium plasmas at half magnetic field will support integrated commissioning of magnets, heating systems, plasma control, fuelling and impurity management, diagnostics, and disruption mitigation strategies. Subsequent full-field deuterium operation will refine scenario development and prepare for D-T campaigns through pellet fuelling tests, wall conditioning, high-power RF commissioning, and advanced control algorithm deployment.

The first D-T plasmas will begin at moderate current (3-4 MA), followed by systematic optimization at higher plasma current (up to 6-7 MA). Conservative inductive scenarios, based on ITER physics and recent D-T campaigns at JET, are predicted to generate more than 50 MW of fusion power with $Q > 1$ – approximately three times the historical fusion power record achieved at JET. These scenarios directly support the high-level objective of demonstrating scientific breakeven in BEST.

Long-pulse operation exceeding 1000 seconds will then enable integrated testing of fuel cycle technologies, tungsten divertor solutions, control systems, and TBMs, offering critical learning for CFEDR. At the same time, large alpha-particle and fast-ion populations in D-T plasmas on BEST will permit significant advances in alpha-particle physics, expanding upon discoveries from JET DTE2 and DTE3 and contributing to the global understanding of burning plasmas.

As ITER will begin its first D-T operations in the early 2040s, BEST fills a crucial strategic gap. It will provide ITER with validated operational scenarios in a tungsten environment, insights into pedestal behavior, confinement with low external torque, impurity control, ELM mitigation and no-ELM regimes, RF optimization, and early testing of AI/ML plasma control strategies. BEST also offers significant value through materials testing at moderate neutron wall loadings and through early demonstration of breeding blanket elements and tritium management strategies, all of which de-risk CFEDR design choices.

A major upgrade of EAST, launched in 2025, further strengthens the ecosystem of ASIPP. EAST will support BEST by providing a platform for scenario development, divertor testing, H&CD optimization, and advanced profile control, ensuring rapid feedback loops between the two devices.

In summary, BEST is an essential step in the ASIPP strategy for the accelerated development of fusion as energy and electricity source. By tightly integrating high-performance plasma physics, fusion technology qualification, and nuclear safety demonstration, BEST not only enables the timely realization of CFEDR but also provides essential data and expertise to the international fusion community and to ITER. Together with EAST and CRAFT, BEST forms a comprehensive scientific and engineering foundation that advances China and the world toward the realization of practical fusion energy.

Table of Contents

Chapter 1: Overview of the BEST Project

Coordinators[†]:
J.P. Qian (ASIPP), Ye.O. Kazakov (LPP-ERM/KMS, Brussels, Belgium)

With contributions from:
ASIPP Team: Y.T. Song, J.G. Li, K. Lu, G.S. Xu, B. Zhang, S.L. Zheng, G.Q. Li, X.B. Peng, J.G. Qin, X.J. Wang, V. Chan, R. Ding, Z.H. Liu, S.Z. Huang, J.X. Zheng, Y.Y. Huang, B.J. Xiao, X.Z. Gong, B.N. Wan
EUROfusion Team: G. Federici, M. Wischmeier, R. Kamendje, J. Elbez-Uzan, E. Joffrin (CEA-Cadarache, France), P. Mantica (CNR-Milan, Italy)
ITER Organization: A. Loarte
UKAEA Team: D. King, L. Garzotti

1.1: Fusion strategy at ASIPP

Nuclear fusion holds great promise as a vital component of the future global energy mix. In addition to being inherently safe, it offers several distinct advantages, including extremely high energy density, abundant fuel availability, and minimal long-lived radioactive waste. The Government of China places a strong emphasis on modernizing its energy infrastructure and system [1], with a strong support on accelerating the development of nuclear fusion energy as a part of a sustainable and low-carbon energy strategy [2].

Fusion research and development for peaceful energy production is a global endeavor from which all nations stand to benefit. Historically, fusion science has exemplified international cooperation and collaboration. The ITER project, the world largest and most ambitious fusion experiment, continues to make steady progress toward achieving its first DD plasma (currently targeted for 2035), followed by the demonstration of the $Q \geq 10$[††] operation starting from 2044 [3, 4].

The Institute of Plasma Physics, Chinese Academy of Sciences (ASIPP), established in 1978 in Hefei, Anhui Province, is a key national research institute in China, specialized in the development of fusion energy using the tokamak approach [5]. The ASIPP's expertise spans high-temperature plasma physics, fusion engineering and fusion reactor technology, as well as supporting work in cryogenics, superconducting systems, power supplies, diagnostics and vacuum technologies.

ASIPP has designed, constructed and operated major tokamak devices, including HT-6B, HT-6M, HT-7 (China's first superconducting tokamak) and EAST (Experimental Advanced Superconducting Tokamak) [6, 7]. In January 2025, EAST achieved a continuous H-mode plasma discharge lasting 1066 seconds (almost 18 minutes),

[†] *The two lead authors contributed equally to this work and share first authorship.*

[††] *Throughout the Research Plan, the fusion gain factor is defined as* $Q = P_{fus}/P_{aux}$*, where* P_{fus} *is the generated fusion power and* P_{aux} *is the injected auxiliary heating power.*

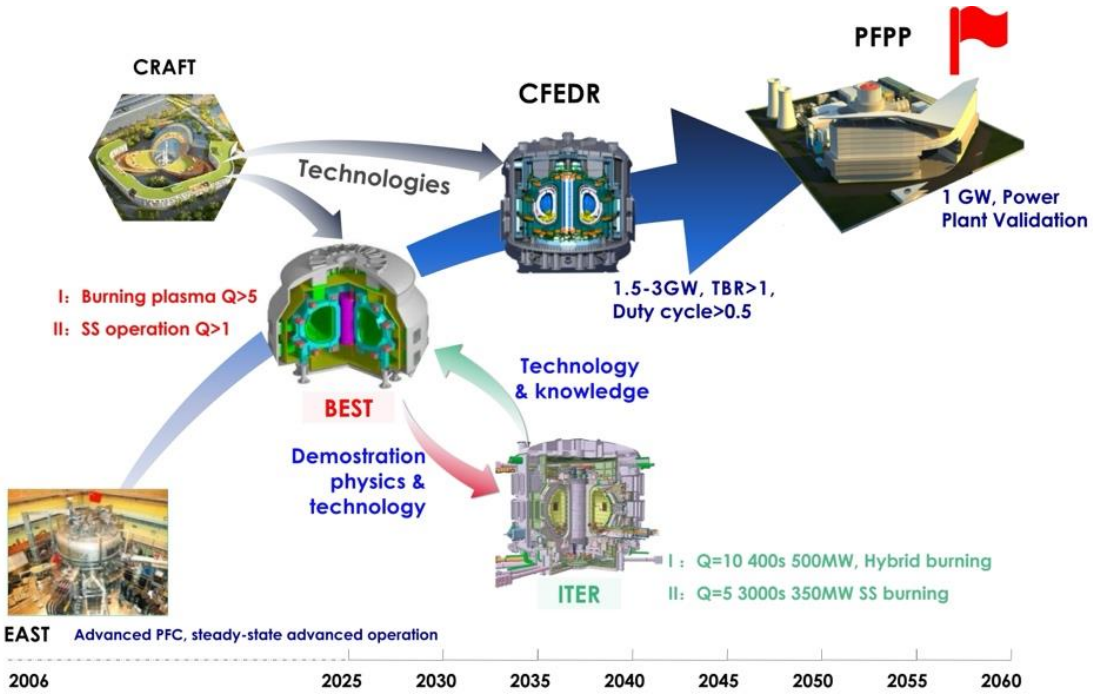

Figure 1.1: Fusion strategy at ASIPP.

setting a new world record [8]. Beyond its domestic achievements, ASIPP plays a central role in international collaboration. It is responsible for more than 70% of China's procurement packages for ITER, covering components such as superconducting conductors, magnet feeders, correction coils, power supply systems and diagnostics. Moreover, ASIPP manages numerous in-cash contracts for ITER, either directly with the ITER Organization or through Fusion for Energy (the European Domestic Agency for ITER), such as the poloidal field coil #6, port-plug structures, duct liner for the Neutral Beam Injection system, cryostat rectangle bellows, etc.

ASIPP have recently outlined a new approach to fusion power production with the China Fusion Engineering Demonstration Reactor (CFEDR) that should serve as a bridge between the existing generation of experimental tokamaks in China and a fully functional Prototype Fusion Power Plant (PFPP). The mission of CFEDR is to demonstrate high fusion gain (Q = 10-30), high fusion power output, net electrical power generation, tritium self-sufficiency, and to validate reactor-relevant materials and components under high-neutron-flux and fluence conditions [9].

To accelerate progress in both physics and technology towards CFEDR, ASIPP is developing a complementary suite of large-scale facilities – notably CRAFT and BEST – that address key scientific and engineering challenges relevant to future fusion power plants, see Fig. 1.1. The construction of CRAFT (Comprehensive Research Facility for Fusion Technology) began in September 2019. CRAFT hosts around 20 specialized test platforms for superconducting magnets, plasma heating systems, breeding blanket and tritium technologies, and other critical fusion components [10]. The CRAFT project aims to master, standardize, and industrialize key fusion technologies, materials, and systems for BEST, CFEDR and beyond.

A new superconducting tokamak, BEST (Burning Plasma Experimental Superconducting Tokamak), designed for deuterium-tritium (D-T) plasma operation, is now being constructed next to the CRAFT campus and makes extensive use of CRAFT's advanced technology facilities. While design activities started in February 2021, construction of the BEST facility began on 30 June 2023 and is expected to be completed in the second half of 2027, see Fig. 1.2. Positioned between JET and ITER in scale, BEST will provide essential insights – in plasma physics, fusion technology and nuclear safety demonstration – to support the design, licensing, operation and exploitation of CFEDR and future fusion power plants. With a target of achieving $Q \geq 1$ D-T plasmas before the end of 2030, the BEST timeline is designed to accelerate fusion development in parallel to ITER. The two programs are highly synergistic: while BEST builds upon ITER physics and technological foundations, it will, in turn, provide timely experimental data and operational experience to optimize future ITER operations and inform the design of next-generation fusion devices.

1.2: BEST missions and objectives

BEST is a new superconducting D-T tokamak with a full-tungsten first wall and divertor, designed for high magnetic field operation (B_0 = 6.15T) and steady-state plasma performance. With a plasma volume of approximately 140 m^3 (R_0 = 3.6 m, a = 1.1 m), it represents a substantial advancement beyond EAST within the ASIPP's tokamak portfolio and serves as a key step towards CFEDR. Once completed and operational, BEST will be the largest D-T tokamak in the world prior to ITER. Figure 1.3 illustrates the projected position of BEST in terms of major radius and central magnetic field relative to current-generation tokamaks (EAST, JET†, and JT-60SA [11]) and future facilities (ITER and CFEDR). This comparison, together with the planned timeline of BEST, highlights its strategic role as a bridge facility, addressing critical physics, technology, nuclear safety and licensing gaps and providing essential experimental and engineering data to mitigate construction risks and accelerate the realization of next-generation fusion reactors.

Figure 1.2: Construction of the BEST campus started in June 2023. The photo shows the site in November 2025.

† *JET has entered decommissioning, with its final plasma operations conducted in December 2023.*

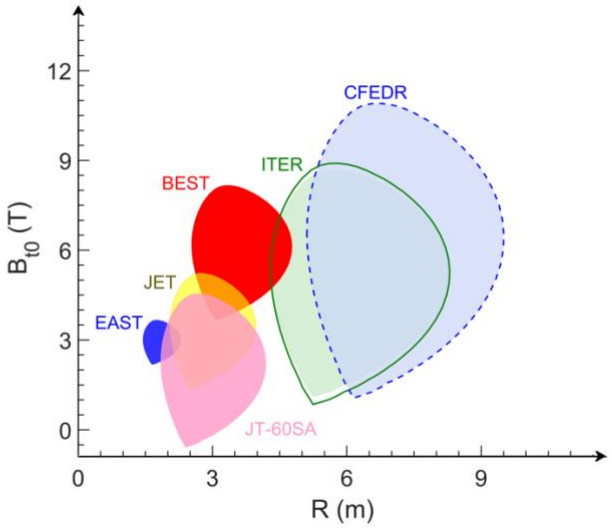

Figure 1.3: Relative position of the BEST tokamak in terms of major radius and central magnetic field, compared with current-generation and future tokamaks.

The missions of BEST encompass plasma physics, fusion technology and nuclear safety goals. On the physics side, BEST will experimentally explore high-performance, long-pulse D-T plasma operation, investigate alpha-particle behavior [12] and develop paths towards burning plasma physics ($Q \approx 5$) studies†. Both conservative and advanced operational scenarios will be developed, providing valuable input for future ITER and CFEDR scenarios.

On the technology side, BEST will focus on the development, validation, and optimization of key fusion technologies directly relevant to CFEDR as a nuclear facility and future fusion power plants. Key items include high-field superconducting magnets, reactor-relevant divertor solutions, remote maintenance, heating and current drive (H&CD) systems, burning plasma diagnostics and control. Importantly, BEST also aims to demonstrate an integrated tritium fuel cycle and to serve as a platform for early testing of tritium breeding technologies, providing essential data and engineering experience in support of CFEDR (see Chapter 3 for further details).

Regarding nuclear operation, with a total initially allowed tritium inventory of 110 g††, BEST will provide an excellent platform to advance the important topic of tritium inventory control that represents the basis of a license (see Chapter 11 for further details). In addition, the validation and demonstration of the efficiency of confinement barriers is a key objective, the achievement of which will directly inform the nuclear dimensioning of next step devices.

† The fraction of plasma self-heating by alpha-particles is given by Q/(Q+5). For Q ≥ 5, over half of the heating comes from fusion-born alphas, characteristic of a burning plasma.

†† Plans for subsequent phases of the project include a possible increase of the tritium inventory. For reference, the tritium site inventory for recent record fusion energy experiments in JET DTE2 and DTE3 campaigns was 69 g and 42 g, respectively.

Achieving the high-level scientific and technological objectives of BEST is currently structured around three main targets:

- **T1:** Achieve scientific breakeven ($Q \geq 1$) in magnetic confinement fusion and establish the operational basis for steady-state D-T plasmas;
- **T2:** Develop and demonstrate long-pulse operation and integrated fusion technology applications, including the tritium fuel cycle;
- **T3:** Explore alpha-particle physics and burning plasma ($Q \approx 5$) physics.

The realisation of the high-level targets T1, T2, and the alpha-particle-relevant aspects of T3 can be accomplished using conservative operational scenarios, largely based on current ITER physics knowledge and recent experience from JET DTE2 and DTE3 campaigns [13-16]. While ITER is designed to achieve $Q \geq 10$ plasmas, the conservative scenarios in BEST are not sufficient to reach comparable Q-values due to the smaller size of BEST relative to ITER.

In parallel, the experimental strategy of BEST foresees the development of advanced operational scenarios [17-19], which explore more ambitious regimes with enhanced plasma confinement and performance. This complementary approach is intended to provide conditions towards burning plasma studies ($Q \approx 5$), possibly in short pulses, where self-heating from fusion-born alpha particles becomes comparable to the external auxiliary heating power. Advanced regimes will also be explored for long-pulse operation at higher fusion gains than those achieved under conservative assumptions.

In this first edition of the BEST Research Plan, the focus is placed primarily on conservative operational scenarios, providing a solid and achievable foundation for early plasma campaigns. The integration of advanced scenarios will be addressed in the next edition of the Research Plan.

1.3: Main parameters of BEST

The poloidal cross-section of BEST, together with the elements of the magnetic system and a summary of the main parameters of the tokamak are shown in Figure 1.4. The device features a major radius R_0 = 3.6 m and a minor radius a = 1.1 m, with plasma ellipticity and triangularity up to $k \approx 1.88$ and $\delta \approx 0.49$, respectively. The corresponding plasma volume is approximately 140 m^3, and the plasma surface area is about 220 m^2.

BEST is designed for operation with plasma currents up to 7 MA and a nominal central magnetic field of B_0 = 6.15T. The total auxiliary heating power is $P_{aux} \approx 50$MW, provided by a combination of neutral beam injection (NBI) and radiofrequency (RF) heating systems.

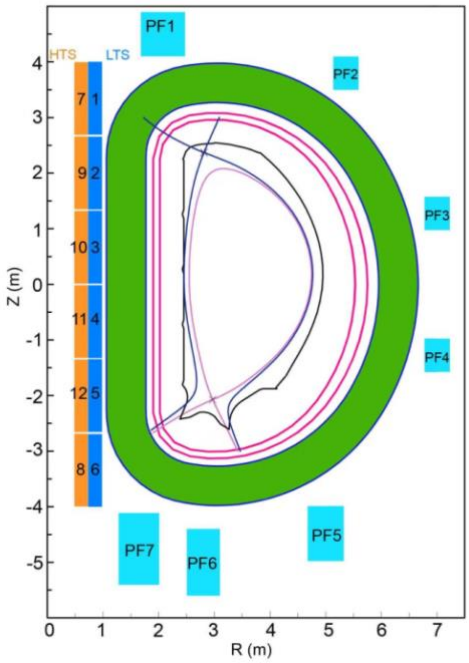

Major radius, R_0	3.6 m
Minor radius, a	1.1 m
Elongation, k	1.88
Triangularity, δ	0.49
Plasma volume	142 m^3
Magnetic field, B_0	6.15T
Plasma current, I_p	up to 7MA
Auxiliary heating power (nominal power) ECRH ICRH LH NBI	 15MW (24MW) 10MW (16MW) 10MW (16MW) 12MW (15MW)
Tritium inventory	110 g

Figure 1.4: (a) The poloidal cross-section of the plasma in BEST, together with the poloidal field coils and elements of the central solenoid. (b) Overview of the main machine and operational parameters of BEST.

Superconducting magnetic system

Details of the superconducting magnetic system are shown in Fig. 1.5. The system employs state-of-the-art superconducting technologies and consists of the following components:

- Toroidal Field (TF) coils: 16 coils, each weighing 87.2 tons, are fabricated using cable-in-conduit conductor (CCIC) technology. The TF coils are graded, employing ITER-standard Nb_3Sn for low-field regions and high-current-density Nb_3Sn for high-field regions.
- Poloidal Field (PF) coils: The PF system comprises 7 coils (see also Fig. 1.4(a)). Coils #1, #6, and #7 are made of Nb_3Sn, while coils #2-#5 use NbTi, forming a hybrid configuration optimized for magnetic field requirements.
- Central Solenoid (CS): The CS consists of 6 independent modules with a total weight of 180 tons. Each module employs a hybrid CCIC conductor combining Nb_3Sn (low-temperature superconductor, LTS) and YBCO (high-temperature superconductor, HTS). The nominal CS current is 46.5 kA, achieving a peak field value of 18.8 T (HTS) and 12.4 T (LTS), respectively. The total flux capacity of the CS is 53 V·s;
- Correction Coils (CC): A set of 8 coils, utilizing the same conductor technology as the ITER correction coils, to provide fine magnetic field adjustments.
- Ferromagnetic inserts (FI): similar to ITER, FIs will be installed inside the vacuum vessel to reduce the magnetic field ripple due to the finite number of TF coils to a level below 0.9%.

The total mass of the BEST magnetic system is approximately 2000 tons.

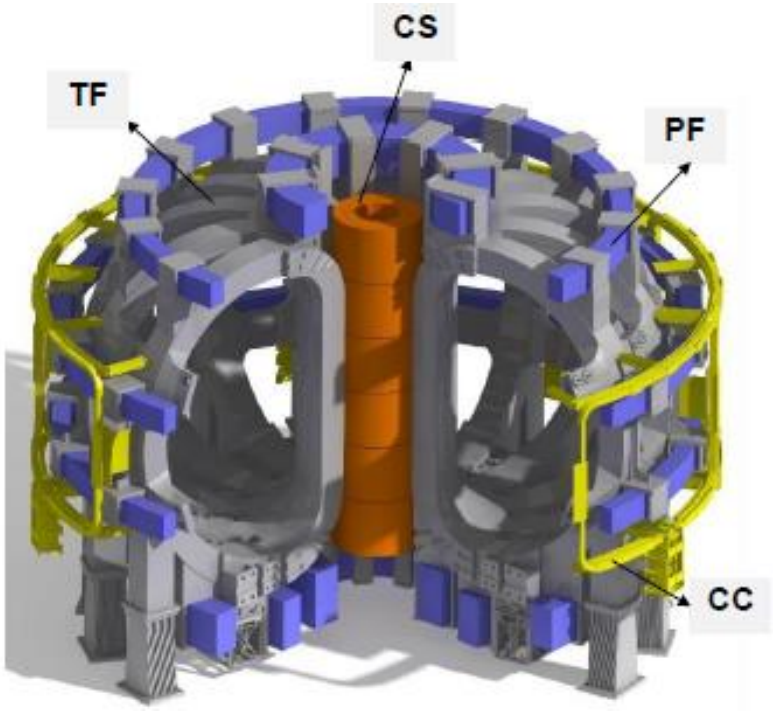

Figure 1.5: Schematic view of the magnetic field system in BEST, including the central solenoid, a set of 16 toroidal field and 7 poloidal field coils, and the system of magnetic field correction coils.

Plasma-facing components and divertor

Following an international R&D effort and in alignment with recent ITER re-baselining, BEST will employ a full-tungsten first wall and divertor. The first wall consists of two type of components – high and normal heat flux – totaling 240 modules. The first wall is primarily composed of copper tiles coated with tungsten, see Fig. 1.6(a). A chromium-zirconium-copper heat sink is incorporated, actively cooled by water at 4 Mpa and 70°C. The heat sink structure features multiple slits to reduce thermal stress and electromagnetic loads on the first wall, and the overall design is compatible with remote maintenance.

The actively cooled divertor is made of 48 cassette assemblies, each weighing approximately 1.6 tons and covering 7.5° toroidally. As shown in Figure 1.6(b), each cassette includes outer and inner vertical targets, dome structures, and cassette bodies. The divertor design emphasizes efficient cooling to manage high heat loads. Plasma-facing components (PFCs) are designed to withstand up to 10 MW/m^2, with the most exposed units (flat-type and monoblock designs) tolerating up to 15 MW/m^2. Detailed descriptions of the PFC and divertor design are presented in Chapter 6.

During D-T operation, the removal and installation of PFC modules will be performed using remote handling systems equipped with manipulators and specialized front-end tools.

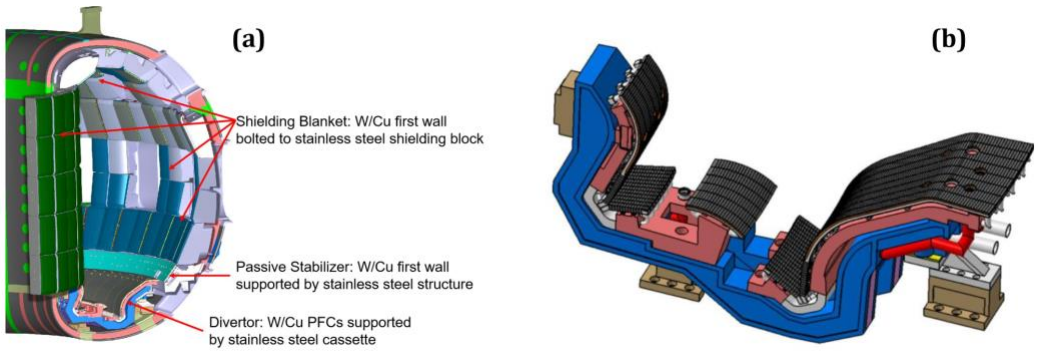

Figure 1.6: BEST has a full-tungsten first wall (a) and an actively cooled divertor (b).

Auxiliary heating and current drive systems

BEST will be equipped with a comprehensive set of auxiliary heating systems, comprising both NBI and RF heating. Figure 1.7 shows the top view of the device and the corresponding layout of the H&CD systems.

During the initial operational phase, a positive-ion-based NBI system (deuterium), operating at acceleration voltages up to 120 kV and injecting ~12 MW of heating power, will be installed in port O. The design is similar to that of the JET NBI system. In parallel, R&D activities at the CRAFT campus are ongoing towards the development of a negative-ion-based NBI (N-NBI) system†. A future upgrade is planned to enable N-NBI beam energies of 500-800 keV.

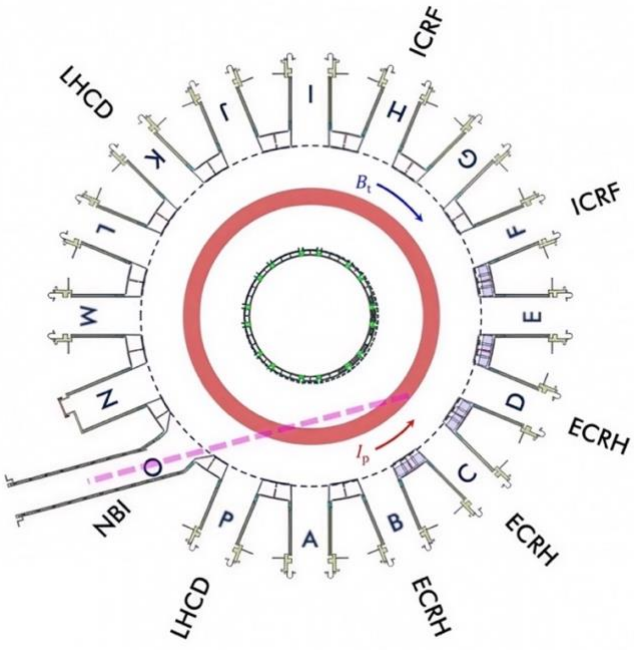

Figure 1.7: Top view of BEST showing the layout of the auxiliary heating systems. The heating mixture includes ECRH (15MW), ICRH (10MW), LH (10MW) and NBI (12MW).

† CRAFT has already demonstrated reproducible production of H^- beam ions with E_{NBI} = 202 keV and P = 2.3MW for 120 s [4].

Consistent with the approach of ITER, auxiliary heating in BEST will primarily rely on RF systems. To support long-pulse operation in a full-tungsten environment, 15 MW of Electron Cyclotron Resonance Heating (ECRH), operating at 170 GHz will be installed using three equatorial launchers (ports B, C and D). The design also includes 10 MW of coupled ICRH power delivered by two equatorial antennas (ports F and H). Initially, the ICRH system will operate in the frequency range f = 40-65 MHz, with further R&D planned to extend the frequency coverage to 90 MHz†. Both ECRF and ICRF systems have been designed to provide central heating, with flexibility for combined core and off-axis power deposition. Two high-power lower hybrid current drive (LHCD) systems (f = 4.6 GHz) capable to couple 10 MW for plasma heating and current drive applications will be installed (ports K and P). Additional details of the heating and current drive (H&CD) systems are provided in Chapter 5.

Tritium fuel cycle and test blanket modules

To support D-T operations, a tritium plant and associated subsystems have been developed for BEST. The device will rely on external tritium supply, with an initially licensed on-site inventory of up to 110 g. Various tritium handling techniques will be tested and explored including tritium fuelling, monitoring, removal, recovery and the direct internal recycling technology through the long pulses. In support of the fusion nuclear safety demonstration mission, most promising detritiation systems and technologies will be tested in view of demonstrating their reliability, effectiveness and the required technology readiness level for application in next step devices.

Although tritium will be externally supplied, BEST will also serve as a test platform for the development of tritium breeding technologies relevant for CFEDR and future fusion reactors. For this purpose, three dedicated Test Blanket Module (TBM) ports are available to validate breeding blanket concepts, assess in-service performance and RAMI characteristics, and support the optimization of blanket designs for CFEDR. Test areas for the TBMs in BEST measure 0.6×1 m^2 with a volume of 0.3 m^3. Further information is provided in Chapter 3.

BEST diagnostics

BEST relies on a comprehensive suite of diagnostics to support tokamak operation, plasma control, machine protection, and advanced physics studies. The system integrates mature and state-of-the-art technologies, including electromagnetic, laser-aided, microwave, spectroscopic, radiation, neutron, and fusion-product measurements. These are further complemented by nuclear electronics, first-mirror systems, synthetic diagnostics, and port-integrated components. Diagnostics in BEST provide measurements through robust, redundant designs optimized for the harsh nuclear environment and the need to minimize first-wall occupation. A detailed summary of BEST diagnostics is provided in Chapter 12.

† ICRH operation at $f \approx 90$MHz will enable the use of a hydrogen minority scenario at the nominal field $B_0 = 6.15$T, particularly relevant for long-pulse operations in BEST. More details are provided in Chapter 5.

1.4: BEST timeline

The construction of BEST is scheduled for completion by the end of 2027. The project's ambitious timeline is designed to achieve its high-level objectives as early as possible, see Fig. 1.8. Notably, the demonstration of scientific breakeven plasmas ($Q \geq 1$) is targeted before the end of 2030. Efforts towards this objective will start immediately after the first plasma, currently planned for the end of 2027 – beginning of 2028. The initial phase will focus on integrated commissioning, interleaved with plasma operations using hydrogen and deuterium at half-field conditions ($B_0 = 3.1$T) and plasma currents up to ~3MA. Key milestones during this stage include the demonstration of a robust plasma start-up scheme, validation of plasma position and current control algorithms, setup and initial operation of H&CD systems, including ICRH†, first tests of disruption control strategies, diagnostics validation, H-mode access, development of fuelling and isotope ratio control.

In the next stage, BEST will advance to deuterium plasmas, increasing the toroidal field to its nominal value $B_0 = 6.15$T. During this phase, several key developments will be implemented: wall conditioning techniques, incremental increase in H&CD system power capability, implementation of real-time kinetic and disruption control. These activities aim to prepare and optimize the scenarios for future $Q \geq 1$ D-T operations. Additional goals include further technical validation for D-T readiness, deep fuelling (pellet and compact torus injection) tests, demonstration of ELM and radiated-divertor control, tungsten impurity control, commissioning and optimization of the ICRF system with a ^{3}He minority scenario ($f = 60$-65 MHz), comprehensive diagnostic validation including neutron measurements and calibration. At this stage, plasma currents up to ~5-6MA are anticipated prior to first D-T experiments.

The first D-T plasma is planned at a reduced plasma current (~3-4 MA). This will be followed by systematic scenario development and a gradual plasma current increase toward 7 MA. Based on experience from JET and the ITER operational strategy, BEST will interleave D-D and D-T operations to accelerate scenario optimization. In this version of the Research Plan, we focus on conservative inductive scenarios as one of the viable pathways toward $Q \geq 1$ plasmas. As shown in Fig. 1.9, this route involves

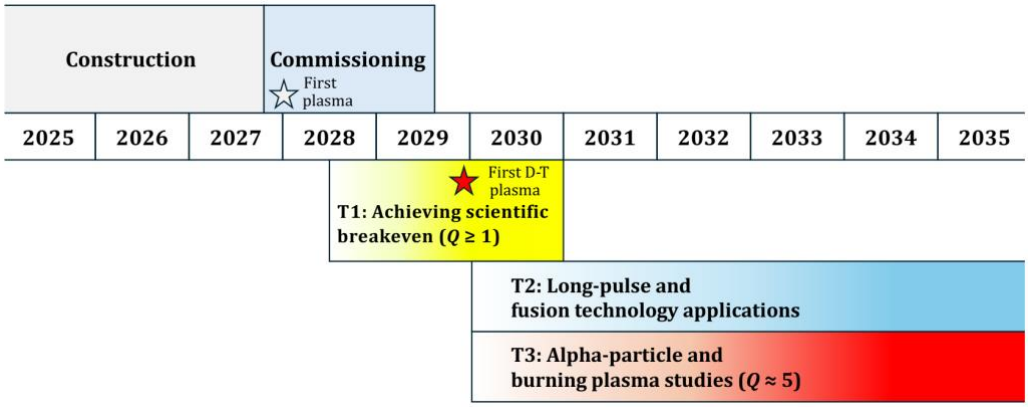

Figure 1.8: The provisional timeline of BEST.

† *At half-field ($B_0 = 3.1$T), hydrogen minority ICRH at $f = 45$-50 MHz will be applied in D-D plasmas.*

raising the plasma current to I_p = 6-7 MA, as further detailed in Chapters 2 and 4. State-of-the-art transport simulations predict that these scenarios can produce over 50 MW of fusion power with a fusion gain factor $Q \approx 1.5$ (with >90% thermonuclear neutrons), directly supporting high-level target #1. For comparison, this exceeds the previous fusion power record $P_{fus} \approx 16$ MW ($Q \approx 0.67$) – achieved transiently at JET in 1997 – by more than a factor of three.

Progress in D-T operations and towards high-level target #1 will naturally initiate activities supporting targets #2 and #3. Long-pulse operation ($t > 1000$ s) will demonstrate the integration of all physics, plasma control and technology elements required for continuous power production. It will also enable major technological advances – particularly relevant to the tritium fuel cycle and direct internal recycling – in support of CFEDR and future fusion power plants. Moreover, long-pulse operation will provide required conditions for the integrated testing of TBMs, including the experimental determination of the respective tritium breeding ratio. Promising long-pulse scenarios, capable of delivering $P_{fus} \approx$ 10-20 MW, are identified and discussed in Chapter 2.

Work on target #3 will begin already in the first D-T campaigns, when substantial fusion power and alpha-particle populations will be generated. Based on recent D-T results at JET, where several novel alpha-particle effects were observed [20], BEST offers unique opportunities for further discoveries, with its extended set of actuators for controling fast-ion and alpha-particle dynamics. These developments will proceed along the advancement of $Q \geq 1$ scenarios in support of target #1.

As mentioned in Section 1.2, achieving $Q \approx 5$ conditions will be more challenging and is expected to require advanced operational scenarios, potentially involving internal transport barriers or new high-confinement regimes. Of particular interest is the possible stabilizing effect of MeV-range fast ions and alpha particles on turbulence. Some of the simulations addressing these aspects are presented in Chapters 2 and 4, with further details to appear in the next edition of the Research Plan.

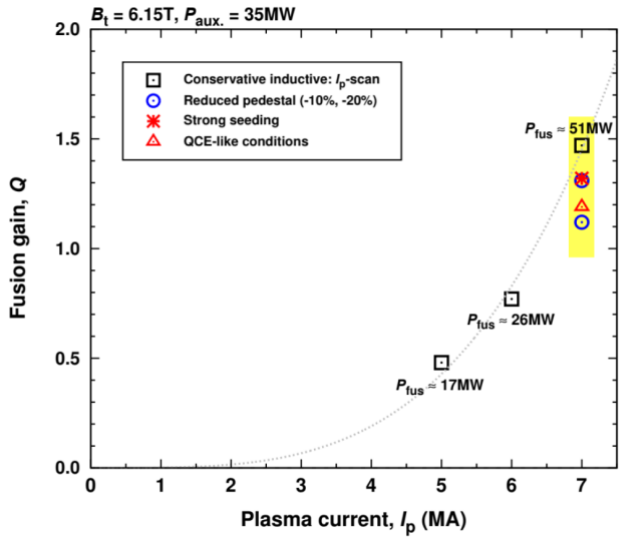

Figure 1.9: Achieving $Q \geq 1$ with conservative scenarios in BEST requires progress in scenario development at high plasma current.

1.5: BEST in support of ITER and CFEDR

As outlined in Section 1.1, BEST will provide valuable insights in plasma physics, fusion technology and nuclear safety, supporting both the operation of ITER, and the design and licensing of CFEDR and future fusion reactors. Currently, there is no D-T tokamak worldwide in operation. According to the recent ITER baseline, the first D-T operations in ITER are scheduled for 2041-2042, followed by the $Q \geq 10$ plasmas in 2044.

BEST features a full-tungsten wall and divertor, a similar mix of H&CD systems, and to a large degree relies on ITER-relevant plasma scenarios. In return, BEST will provide ITER with unique demonstration of D-T operation under full-tungsten wall environment and validation of ITER-relevant operational scenarios, together with a set of actuators envisaged for ITER such as wall conditioning techniques (e.g., boronization, ion cyclotron wall conditioning, and boron-powder injection).

In support of ITER, CFEDR and future fusion reactors, BEST will provide valuable data on the physics and operations in a full-W tokamak, including long-pulse operation [21, 22]. It will improve understanding of core confinement with a low torque, pedestal physics, core-edge coupling and full-integrated modelling (both interpretative and predictive), alpha-particle and fast-ion physics, heating system optimization, and control strategies. BEST will also facilitate the qualification and development of small-ELM and no-ELM regimes [16, 23], and the testing of AI/ML-based plasma control techniques aimed at reducing the risk of major disruptions.

In addition to physics advancements, BEST serves as a testbed for key technologies for CFEDR and future fusion reactors. These include:

- High-field superconducting magnets;
- Reactor-relevant divertor solutions;
- Burning plasma diagnostics and control;
- Remote handling and maintenance systems;
- Heating and current drive systems;
- Tritium fuel cycle and testing breeding technologies;
- Fusion nuclear safety.

The average neutron wall loading (NWL) is expected to range from ~0.05-0.1 MW/m^2 (at P_{fus} = 10-20 MW, long-pulse operation) up to over 0.4 MW/m^2 (at P_{fus} > 100 MW), assuming successful experimental development of high-Q pulses. Over 10 years of operation, BEST is projected to generate an accumulative fluence of >10^{26} neutrons, provided the device operates at least 10% of the time with P_{fus} > 10 MW. For reference, ITER will achieve a total fluence of 3.5×10^{25} neutrons by the end of its DT1 phase in 2048 [3]. Consequently, BEST provides a platform for early testing of materials and components under relatively low to modest neutron wall loadings. The experience gained at BEST will supply timely data to advance the required nuclear qualification of components towards the CFEDR programme†, where

† *In Europe, a dedicated new facility for nuclear qualification of components [24] is being considered to close outstanding gaps in readiness for fusion power plant deployment.*

Table 1.1: Main parameters of BEST compared to other facilities, illustrating its important mission as a supporting facility for ITER and CFEDR.

	EAST	**BEST**	**ITER**	**CFEDR**
R_0	1.8 m	3.6 m	6.2 m	7.8 m
a	0.45 m	1.1 m	2.0 m	2.5 m
V_{pl}	10 m^3	142 m^3	830 m^3	1600 m^3
B_0	2.5 T	6.15 T	5.3T	6.3 T
$I_{p,max}$	~1 MA	7 MA	15 MA	15 MA
$P_{fus,\ D\text{-}T}$	--	~10-200 MW	500 MW	1.5-3.0 GW
Tritium	--	Test fuel cycle and tritium breeding technologies	Test fuel cycle (including direct recycling) and tritium breeding technologies	Tritium breeding and self-sufficiency with TBR > 1
Fusion technologies (SC magnets, plasma-facing components, H&CD systems, diagnostics, etc.)	Support for BEST	Platform to develop key technologies for CFEDR and future fusion reactors	Test key technologies in reactor-relevant conditions	Demonstration of key technologies for commercial fusion power plant
Materials	Support for BEST	Test structural and functional materials under steady-state NWL ≈ 0.05-0.1 MW/m^2	Test structural and functional materials under NWL ≥ 0.5 MW/m^2 in high-duty operation (DT-2 phase [3, 4])	R&D of structural and functional materials with high neutron flux resilience, NWL > 1 MW/m^2

R&D on structural and functional materials with high neutron-flux resilience in support of PFPP will be undertaken in the next step (see Table 1.1). The cumulative damage is estimated at 0.04 dpa, comparable to 0.02-0.03 dpa expected at the end of DT1 phase in ITER.

BEST will also support the development of the tritium programme for CFEDR, where a tritium breeding ratio (TBR) above 1 and tritium self-sufficiency will eventually be demonstrated. This support is provided in two ways. First, BEST will demonstrate the tritium fuel cycle and accountancy, including the validation of the direct internal recycling (DIR) technology for tritium. Second, BEST provides a platform for the integrated tests of test blanket modules (TBM) in a tokamak environment. While the neutron fluence in BEST is limited for a full demonstration of tritium breeding, the TBM programme will support intermediate steps such as demonstrating the integrity and reliability of TBMs under normal and accidental operations, as well as

assessing tritium production and proving the feasibility of extraction processes[†]. As noted in Section 1.3, three TBM ports of 0.6×1 m^2 each are available on BEST. Further details on the tritium fuel cycle and TBM programme are provided in Chapter 3.

Finally, Table 1.1 summarizes the main parameters of BEST and highlights its important role as a research and technology support facility for ITER and CFEDR. One of the ambitious objectives of BEST includes the test of high-temperature heat removal and extraction systems suitable for the demonstration of electricity production. The comprehensive physics, technology and nuclear safety programme of BEST hence contributes to the preparation for CFEDR and accelerates the development of fusion energy production in China.

1.6: EAST in support of BEST

Finally, similar to how BEST serves as a supporting facility for CFEDR, a major upgrade of EAST was launched in September 2025. These planned upgrades aim to enhance the role of EAST platform for BEST physics and operations. The main upgrade items include [8]:

- Enlarged plasma radius and plasma volume to accommodate larger plasma currents up to 1 MA;
- Increased available injected power from 12 MW to 18 MW;
- Redesigned upper divertor with a BEST-like cooling structure capable of handling 12 MW/m^2;
- Installation of a new BEST-like divertor to further enhance power handling capability;
- Installation of a 3-strap ICRF antenna to reduce impurity sources and enable further development of ^{3}He and fast-ion ICRF scenarios;
- Addition of two new dual-frequency gyrotrons for flexible q-profile and current profile control;
- Deployment of a new passive-active multijunction (PAM) launcher to improve long-distance LHCD coupling.

[†] In addition to the TBM programme at BEST, the dedicated nuclear qualification facility under consideration in Europe [24] will be able to support preparations for the breeding blanket programme of CFEDR.

1.7: References

[1] Communique of the Fourth Plenary Session of the 20th Central Committee of the Communist Party of China, 23 October 2025
[2] IAEA, IAEA World Fusion Outlook, 3rd Edition, IAEA/PAT/012 (2025)
[3] P. Barabaschi and the ITER team, *30th IAEA Fusion Energy Conference* (2025)
[4] A. Loarte et al., *Plasma Phys. Control. Fusion* **67**, 065023 (2025)
[5] http://english.ipp.cas.cn/au/in/
[6] Y. Song et al., *Science Advances* **9**, eabq5273 (2023)
[7] X. Gong et al., *Nucl. Fusion* **64**, 112013 (2024)
[8] X. Gong et al., *30th IAEA Fusion Energy Conference* (2025)
[9] R. Ding et al., *Plasma Sci. Tech.* **27**, 100101 (2025)
[10] J. Li et al., *30th IAEA Fusion Energy Conference* (2025)
[11] H. Shirai et al., *Nucl. Fusion* **64**, 112008 (2024)
[12] M. Salewski et al., *Nucl. Fusion* **65**, 043002 (2025)
[13] C. Maggi et al., *Nucl. Fusion* **64**, 112012 (2024)
[14] F.G. Rimini et al., *Plasma Phys. Control. Fusion* **67**, 033001 (2025)
[15] A. Kappatou et al., *Plasma Phys. Control. Fusion* **67**, 045039 (2025)
[16] N. Vianello et al., *30th IAEA Fusion Energy Conference* (2025)
[17] C. Gormezano et al., *Nucl. Fusion* **47**, S285 (2007)
[18] Y.S. Na et al., *Nucl. Fusion* **65**, 093001 (2025)
[19] S. Ding et al., *Nature* **629**, 555 (2024)
[20] J. Garcia et al., *Rev. Mod. Plasma Phys.* **9**, 10 (2025)
[21] X. Litaudon et al., *Nucl. Fusion* **64**, 015001 (2024)
[22] J. Bucalossi et al., *30th IAEA Fusion Energy Conference* (2025)
[23] H. Zohm et al., *Nucl. Fusion* **64**, 112001 (2024)
[24] C. Bachmann et al., *Fusion Eng. Design.* **211**, 114796 (2025)

Chapter 2: Plasma Scenarios

Coordinators: E. Joffrin (CEA-Cadarache, France), B. Zhang (ASIPP), D. King (UKAEA)

With contributions from:
ASIPP Team: M.H. Li, W.B. Liu, D.H. Chen, H.L. Wang, K.D. Li, J.R. Wu, Z.F. Guan, W.Y. Lu, C.B. Wu, Y.H. Wang, P. Li, X.M. Zhong, T. Tang, X.D. Yang, Y. Tao, W. Zhang, K. Wu
EUROfusion Team: R. Ambrosino (Consorzio CREATE, Italy), E. Acampora (Consorzio CREATE, Italy)

2.1: Introduction: strategy to build up BEST scenarios

BEST is a burning plasma facility which bridges the gaps between ITER and CFEDR with compact high field advanced performance for steady-state operation. To achieve its objectives (cf. Chapter 1), several plasma scenarios are designed for BEST, using the tools like METIS and FFEQS [1, 2]. Table 2.1 below summarizes the main parameters and characteristics of the workhorse D-T scenarios of BEST.

To reach these scenario targets quickly and robustly, the building blocks of the scenario must be addressed in successive steps, synchronized with the machine and heating system development plan, see Fig. 2.1. In the first phase, plasma operation at reduced toroidal magnetic field $B_0 \approx 3.1$T will allow the validation of several important items prior to development of BEST operation at nominal toroidal field $B_0 = 6.15$T. At half-field, several items should be examined in details such as: robust plasma start-up scheme, plasma position and current control, isotope ratio control, coupling conditions of the RF power (mainly ICRF and LHW), disruptivity and disruption forces, disruption mitigation & avoidance, and runaway generation. If sufficient heating power is available, the following H-mode related issues will also be addressed: the control of tungsten, exit and entry to the H-mode in a full tungsten device, the H-mode operation with type I ELMs, the mitigation of ELMs and the MHD stability domain.

This first phase is also close to the operational domain of JET. A thorough comparison with JET data can be carried out and optimize the performance of the machine before moving to higher toroidal field. JET, BEST and ITER have very similar shape. BEST can reproduce JET shapes except perhaps the divertor geometry which is more triangular in BEST. The aspect ratios of BEST and JET are nearly the same. The identity match between JET and BEST (identical ρ^*, β, and ν^*) would lead to a BEST pulse at 3MA/2.1T. JET similarity at higher toroidal field and therefore at lower ρ^* is achieved at 4.3MA/3.0T, suitable for all RF heating systems at BEST. If done in D-T, this pulse would already generate about 10 MW of fusion power in D-T for a $\beta_N = 1.94$, according to the dimensionless calculations. This can be achieved with a moderate total heating power of 20-25MW when using the H_{98y2} scaling and could be a candidate for extending the duration and approaching the fully non-inductive scenario.

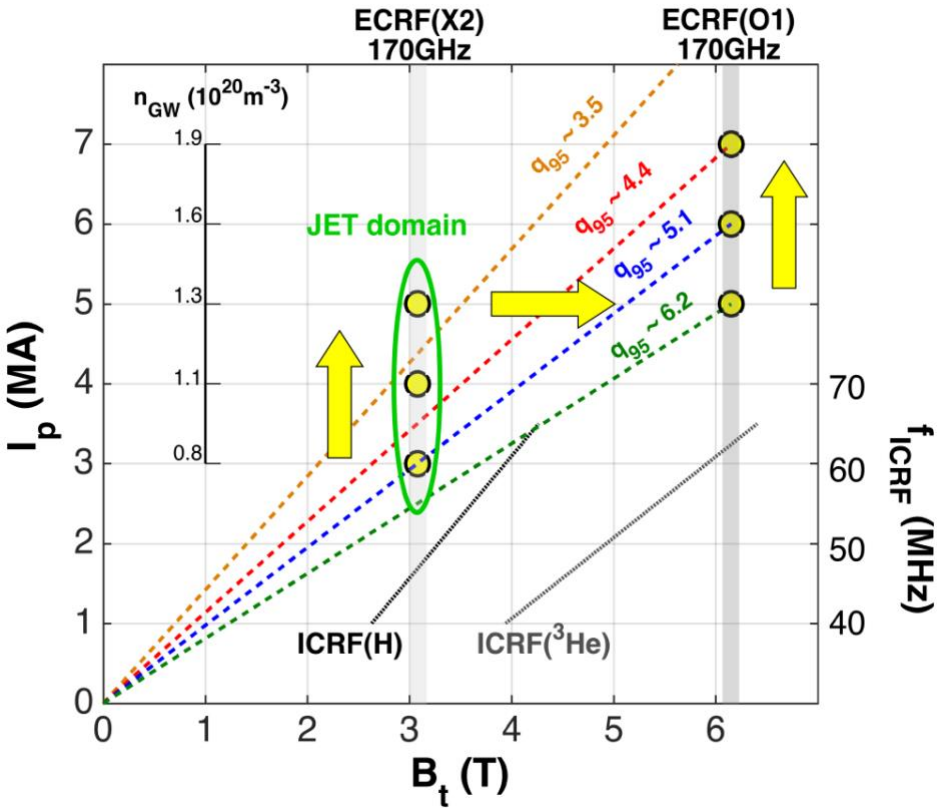

Figure 2.1: Schematic strategy for developing plasma scenarios in BEST.

Once the maximum plasma current is determined at half field, the second envisaged step is to move to the nominal toroidal field of 6.15T (yellow horizontal arrow in Fig. 2.1) and then further increase the plasma current step by step up to I_p = 6MA and then to 7MA (q_{95} = 4.4) using the O1 mode of ECRF power. At B_0 = 6.15 T, ICRF can be used efficiently with ^{3}He minority, and also with H minority scheme, depending on ICRF hardware availability and working frequency range. At each step in plasma current, the performance, disruptivity and reliability will be assessed before proceeding further. The stepwise approach to high current is important to establish a reliable and robust high performance H-mode with minimized risk to the machine.

It was consistently demonstrated both using METIS and ASTRA (see Chapter 4) that 6 MA was not sufficient to reach Q = 1 in this scenario with a conservative energy confinement enhancement factor of 1.1. The increase to 7 MA leads to an improved confinement and consequently the access to higher reactivity for the same amount of injected power (see Table 2.1). The controllability of the scenario at 6.15T/7MA is developed in the sections below particularly with respect to the flux consumption, potential MHD instabilities, fast-ion losses, heat loads, X-point formation time, access to a stable H-mode regime and exit of the burn phase.

Table 2.1: Overview of main parameters and characteristics of D-T scenarios in BEST (R_0 = 3.6 m, a = 1.1 m), as computed with the METIS code.

	$Q \geq 1$ scenario 1	**$Q \geq 1$ scenario 2**	**Long-pulse scenario**	**$Q = 5$ scenario**
B_0 (T)	6.15	5.0	6.15	6.15
I_p (MA)	7	7	4.5	7
q_{95}	4.25	3.46	6.85	4.7
Elongation, k	1.85	1.85	1.85	1.87
Triangularity, δ	0.4	0.4	0.4	0.51
P_{NBI} (MW)	12	11.5	11.5	10
P_{ECRH} (MW)	13	13	13	10
P_{ICRH} (MW)	10 (^{3}He minority)	10 (^{3}He minority)	10 (^{3}He minority)	10
P_{LH} (MW)	/	10 (ramp-up)	10	10
P_{rad} (MW)	9.8	9.1	8.0	10.3
$\langle n_e \rangle$ (10^{19} m^{-3})	8	8	5.4	16
$\langle T_e \rangle$ (keV)	7.3	7.5	6.45	7.3
$\langle T_i \rangle$ (keV)	7.4	7.2	5.7	7.3
W_{th} (MJ)	40.8	44	24	92
β_N, β_p	1.33; 0.68	1.7; 0.89	1.4; 1.2	2.7; 1.3
Non-inductive fraction	41%	48%	80%	55%
Bootstrap current (MA)	2.6	2.7	1.5	2.6
Flat-top duration (s)	50	50	1000	16
Fusion power (MW)	41	38	14	200
Fusion gain, Q	1.18	1.12	0.3	5

2.2: $Q \geq 1$ scenario development

2.2.1: Initial scenario design under nominal B_t = 6.15T

To achieve one of the main scientific goals of BEST, high-performance plasma operation with a fusion gain $Q \geq 1$, a baseline inductive scenario was designed using the METIS code [1]. This scenario features a plasma current I_p of 7MA, toroidal field B_t of 6.15T, volume-averaged density $\langle n_e \rangle$ of 8×10^{19} m^{-3} and total auxiliary heating power P_{aux} of 35MW, comprising 13 MW of Electron Cyclotron Resonance Frequencies (ECRF), 10MW of Ion Cyclotron Resonance Frequencies (ICRF), and 12 MW of Neutral Beam Injection (NBI), resulting in 41MW of fusion power at a confinement enhancement factor H_{98} of 1.1.

In this reference scenario, 5 MW of ECRF power is injected to assist initial plasma start-up. Following the establishment of a stable lower single null divertor configuration, the additional 8 MW of ECRF power is designed to inject in two subsequent steps: i) 3 MW of ECRF power expecting to heat the plasma and tailor current density redistribution during ramp-up phase and then ii) 5 MW of ECRF power to make contribution on the L-H transition at the flattop, see Fig. 2.2. On-axis ICRF working with ^{3}He minority scheme along with 120 kV NBI power are activated immediately after the plasma current reaches its flattop of 7 MA. The L-H transition occurs simultaneously and sustains under the condition of $P_{sep}/P_{L\text{-}H} \approx 1.5$ (where $P_{sep} = P_{in} - P_{rad} + P_{alpha}$ and $P_{L\text{-}H} \approx 22$ MW). Central plasma temperatures, as calculated by the METIS code, are $T_{e0} \approx 18$ keV and $T_{i0} \approx 14$ keV. Note that an extra 10 MW of Lower Hybrid Wave (LHW) power could be employed during the plasma current ramp-up phase for electron heating and current profile tailoring, reducing flux consumption and potentially enhancing plasma performance and pulse length. The extra LHW power can also be explored as one of the actuators for increasing $P_{sep}/P_{L\text{-}H}$.

In a next step, we have assessed the sensitivity of the fusion gain factor to the plasma current and assumed values of the confinement factor, H_{98}. Figure 2.3 shows the comparison of the operational domain for achieving $Q \geq 1$ at I_p = 7MA and 6MA, based on the results of METIS modelling (P_{aux} = 35 MW and B_0 = 6.15 T). The figure shows that in the case of I_p = 7 MA, $Q \geq 1$ plasmas can be reached with $H_{98} \geq 1.1$, in line with the integrated modelling results discussed in Chapter 4. Figure 2.3(a) also shows that scenarios with higher density would elevate fusion gain a little, up to $Q \approx 1.2$. Lower plasma current operation is preferable, in view of mitigating disruption risks and reducing flux consumption. Specifically, METIS simulations predict that at I_p = 6 MA, the confinement factor $H_{98} \geq 1.2$ is needed to optimize the performance and reach $Q \geq 1$ (see Fig. 2.3(b)), whilst effectively decreasing disruptivity risks and conserving flux resources well within the machine capabilities.

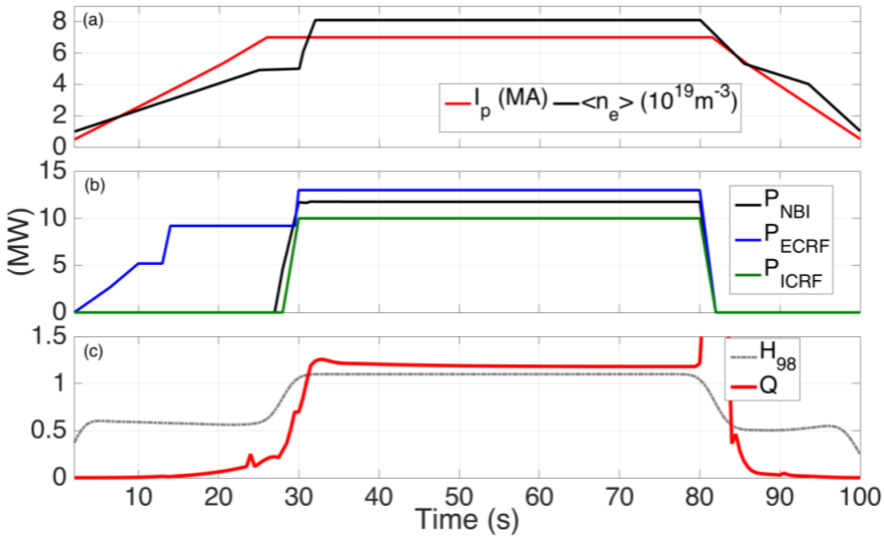

Figure 2.2: Overview of the reference inductive scenario at I_p = 7MA and B_0 = 6.15T for achieving $Q \geq 1$, as computed by METIS.

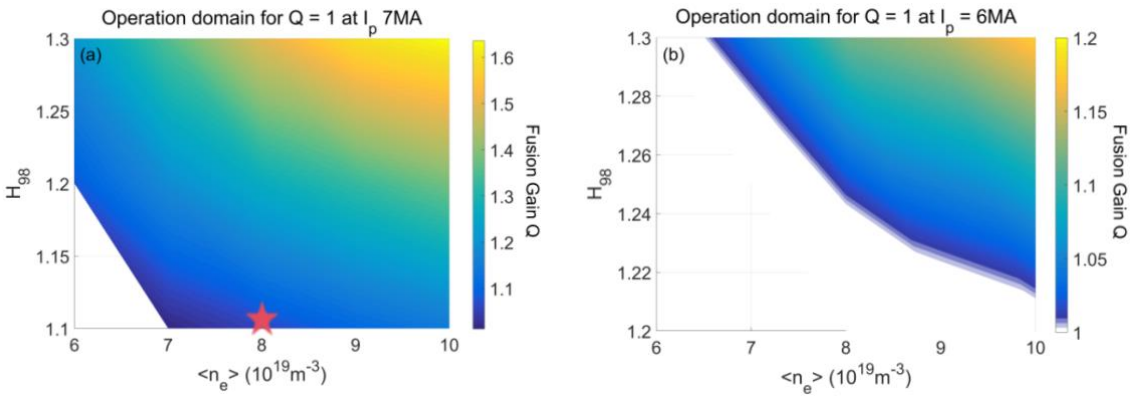

Figure 2.3: Operational domain to achieve $Q \geq 1$ plasmas at $B_0 = 6.15$T and $P_{aux} = 35$MW, as predicted by the METIS code: (a) $I_p = 7$MA and (b) $I_p = 6$MA. The star symbol indicates the parameters of the 7 MA scenario shown in Fig. 2.2.

2.2.2: Controllability of the $Q \geq 1$ scenario

As discussed in Chapter 1, the primary parameters of BEST are as follows: the major radius $R_0 = 3.6$m, the minor radius $a = 1.1$m, the maximum toroidal field $B_0 = 6.15$T, the maximum plasma current I_p reaching up to 7 MA, and the elongation ranging from 1.7 to 1.9. The total auxiliary power amounts to 50 MW, which can be utilized under various toroidal field conditions. ECRF launchers from three ports collectively supply 12 MW of power at a frequency of 170 GHz. Two ICRF antennas, operating at a frequency range of 40-65 MHz and with a power of 5 MW each, enable the implementation of hydrogen and ^{3}He minority heating schemes as needed. A 10 MW LHW at 4.6 GHz is anticipated to provide high-efficiency current drive capability, facilitating long pulse operation in particular. The NBI is projected to provide up to 15 MW of power at a beam voltage of 120 kV and even higher (800 kV) in the second phase of the machine. In addition to conventional fuelling technology, the newly developed compact torus injection system will be implemented to achieve deep fuelling with a velocity faster than 300 km/s. Boronization is also considered for wall conditioning in BEST.

Breakdown reliability (ECRF assistance). A robust plasma startup scheme characterized by a low toroidal electric field is of paramount importance for large superconducting tokamaks such as JT-60SA, BEST and ITER. Over the past several decades, ECRF pre-ionization and assisted plasma startup have undergone extensive research [3-12]. The magnetic field geometry serves as a decisive determinant during the tokamak plasma startup process, a wide null field configuration (NFC) with as low stray field as possible is preferable owing to its long connection length and superior particle confinement capabilities [13]. In large-scale devices, the plasma typically forms in the vicinity of the wall and subsequently expands gradually [14]. A centered breakdown was achieved on JET through an optimized hexapolar null field [15], while a quadrupolar and dipole-like null field were applied to Tore Supra [6] and KSTAR [8],

respectively. Conversely, the magnetic geometry featuring a curved vertical field, termed the trapped particle configuration (TPC), can confine charged particles by trapping them in a region with a lower magnetic field, which has been successfully demonstrated in JT-60SA at toroidal electric field $E_{\parallel} \sim 0.12\text{-}0.15$ V m^{-1} that is lower than the value in ITER (maximum 0.3 V m^{-1}) [4] recently and other devices [16-21]. The correlation between plasma startup and prefill gas pressure and ECRF power was quantitatively explored through parametric scans using the TPC [22], see Fig. 2.4. A linear relationship was observed between the critical gas pressure and the ECRF power, in line with the DYON code [23]. In scenarios with a higher impurity level, a higher amount of ECRF power was required. The ECRF power required for plasma startup in BEST can be estimated to be around 4 MW ($P_{\mathrm{ECRF}} \sim R_0^3$). Accordingly, 5 MW of ECRF power was selected for assisting initial plasma breakdown and start-up in the designed scenario, as discussed in Section 2.2.1.

Volt-second consumption. The volt-second consumption for the I_p = 7MA scenario was evaluated with the FEEQS code [2], using C_{Ejima} = 0.45 and input parameters from the METIS simulations described in Sections 2.1 and 2.2. In METIS simulations, the plasma current ramp rate of 0.25 MA/s was considered. The X-point is formed at 4 s after plasma breakdown. Early X-point formation and a short limiter phase are important to minimize tungsten erosion in the limiter phase and subsequent W contamination to the plasma. After X-point formation, the plasma current reaches the flat-top around 26 s, with a total volt-second consumption of ~26 V·s, including the breakdown phase. Assuming a pre-magnetization flux of 34 V·s, this leaves ~14 V·s available for the flat-top phase, allowing to sustain the 7 MA current phase for over 100 s. This result is consistent with CREATE-NL simulations [24], which confirm that a 100 s flat-top duration can be achieved over a wide range of C_{Ejima}, up to ~0.6. A detailed modelling and optimization of the breakdown phase, the optimization of the shape evolution during the current ramp-up & ramp-down, and L-H & H-L transitions will be addressed in future simulations to check additional flux losses and to assess the voltage and current limits during the evolution of the whole discharge.

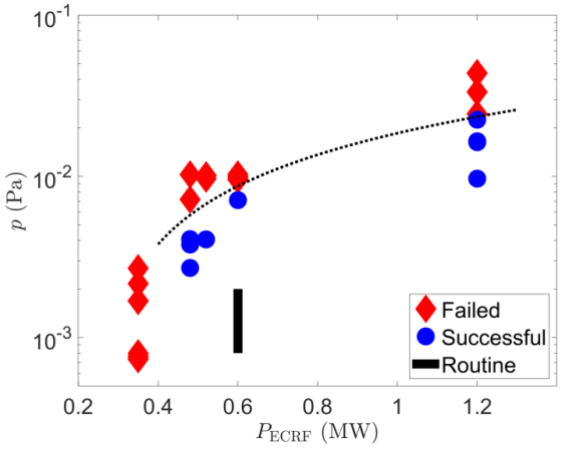

Figure 2.4: Impact of ECRF power and the prefill gas pressure on the plasma startup in EAST. Figure reproduced from [22].

Entry and exit burning phase (safe termination). The entry and exit to the burning phase are critical for the reliability of the scenario. Plasma current ramp-up of 0.25 MA/s is sufficient in principle to avoid external kink modes developing and hampering the access to the flat top phase. However, the use of LHCD or ECRF in the current ramp-up could lower the internal inductance in the ramp-up and external kink modes could develop as a result. The use of external electron heating (such as LHCD or ECCD) could also generate supra-thermal electron in the ramp-up [25] if the density is too low. These points are developed in Chapter 8 (MHD). The entry to the H-mode phase also requires attention as they could generate long ELM-free phase and giant ELMs which are often deleterious to the subsequent phase of the scenario. These could be avoided using adequate gas injection and plasma shape transition (i.e. increasing the shaping factor progressively when the main heating is applied).

Exiting from the main heating phase has been proven as a delicate phase in other metallic devices such as JET and ASDEX Upgrade [26]. Similarly, to the entry, long ELM free phases have been observed in several metallic devices as the plasma approaches the H-L transition which leads to uncontrolled build-up of impurities in the core and radiative collapse. The use of ELM control (using pellet pacing), core electron heating such as ECRF or ICRF (to reduce core tungsten peaking) and adequate ramp-down and shape reduction (lower elongation) are means used in other metallic devices to keep the burning termination safe [26] in addition to real-time control [27]. The active removal of impurities in this phase is essential to prevent the plasma becoming excessively radiative as the input power, plasma current and gas injection are reduced. Modelling the impact of ELMs in the termination has been carried out in the past for JET and could be applied to BEST in the future [28].

Required scenario kinetic control. Given that the $Q \geq 1$ scenario is designed to operate at I_p = 7MA, the most critical aspect of kinetic control is the identification and management of disruptions to prevent significant damage to the machine. Successful experience on JET suggests that a shifted ramp-down strategy could be implemented. Advanced algorithms should also be developed to predict disruptions in advance allowing an appropriate response. Since the quasi-continuous exhaust (QCE) regime could be compatible with the $Q \geq 1$ scenario (see Section 2.2.4 for more details), transient high heat fluxes should be minimized. Consequently, a strategy for dealing with stationary heat flux needs to be developed in compatibility with the QCE regime to safeguard the divertor target. Additionally, MHD stability control, such as sawtooth control, may be necessary for the $Q \geq 1$ scenario. The precise control and optimization of the plasma current profile is crucial for achieving and maintaining non-inductive current drive in tokamak operations, while simultaneously preventing the formation of excessively deep reversed magnetic shear configurations that could potentially trigger MHD instabilities. This requires careful adjustment of the current distribution through active feedback control systems and advanced plasma shaping techniques to ensure stable confinement conditions while maximizing the efficiency of non-inductive current generation mechanisms such as neutral beam injection or radio frequency

wave heating. The balance between these competing requirements, sustaining sufficient non-inductive current for steady-state operation while avoiding dangerous current profile distortions, represents an essential item in the BEST plasma control strategies, especially for achieve the long pulse and $Q \approx 5$ scenario mentioned in Section 3.4. The kinetic control also needs to take into account the real-time monitoring of plasma parameters. High-frequency diagnostics can be used to detect any sudden changes in plasma density, temperature, and current distribution (see the complete list in Chapter 12). This real-time data can help operators respond promptly to potential disruptions.

ECRF optimization at various magnetic fields. ECRF launchers, featuring high flexibility with mirror adjustment, accommodate diverse working conditions, thereby expanding the potential operational domain for BEST. For the nominal field B_0 = 6.15T, the ECRF power can be launched for co-I_p current drive from the on-axis to the off-axis region with a normalized minor radius $\rho \approx 0.5$ (mid-radius), achieving an average efficiency of 20 kA/MW, as follows from TORAY simulations. When the toroidal magnetic field is reduced to 5.5T, the ECRF system can offer even higher current drive efficiencies, averaging 35 kA/MW in the co-I_p direction. It has been discovered that the ECRF power remains effective at an even lower toroidal magnetic field of 5T, providing both heating and off-axis current drive capability.

2.2.3: High β_N candidate scenario at reduced B_t

The baseline scenario at 7MA/6.15T may be limited in terms of access to the high performance H-mode regime due to the high field. To give more margin for this scenario, a modified scenario at somewhat lower toroidal field, B_0 = 5-5.5T has also been investigated. According to the ITPA TC-26 scaling law [29], at B_0 = 5T the L-H power threshold shall be lowered by typically 20%. In addition, as discussed below the transient heat loads by ELMs are less severe than at 6.15 T. However, decreasing the toroidal field to B_0 = 5-5.5T in turn leads to two questions about: i) the loss of directivity and central deposition of ECRF and ii) the increase of the disruption risk because of the lower q_{95}.

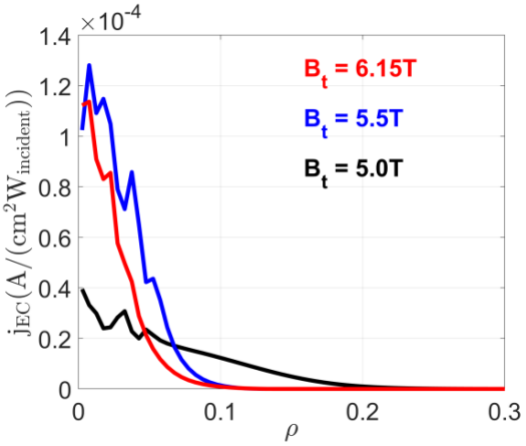

Figure 2.5: Comparison of ECCD profiles at the nominal toroidal field B_t = 6.15T and at reduced fields B_t = 5.5T and 5.0T.

Regarding the ECRF power deposition, calculations with the TORAY code show that reasonably central deposition is still feasible with, however, a broader deposition profile which may impact scenario central profiles, see further details in Section 2.2.2 and Fig. 2.5. Operating at lower q_{95}, may also increase the risk of disruptions at I_p = 7 MA since q_{95} goes down to 3.5. Therefore, a careful development approach should be applied with possibly a step at 5.5 T together with disruption prevention and mitigation measures integrated in the scenario (see Chapter 8).

2.2.4: Scenario challenges

L-H transition domain. The L-H power threshold for the 7MA/6.15T scenario was evaluated using the recent ITPA TC-26 scaling law, derived from the metallic-wall tokamak database [29]. Figure 2.6 shows the estimated $P_{L\text{-}H}$ for both D-T = 50%-50% and pure deuterium plasmas in BEST. The low-density branch is mimicked using the density correction factor as in [30]. Within the projected range of plasma densities for the target $Q \geq 1$ scenario, $\langle n_e \rangle \approx 0.65\text{-}1.0\times10^{20}$ m^{-3}, the operating domain corresponds to the high-density branch. For the considered conditions, the predicted $P_{L\text{-}H}$ for D-T plasmas is 15-22 MW, below the lower bound of the expected power through the separatrix, P_{sep} = 25 MW (counting only auxiliary heating and excluding alpha heating).

It should be emphasized that the scaling is sensitive to the divertor flux geometry relative to the pumping louvers, introducing a significant uncertainty in the $P_{L\text{-}H}$ estimate. To enlarge the L-H operational window and ensure stable type-I ELM H-mode access, additional measures have been considered. For example, operation at a slightly reduced toroidal field, B_0 = 5.0-5.5T, as discussed in Section 2.2.3.

Finally, it should be noted that the L-H threshold in pure deuterium plasmas is about 20% higher than in D-T, as demonstrated in JET. Consequently, without alpha heating, access to a robust H-mode at B_0 = 6.15T in D-D plasmas may be marginal.

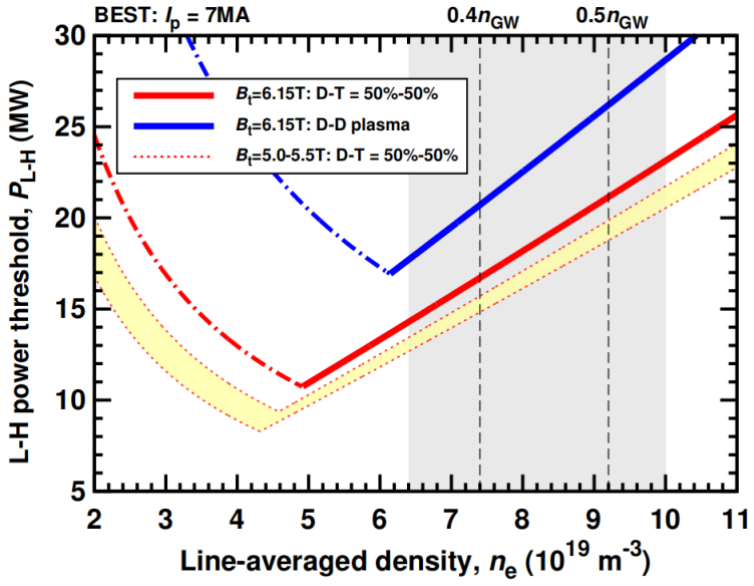

Figure 2.6: Estimate for the L-H power threshold in D-T plasmas in BEST (B_0 = 6.15T, I_p = 7MA), based on the recent TC-26 scaling law for metallic-wall tokamaks.

MHD instabilities and their control. Several MHD instabilities may impact the BEST scenario and are further discussed in Chapter 8. Given the moderate β_N, it is not expected that the considered $Q \geq 1$ scenarios will reach any ideal pressure limits. On the other hand, 2/1 neoclassical tearing modes (NTM) may become a concern as they can lead to disruption. Therefore, some dedicated ECRF power should be considered and kept in reserve in the scenario integration to ensure that these modes are under control if they occur.

Heat loads control and ELM size estimate. To guarantee the safe operation of the BEST facility, advanced control strategies have been developed and tested on the EAST tokamak utilizing the multi-view infrared camera system [31]. The infrared cameras provide real-time temperature information of the divertor target surface to a well-trained artificial intelligence (AI) actuator. Subsequently, the AI transmits the processed commands to the plasma control system to activate the feedback control function or the shifted ramp-down function, aiming to prevent divertor target damage induced by unacceptably high temperature.

In addition, ELM induced heat loss has also been assessed for BEST for the reference $Q \geq 1$ scenario at 7MA. The ELM parallel peak energy fluence can be described by the pedestal top pressure and can be expressed as: $\varepsilon_{\parallel} \sim 6\pi P_e R q_{edge}$ with $q_{edge} = ((1 + \kappa^2)/2)^{0.5}(a/R)(B_{tor}/B_{pol})$ [32]. Assuming an energy per ELM from 1.5 MJ to 6 MJ and an angle of incidence of 3 deg, the perpendicular energy to the target amounts to 0.9 MJ/m^2 at 6.15T and 0.73 MJ/m^2 at 5T. The original specification on targets of a maximum energy per ELM ~0.6 MJ for ITER was based on the avoidance of full surface melting on perfectly aligned, unshaped, castellated tungsten divertor targets. Using the same hypothesis for BEST, ELMs would be damaging above 2 deg of incidence.

As a result, ELM pacing and/or the development of no-ELM scenarios would be necessary on BEST to reduce divertor erosion, in particular for long pulses. Among the candidate approaches, the quasi-continuous exhaust (QCE) regime [33], recently demonstrated in D-T plasmas on JET [34], appears especially promising for exploration in BEST. Importantly, the high separatrix density, $n_{sep} \approx 4.5\times10^{19}$ m^{-3} (see Chapter 6), together with the reference plasma shape of BEST characterized by a high shaping parameter [33], $\kappa^{2.2}(1 + \delta)^{0.9} \approx 4.7$, provide favorable conditions for accessing this regime.

High-*Z* impurity control. In the context of BEST, which is a metallic device equipped with a tungsten divertor target, the high concentration of high-Z impurities presents substantial challenges. These impurities can originate from multiple components within the device, including tungsten. In the process of screening, it is arduous to efficiently segregate these high-Z impurities from the plasma. The screening mechanisms that were developed and utilized in JET by establishing an adequate ion temperature gradient in the pedestal region during the early stage [35, 36] should be tested and regularly implemented as soon as possible in the early plasma operation phase starting at B_t = 3.1T.

Regarding the control of high-Z impurity transport, sufficient on-axis electron heating power (such as ECRF or ICRF) should be considered to initiate effective outward particle transport through trapped electron mode (TEM) turbulence [37] or other mechanisms via a sufficiently high central electron temperature gradient.

2.3: Long-pulse scenario with $P_{fus} \approx 15$MW

In this section, we present the METIS modelling results for the BEST long pulse at 4.5MA/6.15T. This long-pulse scenario relies on a 4.5MA/3.1T plasma described in Section 2.1 and derived from the JET similarity. To reduce further the flux consumption, 10 MW of LHCD is applied during the ramp-up as well as the main heating phase. In this configuration it is assumed that the beams have an energy of 120 keV and ICRH ^{3}He minority scenario is applied†. The METIS results show that this pulse can reach ~14 MW of fusion power, divided into ~13 MW thermal D-T and ~1 MW of beam-target fusion. This pulse exhibits a total non-inductive current approaching 80%, which is composed of 1.5 MA of bootstrap current, 0.85 MA of LHW driven current, 0.75 MA of ECRF driven current, and 0.4 MA of NBI driven current. It could last more than 1000 s and possibly more making a record fusion energy of approximately 15 GJ and provides an excellent basis for the fusion technology goals of BEST. More detailed calculations are required to consolidate this result and optimize its duration.

With ~45MW of input power, a density of 6×10^{19} m^{-3} and a q_{95} of 6.7, the disruption risk are minimized and the ELMs are likely to stay at small amplitude. With a $\beta_N \sim 1.4$, the MHD (such as neo-classical tearing mode) threat should be minimized. Nevertheless, active control, will be mandatory in particular to control particle and heat flux for the whole duration of the discharge on the ICRF antenna and LHW launchers.

A first assessment of the flux consumption with the FEEQS code shows that this pulse would consume typically ~1 Wb every 33 s. With this flux consumption, the duration could be in excess of 1000 s, making a total injected energy (including P_{aux} and P_{fus}) of greater than 50 GJ using the same hypothesis that for the $Q \geq 1$ scenario regarding the flux consumption in the start-up phase. A further optimization of this phase would be necessary to extend further the duration of this long pulse.

The heat load control strategy will also be necessary for this long pulse scenario. Furthermore, the well-developed loop-voltage/flux loop feedback control scheme from EAST could also be implemented to BEST to facilitate control of flux consumption. This control strategy requires sufficient current drive capability source as actuator, such as LHCD or ECCD and needs further optimization for BEST future operation.

† At half-field $B_0 = 3.1$T, central ^{3}He minority ICRH requires RF frequency $f \approx 31$ MHz, outside the capability of the ICRF system on BEST.

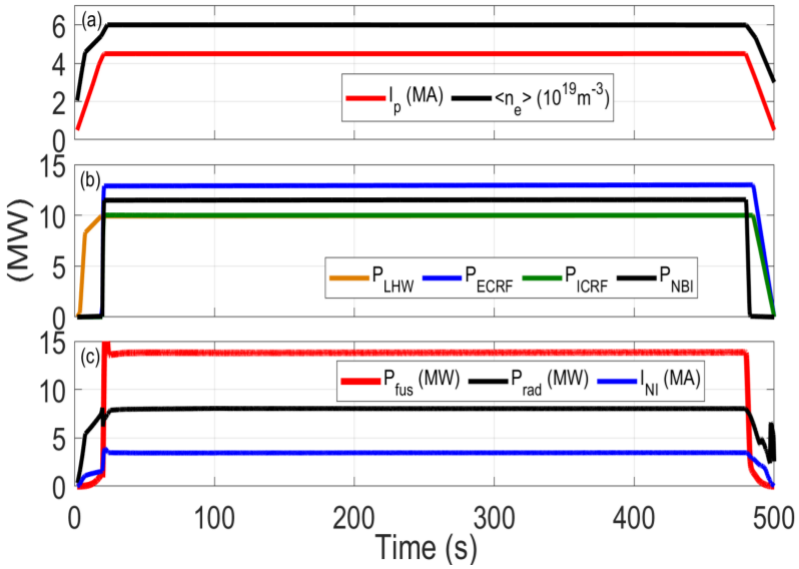

Figure 2.7: METIS modelling results for the BEST long-pulse scenario at 4.5MA/6.15T. With $P_{fus} \approx 14$ MW ($Q \approx 0.3$), this scenario makes it an excellent basis for the fusion technology studies on BEST.

The relationship between the triple product and the plasma duration has been established for existing devices based on the multi-machine international CICLOP database [38]. For the BEST device, the data points are calculated from the scenario METIS simulation described in this Chapter. Regarding the ITER device, the points correspond to the 400 s baseline scenario (I_p = 15 MA), the 1000 s hybrid scenario (I_p = 13.8 MA), and the advanced tokamak scenario (I_p = 9 MA), respectively [39]. The BEST device serves as an intermediate stage between existing devices and ITER, see Fig. 2.8.

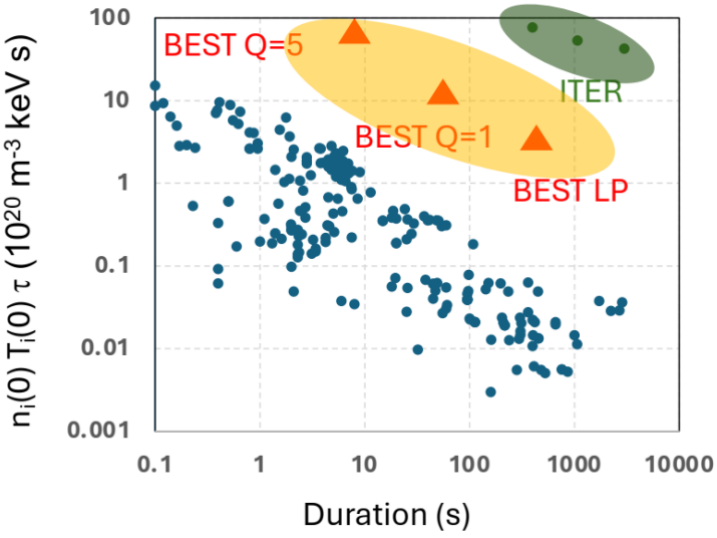

Figure 2.8: Projection of BEST as an intermediate step between existing devices and ITER. The figure shows the fusion triple product as a function of the plasma duration for existing devices (blue dots) [38], and the predicted values for BEST (red triangles) and ITER (green diamonds) [39].

2.4: $Q \approx 5$ scenarios for burning plasma physics studies

Apart from the study of alpha particles under the $Q \geq 1$ scenario, BEST is also tasked with investigating burning plasmas with high fusion gain. The initial evaluation of the feasibility of attaining high fusion gain plasma with a target of $Q \approx 5$ was carried out using the METIS code. In these simulations, we assume P_{ECRF} = 10 MW, P_{LHW} = 10 MW, P_{ICRF} = 10 MW and P_{NBI} = 10 MW, see Table 2.1. Note that this high fusion gain scenario should be regarded as an optimistic and idealized estimate, which needs much more effort experimentally.

The objective of this case is to exploit the maximum engineering capability of BEST device under favorable assumptions. To this end, two confinement enhancement factors H_{li} and H_{ITB}, available in the METIS code, are taken into account in our simulation. These enhancement factors will contribute to a higher H factor associated with the reductions in magnetic shear and increases in the pressure/temperature gradient, respectively. Therefore, compared to the $Q \geq 1$ case, the $Q \approx 5$ scenario can exhibit greater energy content and better confinement. The temporal evolution of the auxiliary heating power and key plasma parameters is depicted in Fig. 2.9. With a ramp-up rate of 0.25 MA/s, the plasma in this 75 s discharge attains the steady flat-top phase at approximately 28 s. Subsequently, it sustains a 7 MA current and a volume-averaged density of 1.6×10^{20} m^{-3}.

This scenario is distinguished by a predominant inductive Ohmic current fraction of approximately 50%. During the flat-top phase, the alpha particle power reaches around 40 MW, facilitating sustained burn with $Q \approx 5$. The normalized parameters $\beta_p \sim 1.3$ and $\beta_N \sim 2.7$ also signify enhanced confinement and high-performance ($H_{98} \sim 1.2$) inductive plasma. The results of the modeled profiles further reveal central electron temperatures T_{e0} of 26 keV and ion temperature T_{i0} of 33 keV at 45 s, accompanied by the formation of an internal transport barrier. A reversed-shear

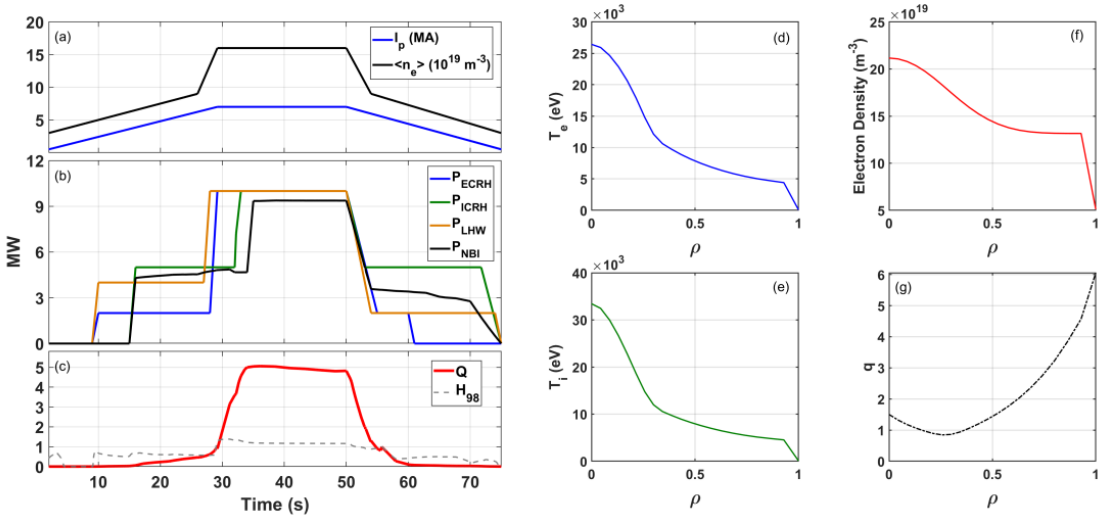

Figure 2.9: METIS modelling results for the high fusion gain $Q \approx 5$ scenario in BEST.

safety factor profile is also established with $q_0 \sim 2$ and $q_{\min} \sim 1$. These results suggest that this well-designed configuration, which integrates auxiliary heating schemes with tailored current and pressure profiles, enables access to higher-Q operational scenarios within the engineering limitations.

Incorporating more robust and physics-based models to account for transport physics, effects of MHD stability and power exhaust, and validating with other free-boundary equilibrium codes are planned to improve the fidelity of this scenario prediction.

2.5: Summary and future work

Scenario design and modelling has been initiated to prepare the operational regimes required for BEST to achieve its three key targets. Promising results have been found for the $Q \geq 1$ and long-pulse scenarios showing that the goals of BEST are consistent with the machine capabilities. A pathway to success in the $Q \approx 5$ scenario has been shown although more work is required to further develop this strategy.

The preparation of all the scenarios will continue, including the development of a generic platform for control schemes using plasma state reconstruction, monitoring, supervisory controller and actuator manager. Further modelling of each scenario is also in progress to study small/no ELM regimes, entry and exit to the H-mode, optimization of the non-inductive current, ramp-up/ramp-down analysis, heat and particle load control etc. These studies will be assisted by specific experiments on EAST and using the capabilities of other devices.

2.6: References

[1] J.F. Artaud et al., *Nucl. Fusion* **58**, 105001 (2018)
[2] H. Heumann et al., *J. Plasma Phys.* **81**, 905810301 (2015)
[3] J. Zhang et al., *Nucl. Fusion* **63**, 076028 (2023)
[4] M. Yoshida et al., *Plasma Phys. Control. Fusion* **67**, 065010 (2025)
[5] G. Granucci et al., *Nucl. Fusion* **55**, 093025 (2015)
[6] J. Bucalossi et al., *Nucl. Fusion* **48**, 054005 (2008)
[7] J. Lee et al., *Nucl. Fusion* **57**, 126033 (2017)
[8] Y.S. Bae et al., *Nucl. Fusion* **49**, 022001 (2009)
[9] K. Kajiwara et al., *Nucl. Fusion* **45**, 694 (2005)
[10] B. Lloyd et al., *Nucl. Fusion* **31**, 2031 (1991)
[11] G.L. Jackson et al., *Fusion Sci. Tech.* **57**, 27 (2010)
[12] R. Chen et al., *Nucl. Fusion* **64**, 066034 (2024)
[13] Y. Gribov et al., *Nucl. Fusion* **47**, S385 (2007)
[14] ITER Physics Expert Group on Disruptions, Plasma Control, and MHD et al., *Nucl. Fusion* **39**, 2577 (1999)
[15] R. Albanese et al., *Nucl. Fusion* **52**, 123010 (2012)
[16] C.B. Forest et al., *Phys. Rev. Lett.* **68**, 3559 (1992)
[17] T. Maekawa et al., *Nucl. Fusion* **52**, 083008 (2012)

[18] J. Sugiyama et al., *Plasma and Fusion Research* **3**, 026 (2008)
[19] Y. Ko et al., *Plasma and Fusion Research* **16**, 1402056 (2021)
[20] M. Ishiguro et al., *Journal of Physics: Conference Series* **511**, 012041 (2014)
[21] Y. An et al., *Nucl. Fusion* **57**, 016001 (2017)
[22] W. Liu et al., *Nucl. Fusion* **64**, 126072 (2024)
[23] H.-T. Kim et al., *Plasma Phys. Control. Fusion* **55**, 124032 (2013)
[24] R. Albanese et al., *Fusion Eng. Design* **96-97**, 664 (2015)
[25] A. Matsuyama et al., *Nucl. Fusion* **63**, 026001 (2023)
[26] E. de la Luna et al., *27th IAEA Fusion Energy Conference* (2018)
[27] S. Van Mulders et al., *Plasma Phys. Control. Fusion* **66**, 025007 (2024)
[28] F. Koechl et al., *Plasma Phys. Control. Fusion* **60**, 074008 (2018)
[29] P. Vincenzi et al., *Plasma Phys. Control. Fusion* **67**, 045013 (2025)
[30] J.W. Hughes et al., *Nucl. Fusion* **65**, 052001 (2025)
[31] J.Y. Zhang et al., *Rev. Sci. Instrum.* **91**, 116101 (2020)
[32] T. Eich et al., *Nucl. Mater. Energy* **12**, 84 (2017)
[33] M. Faitsch et al., *Nucl. Fusion* **63**, 076013 (2023)
[34] M. Faitsch et al., *Nucl. Fusion* **65**, 024003 (2025)
[35] A.R. Field et al., *Nucl. Fusion* **63**, 016028 (2023)
[36] O. Linder et al., *Nucl. Fusion* **59**, 016003 (2019)
[37] W.L. Zhong et al., *Phys. Rev. Lett.* **111**, 265001 (2013)
[38] X. Litaudon et al., *Nucl. Fusion* **64**, 015001 (2024)
[39] B.J. Green and ITER International Team and Participant Teams, *Plasma Phys. Control. Fusion* **45**, 687 (2003)

Chapter 3: Tritium Breeding and Fuel Cycle

Coordinators: R. Kamendje (EUROfusion), R. Villari (ENEA, Italy), S.L. Zheng (ASIPP)

With contributions from:
ASIPP Team: L. Chen, H.S. Zhou, S.L. Liu, K.C. Jiang, Q.J. Zhu, W.B. Li, X.K. Zhang, K. Xu, J. Wu, X.M. Ren, Y. Lan
EUROfusion Team: S. D'Amico (KIT, Germany), G. Aiello, J. Elbez-Uzan

3.1: Introduction

One of the set objectives of the BEST facility is to serve as a platform the validation of key breeding blanket and fuel cycle technologies and processes necessary for the successful design, construction, licensing, operation and exploitation of next step facilities such as CFETR or EU DEMO. This chapter aims at articulating the research and development work that is foreseen to be conducted on BEST in order to fulfil this objective.

3.2: Integral testing for the validation of breeding blanket concepts and technologies

With the objective of testing tritium breeding technology for CFEDR, provision has been made in the BEST design for three dedicated equatorial ports for the installation of Test Blanket Modules (TBM), see Fig. 3.1. Each port is planned to accommodate a different blanket concept including corresponding auxiliary systems, such as cooling system, nuclear measurement system, tritium extraction and accountancy system, and data acquisition and control system. ASIPP will install and test two TBMs based on the CO2 COOled Lithium lead (COOL) [1] and Water Cooled Ceramic Breeder (WCCB) [2] blanket concepts, respectively. Europe is currently considering the installation and testing of a TBM based either on the Water Cooled Lithium Lead (WCLL) [3] or the Helium Cooled Pebble Bed (HCPB) [4], or the Water Lead Ceramic Breeder (WLCB) [5] concept.

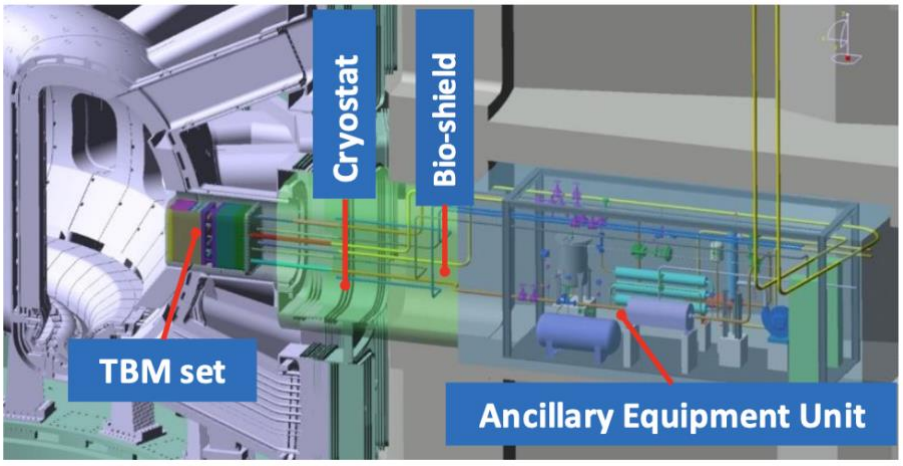

Figure 3.1: Port configuration for Test Blanket Modules (TBMs) in BEST.

The main objective of the TBM testing programme in BEST is to provide essential data to contribute to demonstrate:

- the integrity and reliability of TBM under normal and accidental conditions;
- tritium production and extraction performance, and the characterization of tritium technologies and nuclear interactions;
- high-temperature heat removal and high-grade heat extraction suitable for electricity generation

and validate:

- design tools and the database used in the neutronics, electromagnetic, thermal-hydraulic, tritium transport, failure rates and safety analysis for the blanket design.

3.2.1: Tritium production evaluation

Ensuring tritium self-sufficiency is a key objective in the development of fusion reactor blanket systems. Therefore, a primary goal of the testing program is to measure the actual tritium generation capability of the TBM, expressed as the Tritium Production Rate (TPR) during D-T operation, and validate the neutronic predictive models and measurements techniques (see Section 11.3).

While validating tritium generation remains a complex and uncertainty-prone task, it is crucial for confirming the accuracy of design tools and supporting the advancement of self-sufficient fusion reactor technologies.

3.2.2: Tritium extraction and accountancy

An essential process for achieving tritium self-sufficiency in fusion systems is not only sufficient tritium production but also effective extraction and accountancy. This includes extracting tritium from the TBM and accounting for all tritium streams within the blanket system – from generation in the breeding material to its delivery back to the fuel cycle (see Section 3.3). Tritium accountancy is a primordial safety objective to control the total tritium inventory within a fusion plant.

One of the core objectives of the testing program is to demonstrate tritium extraction technology from blankets. Each TBM features a suitable tritium extraction scheme relevant to the DEMO reactor. In general, solid blanket concepts use helium purge gas mixed with few amounts of hydrogen for extracting tritium from TBM breeder zones, the hot metal reduction bed or cryogenic molecular sieve bed for separating hydrogen isotopes from helium, and the hydrogen absorption bed for storing hydrogen isotopes. While for the liquid blanket concepts, permeator against vacuum, gas-liquid contactor or vacuum sieve tray can be used for extracting tritium from the liquid breeder.

Another core objective is to achieve accurate tritium accountancy across the entire system. This involves evaluating the performance and efficiency of recovery components, estimating tritium inventories in structural materials and system components, and quantifying any losses to the environment, particularly through

permeation. Currently, a tritium accountancy system involving catalytic oxidation, cold traps, and liquid scintillators will be selected for the WCCB TBM while accounting equipment of quadrupole mass spectrometry and ionization chambers will be used for the COOL TBM. The EU TBM will choose suitable accountancy schemes according to the corresponding blanket concept selected.

The system is designed to manage the tritium fuel cycle and operate with materials and components relevant to future reactors and includes a complete tritium extraction and accountancy loop. This allows for end-to-end tracking of tritium, from its creation in breeding units to its capture, concentration, and transfer to external processing systems.

Accurate tritium accountancy is relevant for safety purposes and for granting the operation license. Efforts will focus on developing measurement technologies to ensure consistent and reliable data collection. Key areas include:

- Detector calibration (standardized calibration and cross-calibration procedures should be developed to ensure accuracy over time in a DT environment);
- Control of measurement conditions (controling environmental factors such as temperature, humidity, and electromagnetic interference is crucial for obtaining precise online measurements. Protocols should be established to minimize variability in measurement conditions).

3.2.3: Heat removal function

High-grade heat extraction is essential for effective electricity generation. This is based on high-temperature heat removal of nuclear heat and first wall heat flux from the blanket itself. Therefore, it is important to validate in BEST the heat removal capability of the TBM systems under test. In view of this, each TBM has a corresponding cooling system. The main functions of the cooling system are: (i) provide the coolant and remove heat from the TBM during plasma operation; (ii) preheat the TBM before plasma operation; (iii) supply and drain the coolant in case of system maintenance; and (iv) contain the low-activity coolant and ensure safety operation.

The following possible thermal hydraulic experiments can be done with the BEST TBM systems:

- Flow resistance and flow distribution inside the first wall and other cooling components;
- Heat transfer characteristics and temperature distributions of the TBM structures;
- Flow and heat transfer characteristics of the breeder zones of ceramic pebble beds;
- MHD effects and pressure drop in the breeder zones of the liquid metal;
- Thermal hydraulic response of the TBM systems under pulsed, steady state and accidental scenarios.

Several coolant systems will be constructed for TBM testing. For example, the high-pressure water loop will operate for the water cooled TBM, while the PbLi loop and S-CO_2 loop will run during the COOL TBM operation. Different TBMs can share similar coolant systems and be tested one by one according to the test plan.

3.2.4: Technology relevance for sub-systems components

Each test blanket system includes several auxiliary sub-systems beyond the main module itself, such as cooling loops, tritium recovery systems, liquid metal circuits, purification units, and monitoring systems. While these sub-systems are primarily designed to meet operational and safety requirements of the host facility, some of their technologies may also be relevant for application in future power-producing reactors.

The core objective is to ensure these sub-systems operate reliably and safely under reactor-relevant conditions. Components are selected and optimized mainly based on their ability to comply with regulatory requirements, minimize failure risks, and allow maintainability. However, relevance to future reactor systems is also considered, particularly where scalability, modularity, or functional similarity exists.

Technological relevance is defined as the ability of a system or component to perform its intended function under the more demanding conditions of a pilot reactor, without needing substantial design changes. This includes maintaining technical and economic feasibility when scaled up in terms of throughput, integration, and efficiency. Examples of sub-system components with potential relevance in BEST include:

- Coolant purification units, which manage water chemistry and control corrosion products;
- Tritium recovery units, such as getter beds or extraction modules;
- Liquid metal processing systems, including cold traps and tritium extraction devices;
- Tritium accountancy systems, capable of compact, accurate mass flow and inventory tracking.

Ongoing design work includes assessing the scalability and applicability of these sub-systems to power reactor conditions and identifying which components can contribute to future reactor development goals without requiring major redesign or reinvestment.

3.2.5: Instrumentation development

Achievement of the technical objectives of the TBM programme is derived from the analysis of operational data. Therefore, the development and deployment of advanced instrumentation systems is a critical part of the overall strategy. The main goal is to ensure the system is equipped with sensors capable of monitoring all key physical parameters that influence performance, safety, and scientific analysis. These include:

- Magnetic fields;
- Electric currents;
- Mechanical forces and strain;
- Displacement and vibration;
- Temperatures and pressures;
- Flow rates and flow patterns;
- Tritium concentrations and chemical composition;
- Neutron and photon fluxes and spectra;
- Tritium production rates.

This comprehensive set of measurements is essential for two purposes: first, to provide real-time operational control and safety assurance; second, to support post-processing and validation of theoretical models and simulation tools.

Since the materials and technologies used in the test blanket are aligned with those foreseen for future reactors, many of the instruments tested in this environment will be directly applicable to larger-scale systems. Their operation under fusion-relevant conditions will allow for the evaluation of their accuracy, reliability, and durability in a harsh nuclear environment.

Additionally, the testing programme serves as a proving ground for integrating complex instrumentation within compact and highly constrained environments, which mirrors the challenges expected in commercial fusion systems. The insights gained will guide future improvements in sensor design, placement, and data acquisition strategies, supporting the broader goal of validated, predictive reactor modelling and safe, efficient operation.

3.2.6: Development of simulation tools

A core requirement for achieving the objectives of the test blanket programme is the development and validation of simulation tools that can accurately model the physical behaviour of the system during reactor operation. These tools are essential both for interpreting experimental data and for designing future fusion reactor components. The simulations cover a wide range of scientific and engineering domains, including:

- Thermo-hydraulics of high-pressure cooling systems;
- Magneto-hydrodynamics (MHD) of liquid metal flows;
- Tritium transport across solids, liquids, gases, and interfaces;
- Structural mechanics under combined loads;
- Electromagnetic response of components;
- Neutronics for nuclear performance and shielding.

These tools serve two main functions:

- Correlative function: supporting the analysis of experimental data by simulating the conditions and responses observed during operation. This requires detailed physical modelling and high spatial and temporal resolution to reflect real-world behaviour accurately.
- Predictive function: enabling design and optimization of future reactor components by extrapolating performance under different operational conditions. This requires generalizable physics models and robust numerical schemes capable of handling increased complexity and scale.

To fulfil both roles, models must be built with sufficient fidelity to capture key phenomena while also being adaptable to a variety of scenarios. Validation against experimental data from the test blanket system will provide the confidence needed to apply these tools in the design of full-scale fusion reactor systems. Overall, simulation tools form a critical bridge between experimental results and reactor design, enabling both a deeper scientific understanding and practical engineering application.

3.2.7: TBM system safety – accidents and reliability

Operation of the test blanket system in a fusion environment provides a unique opportunity to strengthen the overall safety framework for future reactor designs. The goal is to validate safety principles, assess risk scenarios, and develop reliable methodologies for managing safety-related aspects of blanket technologies. Key objectives include:

- Defining safety functions and classifications for all components of the system, ensuring they meet the requirements for confinement, control, and protection under normal and abnormal conditions.
- Systematically identifying and analysing potential accident scenarios, including both internal failures and external events (BEST-relevant), to determine system responses and mitigation strategies.
- Developing and applying advanced safety analysis tools, such as MELCOR, RELAP5, etc. which simulate the behaviour of the system under accident conditions using reactor-relevant materials and configurations.
- Estimating the radiological inventory and evaluating radioactive waste generation, including its classification, handling, and long-term management strategies.
- Preparing safety documentation and supporting licensing efforts, drawing from real operational data, design validation, and experimental findings.

These activities provide essential input to the design of future fusion reactors, where complex interactions among structural, thermal, and nuclear systems must be thoroughly understood and controlled. The lessons learned and data gathered will directly inform the development of licensing strategies, regulatory compliance pathways, and operational safety measures for future power plants.

3.2.8: Risk, cost, and RAMI analysis

A key long-term goal of the test blanket program is to generate foundational knowledge for assessing and managing the risks, costs, and lifecycle performance of breeding blanket systems. This includes identifying manufacturing challenges, understanding regulatory impacts, and building a database to support design optimization for future fusion power plants. Specific objectives include:

- Identifying cost drivers and risk factors associated with procurement, fabrication, and licensing, especially where novel materials, advanced manufacturing techniques, and regulatory requirements intersect;
- Supporting industry readiness by providing component suppliers and integrators with real-world insights into the full lifecycle of blanket systems, from design through licensing and operation;
- Expanding the RAMI database, focusing on reliability, availability, maintainability, and inspectability by collecting data from operational performance and post-irradiation evaluations.

Post-irradiation examinations (PIE) of materials and components will contribute to:

- Evaluating early-life failures in structural elements and joints;
- Characterizing irradiated materials, including microstructural changes, mechanical properties, and tritium retention behaviour;
- Verifying model predictions and enhancing understanding of fusion-relevant phenomena under low-dose but spectrum-representative neutron exposure;
- Studying functional materials (e.g. ceramics, liquid metals, coatings) for their performance, chemical stability, and compatibility with structural components.

Though irradiation levels in the test environment are lower than in a power reactor, the neutron spectrum is representative, making the data critical for validating materials and systems that cannot be adequately tested in fission reactors. In summary, these activities are essential for reducing uncertainty, guiding design decisions, and supporting the development of economically viable, reliable, and licensable blanket systems for future fusion energy applications.

3.2.9: Materials testing

The BEST facility will provide the first opportunity to test breeding blanket technologies and materials in an integrated fusion environment with a representative 14 MeV neutron spectrum. Although the total neutron fluence will be limited, BEST offers unique prospects for early fusion-relevant material testing – particularly for functional materials such as breeders and multipliers, as well as for structural and interface materials. Importantly, even before the onset of the D–T plasma phase, BEST's non-nuclear phase enables critical material and system-level testing under fusion-like thermal, mechanical, and electromagnetic conditions, but without neutron irradiation. In both phases, the emphasis is placed on assessing the "in-service behaviour" of materials – that is, their operational compatibility and degradation – rather than on the basic characterization of their physical or mechanical properties. A systematic comparison of material properties and performance between the non-nuclear and nuclear phases will allow to decouple and understand the specific effects of neutron irradiation from those induced by other operating loads. The type of investigations that could be realized in BEST are tentatively listed below, broken down in functional and structural materials.

3.2.9.1: Testing of functional materials

For the key functional materials under consideration (PbLi, $Be_{12}Ti$, Li_4SiO_4 and Li_2TiO_3, SiC FCI) the central challenge is to ensure stable and predictable performance within the complex operational environment of a fusion blanket of elevated temperature, cyclic thermal and mechanical loading, and prolonged interaction with surrounding media (structural steels, coolants, and each other). Key phenomena to characterize include:

- Stability: the ability of $Be_{12}Ti$, Li_4SiO_4 and Li_2TiO_3 to retain their structural integrity, phase composition, and functional performance over time – resisting sintering, phase transitions, fragmentation, and microstructural degradation;
- Compatibility and interface performance: the chemical and mechanical compatibility of each material with structural components and with one another, including their resistance to corrosion, interdiffusion, and detrimental reactions at operational temperatures. Special attention must be paid to the behavior and reliability of interfaces, where degradation, such as chemical reaction zones, loss of cohesion, or cracking, can determine the operational limits and safety margins of the entire blanket system;
- MHD effects: for liquid PbLi, it is essential to evaluate magnetohydrodynamic phenomena under strong magnetic fields representative of fusion conditions. MHD effects can significantly influence flow distribution, heat and mass transfer, pressure drop, and the stability of corrosion and deposition layers. Characterizing the long-term performance and compatibility of SiC FCIs within the PbLi environment is therefore a critical element for maintaining efficient coolant performance and protecting structural materials;
- Tritium behavior: for breeder (and multipliers) materials, it is essential to characterize the properties and their evolution that govern tritium production, transport, retention, and extraction. This includes understanding how microstructure, chemical composition, phase stability, and irradiation effects influence tritium generation and release rates and efficiency of extraction processes.

PbLi: Chemical compatibility and corrosivity of flowing PbLi should be quantified. Corrosion rates depend on representative flow, temperature, and magnetic field conditions. These conditions are changed between the non-nuclear and nuclear phase, where volumetric power deposition affects temperature and flow patterns. High-energy neutrons can also accelerate corrosion mechanisms and alter chemistry by transmutations of both PbLi and interfaces materials. PIE of corrosion layers should be performed to compare the microstructure, thickness, and chemical composition of corrosion layers, as well as impurity accumulation in PbLi, before and after neutron exposure. Optical microscopy and surface profilometry can be used to determine the overall thickness and morphology of corrosion layers as well as measure surface roughness and depth of corrosion features or pits. A combination of SEM, EDS, XRD, EELS and TEM techniques can be used to determine the microstructure, composition, and crystalline phases of corrosion layers, from surface features down to the nanometer scale. Chemical analysis of PbLi can be performed by sampling the liquid metal and applying techniques such as inductively coupled plasma mass spectrometry (ICP-MS), atomic absorption spectroscopy (AAS), or spark optical emission spectroscopy (OES), which enable precise quantification of dissolved elements, impurities, and transmutation products within the PbLi alloy. These tests can also investigate the performance of chemistry control in suppressing corrosion, and the integrity of protective barriers. Confirming the spectrum of activation products is instead important for waste management planning.

Neutron irradiation also causes He production in PbLi which, because of the low solubility, can create bubbles, impeding channel flow and heat transfer. The production, size and number of these bubbles could be measured "in-situ" during operation.

Ceramic breeders (Li_2TiO_3, Li_4SiO_4): For solid breeders such as Li_2TiO_3 or Li_4SiO_4, post-irradiation examination (PIE) after exposure in BEST should focus on how neutron irradiation and operational transients affect key properties that control tritium production, transport, retention, and extraction. This involves characterizing the evolution of microstructure – including grain growth, densification, porosity, and microcracking – using optical microscopy and SEM, as such changes can significantly alter diffusion pathways and influence tritium release rates. It is also important to identify tritium retention sites and trapping mechanisms through thermal desorption spectroscopy (TDS), in order to quantify any changes in tritium inventory and release behaviour. Further, any irradiation-induced phase and chemical composition changes should be detected using XRD and TEM, allowing the identification of transmutation, phase instability, or chemical interaction with the purge gas or structural materials. Evaluating the integrity of breeder pebbles and the potential for dust formation, through visual and microscopic analysis, provides insight into fragmentation, which has implications for operational safety and tritium management. Additionally, analyzing the surface chemistry and interface behaviour with purge gas or structural interfaces via SEM/EDS could detect early signs of corrosion or reaction zones that could impact functional performance. These measurements are necessary for benchmarking against non-nuclear test results and for understanding the direct impact of neutron irradiation on breeder behaviour.

In addition to microstructural and tritium-related characterizations, it is important to assess the mechanical properties of the breeder pebble beds after exposure. Mechanical testing such as uniaxial compression and crush tests, shear tests, creep or high temperature relaxation can be used to evaluate the strength and fracture resistance of individual pebbles as well as the collective compressive behaviour of the entire bed. These could be performed at several positions in order to understand the effects of different environmental conditions.

$Be_{12}Ti$: In the case of the neutron multiplier $Be_{12}Ti$, characterization is aimed at ensuring long-term stability and compatibility under fusion-relevant conditions. Detailed microstructural analysis with SEM and TEM can reveal voids, cracks and other dimensional changes which may lead to mechanical stress or loss of dimensional integrity. Phase and composition changes, which may result from transmutation or corrosion, can be assessed through XRD and EDS. If multipliers have been in contact with purge gas or the stability of the corrosion layers at the interface can also be evaluated through SEM and chemical analysis. This suite of measurements allows for a comprehensive assessment of the ability to maintain neutron economy, minimize gas build-up, and prevent excessive dust or hazardous byproducts.

To further understand the accumulation of gases, TDS is used to measure helium and hydrogen retention and release, which is essential for assessing both thermal performance and operational functionality. Importantly it is also necessary to measure tritium retention and release properties, similarly to what is done for breeder materials. This is because neutron interactions with beryllium also generate significant amounts of tritium through nuclear reactions. Assessing the amount of tritium produced, its retention sites, and the efficiency of its release is critical both for achieving the required tritium self-sufficiency in the blanket and for ensuring safe operation.

SiC FCIs: For SiC flow channel inserts, which play a critical role in mitigating MHD effects in PbLi coolant channels, PIE should address the preservation of both microstructural and functional properties after irradiation. Microstructural integrity and the presence of cracks can be assessed by SEM and optical microscopy, as irradiation and thermal cycling could potentially undermine the electrical insulation function of the inserts. Analysis of surface chemistry and the interaction with PbLi – using EDS and XPS – enables the detection of possible corrosion or other forms of chemical degradation at the interface. The electrical resistivity and related thermal conductivity of the FCIs, a key parameter for MHD mitigation and heat insulation, must be measured before and after irradiation to ensure it remains within operational requirements. Where accessible, TEM can be used to detect helium or hydrogen bubble formation, as such gas accumulation might affect both mechanical and insulating performance.

3.2.9.2: Testing of structural materials (RAFM steels)

Reduced Activation Ferritic/Martensitic (RAFM) steels, such as EUROFER97, CLAM and CLF-1, are selected for structural components due to their favorable mechanical properties and reduced long-term radioactivity. Post-irradiation examination (PIE) of these materials is essential to assess their performance under fusion-relevant conditions. Therefore, the focus should be on evaluating environmental effects and compatibility with coolants. Given that the irradiation doses in the BEST facility are relatively low, significant changes in bulk mechanical properties may not be detectable. However, characterizing initial microstructural changes can provide more insight on the irradiation damage phenomena, their genesis and evolution. In this respect, looking at the behaviour of joints and weldments is of particular interest.

Environmental compatibility assessments between RAFM and relevant breeder and neutron multipliers materials have been discussed in the corresponding sections. This section deals with coolants (water, CO_2) and their corrosion behavior and related material degradation. In high-temperature water environments, corrosion of RAFM steels is governed by the formation and stability of oxide layers. Of particular concern in a fusion environment is irradiation-accelerated corrosion: neutron irradiation can induce radiation-induced segregation (e.g., chromium depletion at grain boundaries), create defects that undermine oxide stability, and alter the water chemistry locally

through radiolysis. These effects can increase susceptibility to stress corrosion cracking (SCC), even in water chemistries that are otherwise safe for unirradiated steel. In supercritical or high-temperature CO_2 environments, RAFM steels are prone to oxidation and carburization. Oxide scale formation is influenced by the presence or absence of oxygen and water impurities in the coolant. In pure CO_2, these steels can suffer from substantial carburization, leading to embrittlement and surface hardening; small amounts of O_2 or H_2O can mitigate this effect by stabilizing more protective oxide films. Additionally, irradiation may further exacerbate oxidation and surface degradation by enhancing diffusion and damaging the protective oxide layer. To characterize these effects, post-exposure examinations should include microstructural analysis of oxide and carburized layers (using SEM, TEM, and EDS), measurements of oxide thickness, composition, and adhesion, as well as localized hardness and potential crack initiation near welds or interfaces. Hardness profiling and nanoindentation can reveal localized embrittlement or softening near the corroded surfaces ensile and fracture toughness tests performed on post-exposure specimens – especially those containing welds or heat-affected zones – provide direct measures of any loss in ductility or load-bearing capacity due to corrosion and irradiation. Slow strain rate tests (SSRT) are recommended to evaluate the susceptibility of RAFM steels to stress corrosion cracking.

Microstructural characterization of RAFM steels after low neutron fluences as expected in BEST is important for understanding early irradiation damage and its effects on material performance. Techniques like Transmission Electron Microscopy (TEM), Scanning Electron Microscopy (SEM), and Atom Probe Tomography (APT) enable detailed observation of several key defect types such as: a) nanometer-scale dislocation loops, which cause hardening and embrittlement by hindering dislocation motion; b) vacancy clusters and the initial formation of voids which may act as nucleation sites for swelling or local embrittlement; c) and subtle changes or damage to carbide and carbonitride precipitates, which are critical for maintaining strength and stability. TEM and APT are also sensitive to segregation at grain boundaries or phase interfaces (chromium depletion) which can degrade corrosion resistance and promote embrittlement. These analyses should focus on correlating the presence and density of these defects with changes in mechanical properties (such as increased hardness or shifts in ductile-to-brittle transition temperature) and with potential changes in thermal conductivity or creep resistance. Fractography by SEM, especially near welds or interfaces, can identify localized embrittlement or crack initiation linked to defect clusters or gas bubble accumulation. In addition, focused ion beam (FIB) milling allows the extraction of site-specific TEM lamellae from fracture surfaces, enabling detailed investigation of fracture mechanisms and the microstructural features associated with crack propagation.

Finally, welding can introduce residual stresses, microstructural inhomogeneities, and potential sites for crack initiation. Post-irradiation characterization of welds involves in particular assessing the microstructural changes in the weld metal and heat-affected zones, evaluating mechanical properties such as

hardness and toughness, and identifying any irradiation-induced defects. The samples for investigations of welds should be taken at several significant zones, for example those experiencing the highest irradiation dose, the highest temperature and/or the highest cyclic stress/strain amplitudes.

3.2.10: Foreseen general testing plan – two phases

The testing strategy could be structured around two main phases, each focused on achieving specific technical and operational goals. This staged approach allows for progressive validation, data collection, and system qualification in a fusion environment.

Phase 1 – Learning / Qualification phase. The first phase spans the early operational campaigns. Its primary focus is to verify the system's ability to function as intended under actual reactor conditions. Objectives include:

- Validating the operation of ancillary systems, such as coolant loops, liquid metal circuits, and tritium processing units, including their interaction with magnetic fields and dynamic reactor conditions;
- Confirming integration procedures like remote handling, port plug operations, and compatibility with existing reactor infrastructure;
- Assessing the impact of magnetic perturbations from ferromagnetic components on plasma performance and stability;
- Evaluating system resilience during abnormal scenarios such as plasma disruptions or vertical displacement events by monitoring structural responses and comparing them to design assumptions;
- Resolving interface and alignment issues with adjacent reactor systems;
- Supporting possible licensing efforts by collecting data related to load definition, neutronic behaviour, system integrity, and safety margins;
- Demonstrating the effectiveness of the first wall cooling system and validating thermal performance predictions.

This phase is intended to use specifically instrumented modules focused on electromagnetic and mechanical validation, as well as on neutronic behaviour during early reactor operation.

Phase 2 – CFEDR-relevant data acquisition phase. The second phase follows, and it is designed to obtain detailed technical data needed to support the design and qualification of breeding blanket systems for future power-producing fusion reactors. This includes:

- Validating simulation tools for predicting nuclear responses, including neutron transport, tritium generation, and heat deposition.
- Assessing the thermal and mechanical behavior of components under internal heat loads and irradiation, including the performance of joints and welded structures.

- Demonstrating tritium extraction, heat removal, and coolant purification systems under realistic operating conditions.
- Building a performance and reliability database through extended testing of integrated systems under steady-state fusion conditions.
- Additional modules could be used in this phase targeting both thermo-mechanical and tritium control performance, and possibly others representing a fully integrated system for validation.

This phased testing strategy ensures that each stage of the blanket system's development is aligned with BEST reactor operations, while progressively addressing the requirements for future commercial fusion energy systems.

3.2.11: TBM system requirements

The following components or sub-systems are required for the validation of tritium breeding blanket technologies:

- TBM set, mainly consisting of the TBM and its associated shield, and Pipe Forest (PF) up to the flange connected to the Vacuum Vessel (VV) port extension;
- TBM Port Plug (PP), mainly consists of the frame, dog leg assembly and its associated cooling pipeline, for providing the support of the TBM and the neutron shield of the port;
- Coolant System (CS), directly connects with the TBM, providing the coolant for the TBM;
- Neutronics Measurement System (NMS), for the measurement of tritium production rate as well as neutron intensity and spectrum in the TBM;
- Tritium Extraction and Accountancy System (TES & TAS), for impurity removal and the tritium extraction, concentration, accountancy, and delivery to the tritium processing system;
- Data Acquisition and Control System (DACS), for data collection and control of the TBM system, as well as the communication with external systems.

Similar TBM concepts are possible to share some common components or sub-systems such as port plug, shield, instrumentations, or even coolant systems. In this case, TBMs shall be designed compatible with each other on the interfaces.
The design of the TBS refers to the operation scheme and the load specification of the BEST machine and maintains relevance to CFEDR blankets. The basic requirements are listed as follows:

- TBMs shall be designed in accordance with requirements under the BEST baseline D-T plasma operation condition;
- TBMs shall employ the same structural and functional material with CFEDR blankets;
- TBMs shall maintain the structural similarity with the CFEDR blanket to test the fabrication technologies.;

- TBMs and shield blocks shall provide enough neutron shielding at the VV port and protect the VV and magnets;
- TBS shall adapt the spatial constraint allocated by the BEST machine and buildings. For example, each TBM shall be no more than 1 m poloidally and 0.64 m toroidally for sharing the same space of port plug;
- TBMs shall maintain its structural integrity under the normal and design basis accident conditions and ensure the safe operation of the BEST machine;
- Design, manufacturing, testing, commission, operation, maintenance and decommission of the TBS shall strictly comply with the requirements of safety classification, tritium classification, quality classification, remote handling classification and vacuum classification of the BEST machine. Relevant technical documents such as procurement instructions, drawings, technical manuals, test plans, installation/maintenance instructions, etc. shall be approved.

3.2.12: Tokamak operational requirements

Normally, the TBM will reach a thermal steady state in 10-20 minutes driven by the low nuclear heat and FW heat flux produced in the BEST machine. Therefore, to test the steady state characteristics of TBMs, the system shall run under long-pulse D-T operational scenarios characterized by:

- D-T fusion power of ~15-40 MW;
- Burning time of over 1000 s per pulse;
- Neutron Wall Loading of 0.15 MW/m^2 at fusion power of 40 MW;
- Nominal FW heat flux of 0.3 MW/m^2 at fusion power of 40 MW;
- A few thousand pulses in total.

During the D-D operational stage, TBMs can also be installed to test the structural, electromagnetic, and thermal hydraulic load.

3.2.13: Supporting prior developments

For a successful integral TBM test programme, the following prior developments or R&D activities should be performed in advance:

- Structural and functional materials used in TBMs, such as the RAFM steel, lithium ceramics, beryllide pebbles, and SiC_f/SiC composites, shall be authorized and qualified with an adequate and reliable supporting database;
- The manufacturing technologies of TBMs shall be developed and validated under non-nuclear environment before use in the TBM;
- Thermal hydraulic test of TBMs shall be done out-of-pile before its assembly in the BEST machine;
- Key components and instruments shall be developed and validated out-of-pile before use in the system;
- Relevant safety components and interlocks should be tested regularly before putting them into use.

3.2.14: High-level interface requirements

Space allocation for the TBM and ancillary systems shall be determined. The interfaces with other systems such as the Vacuum Vessel, Shielding Blanket, Cooling System, Power Supply System, Plasma Control System, Central Interlock System, Central Safety System, Hot Cell, and buildings, shall be considered and clarified in advance to prevent unachievable modifications in the implementation stage. Besides, if nuclear materials are used, applications should be submitted and approved according to the local laws and regulations.

3.3: Tritium fuel cycle

Central to any nuclear power plant is the fuel cycle and fusion power plants will represent no exception. Yet, several scientific and technological challenges remain to be addressed when it comes to fusion, and BEST operation represents an excellent opportunity for contributing to closing knowledge and know-how gaps.

In the context of the preliminary indication for the licensing of BEST, a site limit has been proposed for the tritium inventory to be ~110 g, determining the maximum amount of tritium to be mobilisable in the fuel cycle. Figure 3.2 shows the block diagramme of the BEST fuel cycle.

The strategy for the tritium fuel cycle management in BEST has the target to explore and pursue an optimised balance amongst plasma performance, fuelling, vacuum pumping and tritium recycling. It is constrained by the requirement to minimise tritium retention in-vessel and in the fuel cycle loop and has the goal to shorten the tritium processing time aiming to achieve the demonstration of an integrated loop. In the context of the safety demonstration for BEST, the following will have to be addressed:

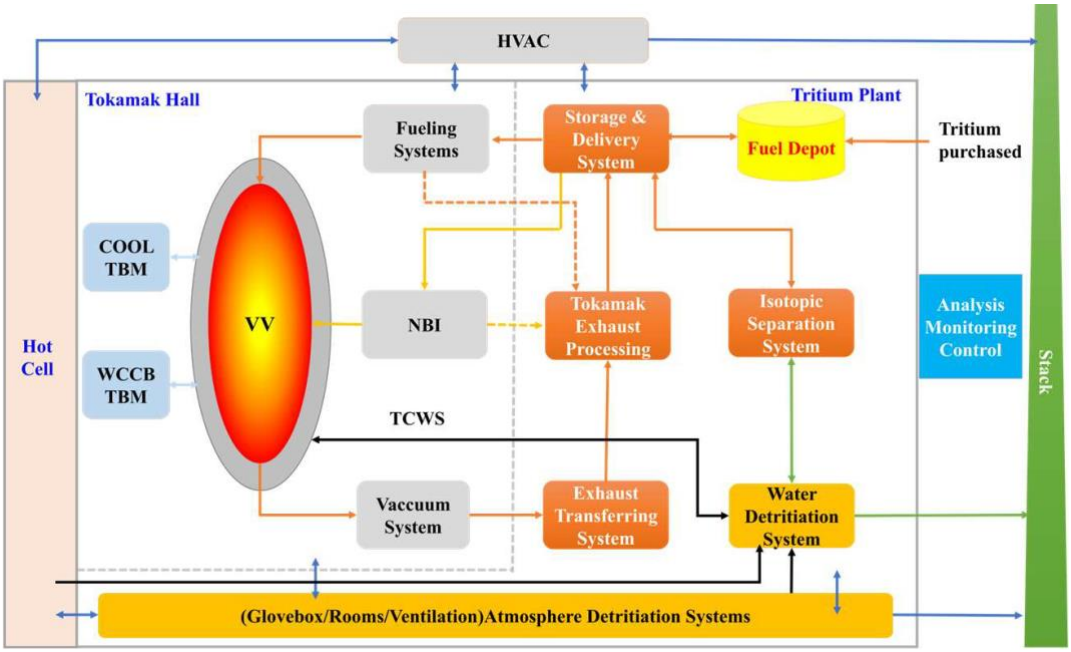

Figure 3.2: The block diagramme of the fuel cycle in BEST.

- Limit of tritium release to the environment to be carefully demonstrated, proved and managed;
- Tritium contamination in man-access areas to be readily controlled by active and/or stand-by detritiation systems for tritium removal in conjunction with tritium measurement and monitoring;
- Exact tritium distribution and safety control to be presented to the nuclear regulators.

R&D missions related to the BEST fuel cycle will hence include:

- Testing and demonstrating the tritium handling process for the inner fuel cycle
  - Exploring ways/options to enhance the burn-up fraction and the fuelling efficiency
  - Exploring tritium removal and recovery techniques
  - Investigating ways to shorten the processing time
- Testing key technologies for the process for the outer fuel cycle with TBMs
  - Tritium extraction and purification technologies
  - Online tritium measurement will be in place for tritium accountability and analysis

Eventually, successful operation of the BEST fuel cycle will allow:

- Validation and qualification of the selected technologies for application in the fusion nuclear environment;
- Demonstration of the functionality of the fuel cycle as a closed system to confine and properly extract tritium in all situations (normal and accidental);
- Demonstration of the control of the tritium inventory that implies an efficient and qualified instrumentation chain.

3.3.1: Recovery time and efficiency

The scope is to outline a set of plans and operation scenarios in close iteration with machine operators to allow the exploration of tritium recovery after various plasma operations. Objectives include: (i) exploring ways to minimise the requirements on tritium inventory with the aim to improve the understanding of tritium recovery methodology and techniques towards CFEDR; (ii) enhancing the technology readiness level for those technologies to be likely employed for CFEDR; (iii) testing the processing efficiency for the technologies adopted on BEST.

This endeavour will require accurate measurement of tritium inventory. The global recovery time and efficiency will be derived from the measurement results by various measurement devices. Flexible plasma operation scenarios will be required fulfil the various objectives and aims.

3.3.2: Direct internal recycling

The DIR (direct internal recycling) [6] technology is seen as the most viable operation mode for the tritium fuel cycle in support of CFEDR that will anticipate steady-state operation and higher duty factor (not lower than 50%).

In BEST the objective is to test and possibly demonstrate the feasibility and effectiveness of the DIR technology. With regard to operational requirements, it is anticipated that the regeneration of cryopumps to discharge the retained tritium inventory will be the most time-consuming in the DIR process. Past experience on EAST operation suggested 20-30 minutes may be required for the regeneration. Therefore, at least two options should be explored: (i) real-time closed loop to be formed within one pulse if the duration of plasma operation can be longer than 30 minutes; (ii) closed loop to be formed over 2-3 pulses with minimum dwell time between pulses.

3.3.3: Detritiation

All the foreseen detritiation systems and technologies in BEST will be tested to demonstrate the technology readiness level, reliability and effectiveness for next generation fusion devices, especially CFEDR. Objectives include testing: (i) the technology readiness level and reliability of detritiation technologies adopted in BEST; (ii) the confinement properties of detritiation systems to establish their qualification; (iii) the recovery efficiency on a system level.

Although tritium recovery from gases, liquids and solids will all be necessary, detritiation will mainly focus on tritiated gases and water. It is anticipated that detritiation systems will be essential when the amount of tritium inventory is significant and/or the related recovery becomes critical. Dedicated studies will have to be conducted prior to D-T operation in consultation with tritium safety management to guide the tests and operation of detritiation systems.

3.3.4: Tritium monitoring

The scope is to, for tritium operation, install, operate and exploit equipment to measure tritium concentration and content in various components/containers/lines. The objectives include: (i) monitoriing tritium concentration in the primary confinement barrier to ensure effective fuel circulation; (ii) monitoring tritium concentration in the secondary confinement zones to ensure tritium safety control; (iii) ensuring that the time required for measurement and analysis is as short as possible to allow real-time adjustment and response. Some developments are needed prior to the operation such as 1) the identification of the need for real-time measurement and analysis, especially with the view for next generation fusion machines, for both the primary fuel cycle and the secondary confinement system; 2) the development of a detailed plan for where the measurements will be conducted and what purpose will be served etc.; 3) uncertainty assessments.

3.3.5: Deep tritium fuelling systems

The scope is to test and validate pellet injection and compact toroid (CT) injection components and systems for deep plasma fuelling with tritium in CFEDR. The objectives include: (i) the demonstration of technology maturity of pellet injection and CT systems for tritium fuelling, including tritium compatibility; (ii) gathering data on fuelling frequency, speed and efficiency as input for future CFEDR.

The development and specification of fuelling requirements for various plasma operation scenarios will be required prior to BEST operation, as well as calibrations for ensuring accurate tritium measurement.

3.4: References

[1] L. Chen et al., *Fusion Eng. Des.* **173**, 112800 (2021)
[2] S. Liu et al., *Fusion Eng. Des.* **177**, 113059 (2022)
[3] P. Arena et al., *Fusion Eng. Des.* **218**, 115205 (2025)
[4] F. Hernández et al., *Fusion Eng. Des.* **124**, 882 (2017)
[5] G. Zhou et al., *Fusion Eng. Des.* **168**, 112397 (2021)
[6] C. Day et al., *Fusion Eng. Des.* **88**, 616 (2013)

Chapter 4: Transport Physics and Integrated Modelling

Coordinators: P. Mantica (CNR-Milan, Italy), J.L. Chen (ASIPP)

With contributions from:
ASIPP Team: V.S. Chan, H.C. Fan, Y.J. Hu, X. Jian, G.Q. Li, H.L. Wang, C.B. Wu, J.R. Wu, G.S. Xu, X.Y. Xu, X.M. Zhai
EUROfusion Team: C. Angioni (IPP-Garching, Germany), L. Frassinetti (KTH, Sweden), A. Mariani (CNR-Milan, Italy), I. Casiraghi (CNR-Milan, Italy), L. Figini (CNR-Milan, Italy), T. Johnson (KTH, Sweden), F. Auriemma (Consorzio RFX, Italy), J. Lombardo (Consorzio RFX, Italy)
UKAEA Team: L. Garzotti, D. King

4.1: Introduction

In this chapter, the possible contributions of BEST to research in the field of tokamak transport and confinement are discussed. Using state-of-the-art integrated modelling frameworks and transport models, physics-based predictions of BEST scenarios are presented, including the expected fusion power output.

This chapter is closely linked to Chapter 2, providing physics-based support for the METIS simulations described there, as well as for the selection of the main operational parameters. These physics-based simulations serve as reference for further analyses, including MHD and fast-ion physics studies. Furthermore, all the proposed scenarios are core-edge integrated, ensuring that separatrix parameters used as boundary conditions for core simulations are consistent with the scrape-off-layer parameters discussed in Chapter 6.

4.2: BEST operational windows from engineering to dimensionless parameter domains

In this section, we analyze the expected achievable parameter domains for BEST, linking key engineering parameters with volume-averaged dimensionless plasma quantities. The results are obtained assuming H-mode confinement, as described by the IPB98(y,2) scaling law [1]. The fusion power is computed using the actual temperature dependence of the fusion reaction rate, while the radiated power includes contributions from Bremsstrahlung, synchrotron, and line radiation, accounting for the temperature-dependent cooling rates of argon (Ar) and tungsten (W) impurities.

A tungsten concentration of 10^{-5} and an argon concentration of 0.003 are assumed. Additional light impurities, helium and boron, are included, resulting in a total effective charge of Z_{eff} = 2.2. Typical H-mode profile shapes are assumed, and the corresponding volume-averaged temperatures are rescaled to match the total thermal stored energy predicted by the H-mode scaling law. Thus, these calculations effectively represent a 0.5D approach – the profile shapes are assumed, but profile effects are retained in the computation of both the fusion power and the radiated power.

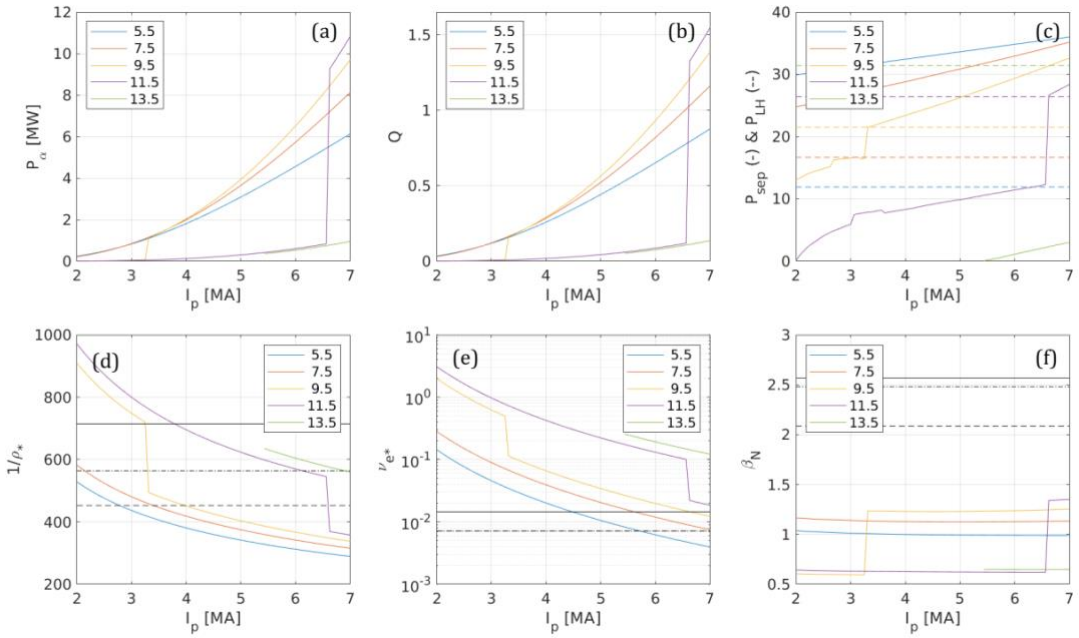

Figure 4.1: Upper row: α-power, fusion gain, P_{sep} (full line) and $P_{L\text{-}H}$ (dashed line) using the TC-26 L-H threshold scaling; lower row: dimensionless plasma parameters (from left to right: volume-averaged values of $1/\rho^*$, ν_e^*, and β_N) as a function of the plasma current in MA, for different values of the line-averaged density, as reported in the legends in 10^{19} m^{-3} units, at 6.15 T, with 35MW of auxiliary heating. Horizontal lines give CFEDR (solid), ITER (dashed) and EU-DEMO (dash-dotted) reference values. In the ν_e^* figure DEMO and ITER are overlapping.

The power reaching the separatrix (P_{sep}) is obtained as the difference between the total heating power (sum of auxiliary and alpha-particle heating) and the radiated power up to $\rho_{tor} = 1$. P_{sep} is then compared with the L-H transition power threshold, calculated using the recent TC-26 scaling law for tokamaks with metallic walls [2, 3]. If P_{sep} falls below the L-H threshold, the L-mode confinement scaling law from IPB98 is applied instead [1].

Figure 4.1 presents an example with 35 MW of auxiliary heating at $B_0 = 6.15$T. The alpha-particle power and dimensionless plasma parameters are plotted as functions of the plasma current for different electron density values. A strong dependence of fusion power on plasma current is observed: operation with $Q > 1$ can be achieved for $I_p \approx$ 6-7 MA, provided the electron density exceeds roughly 0.5 of the Greenwald limit (n_{GW}). The additional alpha-heating ensures that, during the flat-top phase at high plasma currents, the ratio P_{sep}/P_{LH} reaches values well above unity for robust H-mode operation.

From the application of the scaling laws (i.e. H_{98}=1), the thermal stored energy is computed and then used to compute the dimensionless parameters, including β_N. In Fig. 4.1(e), ν_e^* is given by $\nu_e^* = 5\times10^{-5} \ln\Lambda\, Z_{eff}\, R\, q\, n_e/(T_e^2\, (r/R)^{1.5})$, with R in meters, n_e in 10^{19} m^{-3} and T_e in keV. In Figs. 4.1(d)-(f), dimensionless parameter values for ITER (dashed lines), CFEDR (solid lines) and EU-DEMO (dash-dotted) are included for direct

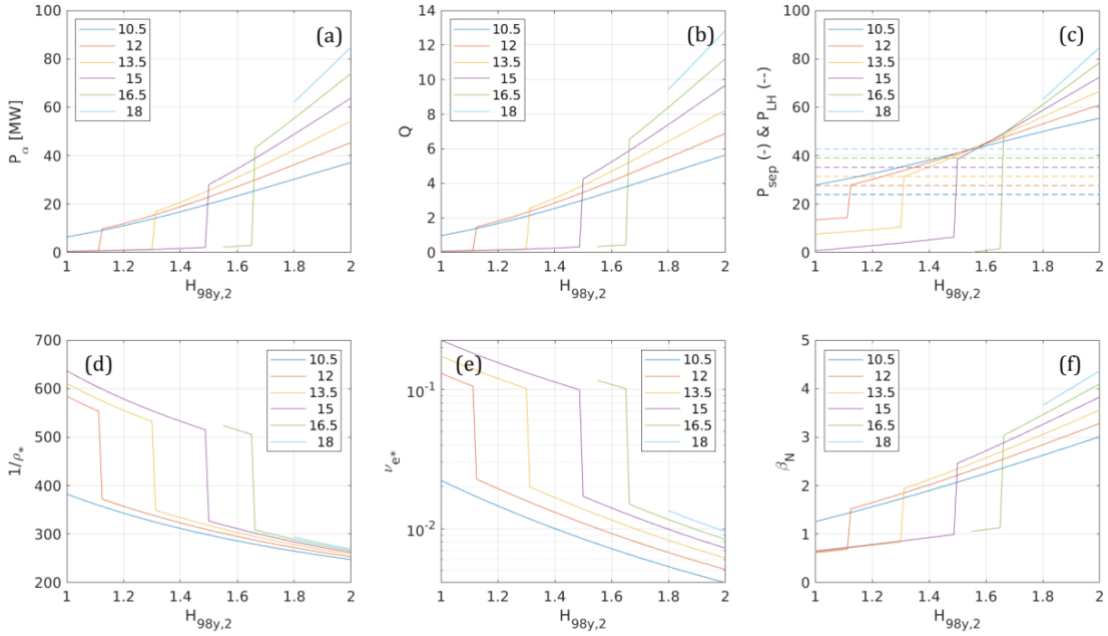

Figure 4.2: Same quantities as in Fig. 4.1 as a function of the $H_{98y,2}$ factor, for different values of the line-averaged density (in 10^{19} m^{-3} units), at 6.15 T and 6MA, with 33MW of auxiliary heating.

comparison. Figures 4.1(d)-(f) show that BEST can reach reactor-relevant values of ρ^* and ν_e^*, with moderate β_N values resulting from the high toroidal field. Operation at higher β_N could be achieved if the energy confinement factor significantly exceeds the standard H-mode scaling (for instance, through the formation of internal transport barriers (ITB) or via turbulence stabilization over extended core regions).

Figure 4.2 shows P_α, Q, P_{sep} and $P_{L\text{-}H}$, $1/\rho^*$, ν_e^*, β_N as a function of the $H_{98y,2}$ confinement factor for different line-averaged densities (extending to higher values than in Fig. 4.1) at B_0 = 6.15T, I_p = 6MA, with 33MW of auxiliary heating. The results indicate that achieving $\beta_N \approx 2.5$ and $Q \approx 5$ requires $H_{98y,2} > 1.6$ at densities ≥ 85% of the Greenwald limit ($n_{GW}=1.6\times10^{20}$ m^{-3} at 6 MA).

4.3: BEST research on transport and confinement

4.3.1: BEST main characteristics relevant for transport and confinement studies

BEST will be a burning plasma facility bridging the gaps towards ITER and CFEDR. The high values of B_t and I_p foreseen in BEST make it also an unprecedented platform for transport and confinement (T&C) studies in D-T plasmas, particularly under conditions of a significant fraction of self-generated plasma heating. The presence of a significant population of highly energetic ions, including alpha particles, will enable novel studies of their effects on thermal plasma confinement, as specifically addressed in Sections 8 and 9. Here, we focus on the general transport properties of BEST plasmas and its potential contributions to advance understanding of transport and confinement in tokamaks.

- As shown in Section 4.2, at B_0 = 6.15T, BEST will achieve reactor-relevant values of ρ^* and ν_e^*. Reactor-relevant β_N could also be attained if scenarios with $H_{98y,2} > 1.6$ can be developed. In addition, the possibility of operating BEST at half magnetic field, $B_t \approx 3.1$T will facilitate access to high β_N scenarios, and will also allow direct comparison with lower field tokamaks such as JET and JT-60SA. It will also be important to compare low and high B_T plasmas within the same device.

- At B_0 = 6.15T, the high plasma current enables operation at high densities, achieving reactor-like conditions of low collisionality at the pedestal top and high density and collisionality at the separatrix. Together with a full tungsten first wall, as currently planned for ITER, CFEDR, and future fusion reactors, these properties will allow BEST to address critical questions on the integration of the plasma core, pedestal and scrape-off-layer (SOL). A key research topic will be the compatibility of high core confinement and high fusion gain, which require sufficiently high pedestal pressure, with tolerable exhaust conditions in the absence of large edge localized modes (ELMs). This will involve studies of ELM-free or mitigated ELM regimes in D-T plasmas, such as grassy-ELM regime [4], EDA H-mode [5], quasi-continuum exhaust regime with type II ELMs (QCE) [6], as well as the *X*-point radiator (XPR) [7].

- Regarding fuelling, the edge opacity will necessitate studies of deep fuelling techniques (pellets and compact torus injector) in reactor-relevant scenarios.

- On the topic of L-H transition studies, BEST will provide valuable data on the parametric dependencies of the L-H threshold in metallic-wall devices (complementing results from AUG, JET-ILW, etc.) and will contribute to improving $P_{L\text{-}H}$ extrapolations for ITER.

- The availability of high ICRH and NBI power will enable further studies of non-linear stabilization of ITG turbulence by low- and medium-energy fast ions [8], a mechanism that can facilitate the access to the burning phase in future reactors.

- Finally, as in future reactors, the electron-ion collisional exchange time in BEST is much shorter than the thermal confinement time over a broad range of parameters (see Fig. 4.3(a)), favouring temperature equilibration. In contrast, the current diffusion time is several times longer (see Fig. 4.3(b)), making it more challenging to shape the current density profile via external current drive.

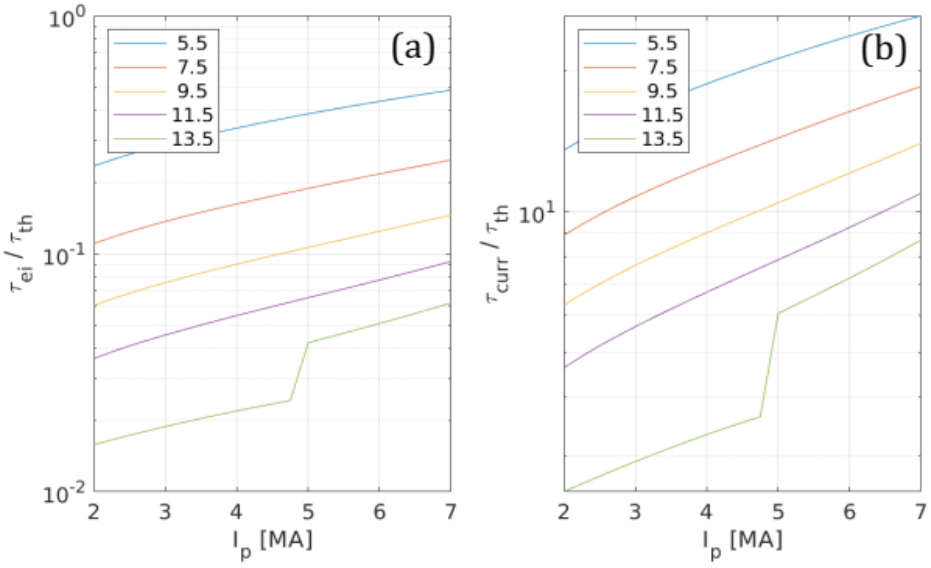

Figure 4.3: Volume-averaged values of the electron-ion energy exchange time (a) and the current diffusion time (b), normalized to the energy confinement time, as a function of the plasma current at different plasma densities (B_0 = 6.15T, P_{aux} = 35 MW).

4.3.2: Transport research areas for BEST scientific exploitation

In this subsection, we summarize the main areas of research in transport and confinement that can be pursued during BEST operations. For clarity, these are organized into five main blocks:

- **General confinement properties**
  - Investigate the I_p and B_t dependence of H-mode confinement scaling under electron-heated conditions, study ρ^* scaling and isotope effects
  - Study the effect of impurity seeding on confinement performance
- **Core transport physics**
  - Investigate ITG, TEM, and ETG turbulence, and associated heat and particle transport including impurities
  - Study ion stiffness mitigation strategies and the effects of fast ions on thermal transport
  - Examine the effect of the q-profile on core transport
  - Develop and validate turbulence models and synthetic diagnostics
  - Explore the physics of high-β plasmas at full- and half-field magnetic field
- **Pedestal transport physics**
  - Characterize residual turbulent transport in the pedestal using global gyrokinetic (GK) simulations. Evaluate ETG role in electron heat transport.
  - Study particle pinch mechanisms in the pedestal
  - Investigate intrinsic rotation and residual stress in the edge region

- **Core-edge integration physics**
  - Assess the impact of ELM mitigation strategies on the pedestal
  - Study ELM-free and small-ELM regimes, including the influence of separatrix density
  - Investigate opaque edge effects, including the comparison of deep fuelling systems versus gas puffing
  - Study impurity-seeded detached scenarios and impurity control strategies
  - Examine the impact of the Greenwald fraction on edge and core transport, including density limit studies
  - Explore plasmas with high density but low collisionality
  - Assess advanced scenarios and their optimization in presence of a metallic wall
- **L-H transition physics**
  - Study L-H transition physics in a tungsten-wall device
  - Investigate operations marginally above the L-H power threshold

4.4: Physics-based integrated modelling of flat-top plasma profiles

4.4.1: Methodology

The integrated modelling of the flat-top phase of different scenarios in support of $Q \geq 1$ operation in BEST was carried out using the ASTRA framework [9, 10], employing physics-based transport models. TGLF-SAT2 [11] in electromagnetic mode was used for turbulent transport, NCLASS [12] for neoclassical transport of the main species, and the FACIT module [13] for impurity neoclassical transport, accounting for centrifugal effects of rotation on impurity transport. The equilibrium was computed with the FEQIS solver [14] in fixed-boundary mode.

Six quantities were evolved in the simulations: electron and ion temperature (T_e and T_i), electron density (n_e), tungsten and argon impurity densities (n_W and n_{Ar}), and plasma current density (j). Plasma rotation was calculated once using TGLF-SAT0 in electrostatic mode and then kept fixed, as it has limited impact via E×B shear. A balanced 50%-50% D-T mixture was always assumed. The transport equations were solved up to the pedestal top for T_e, T_i and n_e, and up to the separatrix for impurities and plasma current density. For pedestal modelling, the Europed code [15] was used, in a version taking $n_{e,ped}$, $n_{e,sep}$, β_N and plasma shape as inputs. Europed generates a set of profiles with increasing p_{ped}, where the pedestal width is determined according to the EPED1 assumption, $w_{ped} = k\,(\beta_{\theta,ped})^{1/2}$. The constant $k = 0.11$ was chosen in agreement with experimental results from AUG, MAST-U, and TCV [16-18]. Low-Z and mid-Z impurities were modelled as an effective ion with $Z = 9$, representing both Ar and He, with a density set to match the prescribed Z_{eff}. For each profile, Europed computed the equilibrium using HELENA and assessed stability with MISHKA. The predicted pedestal pressure profile is the one marginally stable to ideal peeling-ballooning modes.

Heating power and current drive deposition profiles for NBI and ECRH were calculated using ONETWO [19], while ICRH deposition was computed with TRANSP-TORIC [20]. The ECRH power was distributed over a radial region extending up to $\rho_{tor} = 0.45$ by steering the poloidal launch angles of the gyrotrons. Using toroidal angle adjustments, the ECCD was configured to drive counter-current inside $\rho_{tor} = 0.25$ and co-current outside this region, to assist central q-profile flattening. In all simulations, ^{3}He minority ICRH with a minority concentration of $n(^3\text{He})/n_e = 3\%$ was employed, except for one comparison case using a hydrogen minority ICRH with $n(\text{H})/n_e = 3\%$. The ICRH power for ^{3}He heating† was equally divided between two frequencies, $f_1 = 61.5$ MHz and $f_2 = 68$ MHz, to broaden the fast ion profile to enhance the beneficial stabilizing effects on ITG turbulence. No dedicated scan of ICRF parameters and ^{3}He concentration†† has been performed and is reserved for future studies.

Unless otherwise stated, argon seeding was set to achieve a radiated power inside the separatrix ≈ 1/3 of the injected auxiliary heating power, with separatrix density $n_{e,sep} = 4.5\times10^{19}$ m^{-3} and temperature $T_{e,sep} = 150$ eV, to ensure compatibility with detached SOL conditions. TGLF was called with four active species (electron, hydrogenic ion with atomic mass 2.5, Ar, W) and one passive species lumping NBI and ICRF fast ions and He ash for dilution. Non-linear electromagnetic stabilization effects (as described in [8]) were not included in the integrated modelling. Their magnitude has been estimated in stand-alone gyrokinetic simulations and will be discussed separately.

The fusion reaction rate was calculated following [21], while alpha-particle slowing down and collisional alpha heating were computed according to [22-24]. The contribution of suprathermal reactions – originating from interactions between NBI-generated deuterons and thermal tritons – was evaluated separately using TRANSP-NUBEAM [25]. For the considered scenarios, this contribution accounts for ~10% of the total fusion power. In the following analysis, the reported fusion power corresponds to the sum of the thermal fusion power computed from the ASTRA profiles and the suprathermal component. Finally, the confinement factor was determined by comparing the global confinement time from ASTRA simulations with the ITPA IPB98(y,2) scaling [1], both neglecting P_{rad} and considering it.

4.4.2: Conservative inductive scenarios

The results of the integrated modelling simulations are summarized in Fig. 4.4, which shows the total fusion gain, Q as a function of the plasma current. The summary of the global parameters are listed in Table 4.1, while Table 4.2 provides the corresponding Europed input values used in these simulations.

† For the considered conditions, tritium ions absorb ~5-10% of the injected ICRF power through the second harmonic resonance, $\omega = 2\omega_{ci}(T)$.

†† The assessment of whether BEST can employ ^{3}He minority ICRH during the ramp-up and reaching the flat-top phase, followed by switching off the ^{3}He injection, will be carried out in future studies. In addition, the optimization of bulk ion heating during the ramp-up phase using three-ion ICRF scenarios (f ≈40-42 MHz) with heavier impurities (Ar, ^{22}Ne, ^{11}B, etc.) will also be investigated.

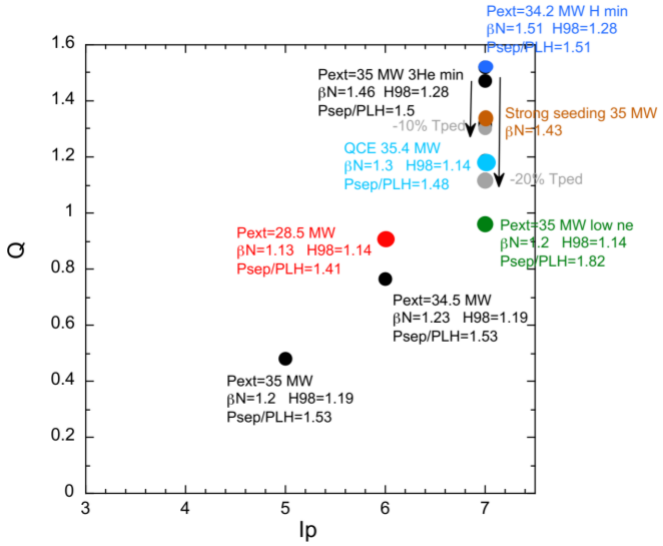

Figure 4.4: Fusion gain, Q as a function of the plasma current for several inductive BEST scenarios discussed in Chapter 4. For all these cases, the suprathermal fusion component contributes approximately 10% to the total fusion power†.

Table 4.1: Summary of global parameters for the simulations shown in Fig. 4.4. In all cases, the total auxiliary power is $P_{aux.} \approx$ 34-35 MW, except for one of the I_p = 6 MA cases, where reduced $P_{aux.}$ = 28.5 MW was used to increase the Q-value. The $H_{98y,2}$ factors are calculated neglecting P_{rad}.

Scenario	Q	P_{fus}	β_N	n_e/n_{GW}	$H_{98y,2}$	$P_{L\text{-}H}$	$P_{sep}/P_{L\text{-}H}$
I_p = 7 MA (reference type I ELM; ^{3}He minority)	1.47	51.3 MW	1.46	0.51	1.12	21 MW	1.5
I_p = 7 MA (reference type I ELM; H minority)	1.52	52 MW	1.51	0.51	1.13	21 MW	1.5
I_p = 7 MA (reduced density)	0.96	33.4 MW	1.2	0.41	1.03	17 MW	1.8
I_p = 7 MA (T_{ped}: 20% reduced)	1.12	39 MW	1.26	0.52	0.98	22 MW	1.4
I_p = 7 MA (strong seeding)	1.32	46 MW	1.43	0.5	1.11	21 MW	1.3
I_p = 7 MA (QCE-like conditions)	1.19	42 MW	1.3	0.53	1.01	22 MW	1.4
I_p = 6 MA	0.76	26.2 MW	1.23	0.53	1.04	19 MW	1.5
I_p = 6 MA (reduced $P_{aux.}$)	0.91	26 MW	1.13	0.5	1.01	18 MW	1.4
I_p = 5 MA	0.48	16.7 MW	1.2	0.62	1.05	18 MW	1.5

† The ICRF frequency range in BEST allows to increase the fraction of suprathermal neutrons by accelerating NBI-generated deuterons ($f \approx 46$ MHz), similar to the scenario developed for recent record DTE2 and DTE3 experiments in tritium-rich plasmas at JET. This assessment will be further done as part of future ICRF optimization studies for BEST.

Table 4.2: Input parameters for Europed for the scenarios shown in Figure 4.4.

Scenario	$n_{e,sep}$ (10^{19} m^{-3})	$n_{e,ped}$ (10^{19} m^{-3})	Z_{eff}	T_{sep} (eV)
I_p = 7 MA (reference type I ELM; ^{3}He minority)	3.8	6.4	2.0	150
I_p = 7 MA (reference type I ELM; H minority)	3.8	6.4	2.0	150
I_p = 7 MA (reduced density)	3.8	5.0	2.0	150
I_p = 7 MA (T_{ped}: 20% reduced)	3.8	6.4	2.0	120
I_p = 7 MA (strong seeding)	3.8	6.4	2.7	150
I_p = 7 MA (QCE-like conditions)	4.5	6.4	2.0	150
I_p = 6 MA	3.8	5.5	2.0	150
I_p = 6 MA (reduced $P_{aux.}$)	3.8	5.5	2.0	150
I_p = 5 MA	3.8	5.5	2.0	150

Three reference cases were analyzed at I_p = 5MA, 6MA and 7 MA, illustrated with black circles in Fig. 4.4, each with a total auxiliary heating power of $P_{aux.} \approx 35$MW (composed of 13 MW ECRH, 12 MW NBI and 10 MW ICRH). These reference cases assume a standard Europed pedestal and a standard level of impurity seeding. A strong dependence of the fusion gain factor on the plasma current is observed, primarily driven by changes in the pedestal performance, as evidenced in Fig. 4.5. The simulations indicate that $Q \geq 1$ can be achieved in BEST for plasma currents between 6 MA and 7 MA. The reference case at I_p = 7MA yields the conditions well above the scientific breakeven, namely $Q \approx 1.5$. This reference case has been further benchmarked against the JINTRAC suite of codes [26], run with the same heating profiles as ASTRA, obtaining similar results†.

A variant of the 6MA case with reduced $P_{aux.}$ = 28.5 MW (10 MW ECRH, 8.5 MW NBI and 10 MW ICRH) was explored to increase the fusion gain, shown as the red circle at $Q \approx 0.9$ and I_p = 6MA. For this specific case, the transport modelling included an empirical mock-up of nonlinear electromagnetic stabilization effects, as described in [27]††, although the model was originally tuned to JET parameters. The results suggest that I_p = 6MA may be marginally below the Q = 1, yet still close enough to reach it withing the expected range of modelling uncertainties.

† In 2025, the JINTRAC team progressed with including self-consistent calculations of NBI, ICRH and ECRH heating sources. Further benchmarking of JINTRAC and its application for modelling other BEST scenarios will be conducted in future studies.

†† No such stabilization effects were included in the other cases shown in Fig. 4.4.

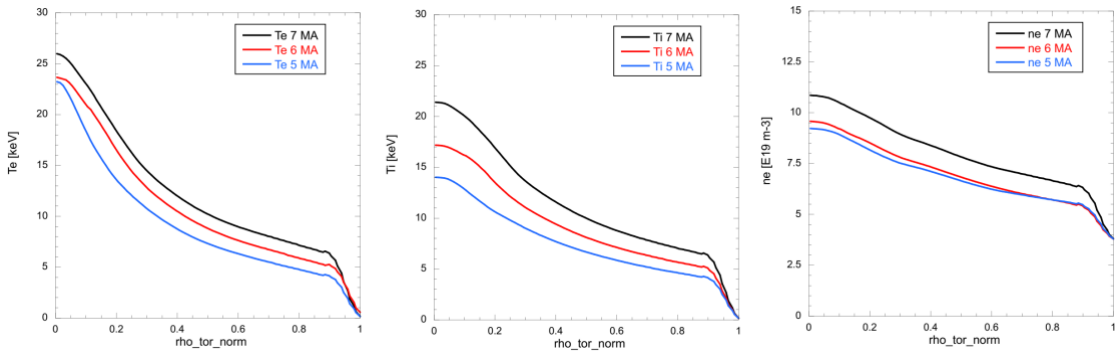

Figure 4.5: Predicted electron temperature (T_e), ion temperature (T_i), and electron density (n_e) profiles for the reference scenarios at I_p = 5MA (blue), I_p = 6MA (red) and I_p = 7MA (black). For I_p = 6MA and 7 MA, the Greenwald fraction is $n_e/n_{GW} \approx 0.5$. The density for the 5MA case was not scaled with plasma current, resulting in $n_e/n_{GW} \approx 0.6$.

For the I_p = 7MA case, several additional variants were studied. First, a comparison was made between the reference option using ^{3}He minority ICRH and a H minority ICRH (black vs. blue circle in Fig. 4.4). The two cases are largely equivalent in terms of Q and fusion power, with slightly higher performance for the H minority at the same concentration, as the slightly larger ion heating with ^{3}He ICRH is offset by a larger main-ion dilution.

Next, a lower density scenario with $n_e/n_{GW} \approx 0.4$ (green circle) was considered, motivated by increasing the ratio $P_{sep}/P_{L\text{-}H}$ above the ~1.5 value, characteristic of the other points. This scenario results in $Q \approx 0.96$ and can be further optimized to achieve scientific breakeven, for example by adjusting ICRF parameters.

The remaining cases at I_p = 7 MA explore options consistent with strategies for ELM mitigation or suppression. As discussed in Chapter 2, at the pedestal collisionallity of the standard 7 MA case, the type I ELM scaling predicts an energy loss of $\Delta W/W_{ped} \approx 15\%$ (~2 MJ), which, if confirmed, is not acceptable for operation and requires mitigation strategies. The cases considered include:

1. ELM mitigation with error field correction coils [28] (grey circles in Fig. 4.4). An average reduction of the temperature pedestal by 10-20% relative to the reference case can be assumed [32,33]. The corresponding fusion gain values are $Q \approx 1.31$ and $Q \approx 1.12$, respectively.
2. Strong impurity seeding regime (brown circle) [29-31]. In modelling this scenario, the argon concentration is increased to $n_{Ar}/n_e = 4.8\times10^{-3}$ (Z_{eff} = 2.7), raising the core radiation to ~16.2 MW. The pedestal is found to be minimally affected, so β_N and confinement remain essentially unchanged. Due to higher dilution, the computed fusion gain is somewhat lower, $Q \approx 1.32$.
3. Quasi-continuous exhaust (QCE) regime (light blue dot) [6]. For the high-triangularity configuration foreseen in BEST, modelling the QCE-like regime is achieved by increasing the separatrix density to $n_{e,sep} = 4.5\times10^{19}$ m^{-3}, while keeping the pedestal-top density and impurity seeding level constant ($n_{Ar}/n_e = 2.6\times10^{-3}$, Z_{eff} = 2.0). The QCE regime is characterized by the plasma

transition into a type II ELM regime, avoiding type I crashes. The pedestal reduction causes a ~10% decrease in β_N and global confinement, yielding a somewhat lower fusion gain of $Q \approx 1.19$.

In this version of the Research Plan, detailed analysis has focused on the QCE-like scenario as the promising candidate for conservative ELM-free BEST operations, enabling $Q > 1$ while maintaining edge conditions compatible with divertor requirements.

4.4.3: QCE regime – radial profiles and global parameters

In this subsection, we present additional details of the integrated modelling results for the QCE-like scenario at I_p = 7MA and $n_e/n_{GW} \approx 0.5$. Figure 4.6 (red lines) shows the electron temperature, ion temperature and electron density profiles as predicted by ASTRA modelling. For comparison, the figure also illustrates the kinetic plasma profiles for the reference type I ELM scenario (black lines) and the strong seeding scenario (blue lines). The global parameters for the QCE-like scenario are as follows: $Q \approx 1.19$, $P_{fus} \approx 42$MW, $P_{rad} \approx 12$ MW, $\tau_E \approx 1.23$ s, $H_{98y,2} \approx 1.0$, $\beta_N \approx 1.3$, $P_{sep}/P_{L\text{-}H} \approx 1.4$.

For completeness, Figure 4.7(a) shows the computed heating power densities , including contributions from alpha-particles to both electrons and bulk ions ($p_{e,DT}$ and $p_{I,DT}$). The external + alpha heating is distributed as 60% to electrons and 40% to ions. Figure 4.7(b) illustrates the computed q-profile and current density components. At 7 MA most of the current density is Ohmic, with a non-inductive fraction of ≈ 30%. The ECCD is not enough to flatten the q profile, but together with the high $q_{95} \approx 4.7$ it helps to maintain the $q = 1$ surface at $\rho_{tor} \approx 0.2$, preventing large sawteeth.

Figure 4.8(a) shows the predicted radial profiles for tungsten and argon impurity densities, as well as the Z_{eff}-profile. Under the considered conditions, no central accumulation of tungsten is observed, and the tungsten remains approximately flat across the plasma radius. This W profile is consistent with a strong pedestal screening and a role of the core ECH to enhance turbulent diffusion, counteracting accumulation.

Finally, Figure 4.8(b) shows the predicted radial profiles for alpha-particle density and effective temperature [22]. In the plasma core the alphas have effective temperatures $T_\alpha \approx 1$ MeV with density $n_\alpha \approx 10^{18}$ m^{-3}.

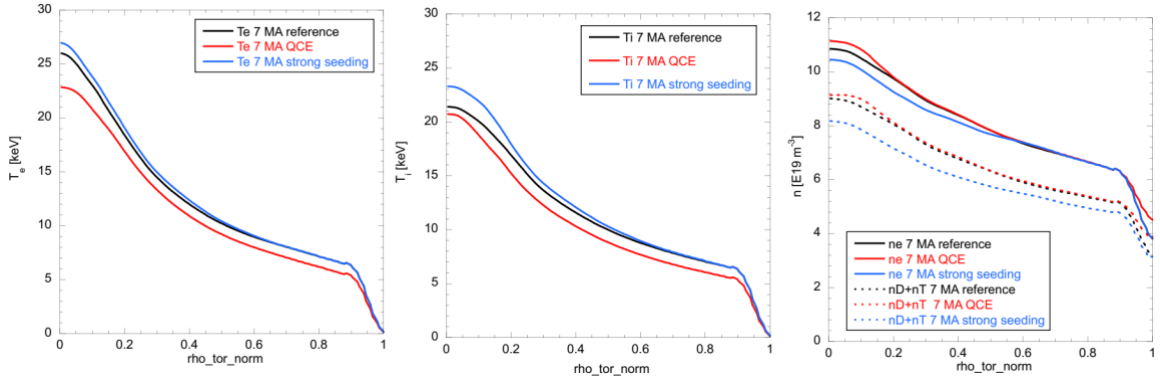

Figure 4.6: T_e, T_i, n_e, n_D+n_T profiles for the QCE (light blue dot in Fig. 4.4) and the strong seeding (brown dot in Fig. 4.4) regimes, compared with the standard 7 MA "type I ELM" scenario (black dot in Fig. 4.4).

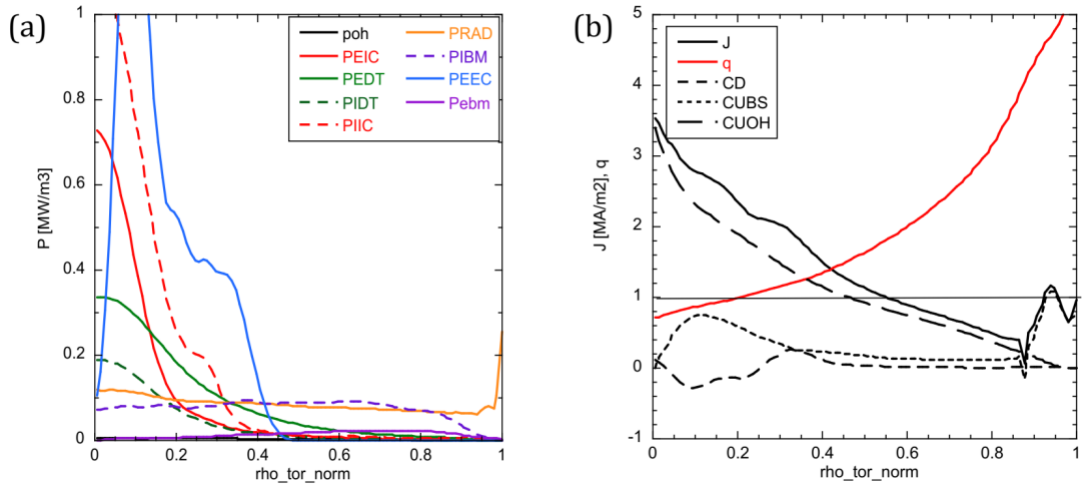

Figure 4.7: Details of the computations for the QCE regime. (a) Radial profiles of the different power deposition terms. (b) Radial profiles of the total and ohmic current density, bootstrap current, current drive and q-profile.

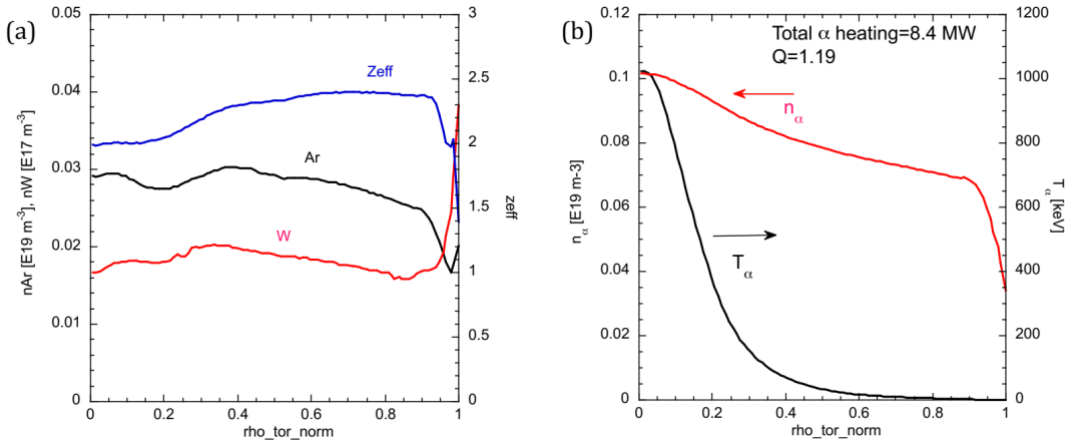

Figure 4.8: Details of the computations for the QCE regime. (a) Impurity density and Zeff profiles (right Y-axis). (b) Alpha-particle density, n_α and effective temperature of alphas, T_α profiles (right Y-axis).

4.4.4: Comparison of BEST dimensionless parameters with other D-T devices

In this subsection, we present the comparison of a set of dimensionless parameters for the BEST QCE scenario described in subsection 4.4.3 and four past and future D-T machines, JET, ITER, CFEDR, EU-DEMO. For JET we have selected the hybrid D-T pulse #99950 [34], for ITER the baseline scenario described in [35], for CFEDR the most recent set of predicted profiles [36], for DEMO the 2018 version from [37].

We used the following definitions: $\nu_e^* = 69.21\ (q\ R\ n_e\ Z_{eff}\ \ln \Lambda_e)/(T_e^2\ \varepsilon^{3/2})$ [38] with $\ln \Lambda_e = 15.2 - 0.5 \ln n_e(10^{20}\ m^{-3}) + \ln T_e(keV)$, $\varepsilon = r/R$, with local values r [m], q, Z_{eff}, n_e [10^{19} m^{-3}], T_e [eV]; $\rho^* = 4.57\times10^{-3}\ (T_i\ A)^{1/2}/(a\ B_{tor})$ with T_i in keV, A = mass number (=2.5 for D-T), B_{tor} in T, a in m; $\beta = 2\mu_0\ p\ /B_{tor}^2$ with p the pressure in Pascal; $\beta_N = \beta\ a\ B_{tor}/I_p$ with I_p in MA.

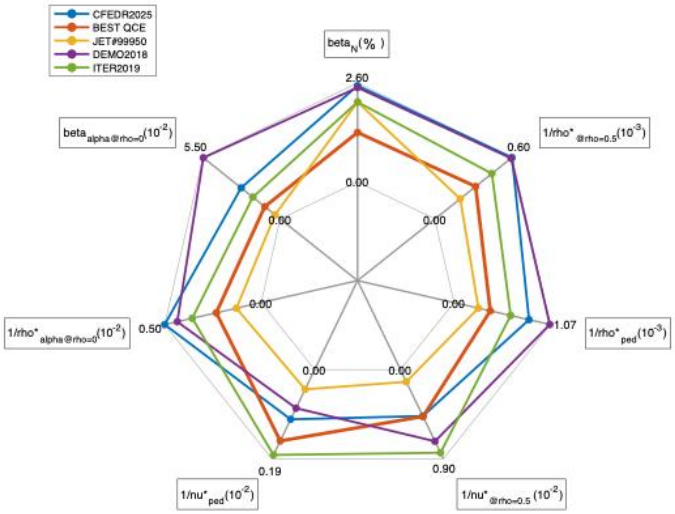

Figure 4.9: Spider plot comparing dimensionless parameters of BEST QCE with JET hybrid pulse #99950 and baseline full power scenarios in ITER, CFEDR and EU-DEMO.

Figure 4.9 presents the spider plot of β_N, ρ^* and ν^* at mid-radius and at top of pedestal, ρ^* and β of alpha-particles. One can see how BEST exceeds the JET parameters, apart from β_N due to the higher toroidal field, and acts as a bridge towards future reactors. Table 4.3 reports a wider set of parameters for a more detailed comparison.

Table 4.3: Summary of parameters of BEST QCE scenario compared with JET hybrid pulse #99950 and baseline full power scenarios in ITER, CFEDR, DEMO.

	BEST QCE 2025	**JET #99950**	**ITER 2019**	**CFEDR 2025**	**DEMO 2018**
R [m] / a [m]	3.6/1.1 =3.27	2.96/0.95 =3.11	6.2/2.0 =3.1	7.88/2.45 =3.21	9.07/2.93 =3.1
I_{pl} [MA] / B_{tor}[T]	7/6.15	2.3/3.45	15/5.3	15/6.3	17.75/5.86
P_{sep}/R [MW/m]	8.7	8.4	14	34.9	18.9
P_{aux} [MW]	35	33	55	102	50
P_{fus} [MW]	37.6	10	510	1460	2012
β_N [%]	1.3	2.1	2.1	2.53	2.48
τ_E [s] Using P_{tot}	1.25	0.22	2.35	2	2.8
ρ^* at ρ_{tor}=0.5 [10^{-3}]	3.16	5.1	2.26	1.67	1.69
ν_e^* at ρ_{tor}=0.5 [10^{-2}]	2.11	8.1	1.19	2.13	1.38
ρ^*_{ped} [10^{-3}]	2.48	3.7	1.59	1.2	0.94
$\nu_e^*{}_{ped}$ [10^{-2}]	6.57	23.8	5.49	9.42	12.15
q_{95}	4.5	4.8	3.2	5.26	3.89
n_{GW} [10^{20} m^{-3}]	1.84	0.8	1.2	0.795	0.66
$\rho_\alpha{}^*{}_{(\rho=0)}$ [10^{-3}]	43	78	28	20	23
$\beta_{\alpha\,(\rho=0)}$ [%]	1.1	0.37	1.95	2.78	5.47

4.5: Gyrokinetic simulations to quantify possible fusion gain enhancement due to non-linear electromagnetic stabilization

4.5.1: Introduction

Local gyrokinetic (GK) simulations with the GENE code [39, 40] were performed in the inner core of the BEST reference 7 MA "type I ELM" scenario (black dot in Fig. 4.4), to study the impact of electromagnetic (EM) fluctuations on the heat transport, potentially giving a beneficial stabilizing effect which could result in a de-stiffening of the T_i profile [8, 41, 42]. The transport reduction due to the fast ions (FI) produced by NBI and ICRH, which can in principle contribute to suppress micro-turbulence [43-46, 35], was also investigated, but not the effect of alphas, which would require very heavy GK global non-linear EM simulations. Both these mechanisms are only partially included in the quasi-linear model TGLF, used for the integrated modelling of the scenarios described in Section 4.4. Therefore such simulations could result in an underprediction of the fusion gain Q.

The radius $\rho_{tor} = 0.33$ has been selected for the analysis, since it has a good combination of a relatively high $\beta_e \approx 1.4\times10^{-2}$ and a non negligible FI density $n_{FI}/n_e \approx 3.7\%$, so that both thermal EM stabilization of ITG modes, due to a finite β_e, and FI-induced stabilization could in principle impact the T_i profile. The FI have been simulated as a single 'lumped' gyrokinetic species, obtained by considering both the ^{3}He FI from ICRH and the deuterium FI from NBI, merging them while keeping the same Z_{eff} and neutrality. The D-T mixture is modelled as a single species with the atomic mass $A = 2.5$. To include the effect of impurities on the transport, Ar, ^{3}He and ^{4}He ash are added as a single gyrokinetic 'lumped' species. The impurities are assumed at thermal equilibrium with the main DT ions. The density profiles of the lumped species (impurities and FI) are shown in Fig. 4.10, together with the effective FI temperature.

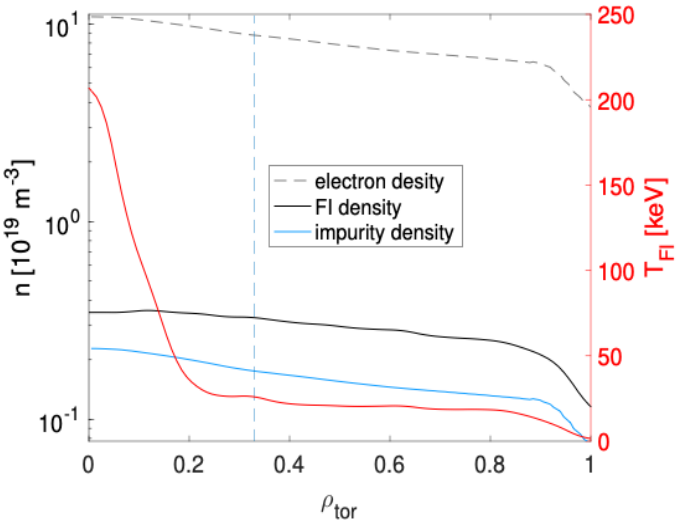

Figure 4.10: Radial profiles of the electron (dashed black), fast-ion (solid black), and impurity (solid blue) densities. The effective fast-ion temperature (solid red) is shown on the right-hand Y-axis. The vertical dashed line corresponds to the radius used for the local GK analysis ($\rho_{tor} = 0.33$).

The GENE code solves the GK equations, coupled with the Maxwell equations, within a δf-approximation. The simulations were carried out in the flux-tube (radially local) limit using realistic magnetic equilibria, reconstructed with the MHD solver CHEASE [47], accounting for collisions and finite-β effects from $\delta B_\perp$ and $\delta B_\parallel$ fluctuations.

4.5.2: Linear simulations at ρ_{tor} = 0.33

Linear flux-tube GENE runs were performed first, to characterize the micro-instabilities at the radius of analysis and assess the entity of the linear stabilization effects (thermal and FI-induced). For this purpose, the spectra of the linear eigenvalues were computed for three different cases: without FI, electrostatic (ES); without FI, electromagnetic (EM); with FI, EM. The results are shown in Fig. 4.11, by red, green and black lines, respectively. In the figure, the growth rate γ and the real mode frequency ω are normalized with respect to c_s/a, where $c_s = (T_e/m_i)^{1/2}$ is the sound speed and $a = (\Phi_{edge}/\pi B_0)^{1/2}$ provides an estimate of the average minor radius of the tokamak, where Φ is the toroidal flux, while the binormal wavenumber k_y is normalized with the inverse of the ion sound Larmor radius $\rho_s = c_s/\Omega_i$, with Ω_i the ion cyclotron frequency.

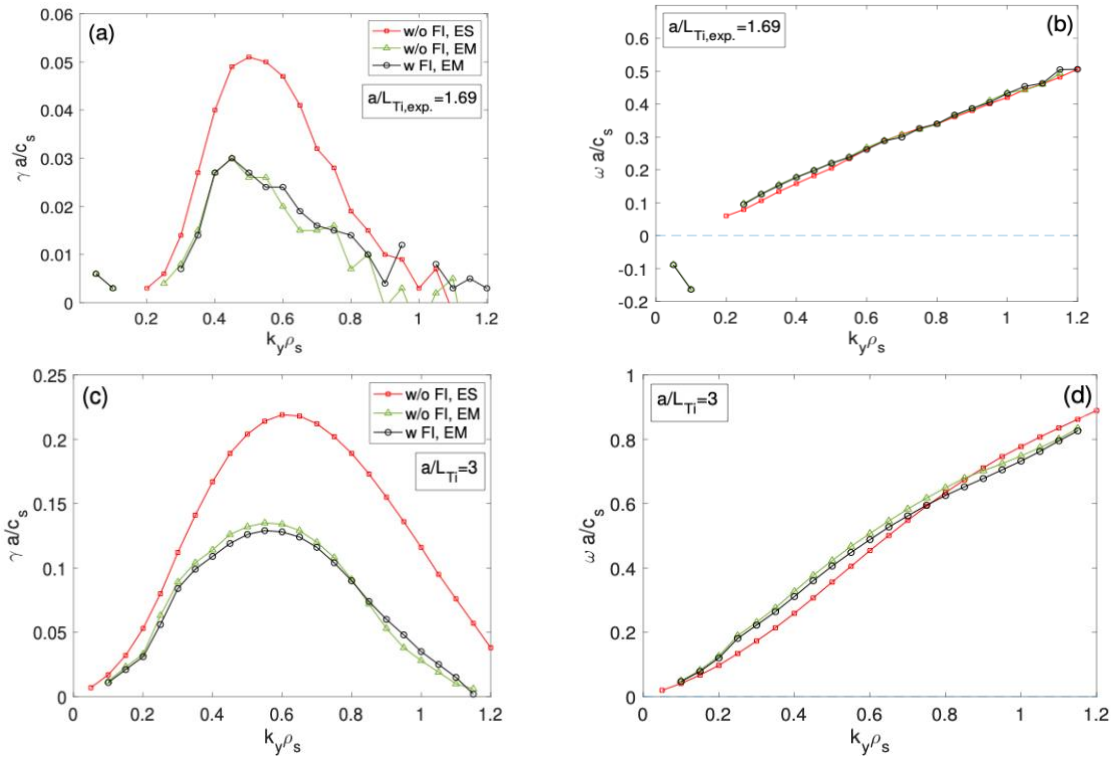

Figure 4.11: Results of the linear flux-tube GENE simulations at ρ_{tor} = 0.33 for the three modelling cases: i) without fast ions and electrostatic ('w/o FI, ES'); ii) without fast ions and electromagnetic ('w/o FI EM'); iii) with fast ions and electromagnetic ('w FI EM'). (a) and (b) Spectra of the growth rate γ and real frequency ω ($\omega > 0$ means ion direction) of the most unstable linear mode, computed at the nominal a/L_{Ti} = 1.69; (c) and (d) Spectra of γ and ω, computed at a larger a/L_{Ti} = 3.

An ITG dominant micro-instability regime is found, with micro-tearing modes (MTM) at the lower wavenumbers, which a posteriori have been checked not to show in the nonlinear runs. A rather strong thermal EM stabilization is seen, reducing the growth rate peak by ~40% at both nominal $a/L_{Ti} = -d\,\ln T_i/d\rho_{tor} = 1.69$ and at an almost double value $a/L_{Ti} = 3$, selected to test the sensitivity of the results to the main ITG drive. Note a small effect of the FI on γ and ω in linear simulations.

Figure 4.12 shows the results of an additional β_e-scan, performed for the electromagnetic case without fast ions ('w/o FI EM') at $k_y\rho_s = 0.5$ (corresponding to the maximum of the linear spectrum) with $a/L_{Ti} = 1.69$. The reference value $\beta_e \approx 1.3\%$ (obtained from scenario transport modelling) is relatively low compared with the kinetic ballooning mode (KBM) threshold, $\beta_e^* \approx 3\text{-}3.5\%$. These reference conditions lie in a β_e interval which is compatible with linear EM stabilization, as indicated by the monotonic decrease of the growth rate with increasing β_e towards the KBM threshold.

4.5.3: Nonlinear simulations at $\rho_{tor} = 0.33$

A set of nonlinear GENE simulations have been performed at three values of the T_i inverse logarithmic gradient: i) $a/L_{Ti} = 1.69$, ii) $a/L_{Ti} = 2.0$, and iii) $a/L_{Ti} = 3.0$, for each of the 3 cases that were considered for the linear analysis (without FI, ES; without FI, EM; with FI, EM), in order to test if the EM effects would impact the T_i stiffness (i.e. the degree to which the radial T_i profile responds to changes in the applied heat flux). The simulation results are shown in Figure 4.13. The main picture that emerges is that a nonlinear EM thermal stabilizing effect is present, even larger than the linear one, as expected (approximately 70% reduction of the fluxes with finite beta). However, the available ion heat flux is insufficient for this effect to impact the ion temperature profile, since the resulting a/L_{Ti} is placed too close to the ITG threshold. Indeed, by

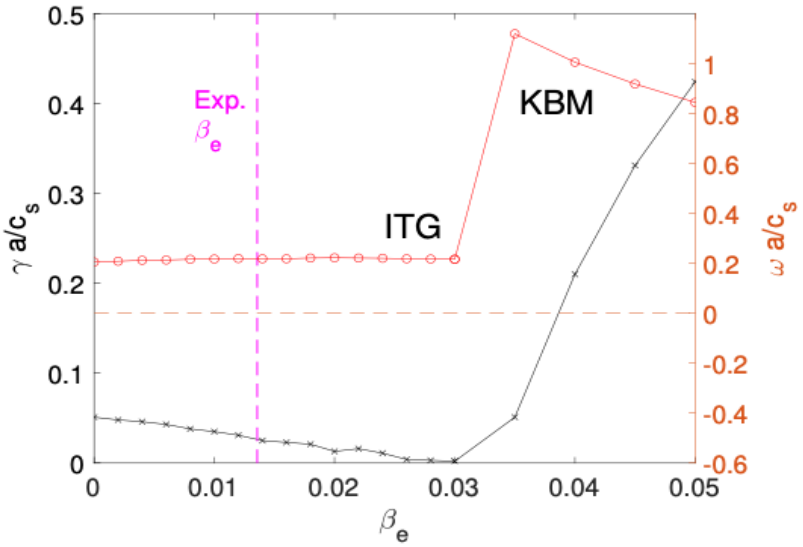

Figure 4.12: Results of an additional β_e-scan for the linear growth rate and mode frequency (right Y-axis) for the electromagnetic case without fast ions, computed at $k_y\rho_s = 0.5$ with $a/L_{Ti} = 1.69$.

looking to the zoomed-in region in Fig. 4.13, one notes that GENE predicts the EM stabilizing effect to only increase a/L_{Ti} by less than 10%, which is a negligible effect within the numerical error bars ~10%. This small improvement is actually comparable to the effect given by the mock-up model used only for the optimized 6 MA case in Section 4.4. The effect of the FI for the considered conditions is negligible, as in the linear analysis.

In summary, a noticeable thermal electromagnetic stabilizing effect is found at work. However, for the considered scenario, the BEST ion heat source is insufficient to allow it to significantly impact the ion temperature profile at the radius of analysis. This implies that a possible future increase in the auxiliary heating power may lead to better exploitation of the effects resulting in ITG stabilization, thereby further enhancing the fusion power production in BEST.

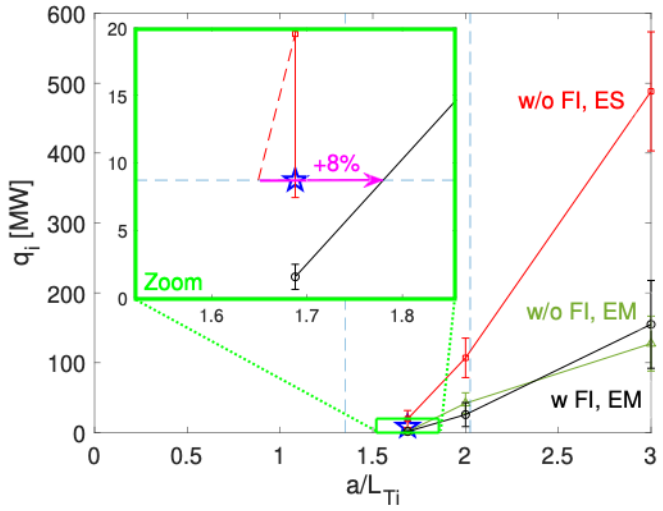

Figure 4.13: Ion temperature stiffness plot at $\rho_{tor} = 0.33$. The ion heat flux q_i is shown as a function of the main ITG drive a/L_{Ti} for three different cases: i) electrostatic simulations without fast ions ("w/o FI, ES", red symbols), ii) electromagnetic simulations without fast ions ("w/o FI, EM", green symbols), and iii) electromagnetic simulations with fast ions ("w FI, EM", black symbols). The reference point ($q_i \approx 8.5$MW and $a/L_{Ti} \approx 1.69$) is marked by a blue star. A zoomed-in view of the region around this reference point is highlighted by a green rectangle. The vertical dashed lines denote $a/L_{Ti} \approx 1.35$ and $a/L_{Ti} \approx 2.03$, representing a ±20% uncertainty range on a/L_{Ti}.

4.6: Outlook

Future modelling work will address physics-based time dependent simulations of the full discharge evolution of the QCE scenario using the ASTRA/TGLF framework, in order to achieve more precise estimates of the duration of the ramp-up, flat-top and ramp-down phases. It will also address possible further optimization of the heating deposition, as well as the possibility to work at higher densities. Finally, other types of scenarios will be addressed, such as the lower $Q \approx 0.3$ long pulse scenario to be used for technology experiments and the high $Q \approx 5$ advanced scenario for burning plasma studies.

4.7: References

[1] ITER Physics Basis Editors et al., *Nucl. Fusion* **39**, 2175 (1999)
[2] E. Delabie et al., "*Scaling of the L-H threshold power for metal wall machines (ITPA task TC-26)*", *66th Conf. of APS Division of Plasma Physics, Atlanta (USA)* (2024)
[3] P. Vincenzi et al., *Plasma Phys. Control. Fusion* **67**, 045013 (2025)
[4] G.S. Xu et al., *Phys. Rev. Lett.* **122**, 255001 (2019)
[5] M. Greenwald et al., *Phys. Plasmas* **6**, 1943 (1999)
[6] M. Faitsch et al., *Nucl. Mater. Energy* **26**, 100890 (2021)
[7] M. Bernert et al., *Nucl. Mater. Energy* **12**, 111 (2017)
[8] J. Citrin and P. Mantica, *Plasma Phys. Control. Fusion* **65**, 033001 (2023)
[9] G.V. Pereverzev and P.N. Yushmanov, "*ASTRA–Automated System for Transport Analysis in a Tokamak*", Max-Planck-Institut für Plasmaphysik Report, IPP 5/98 (2002)
[10] E. Fable et al., *Nucl. Fusion* **53**, 033002 (2013)
[11] G.M. Staebler, *Plasma Phys. Control. Fusion* **63**, 015013 (2021)
[12] W.A. Houlberg et al., *Phys. Plasmas* **4**, 3230 (1997)
[13] D. Fajardo et al., *Plasma Phys. Control. Fusion* **65**, 035021 (2023)
[14] E. Fable et al., "*FEQIS: A free-boundary equilibrium solver for integrated modeling of tokamak plasmas*", *Open Plasma Science* **1**, No. 2 (2025)
[15] S. Saarelma et al., *Phys. Plasmas* **26**, 072501 (2019)
[16] P. Schneider et al., *Nucl. Fusion* **53**, 073039 (2013)
[17] M. Knolker et al., *Nucl. Fusion* **61**, 046041 (2021)
[18] U.A. Sheikh et al., *Plasma Physics and Controlled Fusion* **61**, 014002 (2019)
[19] W.W. Pfeiffer et al., "*ONETWO: a computer code for modeling plasma transport in Tokamaks*", General Atomics Report GA-A16178 (1980)
[20] M. Brambilla, *Plasma Phys. Control. Fusion* **41**, 1 (1999)
[21] P.N. Yushmanov, 11-JUN-87, private communication
[22] R. Bilato et al., *Phys. Plasmas* **21**, 104502 (2014)
[23] D.E. Post, *Applied Atomic Collision Physics* **2**, 381 (1984)
[24] C.M. Roach and I.A. Voitsekhovich, private communication (1999)
[25] A. Pankin et al., *Comp. Phys. Comm.* **159**, 157 (2004)
[26] M. Romanelli et al., *Plasma Fusion Res.* **9,** 3403023 (2014)
[27] F.J. Casson et al., *Nucl. Fusion* **60**, 066029 (2020)
[28] Y. Liang et al., *Phys. Rev. Lett.* **98**, 265004 (2007)
[29] C. Giroud et al., *Nucl. Fusion* **64**, 106062 (2024)
[30] S. Glöggler et al., *Nucl. Fusion* **59**, 126031 (2019)
[31] M. Bernert et al., *Nucl. Fusion* **61**, 024001 (2020)
[32] M. Faitsch et al., *Nucl. Fusion* **63**, 076013 (2023)
[33] M. Faitsch et al., *Nucl. Fusion* **65**, 024003 (2025)
[34] J. Hobirk et al., *Nucl. Fusion* **63,** 112001 (2023)
[35] P. Mantica et al., *Plasma Phys. Control. Fusion* **62**, 014021 (2020)
[36] J. Chen, private communication (2025)
[37] M. Siccinio et al., *Fusion Eng. Design* **176**, 113047 (2022)

[38] O. Sauter et al., *Phys. Plasmas* **6,** 2834 (1999)
[39] F. Jenko et al., *Phys. Plasmas* **7**, 1904 (2000)
[40] T. Görler et al., *J. Comput. Phys.* **230**, 7053 (2011)
[41] G. Whelan et al., *Phys. Rev. Lett.* **120**, 175002 (2018)
[42] J. Citrin et al., *Nucl. Fusion* **54**, 023008 (2014)
[43] A. Di Siena et al., *Nucl. Fusion* **59**, 124001 (2019)
[44] J. Citrin et al., *Plasma Phys. Control. Fusion* **57**, 014032 (2015)
[45] J. Citrin et al., *Phys. Rev. Lett.* **111**, 155001 (2013)
[46] J. Garcia et al., *Nucl. Fusion* **55**, 053007 (2015)
[47] H. Lütjens et al., *Comput. Phys. Commun.* **97**, 219 (1999)

Chapter 5: Heating, Current Drive and Fuelling

Coordinators: J. Hillairet (CEA, France), X.J. Wang (ASIPP), B. Zhang (ASIPP)

With contributions from:
ASIPP Team: B. Cao, M.H. Li, J.L. Hou, Y.Y. Tang, J. Wang, H.L. Wang, J.H. Wu, Y.L. Xie, X.Y. Xu, Y. Ye, J.S. Yuan, C.M. Qin, X.J. Zhang, W. Zhang, B.J. Ding, C.B. Wu, H.D. Zhuang, Y.H. Xie, H.D. Xu, F.K. Liu, G.Z. Zuo, L.Z. Liang, Y.Y. Huang, J.S. Hu
EUROfusion Team: Ye.O. Kazakov (LPP-ERM/KMS, Brussels, Belgium)

5.1: Introduction

The heating and current drive (H&CD) systems, together with plasma fuelling systems are key actuators for achieving the main objectives of the BEST project. The H&CD mix of BEST is composed of both Neutral Beam Injection (NBI) and Radio Frequency (RF) heating systems, which operate across three frequency ranges: i) electron cyclotron (f = 170 GHz), ii) ion cyclotron (f = 40-65 MHz, with future extension planned up to 90 MHz), and iii) lower hybrid (f = 4.6 GHz). The NBI system operates with deuterium and features acceleration voltages of up to 120 keV. In future phases of BEST, a negative-ion-based NBI system is planned, capable of injecting fast neutral particles with energies in the range of 500-800 keV. The overall layout and main system specifications of the H&CD systems are summarized in Fig. 5.1.

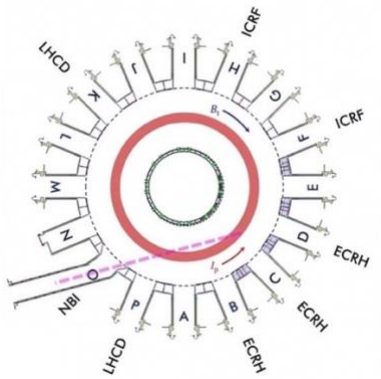

	Injected power	Nominal power	RF frequency
ECRF	15MW	24MW	170GHz
ICRF	10MW	16MW	40-65MHz (40-90MHz)
LH	10MW	16MW	4.6GHz
NBI (120keV)	12MW	15MW	–

Figure 5.1: Schematic layout and main parameters of the BEST H&CD systems.

BEST is also equipped with a comprehensive set of fuelling systems, designed for specific operational functions. These include 9 Gas Injection (GI) modules distributed across various spatial locations (including equatorial, upper, high-field side, and divertor regions) to provide flexible control of plasma density. In addition, the fuelling systems include three Fast Pellet Injectors (FPI) and two Supersonic Molecular Beam Injection (SMBI) systems for efficient core and edge fuelling. A Compact Torus Injector (CTI) is also available to enable deep core plasma fuelling. For disruption mitigation and machine protection, BEST is further equipped with both a Massive Gas Injection (MGI) system and a Shattered Pellet Injector (SPI). The main parameters of the various fuelling and disruption mitigation systems are summarized in Table 5.1.

Table 5.1: Summary of main parameters of the fuelling and disruption mitigation systems in BEST.

System	Number & injection locations	Fuelling region	Gas species	Injection specifications
Fuelling systems				
GI	9 (distributed across equatorial, upper, HFS, and divertor regions)	Edge, antenna regions, divertor	D_2, T_2, He, Ar, Ne	Total 100 Pa·m^3/s (fuelling) 5 Pa·m^3/s (impurity) 10 Pa·m^3/s (WC) Continuous operation
FPI	2 on the LFS, 1 on the HFS	Core	D_2, T_2	<5 Hz Continuous operation
SMBI	2 systems	Edge, core	D_2, T_2, He, Ar, Ne	<500 Hz, <20 Pa·m^3/s Continuous operation
CTI	1 system	Core	D_2, T_2	5 Pa·m^3/s <2 Hz for 10s
Disruption mitigation systems				
MGI	3 ports	Whole plasma volume	He, Ne, Ar, or mixtures	The maximum gas injection capacity > 5000 Pa·m^3 per shot.
SPI	22 ports	Whole plasma volume	Ne, D_2, H_2, Ar, or mixtures	500 m/s

In the following sections, further details for the individual H&CD, fuelling and disruption mitigation systems are presented.

5.2: Heating and current drive systems

5.2.1: Electron cyclotron range of frequency

In BEST, the Electron Cyclotron Range of Frequency (ECRF) system is designed to deliver up to 15 MW of RF power at a frequency of 170 GHz for duration exceeding 1000 seconds. The ECRF plant consists of 24 gyrotrons. Power is transmitted to three equatorial launchers, located at ports B, C, and D, via 24 actively water-cooled evacuated corrugated circular waveguides (63.5 mm diameter). The toroidal and poloidal launch angles of the system provide significant flexibility for plasma scenarios [1], enabling additional functionalities such as plasma breakdown, start-up and ramp-down assistance, and mitigation of impurity accumulation [2, 3].

As a versatile actuator, the primary roles of the ECRF system include plasma heating, current drive and profile tailoring. ECRF heating is an essential component for BEST scenarios at the nominal magnetic field, B_0 = 6.15T, allowing both on-axis and off-

axis power deposition, or a combination of the two (see Fig. 5.2). At lower toroidal fields, ECRH can operate with off-axis heating in O1-mode at B_0 = 5.0-5.5T (see Chapter 2) and central X2-mode heating at half field, B_0 = 3.1T.

The ECRF system can also drive plasma current in BEST across a range of magnetic fields by adjusting the antenna mirror angles to modify the incident angle of the EC waves. For toroidal fields in the range from 5 T to 6.15 T, simulations indicate that the expected EC current drive (ECCD) efficiency can reach 1.2×10^{-4} A/cm^2/W. During the ramp-up phase, co-ECCD can be applied to save magnetic flux.

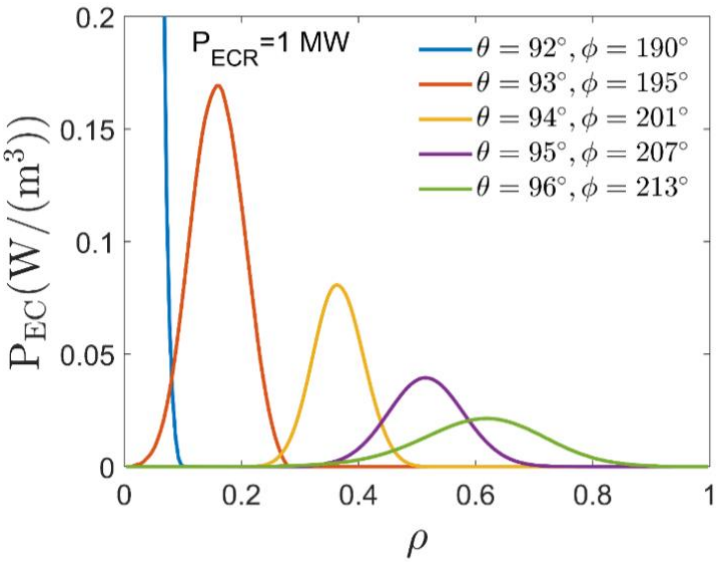

Figure 5.2: Flexibility of ECRF system for on-axis and off-axis power deposition at B0 = 6.15T, achieved by steering the poloidal injection angles of equatorial launchers.

5.2.2: Ion cyclotron range of frequency

In the initial phase of BEST operation, the Ion Cyclotron Range of Frequency (ICRF) system will couple up to 10 MW in the frequency range of 40-65 MHz. In parallel, research and development efforts are ongoing to extend the RF system to higher frequencies (f = 65-90 MHz). ICRF operation at $f \approx$ 90MHz will enable the application of hydrogen minority scheme for core plasma heating at the nominal field of 6.15T.

The RF plant provides a total of 16 MW using tetrode tube amplifier technology. Power is transmitted to two ICRF antennas, located at ports F and H, via actively water-cooled 12-inch and 13.5-inch coaxial lines. As shown in Fig. 5.3, one launcher is a two-strap ITER-type antenna [4], and the other one is a three-strap antenna [5], designed to minimize impurity source from ICRF.

Each launcher can be energized independently at a different frequency, thereby providing flexibility for scenario optimization and fast-particle control [6]. The antenna phasing can also be varied to minimize impurity production, impact fast-ion dynamics, control sawtooth [7] and fast-ion-driven instabilities. Additionally, local gas injection near the antennas will be used to enhance coupling conditions when necessary [8].

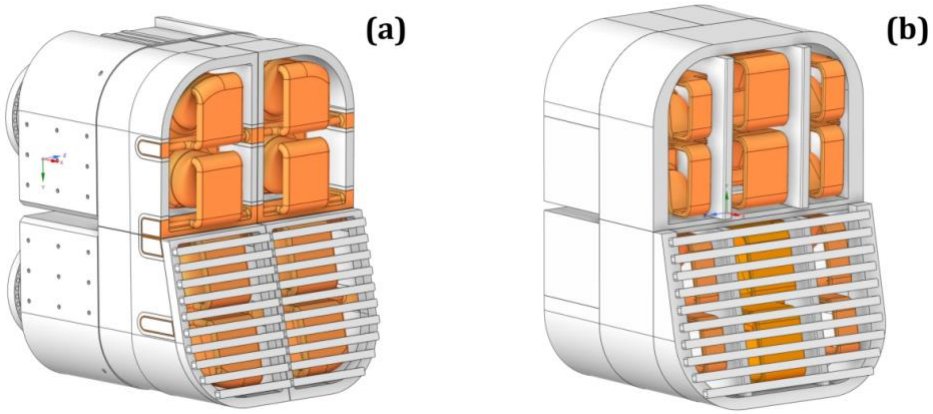

Figure 5.3: Schematic of ICRF antennas in BEST.
(a) A two-strap ITER-type antenna; (b) A three-strap antenna.

A range of efficient ICRF scenarios is available at BEST, both at the half-field and at the nominal field. For the half-field operations (B_0 = 3.1T), the hydrogen minority scheme ($\omega = \omega_{ci}$(H), with partial $\omega = 2\omega_{ci}$(D) absorption) at $f \approx$ 45-50 MHz provides robust absorption for both in D-D and D-T plasmas. For D-T plasmas at B_0 = 6.15T, four efficient scenarios can be obtained depending on the selected ICRF frequency, see Fig. 5.4:
i) $f \approx$ 90 MHz: Hydrogen minority, $\omega = \omega_{ci}$(H) (with partial $\omega = 2\omega_{ci}$(D) absorption);
ii) $f \approx$ 60-65 MHz: ^{3}He minority, $\omega = \omega_{ci}(^3\text{He})$ (with partial $\omega = 2\omega_{ci}$(T) absorption);
iii) $f \approx$ 47 MHz: Deuterium minority heating, $\omega = \omega_{ci}$(D) [9];
iv) $f \approx$ 42 MHz: three-ion schemes with impurity ions (Ar, ^{22}Ne, ^{11}B, etc.) [10, 11].

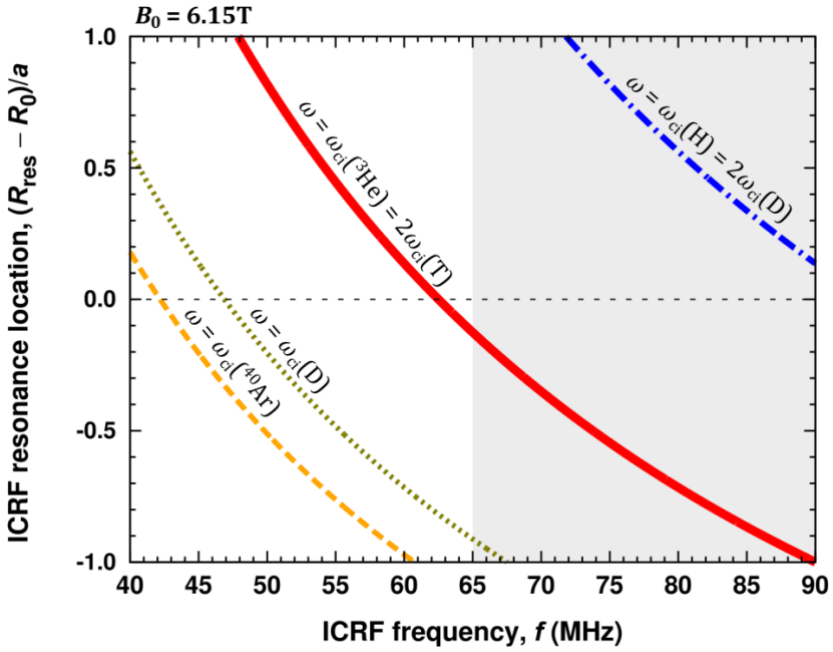

Figure 5.4: Configuration of ICRF resonances in BEST at B_0 = 6.15T for different ion species as a function of ICRF frequency.

As described in Chapters 2 and 4, the current Research Plan focuses on the application of the ^{3}He minority ICRF scheme with $n(^3\text{He})/n_e \approx 3\%$, both throughout the ramp-up and the main phases. Further optimization of the ICRF settings – including ICRF antenna phasing, ^{3}He concentration scan, studying whether switching off ^{3}He injection in the flat-top and maximizing $\omega = 2\omega_{ci}(\text{T})$ absorption, etc. – is left for future studies. The assessment of the potential of $\omega = \omega_{ci}(\text{D})$ and three-ion ICRF scenarios will also be addressed in future work.

The ICRF system will be instrumental for the preparation and validation of alpha-particle diagnostics before their use in D-T plasmas (see Chapter 12). For example, different three-ion ICRF schemes, such as D-(^{3}He)-H (at $f \approx 63$ MHz) and D-(D_{NBI})-^{3}He (at $f \approx 55$MHz), can be applied to generate MeV-range fast ions and fusion-born alpha particles before starting operations with tritium in BEST.

Extending the ICRF frequency range toward 90 MHz is an important objective, as it allows the use of the hydrogen minority scenario at $B_0 = 6.15$T, thereby minimizing the reliance of ^{3}He for D-T studies, including long-pulse operations. Moreover, this ICRF scheme can contribute to the proposed scenarios at $B_0 = 5$-5.5T (see Chapter 2), proving central electron heating with ICRF ($f \approx 77$-85 MHz).

5.2.3: Lower hybrid range of frequency

The Lower Hybrid (LH) system in BEST will provide 10 MW at a frequency of 4.6 GHz for duration exceeding 1000 seconds. The RF plant delivers 16 MW using commercially available klystron tube technology [12]. RF power is transmitted to two launchers, located at ports K and P, via actively water-cooled oversized circular waveguides. Both launchers rely on a passive-active multijunction (PAM) design [13], enabling effective LH power coupling at large plasma-antenna distances [14].

The LH antenna layout and face dimensions are shown in Fig. 5.5. Each antenna consists of 4 rows and 4 columns (totaling 16 units), with a source power of 16 × 0.5 MW = 8 MW. Each klystron module splits tangentially 1 into 4 and poloidally 1 into 3, resulting in 12 active waveguides per module. The antenna dimensions are height = 938.4 mm and width = 364 mm.

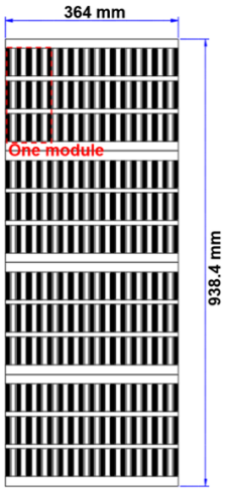

Figure 5.5: The layout of the lower hybrid antenna in BEST.

Using the actual antenna geometry, the ALOHA code [15] was used to analyze antenna coupling characteristics and the wave spectrum. As shown in Fig. 5.6(a), optimal coupling occurs near the cutoff density ($n_{e,cutoff} = 2.6\times10^{17}$ m^{-3}), with a minimum reflection coefficient (RC) below 1%. Near the optimal density, the wave spectrum directivity reaches ~70%. When the density varies between $n_{e,cutoff}$ and 10 $n_{e,cutoff}$, the reflection coefficient remains below 5%, but the wave spectrum directivity decreases gradually from 70% to 58%.

The main spectral peak can be shifted by adjusting the phase difference between waveguides. As shown in Fig. 5.6(b), the range of $N_{\parallel}$ varies between 1.9 and 2.6. The wave spectrum directivity is sensitive to the phase angle: the optimal directivity of 70% occurs at 0° phase with $N_{\parallel} = 2.2$, while at 180° phase, the directivity decreases to 60% with with $N_{\parallel} = 2.6$. Figure 5.6(c) shows the wave spectrum for the 0° phase, with a full width of the main spectral peak ~0.36.

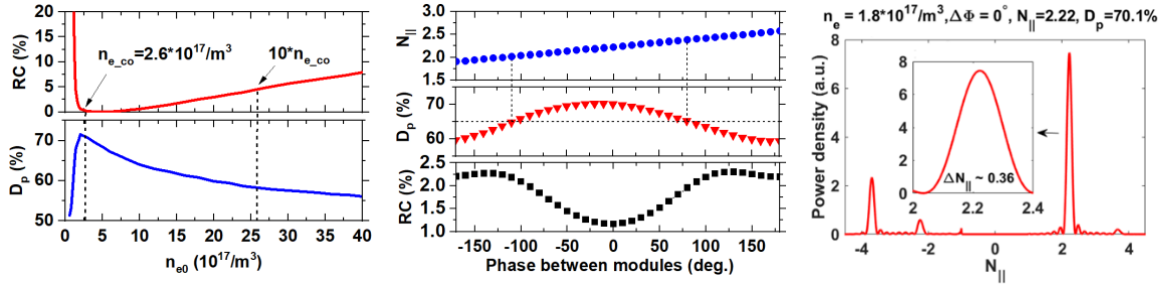

Figure 5.6: LH system characteristics. (a) Reflection coefficient and wave spectrum directivity as a function of plasma density. (b) $N_{\parallel}$, directivity, and reflection coefficient versus phase between the main waveguides. (c) Wave spectrum at a phase angle of 0°.

Lower Hybrid Current Drive (LHCD) is an important actuator for BEST, in particular for the development of advanced scenarios. Also for conservative scenarios, the LHCD system can help save magnetic flux during the ramp-up phase and be applied for q-profile shaping control. The LH system can also support L-H transition power control by providing additional auxiliary heating power and increasing the ratio $P_{aux}/P_{L\text{-}H}$. However, in high-temperature plasmas of large tokamaks, LH wave deposition is typically off-axis. The penetration and current drive capabilities of the LHCD system were assessed for the 7 MA $Q \geq 1$ scenario parameters (density, temperature profiles, and plasma equilibrium; see Chapter 4). As shown in Fig. 5.7, the LH wave undergoes complete single-pass absorption and is rapidly absorbed in the plasma. The peak power deposition occurs at $\rho \approx 0.82$, driving a current of ~380 kA for 10 MW of LH power. In follow-up LH simulations, the reference electron temperature was reduced by 20%, resulting in deeper LH wave penetration. In this case, the power deposition is peaked at $\rho \approx 0.65$, with a driven current of ~400 kA.

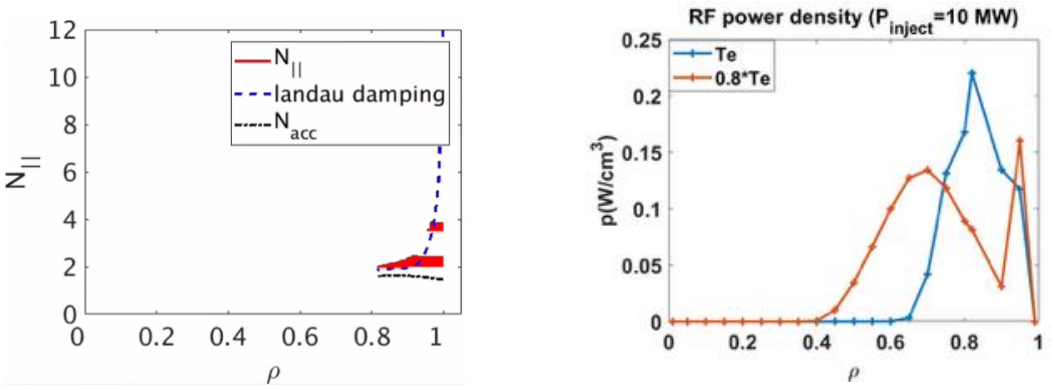

Figure 5.7: Results of ray-tracing of 4.6 GHz LHCD for the 7 MA $Q \geq 1$ scenario in BEST. (a) Evolution of $N_{\parallel}$, Landau damping and wave accessibility condition. (b) Power deposition profile for LH waves for the nominal electron temperature and for T_e reduced by 20%, resulting in deeper wave penetration.

5.2.4: Neutral beam injection

In the first phase of BEST operations, the Neutral Beam Injection (NBI) system is designed to deliver up to ~12 MW of deuterium neutrals into the plasma from a single equatorial beamline, produced by six 120 keV positive-ion sources. In later phases, the system will be upgraded to 4 MW at 500 keV and eventually to 10 MW at 800 keV using negative-ion sources (see Fig. 5.8). These variable energies provide flexibility for different deposition profiles to meet diverse experimental requirements. In this version of the Research Plan, interactions between the ICRF and NBI systems are not considered and will be addressed in the future. The NBI system can also contribute to active q-profile control through Neutral Beam Current Drive (NBCD). The NBI heating power and current drive capabilities are important for the development and sustainment of long-pulse scenarios in BEST, see Chapter 2.

NBI fast-ion losses are estimated to remain within engineering limits; for example, for the 7 MA $Q \geq 1$ scenario, the peak heat flux density would not exceed 0.15 MW/m^2. Due to the large NBI injection port, neutrons from D-T plasma can enter the beam duct, potentially causing atomic displacement damage and material activation. To mitigate this, a layered shielding design has been implemented [16, 17], reducing neutron radiation effects and preserving system integrity.

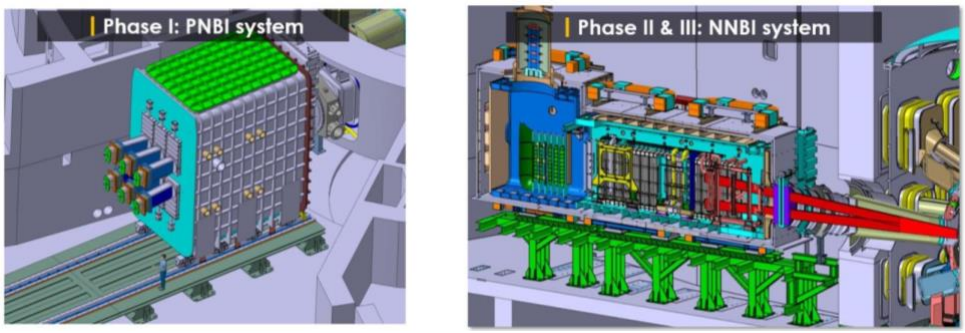

Figure 5.8: The layout of the NBI system in BEST. Initial NBI operations will use a positive ion source (E_{NBI} = 120 keV), with a future upgrade to a negative-ion source capable of injecting energetic deuterium neutrals at 500-800 keV.

5.3: Plasma fuelling

BEST employs four complementary fuelling systems to satisfy diverse operational needs: i) Gas Injection; ii) Fast Pellet Injection; iii) Supersonic Molecular Beam Injection, and iv) Compact Torus Injection. These systems support core fuelling, edge density control, ELM mitigation, heat flux control and long-pulse sustainment.

5.3.1: Gas injection system

The Gas Injection (GI) system serves as the baseline fuelling and wall-conditioning method for BEST, delivering fuel, impurity, and conditioning gases through a ring-distributed supply network. It consists of two subsystems: the gas transport and distribution system and the gas fuelling system.

Working gas is sourced from two facilities: the tritium plant (deuterium D_2, tritium T_2, and $D_2 + T_2$ mixtures) and the gas station (ordinary gases). Tritium-related gases are conveyed via double-walled pipelines for containment integrity. Gas from the station is categorized as low-pressure (≤2 bar: He, Ne, Ar) or high-pressure (≤200 bar: He, Ne, Ar, D_2, H_2). Pipelines from, both sources enter the tokamak hall at level B1, form a toroidal ring at B2, and feed vertical risers to fuelling ports.

The gas injection system includes nine injection locations: equatorial injectors in ports A, E, and I; top injectors in ports C and M; a high-field side (HFS) injector in port M; an inner divertor injector in port D; and outer divertor injectors in ports D and L. Each port delivers six gas species:

- Fuel gases (D_2, T_2, $D_2 + T_2$) from the tritium plant at 100 Pa·m^3/s;
- Impurity gases (He, Ne, Ar) from the low-pressure gas station at 5 Pa·m^3/s.

The wall-conditioning system, located at equatorial port E, supplies D_2 or He at 10 Pa·m^3/s for helium glow discharge cleaning or boronization. Key parameters of the gas injection system are summarized in Table 5.2.

Table 5.2: Main properties of the gas injection system in BEST.

Gas injection locations	Total: 9 (equatorial – A, E, I; top – C and M; high-field side – M; inner divertor – D; outer divertor – D and L)
Gas type	D_2, T_2, D_2+T_2, He, Ar, Ne
Operational pressure	T_2: 0.8 bar Other gases: 1-2 bar
Fuelling rate	Total Fuel: 100 Pa·m^3/s Impurities: 5 Pa·m^3/s Wall conditioning: 10 Pa·m^3/s

5.3.2: Fast pellet injection

Fast Pellet Injection (FPI) is designed to deliver solid D/T pellets within the normalized radius $\rho < 0.7$, thereby enabling deep core fuelling unattainable with GI or SMBI. This improves fuelling efficiency, central density peaking, and the fusion gain Q.

The system comprises three injection lines: horizontal ports A and I (low-field side, LFS) and lower port C (high-field side, HFS), each equipped with a low-loss guide tube (minimized bends, maximized bend radius) to preserve pellet integrity. The FPI system is made up of multiple units, including pellet fabrication unit, guide tube, cryogenic supply and vacuum pumping systems [18, 19]. The pellet injection units are monitored and controlled by local control system located in the cubicles in the tokamak complex. The local control system will exchange data with BEST control system. The key parameters of the FPI system in BEST are summarized in Table 5.3.

Each injector is housed in an N_2-purged glove box (via GDS) for tritium containment. A three-stage differential pumping system (Roots → dry → turbo pumps) extracts He propellant and residual D/T fuel gases; the exhaust is compressed and sent to the tritium plant – facilitated by efficient He/H isotope separation. Pellets (50-60 mm^3, ≤5 Hz) are fabricated continuously via screw extrusion and cutting. Acceleration is achieved by a light gas gun (target velocity ≤1000 m/s). Supercritical He (SCHe) cools the system (≤3.5 g/s per injector, total 10.5 g/s); D/T feed gas is pre-cooled to 50 K using recycled cold He to reduce SCHe consumption. High-pressure He is used as propellant to simplify exhaust handling and avoid H-isotope separation. Pellet size accounts for transmission losses in the guide tube.

Table 5.3: Key parameters of the fast pellet injection system in BEST.

	Specifications	Remarks
Pellet material	D_2, T_2	
Pellet size	Pellet volume: ≤55 mm^3; mass of one D_2 pellet ≤11 mg; mass of one T_2 pellet ≤17.6 mg	D_2 and T_2 pellets have the same size
Injection frequency	≤5 Hz	
Pellet velocity	≤1000 m/s	
Acceleration method	Gas gun	Acceleration gas: He
Cooling method	Liquid helium	Flow rate: ≤3.5 g/s

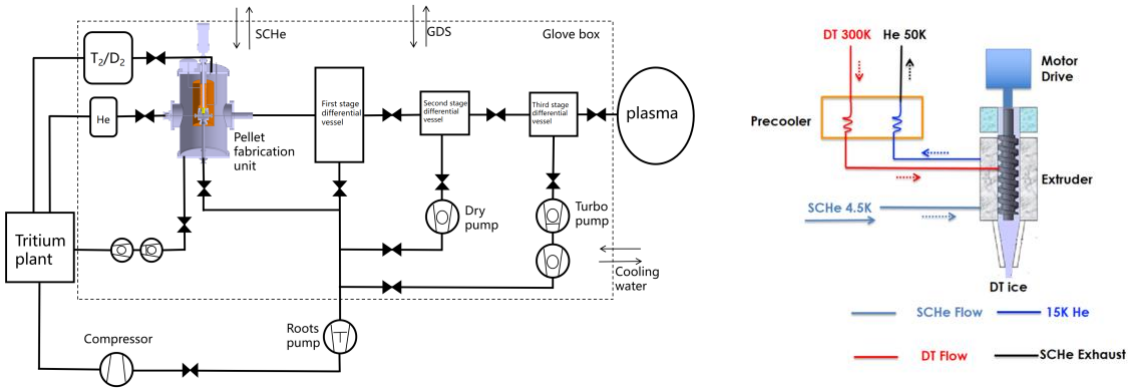

Figure 5.9: (a) FPI flow diagram within the glove box with all interfaces. (b) Cooling process diagram of FPI for pellet fabrication.

5.3.3: Supersonic molecular beam injection

The Supersonic Molecular Beam Injection (SMBI) system provides edge fuelling, ELM pacing, and heat-flux mitigation via supersonic (the Mach number >1), low-divergence molecular beams. Its simplicity, low cost, and high efficiency have led to deployment on HT-7, EAST, KSTAR, and other tokamaks. BEST will install two units at ports A and I (level L1). Each unit comprises a fast-response solenoid valve (<1 ms opening) and a Laval nozzle: gas accelerates to sonic speed at the throat, then expands supersonically before injection.

Neutron shielding requires radiation-absorbing materials in in-vessel windows, preventing direct beam passage. BEST decouples the Laval nozzle from the solenoid valve: the nozzle faces the plasma directly, while in-vessel piping is appropriately bent [20]. Redundant solenoid valves ensure continued operation after single-unit failure.

Tritium gas is transported from the plant at <1 atm and pressurized on-site to 4 bar within secondary containment linked to the GDS. The system supports D_2, T_2, He, Ne, and Ar at ≤20 Pa·m³/s, pulse widths of 1-100 ms, injection frequencies up to 500 Hz, and continuous operation. The SMBI flow diagram is illustrated in Fig. 5.10, together with the summary of the key parameters of the system.

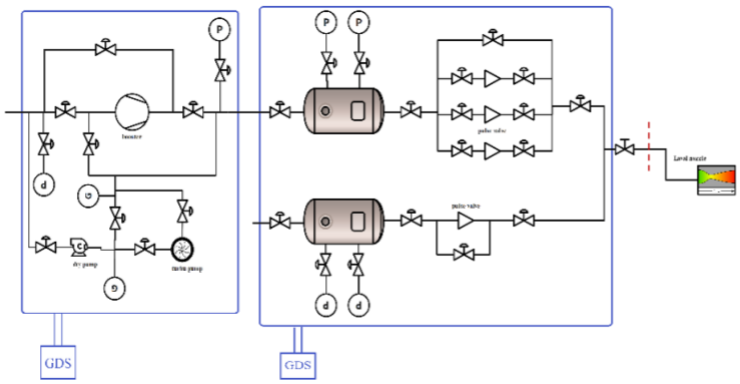

Gas pressure	4 bar
Gas type	D_2, T_2, He, Ar, Ne
Injection frequency	Max. 500 Hz
Injection pulse width	1-100 ms
Fuelling rate	20 Pa·m³/s
Continuous operation	Capable

Figure 5.10: The flow diagram and summary of main parameters of the SMBI system.

5.3.4: Compact torus injection

Compact Torus Injection (CTI) is a repeatable fast-particle injection (D_2, T_2) technique, employed to meet the requirements of high-density scenarios [21-24]. Operating via pulsed electromagnetic acceleration, the working gas is injected into the formation region by a pulsed gas valve. Under a bias magnetic field generated by a solenoid, it undergoes high-voltage breakdown to form a spheromak-configured CT plasma, which is then compressed and accelerated via Lorentz force before being transmitted to the tokamak through a drift tube. For the BEST, the CTI system is designed to achieve an injection rate of 2 Hz for over 10 seconds, with each CT plasma containing 10^{20} particles (plasma mass ~0.5 mg) and an injection speed of 300 km/s, alongside a fuelling rate of 5 Pa·m^3/s (see Table 5.4). A single CTI unit will be installed at port I (level L1).

To achieve these parameters, a high-current, narrow-pulse-width power supply system is required. The demanded high-current switches must reach a peak current of 400 kA with a current rise rate >20 kA/μs, while maintaining continuous operation at 2 Hz. Currently, neither gas switches nor thyratron switches can meet the requirements for long-term high-repetition operation. Thus, the development of all-solid-state semiconductor switch valve groups is necessary, with a focus on key issues such as high-current conduction mechanisms, heat treatment mechanisms, and dynamic uniformity. These areas represent critical priorities for both switch development and the future advancement of the BEST-CTI system.

Table 5.4: Key parameters of the CTI system in BEST.

	BEST-CTI Requirements	Existing Parameters
Working Gas	D_2, T_2	D_2
Location & Quantity	Port I, Level L1	/
CT Plasma mass	~0.5 mg per pulse	~0.2 mg per pulse
Fuelling Frequency	~2 Hz	< 1 Hz
Injection Velocity	~300 km/s	≤ 200 km/s
Particle Inventory	10^{20} particles	10^{20} particles
Main Switch Requirements	Peak current ~400 kA, Current rise rate ~20 kA/μs 2 Hz operation for 10 s	Peak current ~300 kA Current rise rate ~20 kA/μs 1 Hz operation for 5 s

5.4: Plasma disruption mitigation systems

Two disruption mitigation systems are foreseen in BEST to reduce disruption consequences. A disruption mitigation system (DMS) including three shattered pellet injection systems integrating muti-injectors and three massive gas injection systems has been preliminary designed in order to mitigate the deleterious effect resulted from plasma disruption and to ensure the safe operation of tokamak device.

5.4.1: Massive gas injection

The Massive Gas Injection (MGI) system mitigates plasma disruptions in the BEST tokamak by rapidly injecting impurity gases (He, Ne, Ar). Three such systems, each delivering 2000 $Pa \cdot m^3$, are installed. The key component is an eddy current-driven fast valve with a response time < 0.5 ms, operating at up to 5 MPa and 3000 V to inject up to 1.0×10^{23} particles. Comprising four core subsystems (fast valve, gas supply, power supply, and control), the MGI features a pressure-regulating structure for precise gas control (error ≤0.25%) and supports remote operation and gas mixture auto-replenishment. Triggered by a TTL signal, it injects a precise gas quantity within 1-4 ms to fulfil BEST's disruption mitigation requirements [25].

MGI technology is now well-established. In response to the requirement for higher gas throughput in the BEST device, the current MGI system requires a parameter upgrade. The engineering drawings for this upgrade have been completed, and the next steps involve prototype manufacturing and performance testing.

5.4.2: Shattered pellet injection

The Shattered Pellet Injection (SPI) system forms solid pellets through cryogenic condensation of impurity gases and accelerates them with high-pressure propellant gas. Prior to entering the plasma, the pellet is intentionally fragmented into numerous small pieces via a shattering tube. Given that the total surface area of these fragments is substantially larger than that of an intact pellet, the small particles undergo rapid ablation upon entering the plasma, releasing a substantial amount of material within a very short period. This facilitates rapid plasma cooling and notably enhances radiative dissipation. Three sets of SPI systems adopt an integrated design scheme with multiple injectors, amounting to a total of 22 injectors, as depicted in Figure 5.11. One set, consisting of 10 injectors, will be installed at the equatorial port A, while the other two sets will be installed at the upper ports G and K respectively, each set containing 6 injectors. Regarding each pellet injector, it can utilize the cryogenic cooling provided by liquid helium to desublimate the material gases within the gun barrel and form cylindrical pellets.

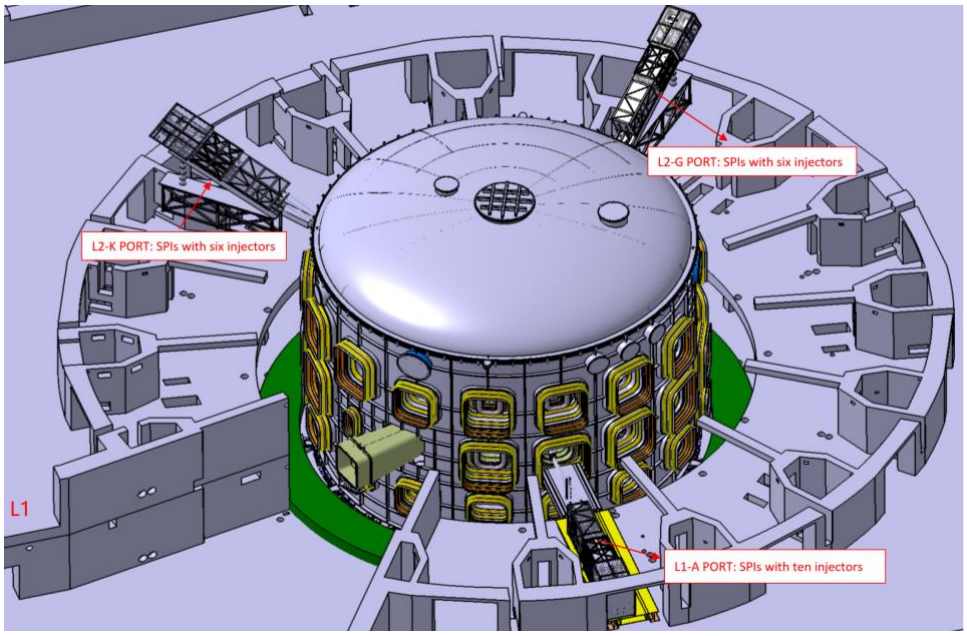

Figure 5.11: Layout of the SPI system in BEST.

Each pellet injector comprises a pellet producer, a gas feeding system, a propellant gas suppressor, a pellet diagnostic system, and either five or three injectors sharing a vacuum pumping system. Each injector can operate independently to generate pellets of different materials (Ne, D_2, H_2, Ar, or mixtures of different gases) with a D×L dimension of 20×30 mm. The material of these pellets can be adjusted in accordance with physical requirements [26-30]. The formed pellet is accelerated to a velocity of 500 m/s by utilizing high-pressure helium exceeding 50 bar. During the process of the pellet and the propellant gas through the suppressor, the propellant gas is removed. Ultimately, the pellet traverses the transmission tube and is fragmented by a shatter mechanism at the tube's end prior to injection into the plasma. The fragment plume and injection direction can be regulated by the structure of the shatter.

5.9: References

[1] H.L. Wang et al., *Plasma Sci. Technol.* **25**, 025105 (2023)
[2] W. Wei et al., *Plasma Sci. Technol.* **21**, 065101 (2019)
[3] W. Xu et al., *IEEE Trans. Plasma Science* **52**, 5159 (2024)
[4] P. Barabaschi et al., *Fusion Eng. Des.* **215**, 114990 (2025)
[5] V. Bobkov et al., *Plasma Phys. Control. Fusion* **59**, 014022 (2017)
[6] A. Cardinali et al., *Plasma Phys. Control. Fusion* **62**, 044001 (2020)
[7] D. Van Eester et al., *Nucl. Fusion* **59**, 106051 (2019)
[8] W. Zhang et al., *Nuclear Materials and Energy* **19**, 364 (2019)
[9] E. Lerche et al., *AIP Conf. Proc.* **2984**, 030005 (2023)
[10] Ye.O. Kazakov et al., *Phys. Plasmas* **22**, 082511 (2015)

[11] Ye.O. Kazakov et al., *Phys. Plasmas* **28**, 020501 (2021)
[12] S. Lenci et al., *2009 IEEE International Vacuum Electronics Conference*, **379** (2009)
[13] P. Bibet et al., *Nucl. Fusion* **35**, 1213 (1995)
[14] M.H. Li et al., *Fusion Eng. Design* **147**, 111250 (2019)
[15] J. Hillairet et al., *Nucl. Fusion* **50**, 125010 (2010)
[16] B. Chuilon et al., *Fusion Eng. Des.* **96-97** 433-437 (2015)
[17] A.J. Shepherd et al., *Fusion Eng. Des.* **146** 765-769 (2019)
[18] H.T. Qiu et al., *Fusion Eng. Design* **222**, 115506 (2026)
[19] H.T. Qiu et al., *Fusion Eng. Design* **215**, 114962 (2025)
[20] B. Cao et al., *Fusion Eng. Design* **178**, 113101 (2022)
[21] D.F. Kong et al., *Plasma Sci. Technol.* **25**, 065601 (2023)
[22] Y. Ye et al., *Nucl. Fusion* **65**, 084002 (2025)
[23] J. Zhang et al., *Plasma Sci. Technol.* **27**, 104001 (2025)
[24] M.S. Tan et al., *Fusion Eng. Design* **205**, 114559 (2024)
[25] H.D Zhuang and X.D. Zhang, *Rev. Sci. Instrum.* **86**, 053502 (2015)
[26] J.S. Yuan et al., *Fusion Eng. Des.* **191**, 113567 (2023)
[27] J.S. Yuan et al., *Fusion Eng. Des.* **205**, 114551 (2024)
[28] J.S. Yuan et al., *Nucl. Fusion* **63**, 106008 (2023)
[29] S.B. Zhao et al, *Nucl. Fusion* **65**, 016048 (2025)
[30] L. Li et al., *Nucl. Fusion* **65**, 086012 (2025)

Chapter 6: Divertor, Scrape-Off Layer and Plasma-Wall Interaction

Coordinators: R. Ding (ASIPP), O. Pan (IPP-Garching, Germany)

With contributions from:
ASIPP Team: G.Z. Jia, X.J. Liu, T.Y. Xia, G.L. Xu, J.L. Chen, B.F. Gao, C.J. Li, H. Wang
EUROfusion Team: M. Wischmeier (IPP-Garching, Germany), M. Faitsch (IPP-Garching, Germany), P. Mantica (CNR-Milan, Italy), S. Brezinsek (FZJ-Jülich, Germany)

6.1: Overview of plasma-facing components in BEST

As described in Chapter 1, BEST is designed to achieve a fusion gain $Q \geq 1$ in its early operational phase, followed by the development of long-pulse operation in the longer term. Power and particle exhaust, together with plasma-material interactions, constitute critical boundary conditions for plasma operation, directly influencing operational limits and overall device performance.

The plasma-facing material in BEST is tungsten, which is currently the preferred solution for nearly all planned tokamak devices, including ITER, SPARC, CFEDR, and EU-DEMO. Compared with carbon-wall devices, metal walls offer key advantages, in particular they drastically reduce tritium fuel retention and offer longer lifetime of plasma-facing components (PFCs). However, even small levels of tungsten in the plasma core can lead to significantly increased radiative losses, degrading plasma performance. Therefore, effective control of tungsten sputtering from both divertor and PFCs is essential. To ensure acceptable divertor lifetime and minimize tungsten sputtering, the divertor target power must be kept below ~10 MW/m^2, while the electron temperature at the target should remain below ~5 eV, conditions corresponding to a detached divertor configuration [1, 2].

BEST employs a V-shaped single-null divertor (see Fig. 6.1), optimized to exploit neutral baffling when the strike point is positioned near the corner of the divertor. This geometry enhances volumetric power dissipation through radiation and charge-exchange processes, thereby facilitating stable detachment access. The high-flux region of the divertor is constructed from tungsten monoblocks, while the far-SOL region is protected by flat tiles. Recently, the V-shaped divertor components have successfully passed 1000-cycle high-heat-flux (HHF) testing at 10 MW/m^2, confirming their mechanical integrity and thermal performance.

All PFCs in BEST are actively cooled and modularly maintainable, allowing for targeted inspection and replacement. The strike point position can be adjusted to explore different divertor regimes, and an alternative configuration with the strike point on the vertical target is also available. The vacuum pumping system is located below the divertor targets, connected through the private flux region to ensure efficient exhaust of neutrals and impurities.

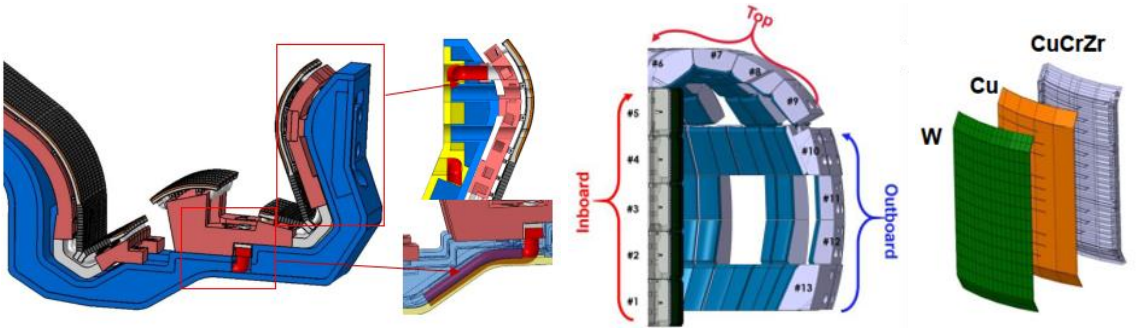

Figure 6.1: Divertor and first-wall modules in BEST. The divertor employs tungsten monoblock elements (designed for heat loads up to 15 MW/m^2) in the strike-point region, and flat-plate tungsten elements (rated for 2-7 MW/m^2) in the non-strike zones. The shielding blanket is divided into 13 poloidal blanket modules, each featuring a tungsten-coated surface.

The first wall consists mainly of copper tiles coated with tungsten, arranged in 240 modules. Each module incorporates a CuCrZr heat sink that is actively cooled with water. The heat sink structure includes multiple slits to mitigate thermal stresses and electromagnetic loads on the first wall, and the overall design is compatible with remote maintenance. The shielding blanket will be installed before the research activities.

Table 6.1 summarizes the expected divertor heat flux parameters for the $Q \geq 1$ operational phase in BEST. During this stage, the power loads on the divertor target remain moderate – lower than in ITER, EU-DEMO [3] and CFEDR [4] – and comparable to those in JET and JT-60SA. The core radiation fraction, as estimated in Chapter 4, ranges between 20% and 40%, depending on the scenario details, and is similar to the fraction expected in ITER. In the later phase of BEST, aiming to explore $Q \approx 5$ plasmas at full heating power, the divertor heat flux and exhaust conditions are expected to reach higher level, thereby enabling reactor-relevant power exhaust studies.

In addition, the combination of reactor-relevant pedestal collisionality and relatively high neutron production will provide a unique environment for advancing the understanding of SOL transport, divertor detachment physics and plasma-wall interactions (PWI). These capabilities position BEST as a bridge between present-day devices and future reactor-scale facilities. Overall, BEST provides an excellent testbed for assessing the performance of the single-null divertor configuration, which currently remains the leading design choice for future fusion devices, although other facilities such as DTT may also offer insights into more flexible divertor designs.

Table 6.1: Key parameters related to the edge heat flux in different tokamaks.

	BEST ($Q \geq 1$)	AUG	JET	JT-60SA	DTT	ITER	EU-DEMO 2018 [3]	CFEDR
R_0 (m)	3.6	1.65	2.96	2.96	2.19	6.2	9.0	7.8
I_p (MA)	7.0	1.2	3.2	5.5	5.5	15.0	17.75	15
B_0 (T)	6.15	2.5	3.45	2.25	5.85	5.3	5.86	6.3
P_{exh} (MW)	42	33	40	35	45	150	450	403
P_{sep} (MW)	32	24	32	25	32	100	170	267
P_{sep}/R_0 (MW/m)	8.9	14.5	10.8	8.4	15	16.1	18.9	34.2

6.2: Power exhaust

6.2.1: Steady-state heat flux

The steady-state heat flux to the divertor in BEST has been estimated using the Eich scaling [5], applied here as a conservative upper-bound estimate. This empirical scaling, originally derived for attached inter-ELM phases of type-I ELMs, provides a useful reference, even though type-I ELMs are not allowed during the BEST $Q \geq 1$ operational phase. While ELM-mitigated and detached regimes generally exhibit broader power fall-off lengths [6, 7], the Eich scaling remains a suitable worst-case boundary condition.

For the $Q \geq 1$ scenario, the relatively high plasma current (I_p = 6-7 MA) results in a very narrow Eich power fall-off length of approximately 1 mm, highlighting the stringent requirements on power exhaust and divertor performance in BEST. Accurate study and validation of the SOL power fall-off length under BEST-relevant boundary conditions are therefore essential for predictive modelling of heat loads in future high-current fusion devices.

A heat flux limit of 10 MW/m^2 has been set as the operational tolerance during the $Q \geq 1$ operation. In future operational phases with higher neutron production, this limit may need to be reduced to account for the impact of neutron-induced material degradation. To minimize tungsten sputtering, the electron temperature at the divertor targets must be maintained below 3-5 eV [1]. The total target heat load includes contributions from electron and ion sheath fluxes, surface recombination energy, plasma radiation, and neutral particle power. Because high particle fluxes can lead to significant recombination energy and enhanced impurity sputtering, reducing the particle flux at the divertor target is crucial [2]. This necessitates achieving a pressure-detached condition.

Argon, also selected for EU-DEMO [3], is planned as the primary seeding impurity for radiative power dissipation in BEST. Its radiative characteristics match the expected divertor temperature range, and its low first ionization energy ensures strong neutral compression. Neon is considered as a backup option – while it produces somewhat greater core dilution and lower compression, its proven performance in JET and relevance for ITER make it a viable alternative.

To quantify steady-state heat fluxes, SOLPS-ITER modelling was performed for the standard $Q \geq 1$ argon-seeded scenario, described in Chapters 2 and 4. The simulated plasma parameters include a separatrix density of 3.8×10^{19} m^{-3}, effective charge $Z_{eff} = 2$, and a power fall-off length of ~1 mm. The modelling predicts that the outer divertor heat flux remains below 2 MW/m^2 (see Fig. 6.2), primarily due to effective neutral compression leading to higher local electron densities and enhanced volumetric radiation. The maximum heat flux occurs at the inner target, reaching approximately 5 MW/m^2, attributed to the less baffled geometry and a shift in the SOL heat flux asymmetry, as the outer target is detached. Near the strike point, the neutral particle heat flux becomes comparable to the plasma heat flux, consistent with ITER simulations [8]. In the far-SOL region, radiative losses dominate the total heat flux. A divertor target heat flux below 5 MW/m2 was also achieved in the simulations with neon seeding (at $Z_{eff} = 2$), while this requires a higher midplane separatrix density of 4.2×10^{19} m^{-3}.

Overall, the steady-state heat flux in the reference $Q \geq 1$ scenario remains below the divertor PFC design limit when impurity seeding is applied. Scenarios with higher separatrix density or increased impurity seeding are expected to further reduce the divertor heat flux through enhanced radiation.

During the early operational phase, comparative studies of argon and neon seeding will be conducted to assess their relative radiative efficiencies and effects on edge plasma distribution. Modelling validation, including the role of magnetic drifts in influencing in-out divertor asymmetries, will be critical for understanding edge plasma behaviour in BEST. To identify acceptable boundary solutions supporting the $Q \geq 1$ scenario, systematic exploration of the boundary operation space, including scans of plasma density, impurity seeding rate, and strike point position, will be required.

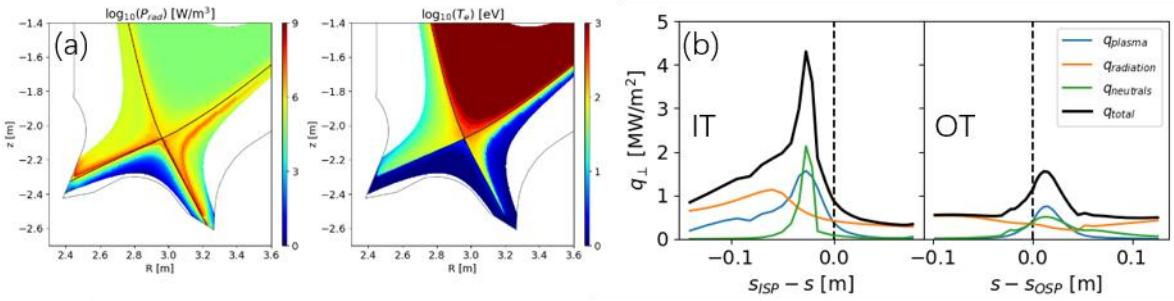

Figure 6.2: Results of SOLPS-ITER simulations for the reference $Q \geq 1$ argon-seeded scenario in BEST. (a) Two-dimensional distribution of radiation power density and electron temperature. (b) Heat fluxes at the inner and outer divertor targets, showing maximum values of ~5 MW/m^2 and <2 MW/m^2, respectively.

6.2.2: ELM mitigation

The ELM peak energy is estimated in Section 2.2. It is well established that large ELMs pose a significant risk to PFCs. ELM mitigation strategies are essential and will be tested in the early operation phase of BEST. As discussed in Sections 2.2 and 4.4, the current primary approach is to prioritize naturally type-I ELM-free scenario (quasi-continuous exhaust (QCE), grassy-ELM and highly radiative regimes). This approach will remain the focus until there is strong and consistent evidence supporting the effectiveness and reliability of active ELM mitigation under reactor-relevant conditions.

The basic strategy of the QCE regime is to raise the critical pressure gradient for large-scale MHD instabilities and concomitantly increase the level of transport at the plasma edge such that this critical gradient is not reached [9]. In the QCE regime, a broadening of the SOL power fall-off length has been observed in ASDEX Upgrade and TCV, and similar behavior has been reported in DIII-D and EAST. Recently, the QCE regime was successfully achieved in JET D-T campaign. The suppression of type-I ELMs and the emergence of the QCE regime are attributed to two key factors. First, strong plasma shaping – characterized by high elongation, triangularity, and proximity to a double-null configuration – is essential. Second, sufficient fuelling is required to raise the pedestal-foot density near the separatrix. This increased edge density is thought to trigger enhanced transport through localized ballooning modes, which may be either ideal or resistive in nature. The high plasma shaping and high separatrix density in the BEST $Q = 1$ scenario make it suited for achieving the QCE regime. The feasibility of QCE should be further assessed during preparatory operational phases.

Grassy-ELMs were first identified in DIII-D in high-β_p plasmas and later in JT-60U as a small high-frequency ELM regime occurring at low plasma collisionality and elevated poloidal beta. Since the 2016 campaign, the grassy-ELM regime has been systematically developed and studied in EAST [10]. The recent studies show that the pedestal of grassy ELM in DIII-D and EAST is close to the marginal stable region around the peeling boundary [11, 12]. The nonlinear mode coupling is thought to be an important mechanism to achieve grassy ELM regime. The appeal of the grassy-ELM regime lies in the fact that its operational conditions are, in principle, compatible with the requirements for steady-state tokamak operation.

Impurity radiation is used to reduce divertor heat loads, and radiative cooling in the plasma edge has also been shown to help mitigate ELMs. At JET, experiments with high levels of neon seeding demonstrated both ELM mitigation and improved core confinement [13]. In DIII-D, nitrogen seeding enabled the simultaneous achievement of high core confinement and a cold SOL [14]. An extreme example is the X-point radiator regime [15], where a stable, cold, and strongly radiative zone forms near the X-point, enabling both divertor detachment and ELM suppression. In BEST, a high impurity seeding scenario with an argon concentration of 0.4% is planned as a backup for the ELM mitigation regime.

6.3: First wall and far scrape-off layer

The first wall (FW) plays a crucial role in plasma-wall interaction, especially during ramp-up and ramp-down phases, and can significantly contribute to impurity contamination of the core due to its large area and relatively poor impurity-screening compared to the divertor. Plasma conditions near the wall, particularly in the far SOL, are poorly defined and require advanced diagnostics and modelling to understand incident particle and heat fluxes. In order to mitigate the divertor heat loads, divertor detached and ELM-mitigated regimes with high separatrix density, SOL broadening can increase FW heat and particle loads – impacting erosion and tungsten migration [16, 17]. The FW must also survive planned transients (numerous current ramps during pulsed operation) and unplanned off-normal events, such as disruptions, ELMs, and vertical displacement events (VDEs), each depositing intense localized energy. The BEST device's tungsten environment serves as a testbed relevant to ITER and CFEDR and EU-DEMO [3], but diagnostics must cover far SOL profiles, FW erosion/deposition, W migration, turbulence, and divertor and upstream profiles – to feed edge turbulence modelling extending to the FW.

6.3.1: Wall heat load

A combined analysis using SOLPS-ITER, PFCflux, and ISSDE estimates a maximum first wall heat load below 1.5 MW/m^2 in the $Q \geq 1$ scenario steady-state phase. This includes contributions from radial power transport, radiation, CX neutrals, and ripple-induced fast ion losses (see Fig. 6.3). Step misalignments between panels, as well as long-wave misalignments, can further increase the heat flux on the first wall. Careful qualification will therefore be required after installation of the wall panels. During BEST operation, the heat load distribution and wall temperature will be monitored with the IR thermography covering the critical regions of the PFCs. Diagnostic validation under BEST operation conditions with consideration of the first wall emission will be performed at the initial operation phase of BEST. Inspection of the 3D first wall heat load distribution as well as the heat load removal ability is needed. Tungsten erosion and migration on the FW will be examined using integrated SOL and PWI modelling.

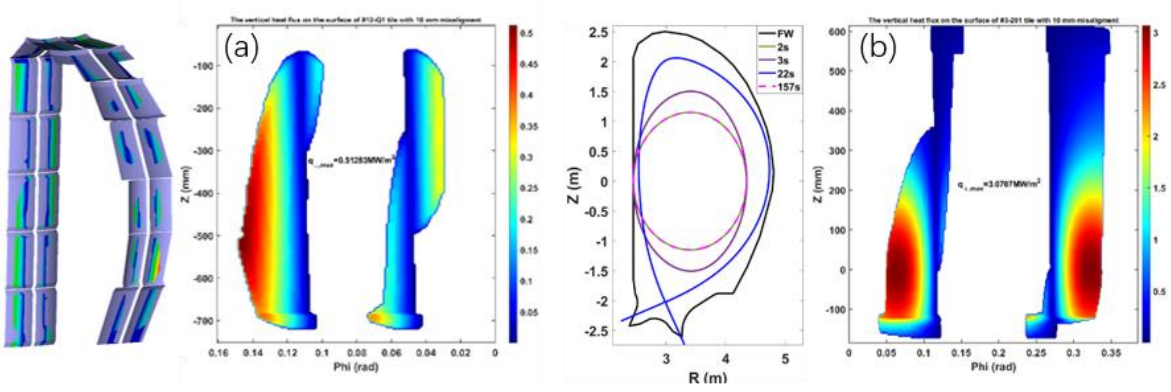

Figure 6.3: First wall heat load pattern in (a) steady-state and (b) ramp-up phases.

6.3.2: Transient events

Robust management of planned transients, such as ramp-up and ramp-down phases in pulsed operation, is essential to prevent excessive heat exposure to the FW. PFCFlux modelling predicts a peak surface heat load of about 3 MW/m^2 on the inboard panel during the start-up phase (see Fig. 6.3(b)). Instead of standard heat-flux panels, high-heat-flux panels will be installed on the inboard and outboard equatorial regions for plasma start-up in the limiter configuration, as well as at the top of the machine to handle the thermal power near the secondary separatrix during divertor operation. Beyond these planned scenarios, unplanned events like disruptions or large single ELMs can also cause substantial heat loads on divertor or FW tiles. VDEs may impact the upper or lower FW regions, while a loss of confinement could lead to contact with the FW. To address these risks, the real-time wall monitoring systems, particularly those using infrared-based thermal diagnostics, along with active feedback the mechanisms to the heating and control systems, are crucial for maintaining FW integrity and ensuring safe, stable reactor operation.

6.4: Edge-SOL integration

The design of PFCs must balance heat-load handling, component lifetime, and core plasma confinement and stability. In current experiments, plasma edge and boundary parameters (including the SOL and divertor) often impose conflicting requirements. For example, improved energy confinement typically requires low collisionality at the separatrix in present devices, implying low density and high temperature. These conditions, however, hinder divertor detachment, making it difficult to suppress the high heat flux and impurity sputtering at the divertor targets. BEST provides a good platform for studying edge-SOL-divertor coupling, as it can access pedestal collisionalities relevant to reactor conditions, not yet achieved in existing experimental devices. The main objective is to find an accessible solution for both the high dissipative divertor and the high pedestal plasma performance.

BEST's capabilities also support the development and validation of integrated models. Current theoretical models of edge-divertor coupling describe plasma behavior at only two or three points along magnetic field lines and lack detailed treatment of radial transport. Under high-density, detached divertor conditions, strong radial variations in transport and significant sources and sinks of particles and energy emerge, rendering traditional models insufficient. On the simulation front, existing core plasma simulation tools – based on gyrokinetic and MHD models – provide transport coefficients for particles and energy, but require artificial assumptions about key boundary conditions, such as neutral particle behavior, and cannot handle complex divertor magnetic geometries. Conversely, divertor fluid and Monte Carlo-based tools excel at modelling plasma-wall interactions and neutral physics under various divertor configurations but lack self-consistent coupling with edge plasma parameters, relying instead on assumed transport coefficients. To enable comprehensive edge-divertor coupling studies, it is essential to develop intermediate coupling codes and validate them in reactor-relevant environments of BEST.

6.5: Plasma-wall interaction

6.5.1: Wall conditioning

Experiences on AUG, WEST and EAST reveal that the high impurity level of full W devices can dramatically restrict the H-mode operation space. The high oxygen concentration in plasma can even impact the start-up phase. Boronization has been proved to be an effective method for minimizing the residual impurities, especially oxygen, and thus ensuring favourable plasma operation conditions [18, 19]. Different boronization techniques, assisting by GDC or ICWC will be tested in the early operation phase of BEST. The effectiveness and optimization of these methods must be rigorously evaluated, particularly regarding their impact on B layer formation, tungsten erosion, fuel retention, and dust production. Diborane will be used on BEST, so dedicated operation time should be allocated to evaluate the B layer covering efficiency on different locations by different GDC electrodes and boron injection points. The achievable B deposition rate with considering the pumping effect should be clarified. Three injection positions are arranged to improve the uniformity of the deposition. The thickness and the uniformity of B layer required for effective oxygen capture on BEST should be elucidated. To replenish the boron layer during operation, 1 or 2 boron dropper systems will be installed in BEST at different machine location. The boron dropper system is proposed to adopt two parallel injection methods: piezoelectric wafer resonance and spiral extrusion. The boron particles are planned to be injected from the upper port using boron powder (diameter of 150 μm) and pellets (diameter of 1-2 mm), with an injection rate of 20-100 mg/s.

Tritium co-deposition in the B layer is also an important issue that needs to be addressed. The in-situ laser-based diagnostics can play an important role on this issue. Wall conditioning is crucial in mitigating impurity influx and fuel retention within BEST. Dedicated plasma discharges should be developed to recover fuel from the deposits. Evaluation of the baking temperature effect on the fuel removal from the wall will also be carried out. The ultimate objective is to develop a robust and effective wall conditioning strategy which can be applied for BEST long pulse operations.

6.5.2: Tungsten erosion and transport

Managing tungsten erosion and transport is critical in BEST, especially since tungsten has been chosen as the primary plasma-facing material for next-generation fusion devices like EU-DEMO [3] and CFEDR. In preparation for long-pulse operation, minimizing both W erosion and deposition is important. In BEST, dedicated experiments will be carried out to quantify gross tungsten erosion from both the main chamber and divertor regions under ELM-free regimes and across a range of divertor detachment conditions.

During the $Q = 1$ phase, the low electron temperature at divertor targets combined with the suppression of large ELMs suggests that physical sputtering of tungsten in the divertor will be minimal. Instead, sputtering caused by high-energy charge-exchange neutrals is expected to be the dominant contribution to tungsten erosion. A high SOL density, as in QCE regimes, can enhance radial transport and thereby increase the particle flux to the main chamber wall. However, simulations [20] indicate that wall erosion decreases with increasing perpendicular transport in the far SOL, due to shallower penetration of recycling neutrals and the reduced energy of CX neutrals. These effects should be directly tested in BEST under reactor-relevant plasma edge conditions.

In BEST, it is also essential to evaluate tungsten screening efficiency across a broad range of plasma conditions. Core W accumulation should be investigated in conjunction with W sources and edge/core transport. This integrated approach is essential for developing scenarios that minimize the impact of W on plasma performance. A pronounced pedestal and internal transport barriers are important for improving confinement; however, the reduction of anomalous impurity transport relative to neoclassical transport can promote W accumulation. Therefore, achieving an optimal balance between W control and confinement improvement requires careful consideration. In this context, the role and effectiveness of external control tools, such as central heating by ECRH, should be systematically assessed. A comprehensive understanding of tungsten behavior requires investigation of both global and localized erosion and deposition patterns, using diagnostics such as visible spectroscopy and material probes, supported by advanced 3D material migration modelling. Additionally, studying the morphological changes tungsten undergoes under long-term reactor-relevant plasma exposure, such as blistering, fuzz formation, and recrystallization, is crucial for improving the performance and lifetime of tungsten components.

6.5.3: Real-time wall monitoring

Real-time wall monitoring is essential for ensuring reactor safety and maintaining the integrity of critical components, particularly in detecting events such as filament burn-through or localized overheating. Advanced diagnostics, e.g. infrared (IR) camera systems, are vital for identifying sudden thermal excursions, changes in emissivity, and surface anomalies that signal potential damage or erosion. In tungsten-based environments in BEST, the reflective nature and variable emissivity of tungsten, influenced by local erosion and redeposition, present significant challenges to accurate IR data interpretation. To address this, it is crucial to develop and validate robust methodologies for interpreting IR signals early in the operational phase. Dedicated operation time should be allocated to establish reliable machine protection algorithms and emissivity monitoring procedures. These efforts will enable prompt detection and mitigation of thermal anomalies, protect actively cooled components from overheating or coolant leaks, and help prevent unplanned downtime.

6.5.4: RF interaction

Radiofrequency heating and current drive systems can influence plasma-wall interactions due to their potential to cause localized changes in wall loads and material migration patterns [21]. The discrete nature and positioning of RF antennae and limiters introduce complex three-dimensional effects, including shadowing and localized deposition. Detailed investigations into the influence of RF-induced sheath potentials and enhanced sputtering, combined with comprehensive 3D modelling, are crucial to quantify and mitigate adverse effects on PFC materials. This requires in-situ monitoring of impurity source. Understanding these interactions will enable optimized RF system design and operational strategies to minimize wall erosion and impurity contamination, contributing positively to overall plasma performance.

6.6: Preparation for long-pulse operation

Long-pulse operation has a significant impact on plasma-wall interactions, particularly in terms of erosion rates, material migration, and deposition patterns. Extended operation requires accurate measurements of material erosion and deposition across reactor surfaces, with special attention to high-heat-flux regions like the outer divertor target. Regular sampling and analysis of dust and co-deposited layers – enabled by the material probes and remote handling systems – are essential for estimating particle inventory and maintaining operational safety. Continuous monitoring of these parameters during long-pulse campaigns will support predictive assessments of PFC lifetimes and guide maintenance planning. The $Q = 1$ phase provides an excellent testbed for addressing these questions in a reactor-relevant environment and for preparing future long-pulse operation.

6.6.1: Detachment and impurity control

Maintaining detached divertor conditions is fundamental to controlling impurity influx and reducing PFC erosion in long-pulse operations. The performance in $Q = 1$ operations will be used to characterize impurity behavior (including radiation distribution, recycling and pumping), PFCs erosion, and plasma profiles under various detachment scenarios, emphasizing impurity seeding strategies for achieving optimized detachment conditions. Understanding and controlling impurity transport within these regimes will be critical for preserving plasma purity, maintaining energy confinement, and extending PFC lifetime in long-pulse operation. Robust feedback detachment control techniques by using the radiation power or spectroscopy should be developed on BEST to support the high heating power long pulse operations.

6.6.2: Helium pumping

Effective helium pumping is crucial for long-pulse DT operations, as helium accumulation significantly impacts plasma performance. BEST will be a platform to investigate He exhaust efficiency in detached divertor conditions, aiming to evaluate effective He confinement time and compression ratios. Elastic collisions between

deuterium ions and He, identified as critical for helium exhaust enhancement, will be investigated. The He pumping efficiency by pumps at different locations will be tested during BEST long pulse discharges. The outcomes will refine divertor design criteria for CFEDR and EU-DEMO [3], requiring further development of He transport simulation tools, particularly regarding metastable He states and atomic absorption effects.

6.6.3: Fuel retention

Minimizing fuel retention is essential in future reactors to ensure safety, reduce in-vessel tritium inventories, and enhance tritium breeding efficiency. Tungsten, chosen for its low hydrogen solubility, nonetheless experiences localized hydrogen supersaturation, leading to surface morphology changes and trapping at defects. Studies reveal that helium presence in hydrogen plasmas reduces retention through nanoscopic helium bubble formation, providing pathways for hydrogen release. Advanced studies must assess fuel retention in reactor-relevant conditions on BEST, considering plasma composition, impurity seeding, and the impact of boronization conditioning. Experiments should also evaluate fuel recovery efficiencies using ITER-relevant cleaning techniques like baking, glow discharge conditioning (GDC), and ion cyclotron wall conditioning (ICWC) [22-23], complemented by in-situ diagnostics [24-25]. Fuel retention and removal results from the deuterium phase will be essential for D-T readiness. Tritium retention associated with neutron exposure, along with its measurement, contamination, and removal, is discussed in Sections 7.1.1 and 12.2.1. Characteristic of the fuel retention at different FW locations during the long pulse discharges will be clarified in the early operation phase of BEST to provide important information for PFCs and tritium breeding design for future reactors.

6.6.4: Ramp-up and ramp-down phases

Optimizing plasma ramp-up and ramp-down phases is essential to long-pulse operational stability. Key objectives include minimizing flux consumption during ramp-up to extend the flat-top phase, avoiding MHD instabilities linked to tungsten influx, and controlling plasma parameters to avoid operational limits. Techniques like rapid transition from limiter phases to divertor configurations and early ECRH applications, which have proven effective in minimizing tungsten influx and wall erosion during these phases, will be tested on BEST. Additionally, assessing the impact of wall conditioning techniques, such as boronization, on tungsten migration and first wall heat loads will enhance scenario robustness and reactor safety.

6.7: References

[1] R. Wenninger et al., *Nucl. Fusion* **57**, 016011 (2016)
[2] M. Wischmeier et al., *J. Nucl. Mater.* **463**, 22 (2015)
[3] M. Siccinio et al., *Fusion Eng. Des.* **176**, 113047 (2022)
[4] R. Ding et al., *Plasma Sci. Technol.* **27**, 104002 (2025)
[5]T. Eich et al., *Phys. Rev. Lett.* **107**, 215001 (2011)
[6] M. Faitsch et al., *Nucl. Fusion* **63**, 076013 (2023)
[7] H.J. Sun et al., *Nucl. Fusion* **65**, 076012 (2025)
[8] R.A. Pitts et al., *Nucl. Mater. Energy* **20**, 100696 (2019)
[9] M. Faitsch et al., *Nucl. Fusion* **65**, 024003 (2025)
[10] G.S. Xu et al., *Phys. Rev. Lett.* **122**, 255001 (2019)
[11] R. Nazikian et al., *Nucl. Fusion* **58**, 106010 (2018)
[12] N.M. Li et al., *Nucl. Fusion* **62**, 096030 (2022)
[13] C. Giroud et al., *Nucl. Fusion* **64**, 106062 (2024)
[14] L. Wang et al., *Nat. Comm.* **12**, 1365 (2021)
[15] M. Bernert et al., *Nucl. Mater. Energy* **43**, 101916 (2025)
[16] S. Brezinsek et al., *Nucl. Fusion* **59**, 096035 (2019)
[17] H.A. Kumpulainen et al., *Plasma Phys. Control. Fusion* **66**, 055007 (2024)
[18] V. Rohde et al., *Nucl. Mater. Energy* **43**, 101923 (2025)
[19] J. Winter et al., *J. Nucl. Mater.* **162**, 713 (1989)
[20] M.Z. Tokar, *Nucl. Fusion* **58**, 096007 (2018)
[21] L. Colas, *Nucl. Fusion* **62**, 016014 (2022)
[22] D. Matveev et al., *Nucl. Fusion* **63**, 112014 (2023)
[23] A. Widdowson et al., *Nucl. Fusion* **65**, 116036 (2025)
[24] M. Zlobinski et al., *Nucl. Fusion* **64**, 086031 (2024)
[25] J. Likonen et al., *Nucl. Mater. Energy* **45**, 102021 (2025)

Chapter 7: Validation of Fusion Technology Systems

Coordinators: X.B. Peng (ASIPP), R. Kamendje (EUROfusion), R. Villari (ENEA, Italy)

With contributions from:
ASIPP Team: Y. Cheng, S.L. Zheng, H. Jin, X.Y. Qian, W. Wen, G. Shen, F. Liu, Z.Z. Song, Z.Z. Zhu, Q.X. Yang
EUROfusion Team: C. Bachmann, V. Corato (ENEA, Italy), P. Bruzzone (EPFL, Switzerland), G. De Marzi (ENEA, Italy)

7.1: Design validation and demonstration of PFC technologies in nuclear environment

7.1.1: Tritium retention due to neutron impact

The measurement and removal of tritium retained in the in-vessel components is addressed in Section 11.2.1 from the viewpoint of the tritium inventory as a safety concern. However, there are still large uncertainties related to how neutron irradiation damage may impact tritium retention in plasma-facing components. In this regard, BEST operation will provide an opportunity to relate the quantification of tritium retention in the plasma-facing components with the neutron measurement and accumulation. Such measurements necessitate the implementation of relevant diagnostics for both tritium and neutrons. This may require developing new measurement methods and techniques. However, it should be noted that neutron irradiation damage in BEST is foreseen to be relatively low.

7.1.2: Joining technology

Two different welding methods, Hot Isostatic Pressing (HIP) and brazing [1, 2], will be applied for joining a tungsten armour block with a CuCrZr heat sink. Both materials are readily available and reliable as established by data from existing non-destructive tests and high heat flux tests. However, the performance and reliability of in-service tungsten monoblocks welded on CuCrZr using these two different methods still need to be established. BEST provides a suitable environment to investigate this crucial point using diagnostic data during operation.

Arranging tungsten monoblocks with different joining techniques in two adjacent plasma-facing units (one with HIP, another with brazing) of one divertor module, real-time monitoring of the surface temperature during operation could be carried out by infrared cameras or other suitable diagnostics equipment during the discharge. By comparing the accumulated diagnostic data over a long period of time, the relative performance and reliability of the two joining techniques could be determined.

7.1.3: Shape impact on passive protection of plasma-facing components

Shaping is applied in the design of PFC, in order to avoid damage caused by leading edges [3]. It is, hence, necessary to monitor whether this shaping can play a role during the BEST operation. PFC surface temperature as monitored by infrared cameras at

relevant locations with shaped PFCs will be applied to provide effective data on whether the shaping can mitigate "hot spots" during a discharge. Furthermore, the in-vessel viewing system configured for BEST can provide morphology and contour profiles of the surface of tungsten monoblocks or tiles with shaping after the BEST shutdown. Comprehensive comparison of diagnostic data will provide a feasible method to study the impact of shaping of PFC with results further usable as basis for guiding the design of PFC shapes.

7.2: Remote maintenance of in-vessel components

7.2.1: In-bore cutting and welding technology for first wall

To improve maintenance efficiency for BEST in-vessel components such as damaged first wall (FW) components (blanket first wall and divertor target) a front-side maintenance strategy will be adopted, where only the damaged FWs are repaired without disturbing intact components [4]. The maintenance process involves key steps such as first wall handling, pipe cutting/welding, and fastener removal.

However, due to limited space for external access for pipe maintenance, conventional external cutting/welding tools used in industry are not feasible [5]. Instead, in-bore cutting and welding must be performed within the small-diameter pipes (ø51×3 mm, 316L stainless steel), significantly increasing the technical challenges in tool development and process implementation.

Therefore, the initial research work here aims to develop in-bore automated cutting and welding tools for BEST first wall, addressing the following key technologies:

- Debris-free mechanical pipe cutter;
- Active vision-based weld seam alignment;
- Real-time welding quality monitoring.

Performance requirements are as follows:

- Cutting: consistency of pipe end surface (after cutting) >99%;
- Welding: success rate ≥ 99.9%, weld quality meets ISO-5817 B;
- Leakage rate: negative-pressure helium leak test ≤ 1×10^{-10} Pa·m^3/s; 20-bar positive-pressure helium leak test ≤ 5×10^{-10} Pa·m^3/s.

The overall effort will be comprised of 3 phases:

Phase 1 – Design and prototyping

- Development and testing of prototypes of in-bore cutting and welding tools on a small test bench;
- Optimization of tools based on prototype performance and implementation of extensive tests on first wall mock-ups to ensure both pipe end consistency and welding success rate are better than 90%.

Phase 2 – Non-nuclear testing

- Integration of cutting/welding tools with in-vessel maintenance manipulator for full-process validation on a cold test platform;
- Improvement of pipe end consistency and welding success rate to 99.9%;
- Upgrading of electronic components for radiation resistance;

- Performing maintenance trials on BEST under non-irradiated conditions and estimation of the reliability and availability of tools.

Phase 3 – Final maintenance validation

This will consist in the demonstration of the maintenance of FW components under irradiation conditions in BEST to establish the RAMI performance based on the usage of a high-precision in-bore cutting/welding system for FW pipelines as radiation-hardened tools capable of operating in harsh fusion environments.

7.2.2: Technology for self-recovery and rescue for first wall maintenance equipment

Maintaining the first wall components (e.g., blanket first wall and divertor target plates) in fusion reactors is a critical but challenging task due to the harsh irradiation environment, confined spaces, and complex operational requirements. To ensure high reliability and continuous operability, the maintenance equipment must incorporate self-recovery mechanisms and rescue capabilities in case of failures.

This research focuses on developing redundant hardware/software architectures and rescue strategies to minimize downtime and ensure successful maintenance operations, even under partial failure conditions. The primary goals of this study are:

- Self-Recovery Mechanisms
  - Hardware Redundancy:
    - Motor redundancy (backup actuators to replace failed ones).
    - Circuit redundancy (dual-redundant control boards for failover).
  - Software Redundancy:
    - Multiple control modes (normal, degraded, emergency).
    - Adaptive algorithms for fault detection and recovery.
  - Performance Targets:
    - System reliability ≥ 99% under normal operation.
    - Failover completion within ≤ 20 minutes after fault detection.
- Rescue Strategies & Equipment
  - Integration of rescue interfaces for external intervention.
  - Failure mode analysis (FMA) to identify critical risks
  - Development of specialized rescue tools for different failure scenarios
  - Performance Targets:
    - Rescue operation completion within ≤ 48 hours for critical failures
    - Successful recovery rate ≥ 95% for predefined failure modes

The effort will involve the following phases:

Phase 1 – Redundant design & self-recovery mechanisms

- Hardware Redundancy:
  - Design of multi-motor actuation systems with automatic failover
  - Implementation of redundant control circuits with hot-swappable backup boards

- Software Redundancy:
  - Development of multi-mode control algorithms (normal, backup, emergency)
  - Integration of real-time fault detection and auto-switching logic

Phase 2 – Failure mode analysis & rescue preparedness

- Conduction of Failure Modes and Effects Analysis (FMEA) to identify:
  - The most probable failure scenarios (e.g., motor jamming, sensor loss, power failure)
  - Critical rescue requirements
- Design of standardized rescue interfaces (mechanical/electrical) for external intervention
- Development of dedicated rescue tools (e.g., mechanical override devices, emergency release mechanisms)

Phase 3 – Integration & testing

- Validation of redundancy systems in simulated failure conditions
- Test of rescue procedures in a mock-up environment
- Refinement of algorithms and hardware based on test results
- Testing of rescue procedures in BEST

7.2.3: Development of precision control technology for the maintenance of the first wall

The first wall of the vacuum vessel's internal components, serving as the critical component directly exposed to high-temperature plasma, endures extreme thermal loads, neutron irradiation, and particle erosion, making it prone to material damage (e.g., blistering, cracking, spalling). As the primary means for maintaining the first wall of in-vessel components, remote handling technology has garnered widespread attention in research. However, traditional remote maintenance methods suffer the following limitations:

- Insufficient accuracy: Millimeter-level positioning errors lead to the risk of collision between maintenance tools and the surface of the first wall.
- Remote operation delay: In a strong radiation environment, remote control is required, and signal delay affects real-time operation.
- Spatial constraints: The vacuum vessel has a small space and complex component layout (including the blanket, divertor, etc.).
- Lack of adaptability to the nuclear environment: The reliability of existing robot systems is insufficient under strong magnetic fields and irradiation.

Therefore, developing an intelligent maintenance control system with high precision, strong robustness, and radiation resistance constitutes a core technical challenge in ensuring high availability of BEST.

The objective of the research work is the verification of the millimeter-level precision maintenance capability of the robot system for the FW of BEST's in-vessel components in a nuclear environment, providing a technical prototype for the future CFETR/DEMO maintenance system. The maintenance performance indexes for the FW of BEST's in-vessel components are listed in Table 7.1.

Table 7.1: The maintenance performance indexes for the FW of in-vessel components.

Item	Parameters	Environment
Position accuracy of manipulator	≤ ±1mm	Non-nuclear phase, nuclear phase
Position accuracy of first wall assembly	≤ ±1mm	Non-nuclear phase, nuclear phase

Implementation plan

1. Design and pre-study stage

a) Bilateral Stability Interaction Technology for Remote Maintenance Manipulator of the First Wall
   - To address issues such as model parameter uncertainty and external environmental disturbances in bilateral tele-operation tasks, this study analyzes the nonlinear characteristics of uncertain terms in complex maintenance operation systems. It investigates parameter identification methods for system states and uncertainties in tele-operation control, while incorporating adaptive approaches to design real-time update strategies for time-varying parameter weights. This forms an artificial intelligence-based bilateral stability control method for tele-operation, ensuring the stability of bilateral maintenance operation systems.
   - Regarding the heterogeneity between the master and slave ends, the study explores mapping methods between different degrees of freedom at the master and slave ends of tele-operation, achieving effective command conversion and stable interaction between the master and slave sides.

b) Multi-sensor fusion-based shared control technology (vision + force sensing)
   - To tackle challenges such as prolonged task completion times and low positioning accuracy in tele-operation maintenance manipulator systems handling complex tasks, this research combines digital twin models in Cartesian space to study robot autonomous path planning technology and human-robot shared control strategies.
   - By leveraging multi-sensor fusion technology, it addresses issues of virtual-real fusion and global positioning for manipulators, improving motion guidance efficiency in tele-operation.
   - To overcome insufficient end-effector positioning accuracy in maintenance manipulators, the study investigates high-precision robot positioning algorithms based on visual and force feedback, thereby enhancing motion efficiency and positioning accuracy in tele-operation manipulators.

Deliverables: High-precision positioning algorithm for manipulators based on visual and force feedback, simulation report on control algorithms, design instructions, source code.

2. Non-nuclear phase testing

- Manipulator positioning accuracy test: Laser tracker measures the repeat positioning accuracy of the end of the manipulator.
- First wall installation accuracy test: Laser tracker verifies the precision of first wall grasping or placement operations.

Deliverables: BEST internal maintenance test videos, maintenance manipulator operation data, first wall grasping or placement accuracy measurement reports, etc.

3. Nuclear phase

- Divertor first wall maintenance: Precision control of manipulators to achieve maintenance of the divertor first wall.
- Blanket first wall maintenance: Precision control of manipulators to achieve maintenance of the breeding blanket/TBM first wall.

Deliverables: Complete precise grasping and placement operations for the blanket and divertor first wall in nuclear environment.

7.2.4: First wall leakage detection techniques

Vacuum leakage in fusion devices during operation is seriously hazardous, causing ingress of impurity gases into the vacuum chamber, thereby affecting plasma performance, and even causing plasma disruption, leading to damage on in-vessel components. At present, vacuum leakage detection and localization in fusion devices mainly rely on mass spectrometer leak detectors and helium gas blowing method, supplemented by manual inspection. However, given the huge volume and complex structure of the tokamak vacuum chamber, manual operation is not only time-consuming and laborious, but also inefficient. In view of the DT operating conditions of future fusion reactors in ultra-high vacuum environment, routine performance of manual leakage detection would not only lead to unacceptable long downtimes and pollution of the surrounding environment by leaking gases but also bring about huge economic losses. For the sake of realizing remote sensing and fast localization of vacuum leakage in the ultra-high vacuum environment of the fusion reactor, and reducing associated safety problems, the development of corresponding remote sensing and fast localization technology is particularly urgent.

This research endeavor aims at breaking through the key technological bottleneck of remote sensing and rapid localization of vacuum leakage in the ultra-high vacuum environment of fusion reactors by relying on the EAST tokamak device and the remote operation and maintenance experimental platform of CRAFT to build a set of active laser spectroscopy vacuum leakage detection systems with the capabilities of online diagnosis, spatial localization, remote operation control for application in BEST. Specifically, the following functions and technical indexes are proposed to be verified:

- Validation of high sensitivity active laser spectroscopy for leakage gas detection: Development of active laser spectroscopy for ultra-high vacuum (10^{-5}~10^{-7} Pa) environments, utilizing laser ablation and double-pulse laser enhancement mechanisms to improve signal response. The technique can be utilized for species identification and concentration monitoring of typical leakage gases such as air, helium, and water gas.
  Validation objectives: identification of leaking gas elements; laser excitation enhanced signal ratio ≥ 3 times; detection sensitivity better than 1×10^{-5} Pa·m^3/s.
- Functional validation of miniaturized spectroscopic leakage detection actuator for fusion reactor conditions: develop a laser spectroscopic vacuum leakage detection actuator and realize remote operation through an optical fiber-flexible coupling system. Flexible coupling system realizes remote operation and completes the spectral acquisition task under complex space structure.
  Validation objectives: the weight of the actuator is < 3 kg, the maximum external dimension is < Φ150 mm×300 mm; the fiber optic system effectively transmits the laser energy ≥ 100 mJ/pulse; it can realize the spatial multi-point scanning measurement and signal transmission.
- Validation of high degree of freedom multi-joint teleoperated robotic arm in vacuum leakage detection task: develop a set of multi-degree-of-freedom high-precision teleoperated robotic arm systems to realize autonomous scanning and precise control of various regions of the vacuum chamber (e.g., the divertor, the first wall, the upper window, etc.).
  Validation objectives: effective arm length ≥ 3.5 m, covering ±45° area of BEST vacuum chamber; movement speed ≥ 0.1 m/s; control and positioning error ≤ ±3 mm; degrees of freedom ≥ 13 DOF, minimum turning radius ≤ 800 mm; support for the end force feedback and path automatic planning function.
- Leaking gas spatial distribution scanning and rapid localization capability verification: the use of remote manipulation system and spectral actuator operation, to carry out multi-point spatial scanning and precise control of the interior vacuum chamber. Study the migration and diffusion characteristics of the leakage gas under different operating conditions and realize rapid inversion identification of the leakage source location with the help of concentration gradient.
  Validation objectives: spatial concentration distribution construction resolution < 15 cm; support identification and distribution reconstruction of multiple leakage gas types (He, H_2O, N_2, etc.); localization time can be controlled to complete leakage identification of the vacuum chamber area in a few minutes; can be used for leakage monitoring and early warning under deuterium/tritium operating conditions in the future.
- System-level validation and verification of platform adaptability: system-level integration testing on BEST platforms. Validate the availability, stability and anti-interference capability of the whole system under high vacuum, high heat and high radiation background.

Validation target: continuous operation of the system in a medium-sized vacuum chamber for ≥ 12 h; ≥ 99% success rate of integration and communication with the control system of the remote operation platform; and process compatibility to meet the actual maintenance and deployment conditions of future fusion reactors.

Implementation plan

1. Design and pre-research phase

Key tasks include: (i) Demonstration of technical solutions and construction of experimental conditions: Define the basic principles and feasibility of active laser spectroscopy for leakage gas diagnosis, design the experimental solution and set up an ultra-high-fidelity cavity suitable for fusion reactor leakage simulation. (ii) Preparation of key equipment and components: completion of the procurement of core devices such as required lasers, spectrometers, optical materials, etc., and preliminary design of vacuum leakage detection actuator and remote operation robotic arm. (iii) Research on the spectral characteristics of leaking gases: systematically study the spectral response characteristics of typical gases such as air, helium and water in different leaking states, and establish a basic database. (iv) Exploration of double-pulse laser diagnostic technology: carry out laser parameter optimization experiments and analyze the influence of laser energy, double-pulse interval and other factors on gas identification accuracy.

2. Non-nuclear phase – physical test phase

Key tasks include: (i) Development of leakage detection actuator and remotely operated robotic arm: Completion of prototyping of a spectral leakage detection actuator with operability as well as remotely operated robotic arm to satisfy the requirements of flexible deployment and vacuum operation. (ii) System testing and performance evaluation: simulate different leakage scenarios in an ultra-high vacuum chamber, and comprehensively test the response time, detection sensitivity, leakage rate calibration accuracy and other key indicators of the system. (iii) Hardware and software tuning and positioning capability development: Integrate spectral detection, robotic arm control and leakage identification algorithms to realize an integrated and intelligent leakage detection process and test the stability and automation degree of the system.

3. Final maintenance and system validation phase

Key tasks include: (i) BEST Device Deployment and Engineering Validation: Conduct field validation tests on BEST and other platforms to assess the stability and adaptability of the system under complex working conditions. (ii) System improvement and standardization output: complete the optimization and upgrading of the whole system hardware and software and the preparation of specifications for use, forming a complete operation manual and technical data.

7.2.5: First wall viewing techniques

First walls of in-vessel components are prone to surface erosion, structural morphology changes, thermal cracks, mechanical fatigue and other forms of failures in the operation process. In order to ensure the continuity and repeatability of high-performance plasma discharges, it is necessary to carry out rapid and accurate defect observation and localization inside the vacuum chamber after each discharge, to timely assess whether it meets the conditions of the next experiment or operation. This sets extremely high requirements for intelligent maintenance systems of vacuum equipment.

This activity focuses on the development of an intelligent inspection serpentine robot system for high-precision observation tasks in the confined space of a fusion reactor. The system adopts a multi-joint rope-driven structure design with high flexibility, precision control and environment sensing capabilities [6], and is capable of quickly reaching into the vacuum chamber in-between discharge operations, realizing precise identification and three-dimensional imaging observation of damage, material accumulation and deposition on key components, and then assisting in judging whether the vacuum environment and components meet the conditions for the next round of discharge experiments.

The project aims to develop a set of multi-joint rope-driven endoscopic robot (REM) system with high flexibility, high-precision observation and adaptive operation capability for the maintenance needs of BEST and future compact fusion devices. The main objectives are as follows:

- Verification of the reliability of the highly flexible structure and decoupled drive design: Through the cable decoupled drive structure, realize a single motor to drive two degrees of freedom (pitch/yaw) joint units, complete the integration test of 8~11 joint modules, and verify the motion performance and structural stability under the environment of confined space, high vacuum, and high temperature (80℃-120℃). Target parameters: overall arm length > 3500 mm; multi-joint arm diameter < 150 mm; maximum turning angle of a single section < 25°; bore diameter > 60 mm.
- Verification of rigid-flexible coupling compensation and high-precision positioning in full workspace: Construct a rigid-flexible coupling deformation model of the REM, introduce the Levenberg-Marquardt algorithm and gridded error modelling, and realize variable parameter real-time compensation and closed-loop position control under different loads. The real-time compensation of parameters and closed-loop adjustment of position control are realized under different loads, and the spatial positioning error of REM end-effector is finally controlled within millimeter level. Target parameters: spatial positioning error < 3 mm; maximum end load ≥ 3 kg; error identification and compensation within the whole working space can be realized.
- Verification of the reliability of the highly flexible structure and decoupled drive design: Through the cable decoupled drive structure, realize a single motor to drive two degrees of freedom (pitch/yaw) joint units, complete the integration test of

8-11 joint modules, and verify the motion performance and structural stability under the environment of confined space and high vacuum. Target parameters: overall arm length > 3500 mm; multi-jointed arm diameter < 150 mm; maximum turning angle of a single section < 25°; bore diameter > 60 mm.

- Verification of end observation and imaging capability: Integration of three-dimensional observation modules based on photometric stereo vision technology, realizing non-contact imaging detection and depth reconstruction of microscopic defects on target plates, cladding surfaces and other components. The system has sub-millimeter surface measurement accuracy and highly robust image recognition capability, which meets the demand for high-precision image acquisition in the maintenance process of nuclear fusion devices. Target parameters: camera observation accuracy < ±1 mm; maximum observation distance < 4500 mm; coverage angle range ±90°.
- Verification of system deployment adaptability and integration performance: The whole system needs to complete the stretching operation through the vacuum channel and realize the cavity operation in the 160 mm × 160 mm window. The system's deployment adaptability, cavity feasibility, and stability were verified within the constraints of the actual channel and window dimensions.

Implementation Plan

1. Design and pre-research phase

Key tasks include: (i) System structure and drive decoupling design: design and develop the REM (Cable-Driven Endoscopic Manipulator) system for the vacuum environment of fusion reactor, adopt the cable traction method to drive the multi-joint structure, and complete the construction of the joint decoupling mechanism with high flexibility and high reliability. (ii) Optimization of vacuum adaptability and arrangement scheme: complete the structural adaptability assessment of the REM system, including the constraint design of the window entrance size, vacuum channel alignment, cooling method, and high-temperature vacuum resistance. (iii) Hardware and software foundation preparation: realize the procurement and integration test of motor ball screw module, decoupling joints, controller and sensors, and set up the structure test platform and simulation model, to lay the foundation for the subsequent force sensing, obstacle avoidance control and other technologies.

2. Physical test in non-nuclear phase

Key tasks include: (i) Obstacle avoidance and path planning algorithm research and development: carry out research on REM trajectory generation method based on tracer geometric planning model, put forward two-way iterative obstacle avoidance algorithm applicable to narrow space, and realize autonomous obstacle avoidance and accurate grasping ability of robotic arm. (ii) Development of end observation tool based on photometric stereo vision: Develop a high-precision three-dimensional observation module based on photometric stereo vision technology integrated in the end of REM.

(iii) Intelligent control system and integration of hardware and software: establish a three-level maturity REM monitoring framework of "virtual and real integration", develop an intelligent control platform with state identification, path prediction and task planning functions, and realize the interaction and synchronization of REM in simulation and physical environment.

3. Final maintenance and system validation phase

Key tasks include: (i) Deploying the completed REM system for precision observation and path operation verification under high vacuum environment to test the performance and reliability of the system in actual maintenance tasks in the BEST device. (ii) Construction of operation and maintenance system and software platform to realize remote control, path planning and status feedback of the robotic arm, and support health management and maintenance of the REM system under long-term operation.

7.2.6: Port plug maintenance and radioactive containment control technology

The BEST Port Plug Maintenance System (PPMS) is a core subsystem of the BEST remote handling system, with its performance directly determining maintenance cycles, costs, and operational feasibility [7]. Due to radiation risks after deuterium-tritium reactions, the system must perform all maintenance tasks entirely through remote operations. It can remove large port plugs from the vacuum vessel (with a maximum load capacity of 15 tons for the upper port plug and 20 tons for the equatorial port plug) and safely transfer them to the hot cell for repair, replacement, or disposal. The system consists of multiple functional modules, including upper/equatorial transfer cask system, docking stations, docking channels, plug maintenance manipulators, and transport mechanisms. These modules work in coordination to establish a sealed connection between the transfer cask and the vacuum vessel, enabling the disassembly and installation of vacuum seals and fasteners, as well as the transfer of port plugs. Additionally, the window plug maintenance system is responsible for returning the refurbished port plugs along the same path and precisely reinstalling them into the vacuum vessel ports, ensuring the safety and reliability of the entire maintenance process.

Based on the maintenance requirements of the BEST port plugs and the sealing containment requirements for radioactive-contaminated components, this study aims to establish a scientifically sound maintenance process, conduct structural design and analysis of maintenance equipment, and ultimately develop a safe and reliable port plug maintenance system. The main research objectives include:

1) Design and Verification of Port Plug Lifting Mechanism

To meet the technical requirement of suspending the plasma-facing end during port plug installation, a dedicated lifting mechanism must be designed to achieve the following functions: lifting the plasma-facing end of the port plug while ensuring tight contact between the plug flange and the vacuum vessel port flange, thereby facilitating

subsequent connection and fastening (bolted or pin-type, with the latter requiring further verification). Two lifting mechanisms are under consideration: a hydraulic jack mechanism (for which a prototype has already been developed and tested) and a balanced lever mechanism (this project will focus on its design and prototype verification).

2) Design and Verification of Vacuum Seal Flange Maintenance Structure

A comparative study will be conducted on two existing sealing solutions: flexible membrane sealing (using a bolted compression flange structure) and lip-welded sealing (employing overlapping dual metal sheets, with dedicated laser welding/cutting tools for sealing and disassembly). This project will develop corresponding tooling and maintenance equipment to systematically evaluate the advantages and disadvantages of both solutions.

3) Design and Verification of High-Precision Docking and Sealed Containment System for Transfer Vehicle

The high-precision docking study includes the structural design of the transfer vehicle docking station and the fastening structure design between the transfer vehicle and the docking channel flange. Key research areas for sealed containment and contamination control include dual-seal door structure design, plug end-cap design, and contamination solidification/cleaning device design. This project will develop a prototype of the transfer vehicle-to-vacuum vessel port docking structure to validate automated docking operations and sealing performance.

Development Specifications of the Port Plug Maintenance System:

1) Maximum maintenance load capacity: ≥20 t
2) Transfer vehicle port docking positioning accuracy: ≤±2 mm
3) Containment structure sealing performance level: ≤ 2.5×10^{-3}/h (Class II, according to ISO 10648-2-1994 Containment enclosures - Part 2 Classification according to leak tightness and associated checking methods)

<u>Implementation Plan</u>

The schedule for the three research items is shown below.

Phase		2025		2026				2027				2028	
Item1	Design	■											
	Mock-up test				■	■							
Item2	Design		■										
	Mock-up test					■	■						
Item3	Design			■									
	Mock-up test							■	■				
	Final test										■	■	

7.2.7: Solid Lubricant Coating Technology for In-vessel bolts of BEST

In-vessel components (such as the first wall, blanket modules) must operate under extreme conditions: ultra-high vacuum, high temperatures, and intense neutron irradiation. Bolted connections, as a critical assembly method, require paramount operational reliability.

Traditional bolts have the following limitations in a fusion reactor:

1) Preload force increases abnormally: Under high temperatures, micro-region oxidation, diffusion, or even micro-welding easily occurs at the bolt/nut contact surfaces, leading to significantly increased disassembly torque or even "seizure."
2) Maintenance difficulties: Difficult to disassemble during repairs, requiring several times the preload force torque or even forced destruction, prolonging downtime and substantially increasing maintenance costs.
3) Reduced reliability: Uncontrolled preload force affects the connection and mechanical integrity of in-vessel components, threatening the safe operation of the equipment.

Therefore, solid lubrication technology is the key direction to break through the bottleneck, as its characteristics of high temperature resistance, radiation resistance, and low outgassing meet the extreme operational requirements of fusion reactors [8].

The research target is to develop high-performance bolt solid lubrication suitable for the extreme environments of a fusion reactor, significantly suppressing the post-high-temperature-service increase in disassembly torque/preload force, ensuring repeatable and reliable bolt assembly/disassembly. Specific research objectives include:

1) Selection and development of high-temperature resistant, strong radiation-resistant, ultra-low outgassing rate solid lubricant coating materials (e.g., MoS_2, WS_2, graphite-based composites, MAX phases, etc.).
2) Optimization of coating processes (such as magnetron sputtering, ion plating, spraying + sintering) to ensure uniform, dense, and strongly adherent coatings on bolt thread surfaces/bearing surfaces.
3) Establishment of a systematic evaluation system to quantify the effects of coatings on bolt friction coefficients, anti-galling properties, and preload relaxation/growth behavior under simulated and actual fusion environments.
4) Development of specifications for solid lubricant treatment processes and service performance evaluation standards for fusion reactor in-vessel bolts.

<u>Implementation Plan</u>

1. Design and pre-study stage

a) Material library construction: Systematic investigation and screening of candidate solid lubricating materials (MoS_2-based, WS_2-based, graphite-based, MAX phase, noble metals, etc.) and their modification strategies (doping, composite, multilayer)

b) Process Development: Optimize coating preparation processes (such as PVD and post-thermal spray treatment) for different bolt models and geometric features, with a focus on addressing overjet characteristics and adhesion at thread roots/sharp corners.

   Deliverables: High-precision positioning algorithm for manipulators based on visual and force feedback, simulation report on control algorithms, design instructions, source code.

c) Basic performance characterization: Laboratory environmental testing of coating hardness, adhesion, friction abrasion of tooth performance, outgassing rate, and microstructure.

   Deliverables: Establish a database of candidate materials/processes; Determine 1 to 3 preferred coating systems and their process parameters; Material Screening and Process Feasibility Report.

2. Non-nuclear testing phase

a) Bench construction: Develop a bolt connection test bench that simulates the working conditions of the vacuum vessel (ultra-high vacuum, high temperature, controllable preload force), integrating high-precision torque/preload force sensors.

b) High-temperature aging test: After applying standard preload, maintain at target high temperatures (e.g., 400°C, 500°C, 600°C) and under extreme vacuum conditions for hundreds of hours, then measure the disassembly torque increment after cooling.

c) Thermal cycle testing: Simulates start-stop operating conditions by conducting multiple heating-insulation-cooling cycles to evaluate the evolution of coating durability and resistance to relaxation/anti-galling performance.

   Deliverables: Complete systematic performance data of the optimized coating under simulated environmental conditions; Performance Verification and Optimization Report in a Non-Nuclear Environment.

3. Nuclear testing phase

a) Divertor first wall maintenance: Precise control of manipulators to achieve maintenance of the divertor first wall

b) Blanket first wall maintenance: Precise control of manipulators to achieve maintenance of the blanket first wall

   Deliverables: Bolts treated with solid lubricant coatings were used for the connection and installation of internal components in the vacuum vessel, followed by performance testing of the bolts after operation.

7.3: Magnet systems technology performance and readiness for application in next-step facilities

Among the wealth of data that BEST will allow collecting, information relating to superconducting magnets will be useful to provide constructive feedback on the design assumptions and possibly on the design approach. Therefore, the plan of activities for the purpose of this research plan is essentially focused on the performance verification of coils, cryogenic and quench protection systems against the backdrop of the declared design targets.

Some of the tests described below are carried out already during the cold test of the individual coils before assembly in the tokamak, e.g. the measurement of the joint resistance. In such a case, performance verification against the design target is already available. The repetition of the tests during the commissioning phase can be viewed as an additional quality control [9].

7.3.1: Verification of the actual cryogenic parameters with respect to the design values

7.3.1.1: Integrity of the electrical insulation

The electrical insulation of superconducting magnets is necessary to prevent current leaks and undesired electrical arcs. The critical points are represented by regions where the insulation is interrupted for penetrations, terminal, joints etc. These require a local application of the insulation, with manual or semi-automatic methods. The verification of the reliability of the techniques adopted for the in-situ insulation is of paramount importance for future insulation schemes. The integrity of the insulation is essential as, in case of fast discharge, degraded insulation may allow electrical arcs with potentially severe damage to the magnet [10, 11]. For all the magnets, a verification of the integrity of the electrical insulation is recommended prior to powering the magnet system, mainly to certify that all the in-situ insulation work on terminal, joints and current leads fulfills the requirements. At best, the verification is made at cold (4K) or at reduced temperature (≈40K). The tests include DC high potential and Paschen discharge [12] tests. No additional, intrusive instrumentation is needed for the tests.

7.3.1.2: Inlet and outlet temperature, flow distribution

For all magnets, at the end of the cool-down, the actual inlet and outlet temperature at zero current at each magnet is recorded over a representative duration (several hours). An important parameter to be verified is the flow distribution among parallel cooling channels in the winding packs and structures. Deviations from the nominal, perfectly homogeneous flow distribution may statistically occur: the quantification of the actual flow distribution provides critical information for the operation and a valuable database for assumptions in future magnets with similar layout [13]. For the flow distribution, additional instrumentation may be needed on the inlet or outlet pipes, e.g. to assess the flow by time-of-flight measurements [14].

7.3.1.3: Preliminary verifications

A number of preliminary verifications can be done before full powering of the magnets. These are already carried out in the cold test of the individual coils and need to be repeated on the magnet system to check parameters after the assembly [15]. Applying up to 20% of the nominal current, the tests in Section 7.3.1.2 can be repeated. Furthermore, the initial joint resistance can be measured, e.g. using the quench detection voltage taps, which can be partly disconnected from the quench detection when the stored energy of the magnet is < 5% of the nominal (20% of the operating current). The occurrence of flux jumps can be monitored by voltage spikes in the quench detection: actions will be taken if the amplitude of the voltage spikes causes false quench signals [14]. A fast discharge at low current may provide preliminary information on helium expulsion rate, peak pressure and re-cooling rate, which are valuable data for verifying assumptions in the thermal-hydraulic analyses.

7.3.2: Magnet performance in DC operation during commissioning

7.3.2.1: First test series

In the first test series the tuning and first operation of the quench protection in the assembled TF coils system can be viewed as a routine procedure [16]. On the other hand, the observation of the alignment, displacement and any dimensional hysteresis of the TF system has a critical impact on the operation of the corrector coils. Learning how good the design targets are achieved in terms of alignment and displacement provides straight feedback into the strategy of the corrector coils for future devices. In the first test series TF coils are connected in series. The current is raised simultaneously in all the TF coils. After powering at 20% of the nominal current in Section 7.3.1.3, the quench detection is fully restored. The current is raised to 50% of the nominal: the initial magnetic alignment (TF coil centering) is measured (instrumentation to be agreed) and compared with the expected values from manufacturing and assembly tolerance. During the charge to 50% current the response of the quench detection is monitored and the bridges for voltage compensation are tuned (common mode rejection). A fast discharge is triggered to verify the response of the quench protection (breaker's opening time, voltage peaks, hydraulic parameters, re-cooling, heat deposited in the TF cases). Then the current is raised in steps up to 100% and held stationary to verify the temperature profile, joint resistance distribution, flow distribution. The displacement at full charge is measured and the dimensional hysteresis after the discharge is assessed. An intentional quench can be triggered, for example by raising the inlet temperature in steps (an appropriate heater must be agreed with the BEST team). The current dump upon a real TF quench is very useful to monitor the voltage build-up to the threshold, energy extraction in the quenched coil compared to the others, any secondary quench in the non-quenched coils due to eddy currents heating of the TF case, deformation of the vacuum vessel due to induced eddy currents.

7.3.2.2: Second test series

After the first full charge and quench, the TF coil system is powered to full current 20 times. At the last charge, the joint resistance, temperature profile, flow distribution and displacement are measured again to assess any evolution. Then the heater to trigger a quench is powered again in steps: the occurrence of a quench after 20 cycles is compared to the first cycle to tentatively assess the performance stability, which is a key aspect for design strategy.

7.3.2.3: Third test series

The modules of the CS and the PF coils are tested individually for DC performance: the current is first raised at 50% to tune the quench detection parameters (same procedure as for the TF coils) and then to full current [17]. If alternative methods of quench detection are installed (i.e. Optical fiber sensing), the response is compared with voltage monitoring. For the CS, a proper DC performance test requires that all the 10 modules are simultaneous powered to full current (to achieve the maximum field). Such a test exceeds the scope of the former cold test of the individual coils and is important to check the effect of the interaction among coils. At full current in the 10 modules, stress in the tie plates is monitored in comparison to the end of the cool-down. The joint resistance and the flow distribution are verified.

7.3.2.4: Fourth test series

The fourth test series is a milestone to validate the magnet system in operation, as all the coils, TF, PF and CS are simultaneously charged 100%. An attempt to trigger a quench by heating at full current the inlet flow is done for each of the CS modules and PF coils (an appropriate heating method must be agreed).

7.3.3: Magnet performance in pulsed and advanced operation during commissioning

In a first step, at zero current in the TF coils, the current scenario for the CS and PF is reproduced (without plasma). During the controlled discharge, the temperature and flow partition (including possible reverse flow) are monitored. The quench protection is expected not to be triggered by the large field transients in pulsed operation (common mode rejection). The AC loss is tentatively assessed by calorimetry [18]. The re-cooling time is assessed by monitoring the temperature at the outlets. As far as the instrumentation allows, the stress in the tie plates is monitored during the current scenario [19].

In the second step, the current scenario is repeated 10 times for CS and PF with the TF coils at full current. The possible evolution of joint resistance, AC loss, re-cooling time and tie plates stress is monitored. The performance stability (DC and AC loss) of the CS and PF systems after several load cycles is a critical test to validate the design strategy of BEST and provide added confidence to the design of similar devices.

7.4: References

[1] M. Merola et al., *Journal of Nuclear Materials* **307**, 1524 (2002)
[2] K. Ezato et al., *Fusion Eng. Des.* **98**, 1281 (2015)
[3] S. Carpentier-Chouchana et al., *Phys. Scr.* **T159**, 014002 (2014)
[4] Y. Kim et al., *Journal of the Korean Welding and Joining Society* **30**, 51 (2012)
[5] R. Buckingham et al., *Nature Phys*. **12**, 391 (2016)
[6] G. Qin et al., *SOFT ROBOTICS,* **0165(00)**, 1 (2021)
[7] J.F. Koning, et al., *Fusion Eng. Design* **87**, 515 (2012)
[8] S. Shi et al., *Industrial Lubrication and Tribology* **70**, 155 (2018)
[9] A. Devred et al., *Supercond. Sci. Technol.* **36**, 053001 (2023)
[10] N. Mitchell et al., *Fusion Eng. Des.* **193**, 113017 (2024)
[11] JT-60SA, "Commissioning Status"; www.jt60sa.org/wp/category/news/
[12] J. Baldzuhn et al., *IEEE Trans. on Plasma Science* **47**, 5125 (2019)
[13] Y. Takahashi et al., *Cryogenics* **132**, 103587 (2023)
[14] P. Bruzzone et al., *IEEE Trans. on Applied Superconductivity* **24**, 9500205 (2014)
[15] F. Savoldi et al., *Cryogenics* **127**, 103415 (2022)
[16] Q. Yan et al., *Superconductivity* **25**, 00099R1 (2025)
[17] M. Wolf et al., *Fusion Eng. Des.* **209**, 113282 (2025)
[18] N. Martovetsky et al., *IEEE Trans. Appl. Supercond.*, **26**, 4200605 (2016)
[19] G. Aiello et al., *IEEE Trans. Appl. Supercond.* **34**, 4200507 (2024)

Chapter 8: MHD, Control and Disruptions

Coordinators: S. Gu (ASIPP), J.P. Graves (EPFL, Switzerland)

With contributions from:
ASIPP Team: H.H. Wang, Y. Zhang, X.J. Wang, M.H. Li, Y.H. Wang, D.L. Chen, Y.W. Sun
EUROfusion Team: S. Van Mulders (EPFL, Switzerland), C.Z. Wang (EPFL, Switzerland), O. Sauter (EPFL, Switzerland), M.D. Kong (EPFL, Switzerland)
CN Universities Team: L. Zeng (Tsinghua Univ.), D. Hu (Beihang Univ.), X.M. Li (Tsinghua Univ.)

This chapter investigates the challenges related to MHD and control in BEST. The QCE plasma scenario is considered for all the investigations, unless otherwise stated. The chapter is broken into three sections, namely, the ramp up phase, flat-top phase and termination phases. Each of these phases have their own features and risks. In particular, the section on ramp up phase examines the challenges of the L-H threshold, and makes suggestions on, for example, heating timing to improve transport properties through the pulse, to avoid impurity ingress and avoid tearing modes. Also investigated during the current ramp is error field tolerance and runaways. For the flat-top phase, beta limits against RWMs are investigated, and the stability to NTMs is also assessed. In addition, unmitigated thermal quenches are modelled in order to assess worst-case heat loads. MGI and SPI mitigated disruptions are also investigated in order to assess the expected runaway electron current under different conditions. Finally, the termination phase is examined, in particular for the impact of heating timing, current ramp-down rate and elongation control, on vertical stability.

8.1: Current ramp-up phase

This section examines the challenges of the L-H threshold, and makes suggestions on, for example, heating timing and current ramp rate. Also investigated during the ramp is the error field tolerance and runaways.

8.1.1: Analysis of the ramp-up phase and full discharge modelling with RAPTOR

Full discharge simulations for both the reference and late L-H transition cases were carried out with the RAPTOR code [1, 2]. The flat-top calculations with RAPTOR were benchmarked against the ASTRA results for QCE (Section 4), and good agreement was obtained. Time traces for the two ramp-up scenarios, as predicted by RAPTOR, are compared in Fig. 8.1(a)-(f). The reference case with the earlier access to H-mode (blue lines) causes a slower evolution of the q-profile and delays the onset of sawtooth instabilities (the first sawtooth occurs at 86.8 s, compared with 64.0 s for the late L-H transition case). A full reconnection model is used, and crash times are calculated according to the Porcelli criteria. The particular criteria of concern here occurs for magnetic shear surpassing 0.3 during the RAPTOR transport evolution. Towards the end of the flat-top phase, the sawtooth period is ~5.2 s. Future work will assess the impact of local current drive on the sawtooth period in the presence of energetic ions, important for tearing mode and disruption avoidance for the sawtoothing QCE regime.

The late L-H transition scenario in Fig. 8.1 causes a clear rise in the central solenoid flux swing consumed during ramp-up, due to the higher plasma resistance. While for both cases the l_{i3} trace continues evolving throughout the full 100 s flat-top phase, the evolution of the current density profile $j_{\parallel}$ during flat-top is far more pronounced for the reference case with the earlier L-H transition, as shown in Fig. 8.1(g), where $j_{\parallel}$ is shown at different times during the flat-top phase. Significant evolution of $j_{\parallel}$ during flat-top could cause varying impact on transport (not modelled here) and on tearing mode stability (this has been described for ITER baseline DIII-D scenarios in [3]). Finally, the faster q-profile evolution of the late L-H transition scenario avoids minima in the q-profile at rational surfaces during the high-β phase, while this is not the case for the early L-H transition scenario. As a consequence, the late L-H transition scenario is expected to be more robust against tearing modes, considering the ASDEX Upgrade observations [4].

Due to tungsten impurity radiation during the ramp-up L-mode phase, auxiliary electron heating is required to avoid a radiative collapse. The required L-mode auxiliary heating is more significant for the scenario with late transition to H-mode. In these simulations, P_{aux} = 7 MW L-mode heating has been applied for both ramp-up scenarios. Note that this value could be reduced, depending on the tolerated margin to radiative collapse.

Late application of heating helps avoid NTMs during L-H transition, though it is noted that electron core heating will be required during L-mode to avoid a radiative collapse, as modeled here for a constant W concentration. Future modelling efforts should also include W transport, assessing the role of heating actuators to avoid central impurity accumulation, following for example the approach described in [5].

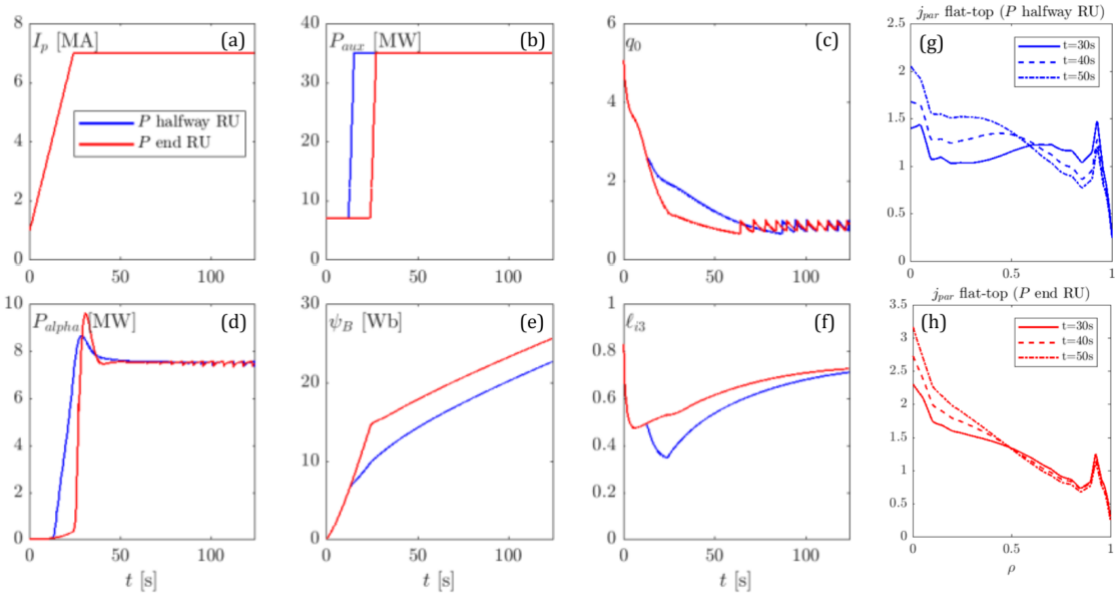

Figure 8.1: Comparison of ramp-up cases for the reference (blue) and late (red) L-H transitions. Panels (g) and (h) show the evolution of $j_{\parallel}$ during the flat-top phase.

8.1.2: Error field tolerance

Evaluation of the error field during the ramp up stage is particularly important, especially the estimate of the error field amplitude on the 2/1 resonant surface. Based on the poloidal field (PF) and central solenoid (CS) currents during the ramp-up stage, EQDSK files are constructed using CHEASE code on the basis of RAPTOR simulations. According to the previous analysis, the error field tolerance of BEST in low density stage is about $B_r/B_t \sim 1\times10^{-5}$ on the 2/1 resonant surface.

The ramp-up analysis with RAPTOR indicates the appearance of the $q = 2$ surface in the plasma at $t \approx 17$s, as shown in Fig. 8.2. After that, a potential lock mode caused by the 2/1 components of the error field was evaluated. The vacuum spectrum analysis for the given equilibrium was obtained using MAPS code. Starting from 17 s, a lock mode may be avoided even when the error field (from shift or tilt) from both the CS and PF coils are the same direction with 1 cm shift or 0.1° tilt. However, the situation changes at 21 s, as shown in Fig. 8.3, when the error field $B_r/B_t \sim 1\times10^{-5}$ is in the critical value of error field tolerance. For the worst case during ramp-up, the correction coils current turns are at 30 kAt when assuming that PF and CS contributions, with 1 cm shift and 0.1° tilt in the same direction.

To conclude, it is found that error field correction is required near the end of the ramping phase of the QCE regime. The requirement of the correction coil current for the worst case is around 30 kAt, which can be satisfied by the BEST correction coils system with capacity at 400 kAt. Further research on the error field correction method during ramp-up phase is required for BEST.

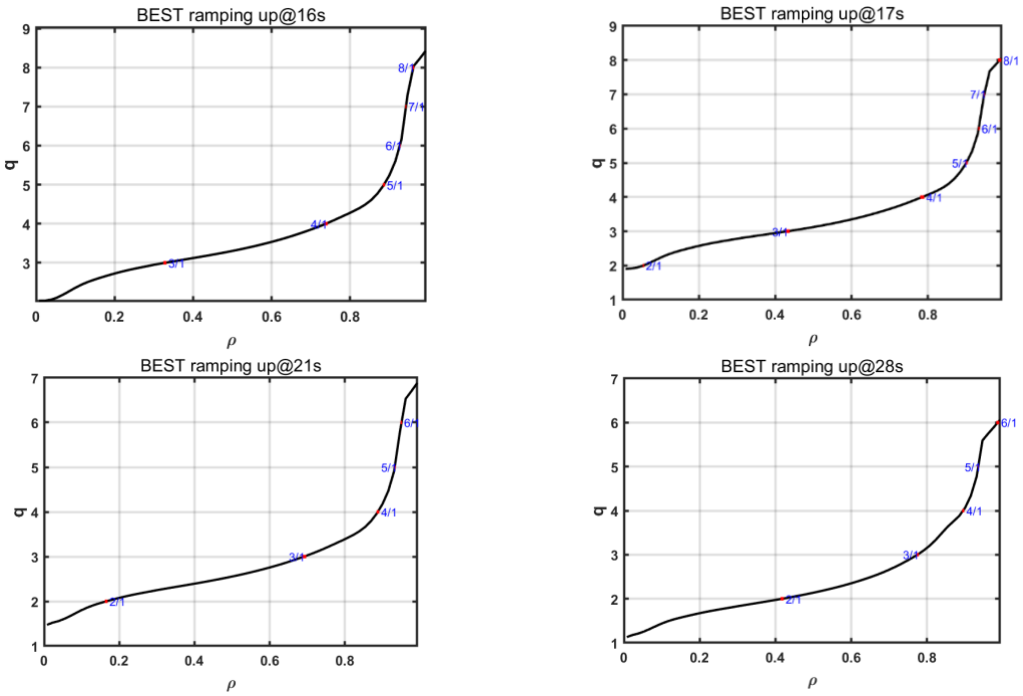

Figure 8.2: Evolution of the q-profile during the reference ramp-up scenario.

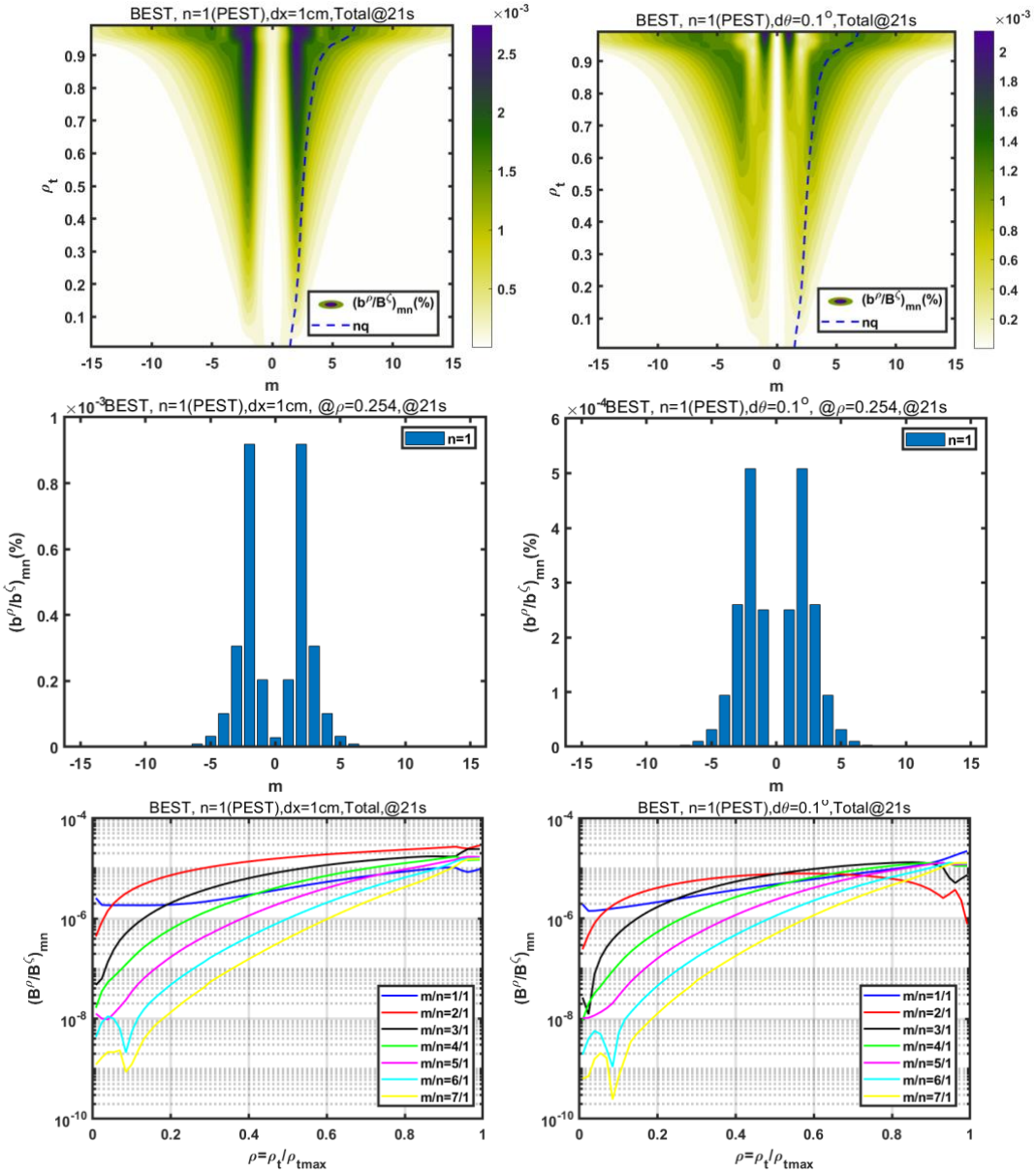

Figure 8.3: The total PF and CS contributions with 1 cm shift or 0.1° tilt at the same direction for error field in plasma ramping up at 21 s.

8.1.3. Runaway electron generation during ramp-up

The generation of runaway electrons (REs) during plasma initiation and the current ramp-up is not only a phenomenon that can prevent successful discharge formation, but anomalous losses of these energetic electrons can also damage in-vessel components. The main RE generation mechanism during plasma start-up is the Dreicer source [6], the amplitude of which is positively correlated to electron temperature and parallel electric field, and negatively correlated with the electron density.

This section explores the process of RE formation during the start-up in a typical QCE-like discharge on BEST. Simulations are performed using the BBS0D code for plasma initiation and initial ramp-up, and self-consistently coupled with RE generation and losses [7].

Figure 8.4 shows the field-null poloidal flux and poloidal field contours at 0 and 290 ms with the current ramp-down rate per turn on CS1LL, $dI_c/dt = -20$ kA/s. The time evolution of plasma parameters during the plasma initiation with pre-fill gas pressure set to 0.5 mPa, including RE formation, is presented in Fig. 8.5, in which the central loop voltage is about 18.8 V at 290 ms. The pure ohmic start-up without any auxiliary heating power is simulated. As seen from Fig. 8.5(e), the RE density decreases quickly during the first 10 ms after breakdown due to the increasing electron density, and then starts to increase again after about 320 ms. The second increase in RE density is mainly caused by the rise in temperature. Improved confinement here is due to the formation of closed flux surfaces. Based on previous experience of EAST simulations and experiments, the RE density is expected to further increase after 330 ms, as the electron temperature continues to rise.

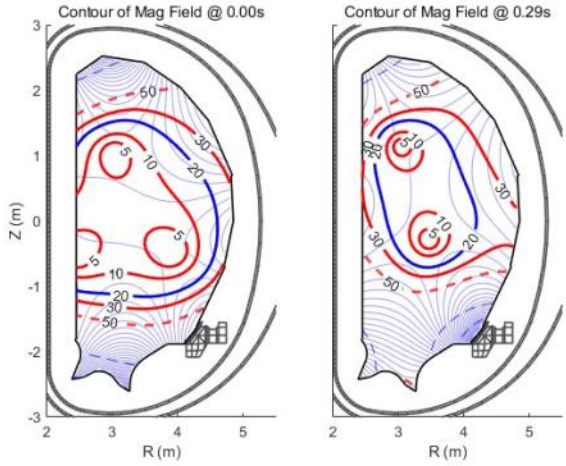

Figure 8.4: Field-null poloidal flux and field magnitude contours for BEST plasma initiation at 0 and 290 ms.

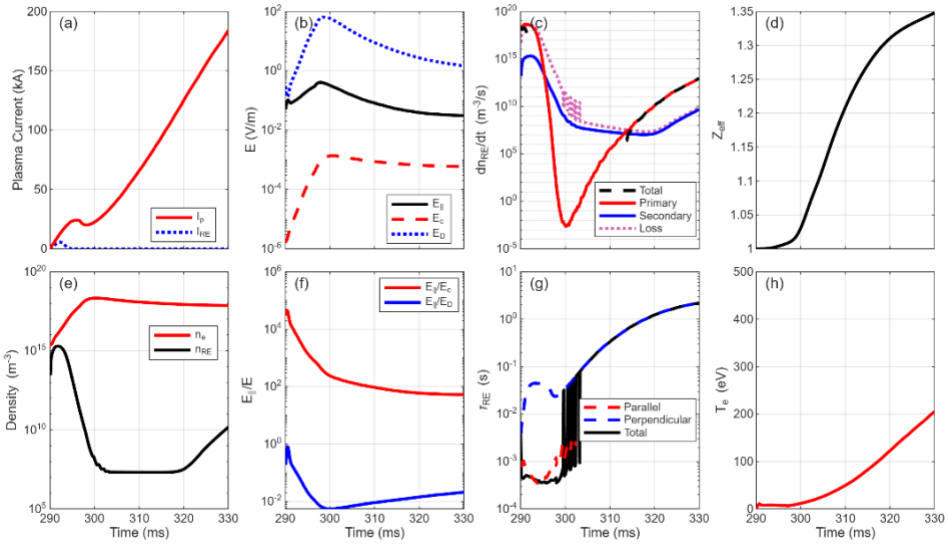

Figure 8.5: Time evolution of plasma parameters with p = 0.5 mPa. (a) Plasma current and RE current; (b) Parallel electric field, critical electric field and Dreicer electric field; (c) dn_{RE}/dt and its components; (d) Effective impurity level; (e) Electron density and RE density; (f) $E_\parallel/E_c$ and $E_\parallel/E_D$; (g) RE transport time; (h) Electron temperature.

Several key parameters, including the current change rate per turn on poloidal coils (i.e. the loop voltage), and pre-fill gas pressure (i.e. the electron density), have been scanned to give more clarity on the RE current generation. Three values of dI_c/dt, maintaining the field-null poloidal flux at 0 ms, were selected. The simulations suggest that the plasma current cannot ramp up successfully in the case of $dI_c/dt = -10$ kA/s. Although the breakdown is predicted to happen according to the Townsend theory, the plasma current cannot keep increasing due to the low loop voltage of about 6 V. If the current change rate is multiplied by a factor of 2 or 3, the plasma burn-through can be successfully achieved. The following cases are considered:

- Case 1: the LTS coil current change rate per turn is about −20kA/s at 290 ms. The central loop voltage is about 12.5V at 290 ms.
- Case 2: the LTS coil current change rate per turn is about −30kA/s at 290 ms. The central loop voltage is about 18.8V at 290 ms.

Figure 8.6 shows the influence of pre-fill gas pressure on RE density at 330 ms under these two cases. The results show that higher loop voltage and lower pre-fill gas pressure cause the RE density to increase. Note that the plasma current fails to ramp up under case 1 when pressure is set to 1 mPa.

In summary, runaway electrons are expected to appear when the loop voltage exceeds about 12 V. During the end of burn-through, the RE current is at a level of about 0.1 kA, which is much smaller than the plasma current of about 200 kA, indicating that RE is not significant during start-up. Lowering the loop voltage and increasing the pre-fill gas pressure will help suppress the generation of RE currents. If auxiliary heating such as ECH is used in the start-up phase, the loop voltage can be further reduced, which will be beneficial for the avoidance of REs.

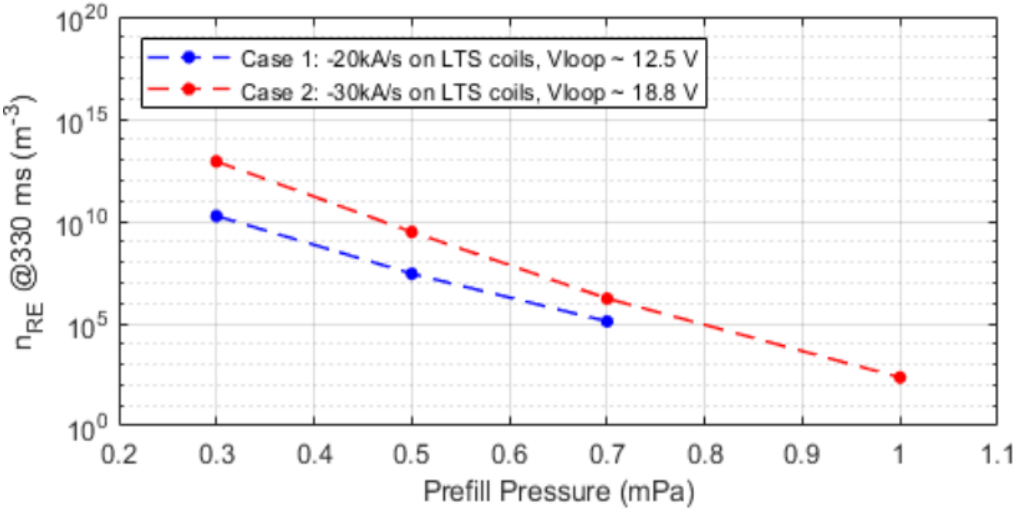

Figure 8.6: Runaway electron density at 330 ms with different pre-fill gas pressure under two cases.

8.2: MHD-related analysis during the flat-top phase

For the flat-top phase, beta limits against RWMs are investigated, and the stability to NTM is assessed. In addition, unmitigated thermal quenches are modelled in order to assess worst-case heat loads. MGI and SPI mitigated disruption simulations calculate the runaway electron current under different conditions.

8.2.1: RWM beta limit evaluation

The MHD stability of plasmas is key for BEST operation in high fusion performance ranges without disruption of the plasma current. Since fusion power is proportional to β^2 (where β is the ratio of the volume averaged plasma pressure to the magnetic pressure), maximizing fusion performance might require operation above the no-wall beta limit, where either passive or active control of the resistive wall mode (RWM) is needed. To avoid potential disruptions, the conservative BEST 7MA and QCE scenarios aim at operating without RWM to achieve the fusion gain $Q \geq 1$ goal. Therefore, it is necessary to evaluate the no-wall beta limit of these scenarios.

In this section, the single fluid MHD code MARS-F [8] is used to assess the MHD stability of BEST 7MA and QCE scenarios, in particular to confirm that these scenarios operate without RWM. The CHEASE calculated equilibrium was scaled with the pressure, holding the plasma current largely unchanged. This therefore provides a scan in normalized beta β_N. The MARS-F code was deployed to calculate the growth rate (normalized by the Alfven time, $\gamma\tau_A$). After β_N exceeds the no-wall beta limit, unstable magnetohydrodynamic modes are driven.

The basic information of the BEST equilibrium is given in Chapter 4. The equilibrium is first processed by the CHEASE code to generate the corresponding equilibrium mesh, where the last close surface is smoothed near the X-point region and the current radial profile are smoothed for the purpose of numerical stability, then is fed into the MARS-F magnetohydrodynamic code to study the variation of the growth rate of the outer twist mode at different beta. The beta limit for the no-wall and ideal-wall condition calculated by the MARS-F code is displayed in Fig. 8.7. The figure shows

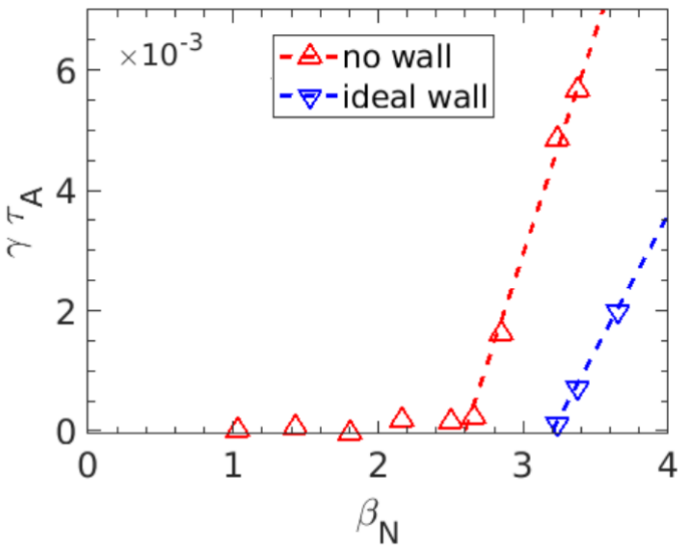

Figure 8.7: Beta limit obtained with no-wall and ideal-wall condition.

that the no-wall beta limit of the BEST QCE scenario at 7 MA is reached at $\beta_N \approx 2.5$, while the ideal-wall limit around $\beta_N \approx 3.2$. As the β_N of the target equilibrium is around 1.3, this means the RWM is stable.

In summary, the BEST QCE and 7MA scenarios are stable to RWMs with large margin. The results shown here are evaluated for BEST conservative scenarios, which target achieving fusion gain $Q \geq 1$. For the advanced BEST scenarios with target at $Q \approx 5$, BEST will operate above the no wall beta limit, and RWM control will be required. The assessment of BEST advanced scenarios will be detailed in the next version of the Research Plan.

8.2.2 NTM stability calculations

The reduced MHD code TM1 [9] has been used for the calculation of tearing modes (TM) and neoclassical tearing modes (NTM) for BEST $Q \geq 1$ scenarios at equilibrium saturation. The input parameters of $Q \geq 1$ scenarios are shown in Table 8.1. Plasma rotation is not included in the simulations, as only weak rotational effects are expected and no double tearing modes are anticipated. The latter is due to the monotonic q-profile, which prevents the formation of double tearing modes (sensitive to rotation shear).

First simulations from TM1 obtained linear tearing mode instability, while the reduced version of JOREK indicated stability during the flat-top. In general, the reduced JOREK slightly underestimates tearing instability, while TM1 significantly overestimates it. Both are due to simplifications related to toroidal effects (see the artificially modified interchange effects which alter the Glasser-Greene-Johnson terms here [10]). In order to assess the effect of current drive overcoming the bootstrap current effect on the NTM, the TM1 code was deployed with modified q-profile, so that it is weakly linearly stable to the tearing mode. See the modified q-profile in Fig. 8.8.

Table 8.1: Input equilibrium parameters for 7MA scenario.

	$m/n = 2/1$
a/R	1.1 m / 3.6 m
B_0; I_p	6.15 T; 7MA
r_s	0.61 a
$T_e\|_{r=rs}$	8.9 keV
$n_e\|_{r=rs}$	7.3×10^{19} m^{-3}
S	1.3×10^{10} (the magnetic Reynolds number)
$\chi_\perp$	1 m^2/s
$\chi_\parallel$	1.4×10^{8} m^2/s

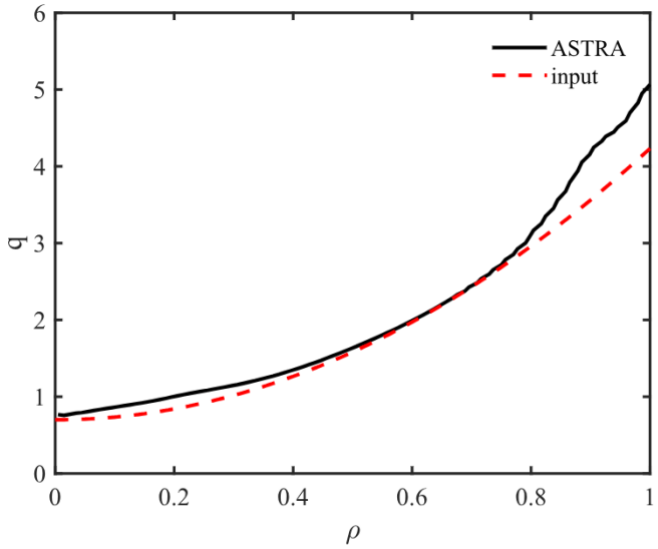

Figure 8.8: Safety factor profile from ASTRA (solid black curve) and for input (dashed red curve).

The time evolution of the $m/n = 2/1$ mode without bootstrap current perturbation is shown in Fig. 8.9 for initial island width, $w_0/a = 0.001$ (solid curve) and 0.01 (dashed curve). The mode saturates at a width of 0.0033 a, consistently with the classical tearing mode being weakly stable to the modified q-profile.

The time evolution of the $m/n = 2/1$ magnetic island width with a local bootstrap current density ratio $j_b/j_p = 0.145$ is shown in Fig. 8.10 by the black curve. The island width grows rapidly, driven by the perturbed bootstrap current, and eventually saturates at 0.134 a. After nonlinear mode saturation, non-modulated current drive (NMCD) is turned on at $t/\tau_R = 0.1$. The red and blue curves in Fig. 8.10 are for $I_{cd}/I_p = 0.014$ and 0.015, respectively. It is seen that the mode can be stabilized totally with $I_{cd}/I_p = 0.015$.

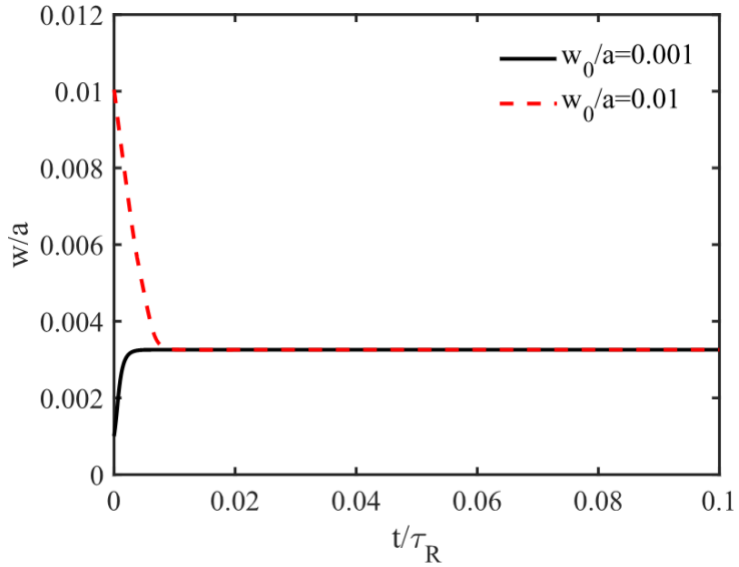

Figure 8.9: Time evolution of $m/n = 2/1$ classical tearing mode width for initial island width $w_0/a = 0.001$ (solid black curve) and 0.01 (dashed red curve).

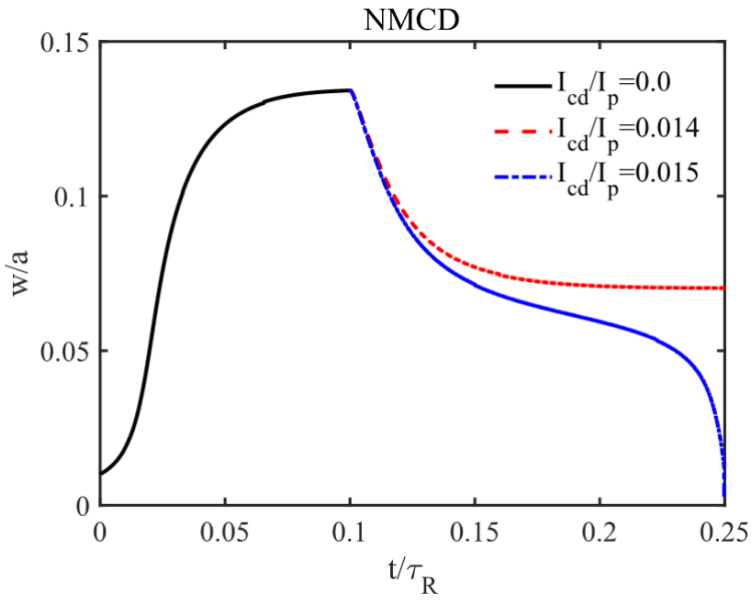

Figure 8.10: Time evolution of the $m/n = 2/1$ magnetic island for different driven current ratios. The black curve corresponds to the case without driven current. The red and blue curves are for non-modulated current drive with $I_{cd}/I_p = 0.014$ and 0.015, respectively.

With the above results, the required RF power for mode stabilization can be estimated. For a current drive efficiency $\gamma = n_e R I_{cd}/P_{EC} = 0.3\times10^{19}$ A/m^2/W [11] and plasma density $n_e = 8.3\times10^{19}$ m^{-3}, the required non-modulated ECRF power for NTM mode stabilization is 10.4 MW. The required ECW power would be saved by around 30% if modulated current drive is applied.

In future work, small island stabilization by ECCD at reduced ECW power should be done in future with realistic ECW deposition profile calculated by a ray-tracing code. In addition, NTM stability will be assessed during the ramp up.

8.2.3: Heat loads associated with unmitigated thermal quench

The heat load asymmetry of a BEST H-mode plasma undergoing unmitigated thermal quench is investigated. We emphasize that this simulation aims at identifying the consequence of the worst situation in which the disruption mitigation methods failed to launch. In real BEST operation, the disruption mitigation system is expected to work, and thereby significantly reduce the heat loads. Technical details about BEST disruption mitigation systems (MGI and SPI) are discussed in Chapter 5.4.

For the unmitigated disruption investigated here, most of the outgoing heat flux is deposited onto the lower divertor region, as would be expected (the "upper divertor region" is a numerical artefact in our simulation). The heat flux distribution shows apparent $n = 1$ asymmetry, as well as a lobe-like pattern which has been observed in previous studies concerning EAST.

The heat flux distribution close to the final core temperature collapses on the inner and the outer divertor regions (at t = 49.01 ms), which is shown in Fig. 8.11. It is seen that local peak heat loads are 2.5×10^9 W/m^2, which is far above safe operation. Exposure to such heat flux for more than 10^{-4} s would result in energy impact approaching the tungsten melting limit at 38 MW s$^{1/2}$/m^2, putting the PFCs at risk. The lobe-like toroidal asymmetry is clearly seen in the inner divertor region, while also present to a lesser degree in the outer divertor. Nevertheless, in both regions the dominant toroidal asymmetry is n = 1, corresponding to the dominant core MHD modes. Another feature is that the maximum heat flux maintains 2:1 asymmetry between the outer and inner divertor during the TQ. This is the reverse of previous observations in DIII-D or ASDEX-U, where the heat flux asymmetry between the inner and outer divertor is around 1:2 during normal operation, and reverses to about 2:1 during transient events such as ELMs or disruptions. The reason BEST maintains the inner-outer heat flux asymmetry during the disruption is currently uncertain and requires future investigation.

In conclusion, 3D nonlinear simulation of unmitigated TQ in BEST has been carried out using the JOREK code [12]. The divertor heat load is found to exhibit n = 1 toroidal asymmetry, corresponding to that of the dominant mode in the later phase of the TQ. Such toroidal asymmetry exists on both the inner and the outer target, and manifests as lobe-like features on the divertor plates. Apart from the toroidal asymmetry on each plate, there also exists an approximately 2:1 asymmetry between the outer and the inner divertors. This contrasts with previous observations on DIII-D or ASDEX-U where the inner divertor heat flux becomes stronger than the outer one during transient events. The heat flux on the first wall is of the order of 10 MW/m^2, which is relatively safe. Future investigations with more realistic first wall are needed to provide improved quantitative assessment of BEST PFC heat loads during unmitigated and mitigated disruptions. Nevertheless, given the peak heat loads, it is clear that mitigation during thermal quench for lowering the peak heat flux by one order of magnitude will be required. It should be noted that the calculations were undertaken with fixed boundary, so that the HALO currents, while included in JOREK, are simplified, and should be improved in future simulations, such as those recently undertaken for ITER [13].

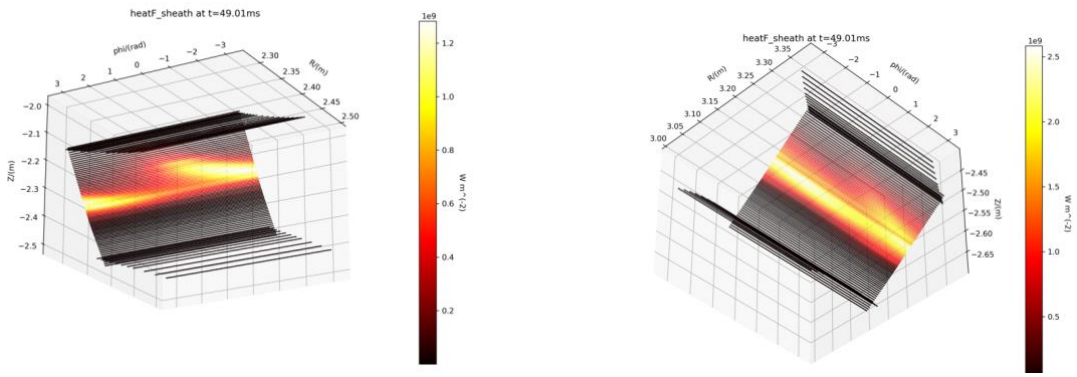

Figure 8.11: The heat flux distribution on the inner and outer divertor regions at t = 49.01 ms.

8.2.4: MHD simulation of runaway electron avalanche in mitigated disruptions

During a disruption event, the high energy runaway electrons (RE) are one of the primary threats that could cause severe damage to the device [14]. During the current quench (CQ), decay of the ohmic current induces a strong toroidal electric field in the cold and resistive plasma, which accelerates a tail of high-energy electrons (so-called RE seeds [15]) to relativistic speed. The RE problem could be more difficult to handle in D-T operations due to extra seeds from tritium decay and Compton scattering of the gamma photon emitted by the activated wall material. The RE population grows exponentially from the seeds via the collisions between REs and thermal electrons during the so-called RE avalanche.

The RE avalanche gain $g_{RE} = I_{RE}/I_{seed}$, where I_{RE} and I_{seed} is the current carried by the REs and seeds separately (proportional to their numbers). Its amplitude roughly follows the equation [14]:

$$g_{RE} = \exp(\Delta\psi/\psi_c).$$

Here, $\Delta\psi$ is the change in the poloidal magnetic flux, which is roughly proportional to the decay of the plasma current I_p, and ψ_c is a machine-dependent factor scaling with the major radius R_0. In this model, I_{RE} grows exponentially with the decay of I_p until the ohmic current approaches zero due to either CQ or until the entire I_p is carried by REs (RE saturation). Considering $I_p \approx 6.5$-7 MA in BEST, g_{RE} would be smaller than in higher-current machines like ITER and CFEDR, but it remains a point to be considered seriously. To estimate the potential RE current amplitude in BEST disruptions, we perform 2D MHD simulations coupled with a RE fluid model on the JOREK code [16].

The initial investigation scans over neon density n_{Ne} from 5×10^{18} m^{-3} to 1×10^{20} m^{-3}, under two hydrogen density values: a) $n_H = 7\times10^{20}$ m^{-3} (with hydrogen injection in disruption mitigation) and b) $n_H = 1.1\times10^{20}$ m^{-3} (no hydrogen injection). Although the main ions should include the D-T fuel, the difference in isotopes can be neglected in the RE avalanche. Considering that j-flattening would decrease $\Delta\psi$ and thus I_{RE}, two cases without j-flattening are given as 'worse-case' scenarios.

Simulation results: The peak I_{RE} and corresponding g_{RE} are shown in Fig. 8.12. As the actual I_{seed} in BEST disruption is highly uncertain, the value of g_{RE} is more meaningful. Under certain values of g_{RE}, it is found that I_{RE} is simply g_{RE} I_{seed} before RE saturation. During the scan, all the cases with H injection and j-flattening give $I_{RE} < 1.3$ kA and $g_{RE} < 2\times10^6$. Only one case without either of these two mechanisms on the top right of the plot results in RE saturation under $I_{RE} = 1.04$ MA. The disruptions without H injection typically result in $I_{RE} \sim 10^2$ kA, and these scenarios without being thermalized by massive hydrogen injection are expected to be susceptible to a large hot-tail seed current. Therefore, D or H injection would be recommended for BEST disruption mitigation. The optimal g_{RE} can be suppressed below 10^4 around the low neon limit of our scan, which corresponds to hydrogen SPI or MGI with 0.85% Ne.

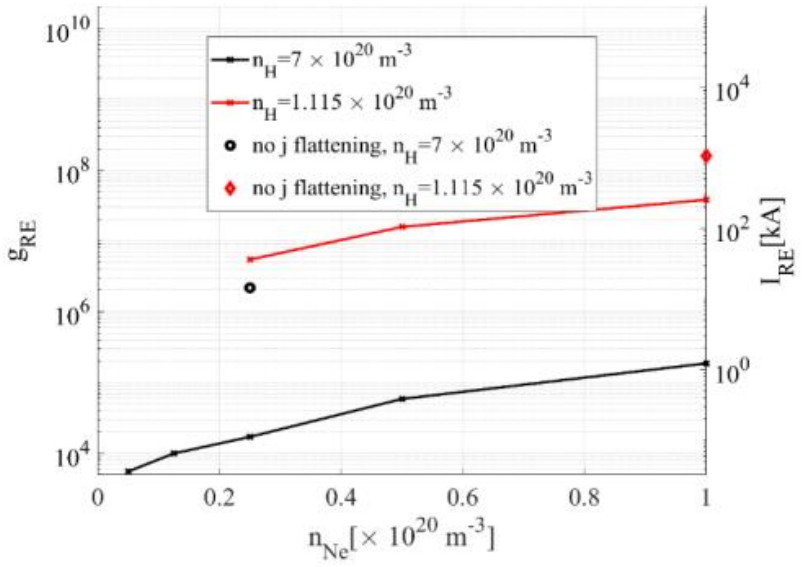

Figure 8.12: The peak RE current and the corresponding g_{RE} over the injection density scan.

In the cases without j-flattening, $\Delta\psi$ is around 21.4 Wb, while it decreases to 14.5 Wb due to j-flattening. Without saturation, the flattening would decrease g_{RE} by one-third. It should be noted that the extent of j-flattening due to the TQ has been assumed here as a best guess, while the real degree of flattening depends sensitively on the scale and amplitude of MHD activity caused by the mitigation injection. Further dedicated studies should be undertaken.

Discussion and outlook. In this work, the REs generated in BEST disruptions are shown to be controllable by mitigation injection even under worst-case scenarios. This result is expected since g_{RE} scales down with increases in both plasma current and machine size. For example, $\Delta\psi$ is only up to 21.4 Wb during CQ, compared to over 90 Wb in ITER. It should be noted that some RE losses during the avalanche are neglected in the present model. Future 3D free-boundary simulations may find that g_{RE} could be even lower due to the RE deconfinement by MHD instabilities and plasma scraping-off on the wall. Furthermore, g_{RE} could be further decreased by reduced neon injection. However, the BEST injection plan is also constrained by the limits in heat load to the wall and the electromagnetic force on passive components. If the neon concentration is insufficient to radiate most of the Ohmic power during CQ, the heat load to the walls could be intolerable. Another problem is that low radiation power might make the CQ time too long, which leads to a strong halo current crossing the wall with resultant Lorentz force on the device. These two limiting factors are outside the scope of this RE study.

Finally, the choice of I_{seed} = 6.5 mA in the simulations is quite arbitrary. Obtaining a reliable value of I_{RE} requires detailed TQ simulations to evaluate the RE seed amplitude on BEST. In addition, the RE peak current calculated here is not sufficient to establish the potential damage to the first wall. 3D simulations of RE beam termination are required to assess the energy load to the wall-facing components [17].

8.3: Termination phase

In this section, the termination phase is examined, in particular for the impact of heating timing, current ramp-down rate and elongation control on vertical stability.

8.3.1 Plasma termination modelling using RAPTOR

Plasma termination is a critically important aspect of tokamak plant operation. This section provides recommendations for safe landing of BEST.

The assumption of the default $dI_p/dt = -250$ kA/s ramp-down with constant LCFS geometry and H-L transition halfway along the ramp-down leads to an increase of l_{i3} to about 3.9 (see Fig. 8.13), which is expected to be challenging for vertical position control, especially as the plasma is maintained highly elongated throughout the ramp-down phase. The aggressive default ramp-down rate leads to a reversal of the current density in a broad region of the outer plasma core, reminiscent of the results reported in [18]. Current density reversal is observed during the H-mode phase and persists throughout the remaining ramp-down segment. Figure 8.14 shows the parallel current density profile at end of flat-top and after the H-L transition, when the current density reversal is most pronounced. MHD stability, and impact on disruptivity of this current density distribution, has not yet been directly assessed.

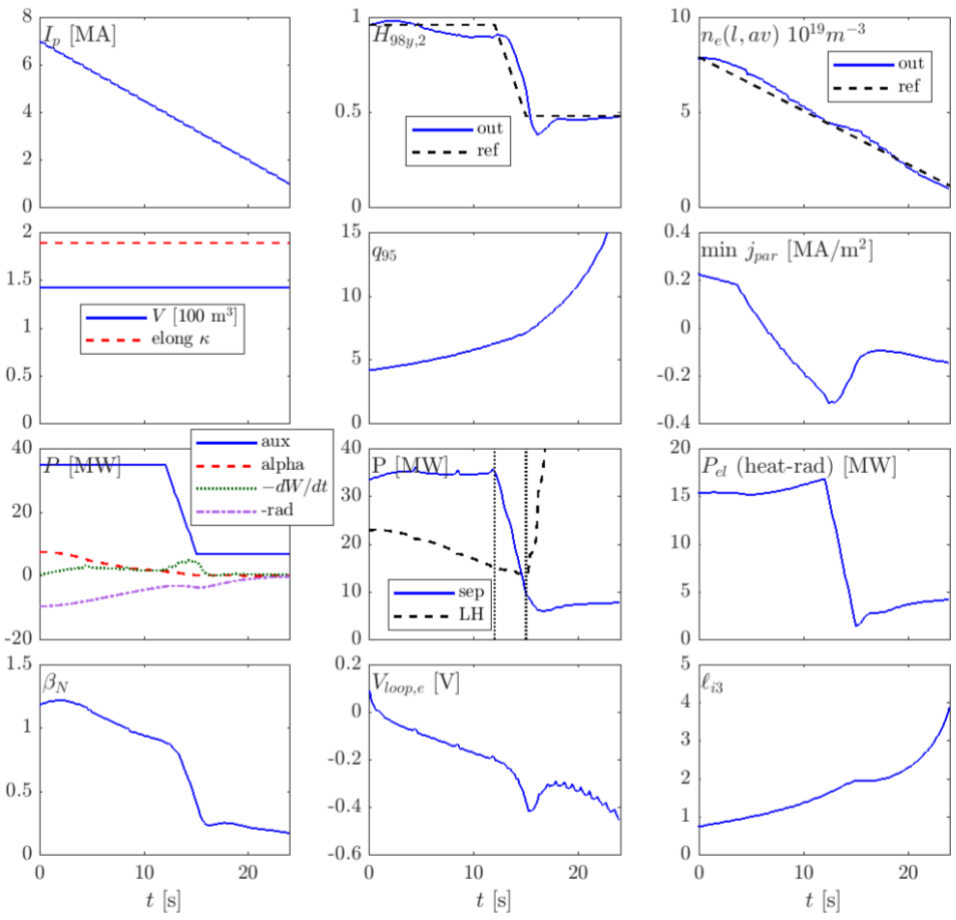

Figure 8.13: Modelling of the default 250 kA/s ramp-down with the constant LCFS geometry.

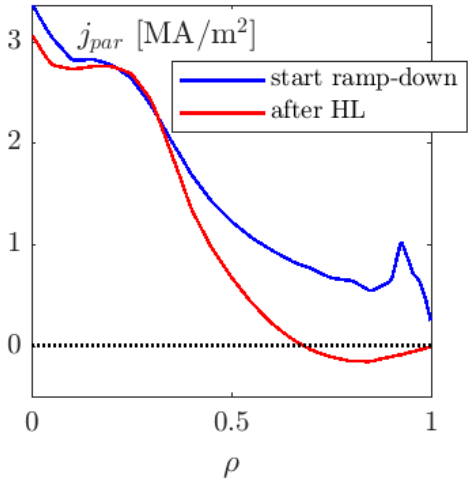

Figure 8.14: 250 kA/s ramp-down: $j_{\parallel}$ at end of flat-top and after the H-L transition, when the current density reversal is most pronounced.

The impact of the H-L transition timing on the l_{i3} increase and the $j_{\parallel}$ reversal is illustrated on the right side of Fig. 8.15 and Fig. 8.16, respectively. Note that the x-axis is $-I_p$, so that moving to the right on the abscissa corresponds to progressing time during the ramp-down phase. Delaying the H-L transition causes further significant l_{i3} increase, to about $l_{i3} \approx 6.6$, as well as a more pronounced inversion of the parallel current density. This can be explained by the prolonged duration of the H-mode phase with slower resistive diffusion. Further studies would be required to assess the expected L-H power threshold for the low plasma densities in the late ramp-down phase (under the hypothesis of constant Greenwald fraction). Advancing (in time) the H-L transition allows for faster current diffusion and consequently the l_{i3} increase is lower for most of the ramp-down phase, although the final l_{i3} value is comparable to the value obtained for the default H-L transition timing. In addition, the reversal of $j_{\parallel}$ in the outer plasma region is significantly reduced in this scenario.

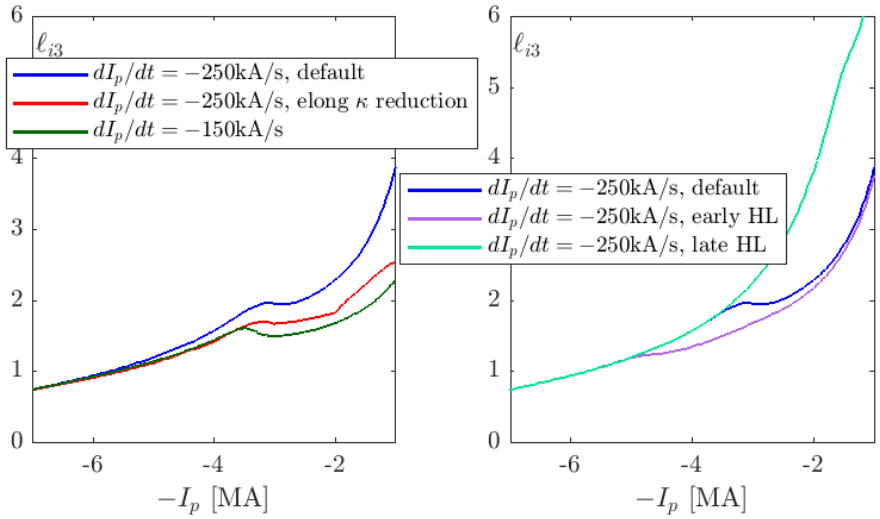

Figure 8.15: (a) Effect of the slower dI_p/dt and the reduction of κ on l_{i3}; (b) Effect of the H-L timing on l_{i3}.

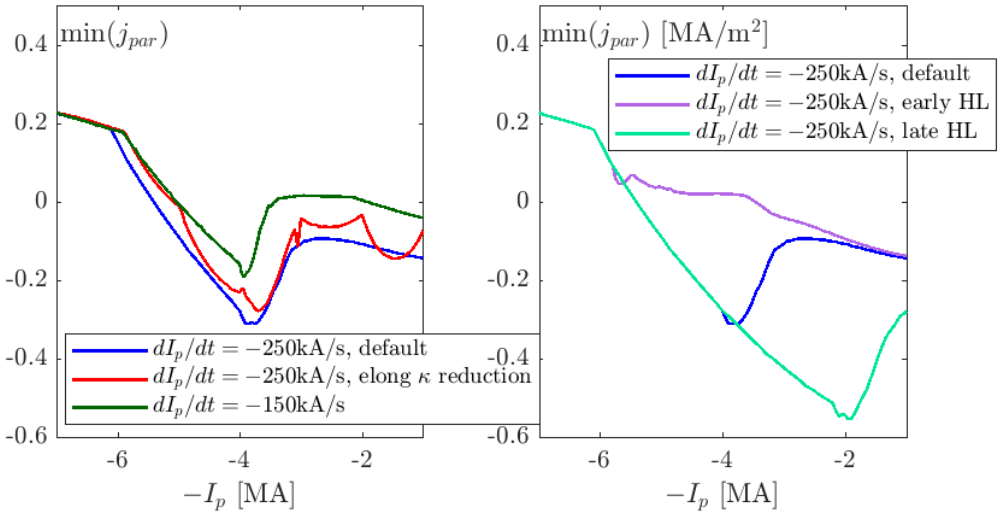

Figure 8.16: (a) Effect of the slower dI_p/dt and the reduction of κ on min($j_\parallel$); (b) Effect of the H-L timing on min($j_\parallel$).

The early H-L transition case shows the most significant peak in impurity radiation power after the H-L transition, since the non-monotonic $L_{imp}(T_e)$ regime is reached while the plasma is at relatively high density. Therefore, P_{aux} = 16 MW needs to be maintained during the initial L-mode phase, in comparison to the P_{aux} = 7 MW for the default and late H-L transition cases. Real-time control of the L-mode power balance, as demonstrated for JET in [19], would increase reliability of such a termination with long L-mode phase and significant heavy impurity content.

Advancing the H-L transition causes a more significant time derivative of β_{pol} during the H-L transition, implying that faster variation of the vertical magnetic field is required in order to maintain tight radial position control and avoid radial excursions of the plasma column. Consistency with the maximum allowable rate of change of the poloidal field coil currents should be assessed. Reducing the plasma current ramp-down rate to dI_p/dt = –150 kA/s leads to a significant reduction of the l_{i3} increase. As shown on the left side of Fig. 8.15, the final value of l_{i3} is about 2.3. Furthermore, as shown in Fig. 8.16, the reversal of $j_\parallel$ is less pronounced for the slower ramp-down, although remaining significant.

Linearly reducing the elongation during ramp-down by adjusting the shape of the LCFS also has a significant mitigating impact on the l_{i3} increase (final $l_{i3} \approx 2.5$), which is consistent with the EU-DEMO simulations reported in [18] and with the ramp-down RAPTOR modelling benchmark against ASDEX Upgrade experimental data described in [20]. Furthermore, the reduction of the elongation leads to a significant increase of the controllability of the vertical position, increasing the maximum value of l_{i3} that can be tolerated. Note that for the proposed reduction of elongation, q_{95} the increase remains monotonic during the full ramp-down.

In summary, it is found that the increase of l_{i3} during ramp-down can be mitigated by slowing down the ramp-down rate to and/or reducing the plasma elongation (and volume) and/or advancing the H-L transition timing. For all performed simulations,

some degree of reversal of the parallel current density in the outer plasma core is observed. Advancing the H-L transition in time can efficiently reduce this effect, by reducing the resistive diffusion time scale at an early stage. Finally, maintaining long L-mode phases with relatively high heavy impurity content likely requires real-time control of power balance. The conclusions drawn here are consistent with previous works for JET, ASDEX Upgrade and EU-DEMO [18-20].

In the future, free boundary equilibrium control calculations could assess the l_{i3} values that maintain vertical stability for different values of elongation, κ and plasma current, I_p, using consistent internal plasma profiles from RAPTOR modelling. These free boundary equilibrium calculations could identify the maximum allowable time derivative $|d\beta_{pol}/dt|$, while considering the maximum tolerated radial position excursion during the H-L transition. Also, it should be possible to identify shape control capabilities to reduce the plasma volume and elongation during ramp-down while meeting the relevant heat exhaust constraints.

8.4: Summary

This study has investigated the stability of BEST during ramp up, flat top and ramp down. During ramp up it is found that late application of heating should help avoid NTMs during L-H transition, though it is noted that electron core heating will be required during L-mode to avoid a radiative collapse, as modelled here for a constant W concentration. Error field correction will be required near the end of the ramping phase of the QCE regime. The requirement of the correction coil current for the worst case is around 30 kAt, which can easily be satisfied with the BEST correction coils system (capacity at 400 kAt). Runaway electrons are expected to appear when the loop voltage exceeds about 12 V. During the end of burn-through, the RE current is at a level of about 0.1 kA, which is much smaller than the plasma current of about 200 kA, indicating that RE are not significant during start-up. Lowering the loop voltage and increasing the pre-fill gas pressure will help suppress the generation of RE currents. If additional heating like ECRF is used in the start-up phase, the loop voltage can be further reduced, which will be significantly beneficial for the avoidance of runaway electrons.

During the high performance flat top phase of $Q \geq 1$ scenarios, it is found that BEST will operate below the no wall beta limit, so that RWM control will not be required. Initial NTM calculations are found to require around 10 MW of unmodulated ECRF to remove an island, though approximately 30 percent less if modulated. More detailed modelling later will clarify the heating and current drive needs. Concerning unmitigated thermal quench (TQ) in BEST, the divertor heat load is found to exhibit $n = 1$ toroidal asymmetry, corresponding to that of the dominant mode in the later phase of the TQ. Such toroidal asymmetry exists on both the inner and the outer target, and manifest as lobe-like features on the divertor plates. The heat flux on the first wall is of the order of 10 MW/m^2, which is relatively safe. Future investigations with more realistic first wall are needed to provide improved quantitative assessment of BEST PFC

heat loads during unmitigated and mitigated disruptions. Nevertheless, given the peak heat loads, it is clear that mitigation during thermal quench for lowering the peak heat flux by one order of magnitude will be required. Runaway electrons generated during BEST disruptions are shown to be controllable by mitigation injection even under the worst-case scenarios.

Concerning safe termination during ramp down, it is important to avoid reversal of the parallel current, and to ensure that the internal inductance does not become too large. It is found that the increase in l_{i3} can be mitigated by slowing down the ramp-down rate, and/or reducing the plasma elongation (and volume), and/or advancing the H-L transition timing. For all performed simulations, some degree of reversal of the parallel current density in the outer plasma core was observed. Advancing the H-L transition in time can efficiently reduce this effect, by reducing the resistive diffusion time scale at an early stage. Finally, maintaining long L-mode phases with relatively high heavy impurity content likely requires real-time control of power balance.

8.5: References

[1] F. Felici et al., *Plasma Phys. Control. Fusion* **54**, 025002 (2012)
[2] F. Felici et al., *Nucl. Fusion* **58**, 096006 (2018)
[3] F. Turco et al., *Nucl. Fusion* **64**, 076048 (2024)
[4] S. Van Mulders et al., *Nucl. Fusion* **64**, 026021 (2024)
[5] D. Fajardo et al., *Nucl. Fusion* **64**, 104001 (2024)
[6] P.C. de Vries et al., *Nucl. Fusion* **65**, 056001 (2025)
[7] X. Li et al., *Nucl. Fusion* **65**, 066017 (2025)
[8] Y. Liu et al., *Phys. Plasmas* **17**, 122502 (2010)
[9] Q.M. Hu et. al., *Phys. Plasmas* **28**, 052505 (2021)
[10] J.P. Graves et. al., *Plasma Phys. Control. Fusion* **61**, 104003 (2019)
[11] N. Hayashi et. al., *Nucl. Fusion* **44**, 477 (2004).
[12] M. Hoelzl et. al., *Nucl. Fusion* **64**, 112016 (2024)
[13] D. Hu et. al., *Nucl. Fusion* **64**, 086005 (2024)
[14] A.H. Boozer, *Phys. Plasmas* **22**, 032504 (2015)
[15] J.R. Martín-Solís et al., *Nucl. Fusion* **57**, 066025 (2017)
[16] V. Bandaru et al., *Phys. Rev. E* **99**, 063317 (2019)
[17] V. Bandaru et al., *Nucl. Fusion* **64**, 076053 (2024)
[18] S. Van Mulders et al., *Plasma Phys. Control. Fusion* **66**, 025007 (2023)
[19] C. Sozzi et al., *28th IAEA Fusion Energy Conference* (2021)
[20] S. Van Mulders et al. *Plasma Phys. Control. Fusion* **66**, 025006 (2023)

Chapter 9: Energetic Particles

Coordinators: R. Coelho (IST-Lisbon, Portugal), G.Q. Li (ASIPP)

With contributions from:
ASIPP Team: T.Y. Xia, Z.Y. Qiu, Y.J. Hu, W. Shen, Y.F. Zheng, W. Zhang, J. Huang, M. Xu
EUROfusion Team: M. Falessi (ENEA, Italy)

9.1: Introduction

The confinement and behaviour of Energetic Particles (EPs), such as fusion-born alpha particles and ions generated by auxiliary heating systems, are critical to the performance and stability of magnetic confinement fusion devices [1]. As scientific achievements are progressing in fusion research and new record values in fusion power, plasma temperatures, confinement times and discharge duration have been established, fusion-born alpha particles and other fast ions play critical roles in the fusion performance which go way beyond the simple paradigm of energy transfer to the bulk thermal plasma. Indeed, EPs can play not only a pivotal role in the mitigation of plasma turbulence [2], but also drive numerous types of meso-scale or global kinetic-MHD plasma perturbations unstable e.g. Fishbones [3], Toroidal Alfvén Eigenmodes (TAEs) [4] or Energetic Particle Modes (EPMs) [5]. The growth and saturation of such modes can potentially lead to the redistribution/diffusion of the EPs away from the plasma core and eventual expulsion from the plasma, thus effectively hampering the continuous energy transfer to the main plasma and consequently requiring high external heating to achieve the targeted plasma discharge scenarios.

The BEST device is in a privileged position for energetic particle physics studies in the landscape of fusion devices considering its operational design specifications (see Chapters 1 and 2) and vast pool of external heating and current drive actuators (see Chapter 5). Targeting long-pulse (at least >100sec) operation at fusion $Q \geq 1$ translates to alpha powers $P_\alpha \geq 20\%$ of the external input power which is a very significant increase over the current best results from JET tokamak ($Q \approx 0.25$ averaged over 5 s with a metallic wall [6]). The long-pulse operation of BEST at $Q \geq 1$ will, for the first time, allow for comprehensive studies of alpha particle mediated phenomena e.g. confinement and transport, MHD stability and wall loads over long time scales and provide useful insight to be accounted for in preparation for CFEDR. Equipped with all consolidated heating schemes adopted so far in fusion devices, in BEST operational scenarios up to 50MW of input auxiliary power is anticipated, split over NBI, IC, LH and EC. With versatile ICRF minority heating schemes including 3-ion schemes [7] and an NBI launcher in D-T operation, a significant fraction of energetic particles ($\beta_{fast}(0)/\beta_{th}(0) \approx 0.15$) with significant high energy tails is expected beyond alphas ($\beta_\alpha(0)/\beta_{th}(0) \geq 0.28$) and their contribution/impact on the overall plasma behaviour should be accounted for.

In the following sections some key research topics related to energetic particles on BEST will be briefly addressed. Firstly, the confinement and loss figures of merit of energetic particles on BEST will be discussed focusing, at this preliminary stage, on alpha particles. Although BEST plasma current can top 7MA, this still yields roughly twice the normalized drift orbit width for alpha particles when compared to ITER while other MeV class energetic particles might have closer normalised widths. However, magnetic ripple might play a role in EP confinement since BEST features only 16 TF coils contrary to ITER's 18. Estimating loss fractions and heat loads from alphas is thus essential. Secondly, considering both the fast hydrogenic ion species from auxiliary heating and alphas particle from D-T fusion reactions, highly energetic ions with $v_{EP}/v_A > 1$ are largely anticipated and one can expect the excitation of several AEs such as Toroidal Alfvén Eigenmodes (TAEs), Ellipticity-induced Alfvén Eigenmodes (EAEs), Reversed Shear Alfven Eigenmodes (RSAEs) in case of advanced scenarios as well as higher frequency modes like Compressional Alfvén Eigenmodes (CAEs), Global Alfvén Eigenmodes (GAEs) and lower frequency modes like (Beta-induced Alfvén Eigenmodes) BAEs and fishbones [1]. Estimating saturation levels of such instabilities, if any, will be of utmost importance while considering the overall power and particle balance involving the energetic particle population and the thermal plasma. Lastly, some considerations on the synergies and joint activities in the area of diagnostics related to energetic particles are made. Diagnostics will play a pivotal role in the understanding of burning plasma evolution and the complex plasma phenomena fuelled by and characteristic of energetic particles calls for a close collaboration between theory, modelling and diagnostic data interpretation and forward modelling.

9.2: Energetic-particle confinement

Achieving high fusion gain, Q in future fusion devices largely relies on the confinement of energetic alpha particles generated by fusion reaction and understanding it is therefore a long-standing goal in the fusion research programme [8]. Energetic ions are prone to redistribution and radial loss due to both classical orbit diffusion-like phenomena e.g. first-orbit loss, ripple but also magnetohydrodynamics (MHD) activity e.g. sawteeth, neoclassical tearing modes (NTMs) and Alfvén eigenmodes (AEs). This may deteriorate the plasma self-heating and, most importantly, potentially lead to localized heating of plasma-facing structure.

BEST features 16 TF coils and an early estimation of prompt and ripple induced losses of alpha particles is of utmost importance. The use of discrete set of coils to generate the toroidal magnetic field in a tokamak causes the field strength to vary slightly in the toroidal direction at given R and Z coordinates. This variation, designated TF 'ripple', breaks the axisymmetry of the toroidal field and can cause radial transport and loss of energetic ions [9]. Since the ripple amplitude is a proxy for ripple transport and is a function of the number of TF coils and their size relative to the plasma, it is essential to calculate both the nominal ripple amplitude in BEST but also investigate to what extent ferritic inserts in the vessel could reduce the ripple amplitude similarly to what was done for ITER [10]. Such calculations are shown in Fig. 9.1, where the magnetic field normalised amplitude $\delta(R, Z) = (B_{max} - B_{min})/(B_{max} + B_{min})$ is shown for the $Q \geq 1$ scenario at $I_p = 7$ MA (see Chapter 4), as a reference.

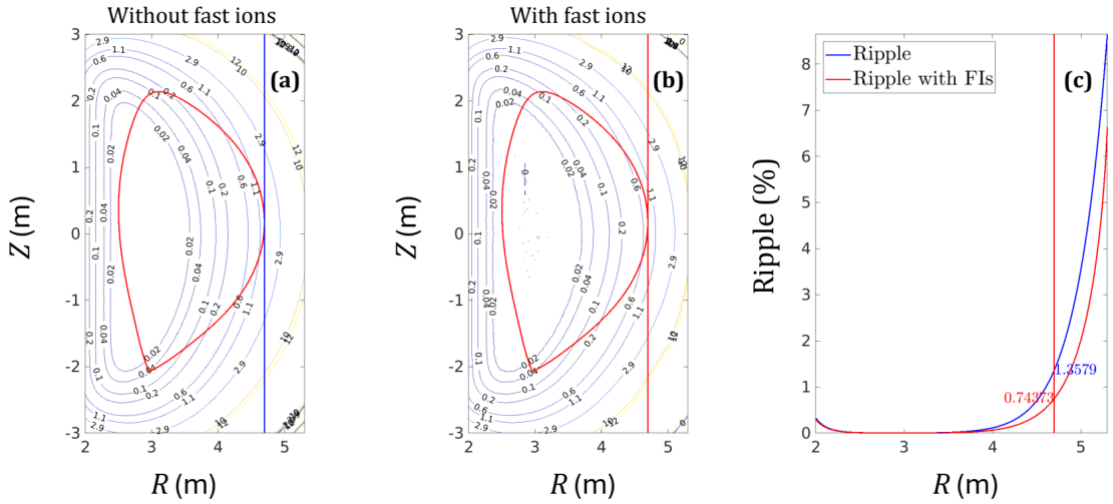

Figure 9.1: Distribution of the toroidal field ripple in BEST with ferromagnetic inserts of 500 mm thickness. The inserts effectively reduce the ripple amplitude across the plasma region.

In order to gain further insight on the prompt and ripple-induced alpha losses in this scenario, independent calculations using TGCO and ASCOT codes were carried out. The modelling shows that the alpha particle flux to the wall increases, on average, from ~1.3% to ~5.7% when considering ripple. The majority of the losses are prompt losses. When adding ferritic inserts (only done with TGCO code), there is an improvement, as shown in Fig. 9.2(a). Ripple also leads to an increase in alpha power loss, from ~0.8% without ripple to ~3.3% with ripple. As for particle flux, ferritic inserts lead also to a reduction in the power loss, see Fig. 9.2(b). In this analysis, the influence of ferritic materials in the TBMs on the effective ripple map has not been included [11] and this effect will be assessed in the future.

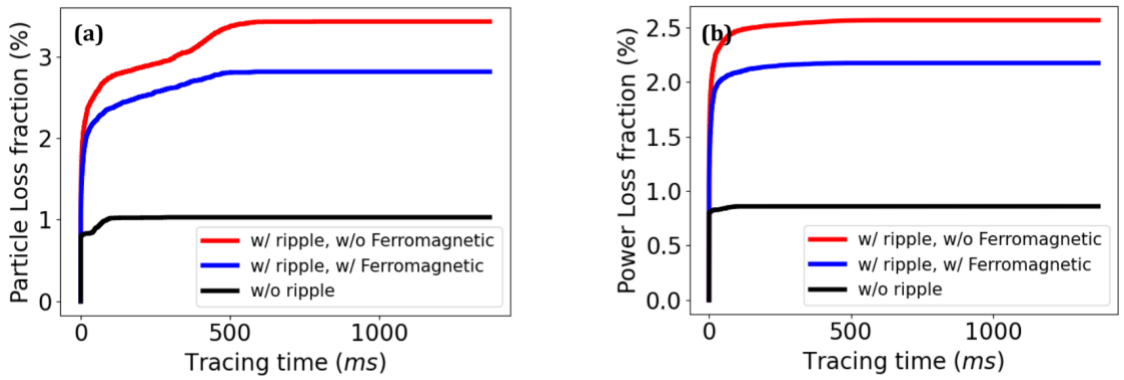

Figure 9.2: Comparison of alpha particle flux (a) and power loss (b) for the $Q \geq 1$ scenario at I_p = 7MA, with and without toroidal field ripple. The application of ferritic inserts leads to an approximate 18% reduction in alpha particle losses.

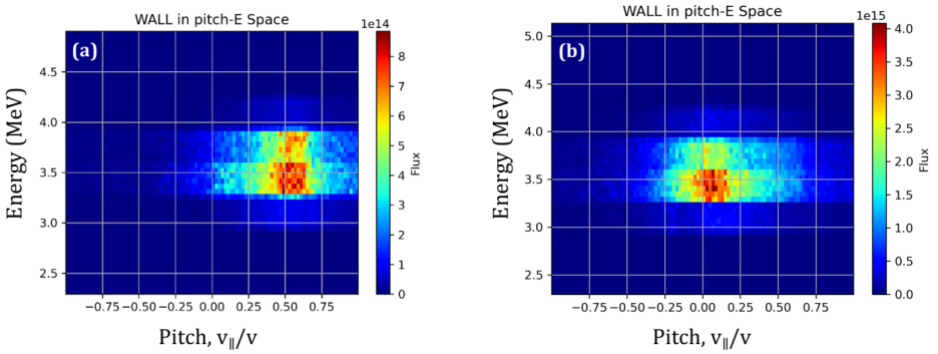

Figure 9.3: ASCOT simulations of energy and pitch-angle distributions of lost alpha particles in the $Q \geq 1$ scenario at I_p = 7MA, without (a) and with (b) field ripple.

While in the case of no ripple the alpha losses stem from counter passing and trapped particles born at the outer regions of the plasma, taking into consideration ripple strongly enhances the trapped particle losses (see Fig. 9.3). As anticipated, with ripple the fraction of losses from alphas born deeper inside the plasma core (exiting the plasma at low energy) increases but most of the losses still stem from alphas born at the outer regions of the plasma (see Fig. 9.4) and with final energy difference from their birth energy of less than ~100keV. In terms of the peak power loads at the first wall, while TGCO estimates ~0.3 MW/m^2, in ASCOT it drops to ~0.1 MW/m^2 and this difference will be further investigated.

When considering finite orbit effects, ASCOT estimates an increase of 50% in power loss and 22% in particle loss. This is somewhat expected considering the small separation between the plasma boundary and the first wall on both the high-field and low-field sides and, consequently, that's where finite orbit enhanced losses are observed (see Fig. 9.5). Lastly, it is worth mentioning that magnetic ripple has just a minor incremental impact on the confined alpha profile since alpha pressure on axis decreases by ~12% when comparing no-ripple to ripple with full gyro orbits.

The analysis so far addressed only collisional and ripple induced alpha losses and should be extended to include other potential sources of non-resonant alpha redistribution or losses namely sawteeth and other macroscopic MHD instabilities which could enhance the ripple induce losses.

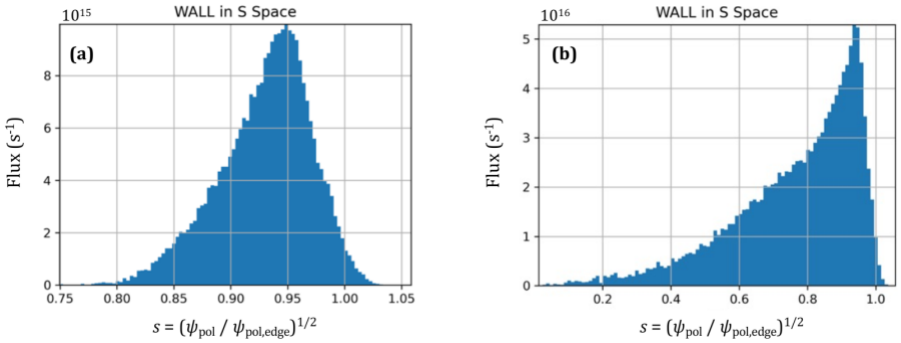

Figure 9.4: Simulated histogram of alpha particle losses to the wall in the $Q \geq 1$ scenario at I_p = 7MA, obtained with ASCOT. The losses are plotted versus the radial coordinate, $s = (\psi_{pol} / \psi_{pol,edge})^{1/2}$ for cases without (a) and with toroidal field ripple (b).

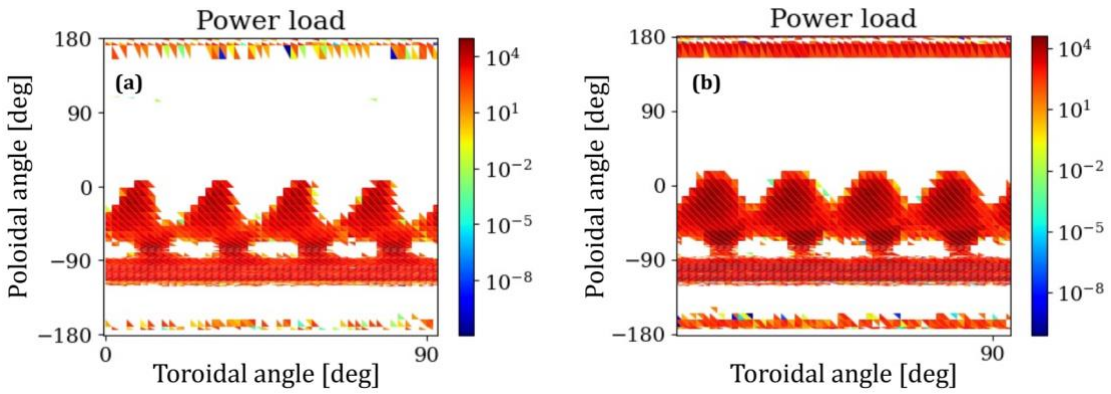

Figure 9.5: Power loads of alpha particles lost to the first wall in the $Q \geq 1$ scenario at I_p = 7MA, simulated with ASCOT. Results are shown for cases with magnetic ripple, using guiding-center approximation (a) and full-orbit simulations (b). Hybrid mode was applied for the full-orbit simulation.

9.3: Modelling of EP-driven modes

BEST is in a privileged position to consolidate and further extend the knowledge of fast-ion-driven instabilities since it will include for the first time a considerable number of alpha particles at relative pressures to the main plasma at much higher levels than previous devices such as JET. Since the relevant ratio determining the overall magnitude of the AE drive is β_α/β_{th} (bulk ion Landau damping scales with β_{th}), it is instructive to get estimates of indicative numbers for JET, BEST and ITER.

Comparing indicative numbers, while at JET $\beta_\alpha/\beta_{th} \approx 0.15$ for the record fusion energy experiments in tritium-rich plasmas at $n_e \approx 10^{20}$ m^{-3} and $T_i \approx 9$ keV [12], the transport modelling for the $Q \geq 1$ D-T = 50%-50% scenario at I_p = 7MA for BEST predicts $\beta_\alpha/\beta_{th} \approx 0.28$, at comparable density $n_e \approx 10^{20}$ m^{-3} and higher $T_i \approx 21$ keV (see Chapter 4). For reference, ITER 15MA scenario is estimated to operate at $\beta_\alpha/\beta_{th} \approx 0.26$ [13]. Therefore, alpha stability conditions at BEST maybe similar to the conditions in ITER. Furthermore, the alpha particle population with densities of the order of $n_\alpha \approx$ 7-8×10^{17} m^{-3} may potentially be sufficient to drive some AEs more readily than observed in the JET D-T campaigns [14]. Should significant alpha particle redistribution or losses occur, given that the alpha power alone is ~25% of the external heating power, some effect on the overall kinetic plasma profiles and figures of merit e.g. neutron yield, stored energy, may become noticeable. This suggests AE stability, saturation levels and resulting alpha redistribution should be taken self-consistently into account in the plasma transport evolution.

In order to gain some insight on the potential AEs which could become unstable in BEST, a preliminary analysis was performed considering the Q = 1 scenario at 7MA as well as the quasi-continuous exhaust (QCE) variant. In practical terms the QCE features a ~3% lower ion temperature and a ~1.5% higher plasma density in the core (see Chapter 4). The implications of the differences in the two scenarios on the spectra of gap modes (TAE, EAE,…) are small, as shown in Fig. 9.6.

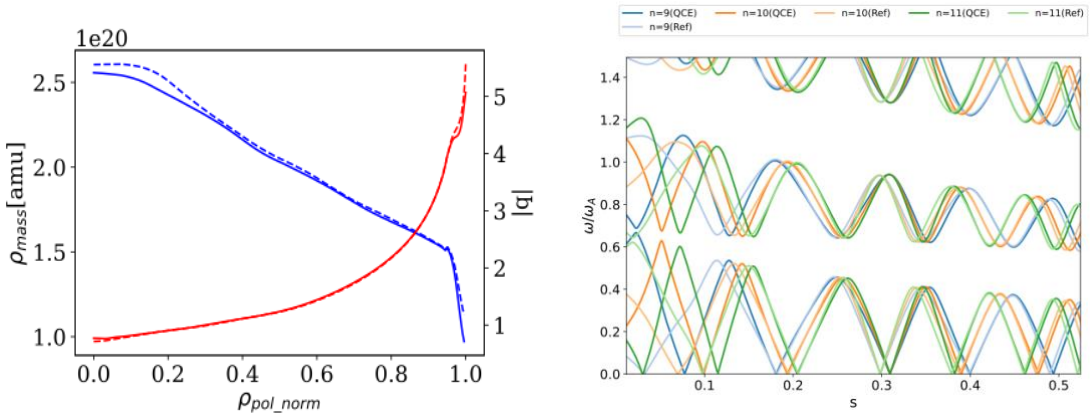

Figure 9.6: (a) Comparison of the mass density and q-profile for the reference (solid lines) and the QCE-like (dashed lines) $Q \geq 1$ scenarios at $I_p = 7$MA. (b) Continuum spectra for toroidal mode numbers $n = 9$, 10 and 11 for the two scenarios.

As anticipated from Fig. 9.6, at the plasma core ($s < 0.2$) it is unlikely that any TAEs will be not strongly damped by the continuum. On the contrary, at the EAE gap there are clearly gaps close to the maximum radial gradient $d\beta_\alpha/dr$ at s ≈ 0.2-0.3. TAEs might be expected at $s > 0.3$, although continuum crossing closer to the pedestal region is also unavoidable. Preliminary analysis using the CASTOR-K code [15] reveal that, when accounting only for thermal ion landau damping from D and T ions and alpha particle drive, only the EAEs, located within the radial region $0.1 < s < 0.3$ are unstable, as observed in Fig. 9.7.

Thermal ion Landau damping stabilises TAE completely ($v_{th}/v_A \sim 1/6$) and thus other damping mechanisms such as trapped electron collisional damping as well as radiative/continuum damping would just make the modes more stable. On the other hand, for EAEs thermal ion damping is not enough to overcome the drive from alphas and, despite the relatively narrow mode structure, the mode frequency is always closer to the upper end of their continuum gap thus minimising the effect of radiative damping. Following analytical formula, suggesting that the optimal power transfer occurs when the drift orbit width of a resonant passing alpha-particle is comparable to the mode width, a range of toroidal mode numbers between $n = 7$ and $n = 12$ was estimated, in reasonable agreement with the modelling results.

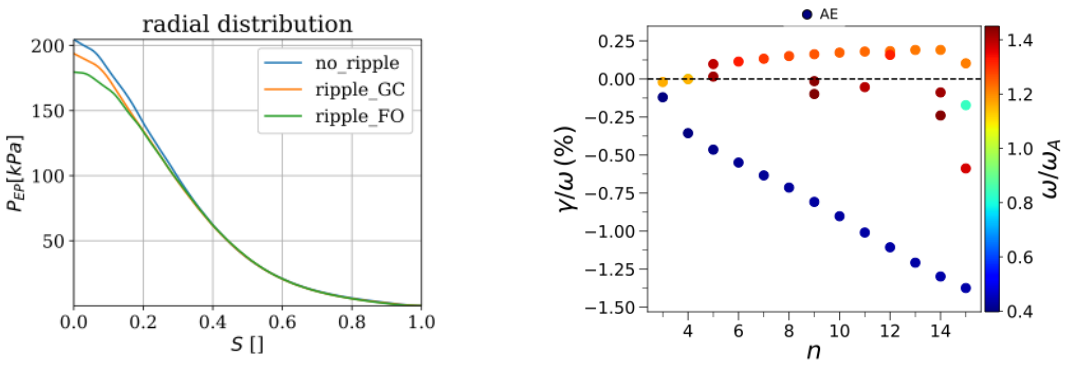

Figure 9.7: Alpha-particle pressure (a) and the normalized growth rates of EAE and TAE modes (b) for the reference $Q = 1$ scenario at $I_p = 7$ MA.

The analysis done so far is just a first step towards a much more detailed modelling effort. On one hand, uncertainty quantification of the stability estimates dependence on the equilibria is suggested considering that the core gap mode's location is sensitive to the q-profile and thus local alpha and thermal pressure gradients will vary. Both the standard baseline and QCE scenario variants (see Fig. 9.6) should be considered for such analysis. On another hand, the mode analysis should also address lower frequency BAEs and higher frequency CAEs and potentially EPMs. Investigating BAEs is particularly relevant for BEST since these modes may be driven unstable not only by energetic ions but also by energetic electrons and even tearing modes [16] when non-linear mode coupling between tearing modes (above a given threshold) and BAE pairs within the island region excite GAMs. In support for ITER, numerical modelling at slightly elevated and reversed q-profile at 9MA evidenced that, despite not necessarily with higher growth rate than TAEs, BAEs may evolve non-linearly to higher amplitude [17] and cause higher energetic particle transport. Also worth considering, EP excited BAE may lead to large electron heat fluxes [18] and this should be accounted for when analyzing in detail the overall mechanisms ruling plasma transport in BEST (see Chapter 4). Considering the several EP actuators featured in BEST, it is crucial to investigate whether the anticipated wave and beam power deposition profiles contribute overall to the mitigation or destabilization of BAEs and if potentially synergistic effects with other AEs are anticipated on the scenario which could be detrimental for alpha confinement.

To consolidate the linear stability analysis of AEs, several other key steps are worth considering. First, alphas are not the only potential pool of energetic particles on BEST which may assist mode drive. Energetic populations from NBI and ICRH ought to be considered as potential additional players on AE stability and their effect should be quantified. ICRH generated EP populations, in particular, would also be particularly relevant in the context of fishbones as currently the $Q = 1$ baseline and QCE scenarios at 7MA feature an on-axis safety factor $|q_0| < 1$ and fishbones could easily be destabilized by the MeV-range ions from ICRH and experimental evidence suggest they are easily prone to enhance fast ion losses. NBI on the other hand especially at high energies as provided by the N-NBI system, could potentially play a stabilizing role on RWM stability and should therefore be investigated. Close collaboration with the Topical Group "MHD, Control and Disruptions" is envisaged (see Chapter 8). Secondly, other mode damping mechanisms beyond ion Landau damping need to be considered. This includes not only accounting for Helium ash or other impurities but also considering mechanisms such as trapped electron collisional damping as well as radiative/continuum damping. Lastly, benchmarking the linear growth rate of some of the pool of potentially unstable AEs against gyro-kinetic calculations is envisaged to validate the prior estimates using the lower fidelity codes.

In addition, in a broader context beyond linear stability, the saturation mechanisms and levels of the potential destabilized modes should be investigated since it could greatly impact overall plasma transport. This calls for both MHD and gyro-kinetic modelling on the non-linear evolution of the pool of EP driven unstable modes

identified beforehand to get a deeper understanding of the relevant mechanisms at play e.g. wave-particle and wave-wave mechanisms. The latter appears quite relevant for a reactor scale device such as BEST where the alphas drift orbits are reasonably smaller than the plasma minor radius (although not at the level of ITER). The relevance of the generation of zonal structures (flows and currents) as well as the non-linear evolution of AEs via ion-induced scattering [19] as saturation mechanisms should be assessed and, potentially, accounted for when addressing the alpha particle lifecycle, transport and power balance and, in particular, alpha channeling [20]. BEST is in a privileged position to explore the possible wave mechanisms, either driven by the external actuators or by the plasma response e.g. three-wave mode coupling involving counter-propagating AEs [19], whereby a significant portion of the alpha energy may be channeled to the main ions instead of the electrons. This major endeavor, in the long term, calls for a self-consistent modelling of the EP transport and discharge evolution, ideally encompassing all EP species e.g. alphas and hot fast-ion tails from ICRH, and should be done in close collaboration with *Theory and Modelling* activities in BEST.

Lastly, the next-step analysis should also address $Q \approx 5$ plasma scenarios, where the contribution of alpha heating power becomes more relevant, and an electron dominated heating regime is expected to prevail. Finding strategies to mitigate plasma turbulence, potentially favoring the onset and sustainment of internal transport barriers, becomes critical to allow for fusion-grade ion temperature of the order 15-20 keV. Energetic particles, and alpha particles in particular, can contribute to the regulation of turbulence in several ways as increasing experimental evidence over the past few years has shown [21-24] e.g. through sheared zonal flows generated by EP driven instabilities such as TAEs [20] and fishbones [25]. As TAEs, fishbones and other EP-driven modes can also enhance the energetic particle transport, the final state depends on a delicate balance between different, competing effects. Predicting the actual EP-driven mode stability, the efficiency of turbulence mitigation and the anomalous heating due to kinetic damping of resonant modes is of utmost relevance and BEST scenarios with $Q > 1$ will offer first-of-a-kind experimental conditions to validate ongoing research on higher fidelity transport models and full discharge transport simulators.

9.4: Development of dedicated diagnostics for EP-physics studies

Considering the crucial role energetic particles will play in most topical research areas of BEST, the machine must be equipped with a comprehensive set of diagnostics capable not only of identifying all energetic particle-mediated phenomena, but also of characterising the phase-space properties and time evolution of the energetic particle population. This includes determining the birth profiles in both physical and velocity space, tracking their evolution throughout the slowing-down process, and analysing lost particles – specifically, their velocity-space characteristics (parallel and perpendicular components) and their spatial origin within the plasma.

There are several diagnostics where energetic particle modelling activities can and should be promoted (see Chapter 12). On Faraday cup systems, a detailed map of unconfined fast ion orbits is required to estimate and validate the diagnostic response dependence on fast ion energy and pitch. Building on the alpha and fast ion simulation databases developed for alpha confinement and energetic particle driven modes, support to validation activities should be promoted. Although no FILD diagnostics is foreseen for BEST considering the large neutron fluence foreseen [26] (comparable though not as high as ITER), in case some feasibility studies are deemed useful supporting modelling activities should be carried out along the same lines as for the Faraday cups. Collective Thomson Scattering (CTS) is likely by far the most instrumental diagnostic at BEST to be able to characterise fast ion phase space (spatial and velocity) considering that Fast Ion D-Alpha won't be available owing to large bremsstrahlung and likely low neutral beam neutral flux. If the latter would be available much better-quality tomographic reconstruction of fast ions e.g. alphas could be attempted (see [27]). However, CTS alone might fall short to enable accurate enough tomographic reconstructions which could be used to track the distribution function of fast ions over time. Combined methods using other diagnostics would be needed using, for instance, Gamma Ray Spectroscopy (GRS) which is included in BEST. Numerical modelling using wither ICRH + NBI codes as well as hybrid MHD-kinetic/gyro-kinetic codes could assist on the interpretation by validating eventual prior information to be included in the reconstructions e.g. slowing down [27] or wave-particle priors [28].

9.5: References

[1] M. Salewski et al., *Nucl. Fusion* **65**, 043002 (2025)
[2] J. Citrin et al., *Plasma Phys. Control. Fusion* **65**, 033001 (2023)
[3] L. Chen et al., *Phys. Rev. Lett.* **52**, 1122 (1984)
[4] Y. Todo, *Rev. Modern Plasma Phys.* **3**, 39 (2019)
[5] L. Chen et al., *Nucl. Fusion* **47**, S727 (2007)
[6] C.F. Maggi et al., *Nucl. Fusion* **64**, 112012 (2024)
[7] Ye.O. Kazakov et al., *Nat. Phys.* **13**, 973 (2017)
[8] N.N. Gorelenkov et al., *Nucl. Fusion* **54,** 125001 (2014)
[9] R.J. Goldston et al., *Phys. Rev. Lett.* **47**, 647 (1981)
[10] K. Tobita et al., *Plasma Phys. Control. Fusion* **45**, 133 (2003)
[11] G. J. Kramer et al., *22nd IAEA Fusion Energy Conference* (2008)
[12] Ž. Štancar et al., *Nucl. Fusion* **63**, 126058 (2023)
[13] P. Mantica et al., *Plasma Phys. Control. Fusion* **62,** 014021 (2020)
[14] M. Fitzgerald et al., *Nucl. Fusion* **63**, 112006 (2023)
[15] D. Borba et al., *Journal of Computational Physics* **153**, 101 (1999)
[16] W.W. Heidbrink et al., *Nucl. Fusion* **61**, 066031(2021)
[17] Y. Todo et al., *Plasma Fus. Res.* **9**, 3403068 (2014)
[18] A. Biancalani et al., *Plasma Phys. Control. Fusion* **63**, 065009 (2021)
[19] Z. Qiu et al., *Rev. Mod. Plasma Phys.* **7**, 28 (2023)

[20] N.J. Fisch, *AIP Conference Proceedings* **1689**, 020001 (2015)
[21] S. Mazzi et al., *Nat. Phys.* **18**, 776 (2022)
[22] J. Garcia et al., *Nature Comm.* **15**, 7846 (2024)
[23] A. Di Siena et al., *Nucl. Fusion* **65**, 086019 (2025)
[24] J. Ruiz Ruiz et al., *Phys. Rev. Lett.* **134**, 095103 (2025)
[25] G. Brochard et al., *Phys. Rev. Lett.* **132**, 075101 (2024)
[26] O. Putignano et al., *Fusion Eng. Design* **173**, 112913 (2021)
[27] B. Madsen et al., *Plasma Phys. Control. Fusion* **62**, 115019 (2020)
[28] M. Rud et al., *Nucl. Fusion* **65**, 056008 (2025)

Chapter 10: Theory and Simulations

Coordinators: M. Falessi (ENEA, Italy), T.Y. Xia (ASIPP)

With contributions from:
ASIPP Team: Z.Y. Qiu, L. Ye, H.H. Wang, S. Gu, Y.L. Li, H.M. Qi
EUROfusion Team: F. Zonca (ENEA, Italy)

10.1: Introduction

Theory development enabling predictive simulations of burning plasma dynamics is a key requirement for designing next-generation fusion reactors. To advance in this field, it is important to derive and validate transport models that account for a significant fraction of heating power originating from alpha particles. For this reason, burning plasma physics is one of the scientific missions of BEST. This task is inherently difficult since it requires an integrated analysis of multiple aspects (see, e.g., the discussion in [1]). In particular, the energetic particle (EP) distribution function should be evolved on the same footing as the thermal populations, as EPs may influence transport processes and plasma self-organization.

Edge physics is another important field for BEST scenario design, including predictive pedestal and edge instability modelling. This is particularly relevant for BEST since Type-I ELM will be intolerable for the first walls and divertor targets. Therefore, theoretical development is necessary for accurate descriptions of pedestal and ELM control. The validation of models in current facilities is important, and evaluating the extrapolation of these models to BEST is crucial.

The accurate modelling of core-edge coupling presents significant challenges under the low-collisionality, high-density conditions expected in reactor-relevant plasmas. While traditional edge simulations have relied on reduced fluid models with Braginskii-type collisional closures, the extreme conditions anticipated in next-generation devices like ITER, BEST, and DTT demand more sophisticated approaches, particularly near the separatrix where magnetic topology changes dramatically. Gyrokinetic theory is being extended to address pedestal and edge physics, though this extension faces considerable challenges due to steep gradients and nonlinear collisional effects. The complex nature of electromagnetic fluctuations in the scrape-off layer (SOL) and various microinstabilities – including microtearing, whistler, and lower-hybrid modes – suggests the need for hybrid modelling approaches that combine gyrokinetic electrons with fully kinetic ion treatments. Furthermore, energetic particle transport, particularly from supra-thermal alpha particles, introduces additional complexity by influencing both core-edge transport dynamics and divertor operations. In this context, the expression “extreme conditions” at the plasma edge of next-generation devices generally refers to the simultaneous presence of high plasma density and low collisionality regimes, where the physics of power and particle exhaust (PPEX) becomes a dominant factor. These regimes are intrinsically associated with the

onset of detached plasma conditions, which are indispensable for protecting plasma-facing components under reactor-relevant loads. A central quantity in this regard is the power-handling figure of merit, P/R, whose values are expected to approach or even exceed the threshold of ~15 MW/m, a characteristic benchmark for reactor-grade plasma operation. The interplay between high-density operation, efficient detachment control, and robust exhaust handling will therefore represent a decisive aspect of the edge physics program in BEST (see Chapter 6) and related facilities, shaping both their operational flexibility and their extrapolation capability towards fusion power plant scenarios.

Consistently, the EAST tokamak plays a pivotal role as a test bed for validating theoretical models and developing predictive capabilities for BEST operations. By conducting theory-guided experiments on EAST, researchers can systematically validate fundamental physics-driven models under conditions that partially replicate BEST-relevant scenarios. This synergy between EAST experiments and theoretical developments is crucial for building robust and reliable predictive tools that can accurately forecast plasma behavior in BEST. Such validation exercises are essential for establishing confidence in the theoretical frameworks that will ultimately guide BEST operations and contribute to the broader understanding of burning plasma physics.

In the following chapter, we first briefly define the concept of reactor-relevant plasma using dimensionless analysis (see, e.g., [2]) and demonstrate that BEST will operate as a reactor-relevant plasma using D-T fuel, thus allowing the study of burning plasma physics relevant to machines like ITER and CFEDR. We then outline the main differences from present-day analyses that must be addressed to enable predictive simulations and introduce a general theory for transport processes in burning plasmas. Next, we describe the important challenges associated with edge physics. Finally, we emphasize the importance of integrating theory, experiments, and simulations.

10.2: Physics of burning plasmas

BEST plasmas can be showna posteriori to follow a weak Kadomtsev scaling based on the ITER 15MA reference scenario, see, e.g., [1, 2]. Following Ref. [1], we refer to all these plasmas, connected by a proper rescaling operation, as reactor-relevant plasmas. By construction, all reactor-relevant plasmas share the same values of β and ν^* as ITER, while their ρ^* values are rescaled, i.e., $\rho^* R^{\varepsilon}$, where the value of ε defines the family of similar equilibria.

Applying the weak Kadomtsev scaling, we get the following relations: $n \sim R^{2\varepsilon - 2}$, $T \sim R^{\varepsilon - 1/2}$, $B \sim R^{3\varepsilon/2 - 5/4}$. As described in detail in [2], the scaling introduces an order relation within machines characterized by similar fundamental plasma physics processes, and the value of ε can be considered a performance indicator, i.e., Tokamaks with lower ε are "closer" to ITER in terms of underlying physics. Besides having a relatively low value of ε the BEST tokamak will operate in D-T eliminating the need to mimic the behavior of EPs through auxiliary heating systems. For this reason, it can be considered a burning plasma experiment in all respects. It is worth emphasizing that present-day devices typically operate at values of ε larger than that

envisaged for BEST. For example, both JET and ASDEX are characterized by $\varepsilon \approx 1$. This choice places BEST on an ambitious trajectory towards reactor-relevant configurations marking it as a step along the pathway to the realization of a fusion power plant. If one applies the weak Kadomtsev scaling in a straightforward manner, the value of β predicted for BEST turns out to be smaller than the rescaled value inferred from ITER. This observation should not be interpreted as a limitation of the weak scaling argument. Rather, it is suggestive that BEST could accommodate additional auxiliary heating, thereby enhancing its performance within established physics scenarios, or alternatively, that it might serve as a platform to explore improved regimes by experimentally accessing new operational conditions. Crucially, this potential flexibility could be exploited without encountering prohibitive stability limits, thus reinforcing the strategic role of BEST as a stepping stone towards future burning plasma devices and ultimately fusion power plants.

This aligns well with BEST's strategic positioning in the ASIPP fusion strategy, as evidenced by its carefully chosen machine parameters and missions. As a bridge between ITER and CFEDR, BEST's compact high-field design offers a unique opportunity to study burning plasma physics at a more manageable scale while still maintaining relevant physics processes. BEST's timeline strategically overlaps with ITER's key operational phases, allowing for parallel learning and optimization of plasma control strategies. This timing, combined with BEST's integration into China's broader fusion research infrastructure alongside CRAFT and EAST, positions it as a crucial stepping stone in the development of fusion energy technology.

The importance of the weak similarity approach lies in its ability to address the challenge of extrapolating results of reactor-relevant plasmas, given their self-organized nature. In burning plasmas, energetic particles, turbulent fluctuations, and macroscopic equilibria can be coupled in a non-trivial way, making it difficult to construct a scaled experiment that preserves all spatiotemporal scale orderings. Under these conditions, it has been shown [3] both analytically and numerically that energetic particles play a central role in influencing plasma dynamics. They resonate with collective modes such as Alfvén eigenmodes, driving or damping instabilities depending on their distribution function. They act as mediators across spatiotemporal scales by generating mesoscale Alfvénic modes, whose characteristic scales bridge the gap between micro-turbulence and macroscopic equilibrium. These modes can excite continuum resonances, propagate energy radially, and modify transport through the formation of zonal electromagnetic fields and solitons [4-7]. As a result, EPs can significantly affect the turbulence saturation level and, more broadly, transport processes. This makes these studies challenging in present devices and calls for a conceptual change in the adopted approach. Particular attention is required for the characterization of the EPs distribution function, zonal flows, and zonal fields. These can be generated by various nonlinear processes that may or may not involve the EP population [8]. Their accurate description is essential for predicting and controlling plasma performance and requires a self-consistent treatment that captures the different spatiotemporal scales arising from the dynamics in realistic equilibria, spatial non-uniformity, and kinetic effects. Experiments on BEST should be designed to

characterize this physics and support the development of reduced analytical models describing their dynamics, which can then be validated against first-principle-based, global, electromagnetic gyrokinetic or hybrid simulations.

10.3: Transport theory for burning plasmas

Following the motivations described in the previous section, accurately modelling transport in burning plasmas requires the description of processes occurring on spatiotemporal scales that may differ significantly from those of background transport. These processes often need to be described in phase space due to the important role of wave-particle resonant interaction. For this reason, high-fidelity numerical frameworks, such as nonlinear gyrokinetic simulations, are typically used. One possible approach to reduce their high computational cost and complexity is the use of the local flux-tube approximation. However, this approximation must be applied carefully, as it may not capture non-local behavior associated with, for example, the formation of zonal electromagnetic fields and EP physics in general.

Theoretical advancements in recent years have led to the development of a phase-space zonal structure (PSZS) transport theory, which enables a self-consistent description of the slow evolution of the equilibrium distribution function of EPs in the presence of weak collisions, external sources, and nonlinear interactions. This approach effectively extends GK simulations of burning plasmas over transport time scales. Following Ref. [9], PSZSs are obtained through a two-step averaging procedure: first, averaging along guiding-center equilibrium orbits; second, applying a filter to remove fast spatiotemporal variations on the characteristic particle orbit length scale and/or the hydrodynamic time scale. As a result, PSZS are not damped by collisionless dissipation processes and depend only on the equilibrium invariants of motion, which can be used as coordinates in phase space to describe transport processes, namely, the particle energy per unit mass $\mathcal{E} = v^2/2$, the magnetic moment $\mu \sim v_\perp^2/2B$, and the toroidal component of the canonical angular momentum P_ϕ. The governing equation for the PSZS is:

$$\frac{\partial}{\partial t}\overline{F_0}^{(\mathrm{O})} + \frac{1}{\tau_b}\left[\frac{\partial}{\partial P_\phi}\overline{\left(\tau_b \delta\dot{P}_\phi \delta F\right)_z}^{(\mathrm{O})} + \frac{\partial}{\partial \mathcal{E}}\overline{\left(\tau_b \delta\dot{\mathcal{E}} \delta F\right)_z}^{(\mathrm{O})}\right]_S = \overline{C^g}_S^{(\mathrm{O})} + \overline{S}_S^{(\mathrm{O})}$$

where $[\dots]_S$ denotes an appropriate spatiotemporal averaging [9], while the overbar indicates an average along unperturbed equilibrium orbits, τ_b is the bounce time characterizing particle motion in the self-consistently evolving equilibrium magnetic field, $\delta\dot{P}_\phi$ and $\delta\dot{\mathcal{E}}$ represent respectively the variation of canonical angular momentum and particle energy per unit mass due to the interaction with the fluctuating electromagnetic fields.

As with standard radial transport analysis, the PSZS equation allows for the description of transport within a hierarchy of approximations. In particular, the fluxes appearing in the previous equation can be computed using a range of reduced models, from nonlinear gyrokinetic theory to quasilinear theory. Consistently, PSZS diagnostics have been implemented in several gyrokinetic codes, such as ORB5 [10], EUTERPE,

and GTC. In Refs. [11, 12], a numerical workflow, named ATEP, has been introduced to evolve PSZS using LIGKA and a simple quasilinear model in the presence of sources and collisions. Fluxes for different plasma scenarios can be compared to validate various models, and data from BEST will provide the basis for verification and validation.

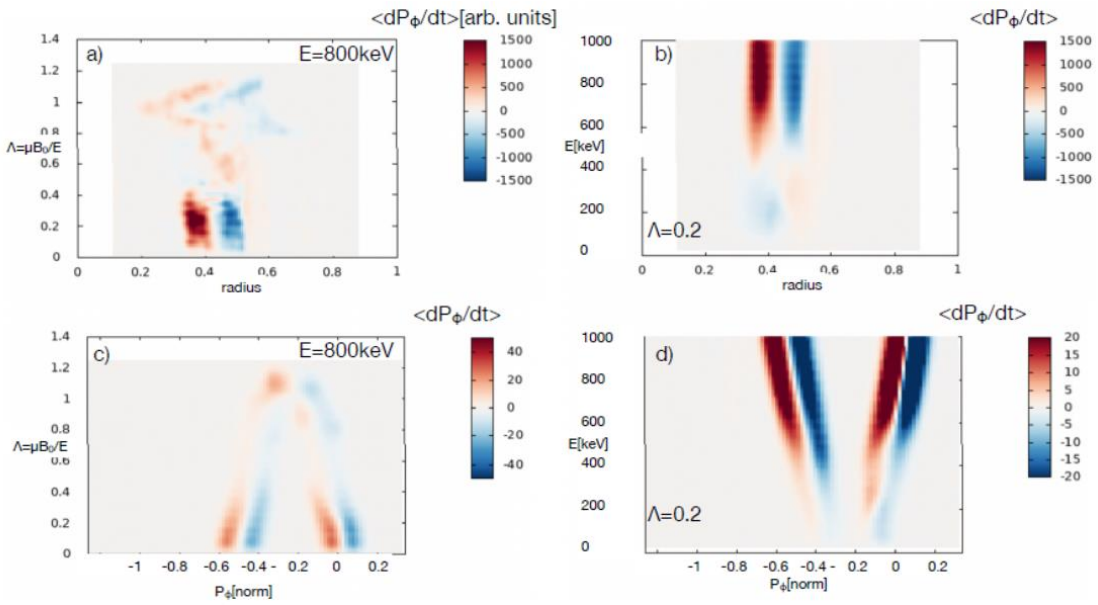

Figure 10.1: $\delta\dot{P}_\phi$ as calculated by the ATEP code [11] to evolve the Phase Space Zonal Structures according to their governing equation. This is calculated for a single n = 13 toroidal Alfvén eigenmode with $\delta B/B = 5\times10^{-6}$ on ITER. $\delta\dot{P}_\phi$ is shown as a function of the real space radial coordinate (panels (a) and (b)) and as a function of the coordinate P_ϕ (panels (c) and (d)). The panels (a) and (c) are shown for E = 800 keV, and the panels (b) and (d) for $\Lambda = \mu B_0/E = 0.2$. The radial coordinate is given in terms of the square root of the normalized poloidal flux.

More advanced transport models to solve the PSZS equation have been proposed, such as the Dyson–Schrödinger transport model (DSM) [10]. This method exploits the characteristic spatiotemporal scales of fluctuations which are decomposed into a parallel mode structure (aligned with the equilibrium magnetic field) and a radial envelope. The parallel mode structure emerges on a time scale proportional to the inverse of the characteristic frequency, ω^{-1}, while distortions to the radial envelope and coupling between different toroidal mode numbers occur on the nonlinear time scale, which is typically much longer for Alfvénic fluctuations. Therefore, in the DSM transport model, the parallel mode structure is determined by linear theory, while the nonlinear dynamics are described in terms of coupling between toroidal mode numbers and modulation of the radial envelope amplitude. This theory is especially relevant for BEST, where $Q \sim 1$ scenarios have been shown to exhibit clear features of global behaviors that are expected for steady state plasma operations, with the potential important role of kinetic Alfvén waves in core-edge coupling. These scenarios demonstrate complex interactions between different plasma regions, where non-local

transport phenomena and self-organized structures become significant. The coupling mechanisms, particularly through kinetic Alfvén waves, create intricate feedback loops that fundamentally affect plasma stability and confinement characteristics.

Exploring higher-Q scenarios represent one of the scientific milestones for BEST. Under these conditions, fusion alpha particles will be possibly playing a dominant role in the hot plasma core and dominate the local power density balance. Thus, strong deviations from a local Maxwellian distribution function are expected. These deviations arise from the complex interplay between alpha particle heating, modified transport properties, and the emergence of energetic particle populations with distinct characteristics. The resulting plasma state may exhibit enhanced confinement properties and novel collective behaviors that are crucial for future fusion reactor operation.

Given these fundamental points, it is readily concluded that BEST will be among the first tokamaks to operate under realistic burning plasma conditions, where it will be crucial to predict the self-organized equilibrium, composed by PSZS, zonal electromagnetic fields and a finite level of core turbulence as well as meso-scale Alfvénic fluctuations. Careful analysis and predictions. to be verified against experimental measurements, will be pivotal to comparing the results of different reduced transport models in the phase space and to the development of reliable predictive capabilities of burning plasma performance. This comprehensive understanding will bridge the gap between current experimental facilities and future fusion power plants, providing essential insights for optimizing plasma performance and validating theoretical models. In addition, reactor-relevant strategies for the control of a dominantly alpha-heated plasma need to be developed, such as fuelling and impurity tailoring.

10.4: High-density pedestal physics

For BEST operation scenarios, high fuelling and recycling are necessary and unavoidable, which will result in high separatrix density and detached operation. Correlations between pedestal structure and separatrix density on experiments have already been observed in the mainstream tokamaks. For example, in Alcator C-Mod, AUG, DIII-D and JET, negative correlations between pedestal pressure and separatrix density have been found [13-18] in the ballooning limited cases. The correlations between $p_{e,ped}$ and $n_{e,sep}/n_{e,ped}$ are considered robust for different plasma current and divertor configurations, and the normalized separatrix density is considered important to affect the pedestal structures. The negative correlations between pedestal heigt and separatrix density can be interpreted as the density outward shift leading to a shift of the pressure profile, which, in turns, can drive the peeling-ballooning mode more unstable. This produces a lower pedestal height. In peeling limited cases, the experiments observe no pedestal degradation increasing $n_{e,sep}/n_{e,ped}$, as shown in JET-ILW and TCV [19].

Another effect caused by the high separatrix density is the outward shift of the density profile. JET dataset shows that the density outward shift is positively correlated with $n_{e,sep}/n_{e,ped}$. When $n_{e,sep}/n_{e,ped} > 0.5$, the dataset shows that the density peak gradient move outside the separatrix. This effect is also observed on other tokamaks. In particular, DIII-D gives the relative shift of the peak gradient region between pedestal density and temperature.

The current EPED or Europed model, is not capable to predict the pedestal height when $n_{e,sep}/n_{e,ped} > 0.4$ for JET high density H-mode operations in the ballooning limited cases [18]. The model will over-predict the height of pedestal. This is due to the under-estimation of the pressure gradient. The resistive MHD effects might become important for this underestimation, and the turbulent transport may be increased in the high separatrix density case. The peeling limited pedestal structure is able to be qualitatively predicted by the Europed model [19], while the broadening or narrowing of the pedestal is underestimated for high values of $n_{e,sep}/n_{e,ped}$.

For BEST, since the high density operation is an important candidate, and the structure of the pedestal is tightly related to the edge instabilities such as ELMs and QCE scenario, the effects of the density shift and pedestal height should be studied systematically based on the current facilities. Further development of accurate parametric models is necessary for improving the predictions of the BEST pedestal.

Pedestal width is determined by $\Delta = c\,\beta_{p,ped}^{1/2}$ based on the KBM scaling, where $c = 0.076$ is a constant in EPED model for the conventional H-mode. However, the high density operation in ballooning limited pedestals has shown that the width is affected by the separatrix density, see e.g., JET, AUG and DIII-D [17, 18, 20], while the width is not qualitatively affected within the experimental uncertainty in the peeling limited cases[19]. The gyrokinetic simulations show that higher $n_{e,sep}/n_{e,ped}$ increases the turbulent transport, which changes the scale length of the density gradient L_{ne}. Therefore, the electron turbulence at the middle of pedestal may play a crucial role. Based on this understanding, the KBM criterion for pedestal width of ballooning limited cases is modified considering the contributions of edge turbulence such as ITG:

$$\Delta = c_1 \left(\frac{\nabla n_e}{n_e}\right)^{a_1} \left(\beta_p^{ped}\right)^{b_1} = c_2 \eta_e^{a_2} \left(\beta_p^{ped}\right)^{b_2},$$

where $\eta_e = L_{ne}/L_{Te}$. Analysis of JET and DIII-D data gives similar values of the parameters for pedestal width: i) $c_1 = 0.56$, $a_1 = -0.48$, $b_1 = b_2 = 0.5$, $c_2 = 0.04$, $a_2 = 0.44$ for JET, and ii) $c_1 = 0.45$, $a_1 = -0.48$, $b_1 = 0.5$, $b_2 = 0.58$, $c_2 = 0.11$, $a_2 = 0.48$ for DIII-D.

The pedestal width is found to be positively correlated with $n_{e,sep}/n_{e,ped}$ for JET and DIII-D, but negative correlations for AUG. The increase in divertor neutral pressure in AUG, which leads to the increase of $n_{e,sep}$ causes the density profile to move outwards and has the effect of strongly decreasing the pedestal width. The decrease of the width makes the height decrease, and the confinement degrade [21, 22]. This conclusion is different from the other two facilities. Therefore, it is important to find out how the pedestal width is affected by the separatrix density in BEST.

Summarizing, the BEST operation scenario design is based on EPED model at pedestal region. More accurate models are necessary for both the density shift and

pedestal width with the considerations of electron turbulence, and the physics understanding of the decrease of width in AUG needs to be clarified. For pedestal height, the isotopic and impurity effects are important to estimate the ballooning criterion. The pedestal model for the QCE case will be developed.

10.5: Modelling in support of ELM mitigation strategies

In support of the inductive scenarios developed to reach scientific breakeven $Q > 1$ (see Chapters 2 and 4), the behaviour of ELMs is important to be analyzed. For these scenarios, the density shift and electron turbulence effects, mentioned in the previous subsection, are not considered here. The considered pedestal parameters are as follows: $n_{e,ped} = 6.4\times10^{19}$ m^{-3}, $T_{e,ped} = 5$ keV, $T_i = T_e$, corresponding to the collisionality $\nu_{e,ped}^* \approx 0.07$. There are two cases studied here. The first considers the low separatrix density $n_{e,sep} = 3.8\times10^{19}$ m^{-3} ($n_{e,sep}/n_{e,ped} \approx 0.6$). The second corresponds to a higher separatrix density, $n_{e,sep} = 4.5\times10^{19}$ m^{-3} ($n_{e,sep}/n_{e,ped} \approx 0.75$), consistent with the QCE regime. For the two considered case, the collisionallity at the separatrix is $\nu_{e,sep}^* \approx 14.3$ and 25.4, respectively.

The stability analysis for the two considered cases is shown in Fig. 10.2. This figure illustrates that the pedestals for both cases are located at the corner of coupled peeling and ballooning mode, near the peeling boundary more than ballooning boundary. When the separatrix density increases (cf. Fig. 10.2(b)), the most unstable mode changes from n = 2-5 to n = 5-7.

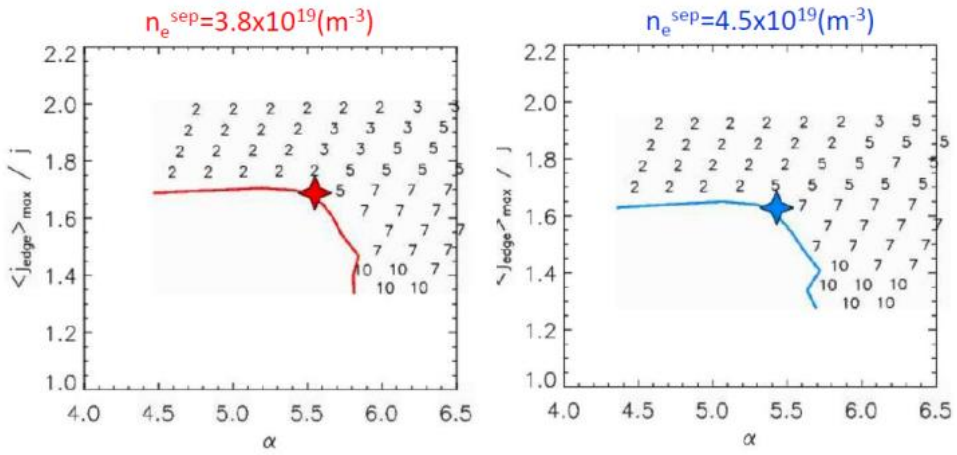

Figure 10.2: Pedestal stability diagrams for the inductive scenarios developed in support of $Q \geq 1$ operations in BEST. The left panel corresponds to the conventional type-I ELM H-mode, while the right panel features a higher separatrix density and mimics the conditions for the QCE scenario.

In addition to ELM mitigation strategies discussed in Chapters 2 and 4, additional mitigation methods should be prepared as backup options. In addition to the scenarios introduced in Chapter 6 (Divertor), there are several ELM control methods developed in EAST using radio-frequency (RF) waves. For example, ion-cyclotron resonant heating (ICRH) is found to be able to suppress ELMs in EAST [24]. The external E×B velocity

shear near the pedestal top and the scrape-off-layer (SOL) induced by the RF sheath potential of ICRH plays the key role in ELM suppression. A positive correlation between the RF sheath and the E×B shear rate in SOL are observed in experiments, and it is also proved by BOUT++ simulations [25]. These findings suggest a new simple approach to access the ELM suppressed regimes in plasma with low torque input as CFEDR discharges. More detailed analysis is needed for the understanding of the correlations between ICRH engineering parameters and RF sheath, which will give the compatible operation window with ELM suppression.

In EAST, low-hybrid waves (LHWs) are commonly used for current driving and heating. Besides these, the ELM control phenomenon by LHW has been observed, including mitigation, suppression, and triggering [26-28]. The detailed research has shown that the ELM mitigation is mainly caused by the formation of helical current filaments (HCFs) in SOL induced by LHW. From simulations, the magnetic flutter induced by HCF is found to be the key factor in the ELM mitigation [29]. HCF enhances the mode coupling at the linear growing phase of ELM, which leads to the absence of the dominant filamentary structures and the mitigation of ELM. HCF can significantly change the edge magnetic topology. Therefore, the transient heat flux on the divertor is effectively reduced, and the SOL width is broadened. The challenge is to find out the relationship between LHW injection power, SOL plasma parameters and amplitude of HCF.

The ELM mitigation strategies should be tested in preparatory operation phases. From the analysis of stability boundary and BOUT++ 2-fluid simulations, both the conventional H-mode and QCE scenarios of BEST are close to the coupled peeling-ballooning boundary. It is important to address that the QCE scenario is able to be achieved experimentally with the similar normalized BEST parameters. More analysis is necessary for RF waves to find out the practical operation window of the ELM mitigation, as well as the validations on other tokamaks. Another important point is how the interactions between energetic particles and pedestal physics. Relative simulation tools must be developed for better understanding and evaluation on the edge physics under burning plasmas.

10.6: Verification and validation

As described in the previous sections, the scientific exploitation of a reactor-relevant plasma, particularly BEST, requires comparing experimental results with predictions from reduced models. This approach enables the development of predictive capabilities for burning plasmas and the optimization of their performance. However, this task is challenging because burning plasmas are complex systems that must be described by integrating results from multiple simulations, e.g., core-EP and core-edge couplings. Therefore, it is essential to establish a modular computational infrastructure with a centralized database where key scenario and machine quantities are recorded and documented.

The Integrated Modelling and Analysis System (IMAS) framework [30] has been developed for this purpose for ITER and can be leveraged for the BEST research plan. A key task will be integrating conventional transport workflows with codes evolving the EP distribution function. A pivotal example of such a coupling scheme is the ATEP code [11]. The ATEP code, along with most of its reduced transport models, relies on results from multiple linear calculations performed using the IMAS infrastructure via the EP stability workflow [31]. A key advantage of IMAS is its standardized data model, which represents experimental and simulated data using identical structures. For example, given the experimental reconstruction of the equilibrium, it is possible to study the stability of Alfvén eigenmodes throughout the entire discharge (see Figure 10.3) and compare the phase space fluxes predicted by different reduced transport models with those produced by these fluctuating fields within nonlinear Gyrokinetic theory. Moreover, the moments of the PSZS distribution function, such as zonal currents and pressure, can be evaluated and directly compared with BEST diagnostic results.

Another example of a key tool for describing burning plasmas that requires the IMAS infrastructure is the EPCOM workflow, developed by the ITER organization [32]. This workflow converts fast-ion marker distributions from Fokker-Planck codes, such as ASCOT and NUBEAM or from experimental measurements, into a 3D PSZS distribution function using a Monte-Carlo based Jacobian transformation and spline representation. This approach enables precise gradient computation for the gyrokinetic codes used to model any discharge.

The scientific mission of BEST calls for the development of workflows similar to those described, enabling the validation of theoretical predictions for burning plasma physics through comparison with experiments and synthetic diagnostics. From this point of view, IMAS not only plays a crucial role as an integrated modelling framework but also enables and facilitates mutual positive feedback between theory, simulation, and experiment.

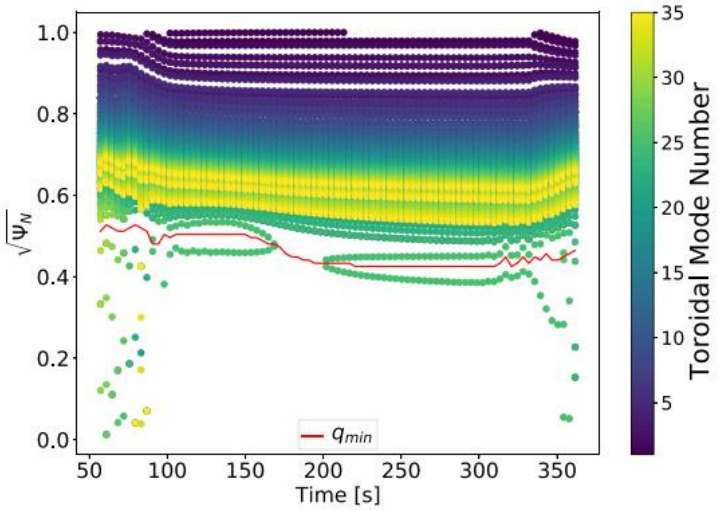

Figure 10.3: Tracking of the radial position (normalized poloidal flux) of TAE modes with given toroidal mode number in an ITER Q = 10 scenario. Courtesy of A. Popa [31].

10.7: References

[1] Divertor Tokamak Test Facility Research Plan Version 1.0, ENEA (2024);
ISBN: 978-88-8286-474-3
[2] A. Pizzuto et al., *Nucl. Fusion* **50**, 095005 (2010)
[3] L. Chen and F. Zonca, *Rev. Mod. Phys.* **88**, 015008 (2016)
[4] F. Zonca et al., *Plasma Phys. Control. Fusion* **57**, 014024 (2015)
[5] L. Chen et al., *Nucl. Fusion* **65**, 054002 (2025)
[6] N. Chen et al., *Nucl. Fusion* **65**, 016018 (2025)
[7] F. Zonca et al., *New Journal of Physics* **17**, 013052 (2015)
[8] Z. Qiu et al., *Plasma Sci. Tech.* **27**, 095101 (2025)
[9] M.V. Falessi et al., *New Journal of Physics* **25**, 123035 (2023)
[10] A. Bottino et al., *Journal of Physics: Conf. Series* **2397**, 012019 (2022)
[11] P. Lauber et al., *Nucl. Fusion* **64**, 096010 (2024)
[12] G. Meng et al., *Nucl. Fusion* **64**, 096009 (2024)
[13] M.G. Dunne et al., *Plasma Phys. Control. Fusion* **59**, 025010 (2017)
[14] M. Dunne et al.., *27th IAEA Fusion Energy Conference* (2018)
[15] L. Frassinetti et al., *Nucl. Fusion* **61**, 016001 (2021)
[16] J.W. Hughes et al., *Nucl. Fusion* **51**, 083007 (2011)
[17] H.Q. Wang et al., *Nucl. Fusion* **64**, 126061 (2024)
[18] L. Frassinetti et al., *Nucl. Fusion* **61**, 126054 (2021)
[19] L. Frassinetti et al., *Nucl. Fusion* **65**, 076028 (2025)
[20] D. Silvagni et al., *Phys. Plasmas* **31**, 022501 (2024)
[21] T. Luda et al., *Nucl. Fusion* **60**, 036023 (2020)
[22] M.G. Dunne et al., *Plasma Phys. Control. Fusion* **59**, 014017 (2017)
[23] X.Q. Xu et al., *Phys. Rev. Lett.* **105**, 175005 (2010)
[24] X.J. Zhang et al., *Sci. China-Phys. Mech. Astron.* **65**, 235211 (2022)
[25] Y.L. Li et al., *Nucl. Fusion* **62**, 066043 (2022)
[26] Y.F. Liang et al., *Phys. Rev. Lett.* **110**, 235002 (2013)
[27] R. Chen et al., *Nucl. Fusion* **55,** 033012 (2015)
[28] Q.Q. Yang et al., *Plasma Phys. Control. Fusion* **61**, 065023 (2019)
[29] T.Y. Xia et al., *Nucl. Fusion* **59**, 076043 (2019)
[30] F. Imbeaux et al., *Nucl. Fusion* **55**, 123006 (2015)
[31] V.-A. Popa et al., arXiv preprint (2023); https://arxiv.org/abs/2306.08442
[32] G. Brochard et al., *29th Meeting of the ITPA Energetic Particles Topical Group* (2023)

Chapter 11: Neutronics and Nuclear Safety

Coordinators: S.L. Zheng (ASIPP), R. Villari (ENEA, Italy), R. Kamendje (EUROfusion)

With contributions from:
ASIPP Team: X.B. Peng, B. Guo, X.K. Zhang, Q.J. Zhu, G.Q. Zhong
EUROfusion Team: J. Elbez-Uzan, S. Rosanvallon (CEA-Cadarache, France), P. Pereslavtsev
UKAEA Team: A. Valentine

11.1: Neutronics and nuclear analysis

To support the development and validation of neutronics methodologies, computational codes, and nuclear data relevant to the design, safety and performance assessment of next-generation fusion facilities such as ITER, CFEDR and DEMO, several experimental and modelling activities are foreseen within the BEST tokamak. These include dedicated measurements, integral experiments, and systematic analyses conducted across the different phases of BEST operations, complementing technological exploitation of D-T operations carried out on the JET tokamak [1]. The aim is to reduce uncertainties in neutron and gamma transport, neutron yield assessment, activation, damage, shutdown dose rate, tritium production and Activated Corrosion Products (ACP), thus enhancing the predictive capabilities and development of current modelling tools and supporting design efforts, licensing and safety for future fusion reactors. Each activity has been defined to align with specific needs and to be fully integrated into the experimental infrastructure and data acquisition systems of BEST. The nuclear methodologies and codes of interest are listed in Annex 1.

11.1.1: Fusion power prediction accuracy

Reliable prediction of fusion power is a fundamental requirement for validating the performance of experimental devices and extrapolating results to future fusion reactors. BEST aims to improve neutron diagnostics calibration methodologies capable of predicting neutron yield and associated fusion power within a 10% accuracy margin in DT operations. Following JET experience [2-3], the approach involves in-vessel calibration campaigns using ^{252}Cf passive neutron source and potential active neutron generators. After a detailed study, these sources will be installed on a remote handling (RH) system equipped with calibrated detectors and located at various positions inside the BEST plasma chamber to calibrate BEST neutron diagnostics for both DD and DT phases. Off-site characterization of neutron generators and monitors will be required before calibration campaigns.

During plasma operations, activation foils placed at irradiation ends will be used to verify neutron yields and the efficacy of calibration. BEST machine requirements include sufficient off-operation time for in-vessel calibration and dedicated plasma shots for in-operation verification. Preparatory work includes detailed pre-analysis for selecting neutron generator, passive source, time, calibration monitors and positions to achieve the objectives. To enable accurate in-vessel calibration, a comprehensive

definition of high-level operational and logistical requirements is essential. These requirements must address system performance targets, safety constraints, risk mitigation strategies, and cost considerations. The calibration process relies on the availability and readiness of the RH system, which will be used to deploy neutron sources and associated monitors within the vessel. Installation of electronics cabinets and the routing of cables will be required for the operation of active neutron detectors. Prior to in-vessel deployment, the neutron sources and monitoring systems must be procured and undergo rigorous off-site characterization. This will be followed by on-site validation of the complete calibration setup, including functional testing of the neutron generator, detectors, and all electrical and data acquisition connections, ensuring full system integrity before in-vessel calibration campaigns.

11.1.2: Neutron Transport Through Shielding and Penetrations

Neutron and gamma transport through complex geometries and penetrations remains one of the most challenging aspects of nuclear analysis for fusion facilities. The BEST tokamak will be used to conduct integral measurements of fluence and dose at various locations. The goal is to benchmark the radiation transport codes and nuclear data libraries with focus to streaming in penetrations in large/complex volumes by evaluating the C/E (calculation-to-experiment) ratio and associated uncertainties for extrapolation of the safety factor for radiation maps during plasma operations (mode 0). Detection systems will be installed both inside and outside the BEST Torus Hall, comprising passive and active detectors designed to measure neutron and gamma fluxes, spectra, and doses during operations. The setup requires dedicated space: in-vessel locations for activation foils and Thermoluminescent detectors (TLDs), and sufficient ex-vessel space to accommodate active and/or passive systems [4]. Control and data acquisition for the active detectors must be integrated into the BEST CODAS system to ensure proper correlation with plasma operations. A neutron plasma source will be developed based on the BEST operational scenario, and a neutronics model will be based on CAD geometry, with radiation transport simulations performed using the codes listed in Annex 1. The machine operational requirements will depend on the sensitivity of the detection systems and their placement, particularly outside the torus hall. While measurements may be feasible even in the pre-DT phase, the primary interest is focused on the DT phase. Preparatory work includes pre-analysis for detector and position selection, minimum neutron yield estimation, and definition of all high-level operational, logistic, functional, performance, reliability, safety, and design constraints. A full risk and cost assessment is also necessary. Appropriate detection systems and assemblies must be selected, off-site calibration protocols established, and installation and retrieval procedures defined. Interface requirements include availability of the irradiation end and pneumatic system, calibrated gamma spectroscopy equipment, and sufficient space, shelving, and shielding for ex-vessel components. Additional needs include cubicles and cable routing for power and signal connections, CODAS integration with neutron diagnostics, and control of temperature for specific systems.

11.1.3: Validation of TBR Predictions

Dedicated measurements and analyses of neutron flux/fluence and tritium production will be conducted in the Test Blanket Modules (TBMs) of the BEST tokamak, with the objective of validating the radiation transport codes and nuclear data used in DEMO-related analyses for the determination of the Tritium Breeding Ratio (TBR). These activities aim to assess the calculation-over-experiment (C/E) ratios and associated uncertainties to ensure tritium self-sufficiency in future reactor designs.
The methodology involves collecting experimental data on neutron flux and tritium production during the nuclear phase of TBM operation (see Section 3.2.10). TBMs use specific nuclear detectors according to requirements of functions and conditions. For example, lithium glass detectors or liquid scintillators can be possible approaches for tritium production rate measurement, while fission chambers, self-powered neutron detectors or nuclear activation foil can be chosen for the measurement of neutron fluence or spectrum. Accountancy of tritium should be performed through measurements through the entire cycle of the breeding medium. A corresponding neutronics model will be developed based on CAD geometry and used in simulations performed with the radiation transport codes listed in Annex 1. These simulations will account for neutron irradiation histories derived from BEST operational scenarios, and the resulting TBR predictions will be directly compared with measurement results. The machine operational plan must accommodate irradiation histories tailored to TBM nuclear phase requirements, with particular interest in comparing TBR performance across DD and DT plasma scenarios and tracking its evolution over the BEST operations. Prior developments include the development and testing of TBM-specific detectors and mock-up experiments [5] using DT neutron generators to refine measurement techniques and validate detection systems for nuclear-phase deployment. Successful execution of this activity depends on alignment with the TBM design and integration within the overarching TBM experimental programme.

11.1.4: Shutdown dose rate

Dedicated measurements and analyses will be carried out to determine the shutdown dose rate (SDDR) in locations within and around the BEST torus hall that are anticipated to require personnel access during shutdown. The goal is to validate SDDR computational models and nuclear data used in ITER, DEMO, and CFEDR analyses, complementing and expanding JET experience data [6-7]. These validations will focus on quantifying C/E ratios and associated uncertainties, supporting the extrapolation of safety margins for radiation maps relevant to both hands-on maintenance scenarios (mode 1) and remote handling operations (mode 2). The reliable prediction of dose rates is also required during operations (mode 0). The experimental setup will involve the installation of active detectors at pre-selected positions throughout the BEST Torus Hall and buildings. These detectors will monitor shutdown dose rates as a function of time, between pulses and at shutdown. Proper allocation of space and supporting structures, such as dedicated shelves for detector installation, will be necessary. The detection control and acquisition systems will be fully integrated with the BEST CODAS

infrastructure to allow correlation with plasma operations and neutron diagnostics. A neutron plasma source model will be developed in accordance with BEST operating scenarios. A comprehensive neutronics model will also be based on CAD geometry, incorporating detailed material chemical compositions confirmed through certified documentation. Simulations will be carried out using the SDDR computational tools identified in Annex 1, incorporating irradiation schedules derived from real plasma operation and neutron diagnostics measurements. The operational feasibility will be influenced by the sensitivity and location of detection systems, with particular consideration required for measurements outside the torus hall where dose rate levels may be lower. While no specific plasma scenario is strictly required, the primary interest is in tracking SDDR evolution during and following the DT phase, where the activation levels are expected to be most relevant. Pre-DT measurements may still be feasible and useful for methodological refinement. Preparatory efforts will include scenario-based pre-analysis to determine optimal detector placement, define minimum neutron yields or yield rates, and estimate dose rate distributions at the end of plasma operations. This includes identifying high-level operational, logistical, performance, safety, and design constraints. A full risk assessment will be conducted, along with cost evaluation. The selection of appropriate detection systems, development of off-site calibration procedures, and definition of installation and retrieval protocols will also be required. Interface requirements include sufficient space and infrastructure for ex-vessel systems, provision for electronics installation in cubicles, and reliable cable routing for power and data connections. Integration with CODAS and compatibility with neutron diagnostics systems are essential. For certain sensitive instruments, such as ionization chambers, environmental control parameters like temperature and oxygen levels will also need to be maintained during operation.

11.1.5: Materials activation

To validate activation codes and nuclear data used in ITER, DEMO, and CFEDR under burning plasma conditions, dedicated measurements and analyses of material activation will be performed in the BEST facility. These experiments will involve exposing DEMO-relevant selected material samples to fusion neutron spectra both inside and outside the vessel. The aim is to assess C/E ratios and uncertainties in predicting induced activity and radionuclide inventories, critical for maintenance planning and radioactive waste classification in future machines. Following JET experience [8-9], the experimental methodology requires the design and installation of appropriate holders to accommodate material samples in proper positions. In-vessel short-term activation will be carried out using the irradiation end and pneumatic systems, followed by gamma spectrometry measurements. Space will be reserved outside the vacuum environment to install these holders safely and accessibly. A detailed neutronics model based on CAD with verified materials chemical compositions, and activation calculations will be carried out using the codes and nuclear data libraries, as specified in Annex 1. These simulations will use irradiation schedules from BEST neutron diagnostics during plasma operations. Operational

constraints will be largely determined by the sensitivity and location of the gamma spectrometry systems, as well as material-specific properties and cooling times when the samples can be retrieved and be available for gamma spectra and isotopes measurements. Preparatory work includes selecting sample materials and positions, estimating neutron yield thresholds, and defining operational, logistical, functional, and safety requirements. This includes risk assessments, design of sample holders, calibration of the gamma spectrometry systems, and development of installation and retrieval plans. Interface needs include access to a calibrated gamma measurement system, pneumatic transport system, adequate space and shielding, and availability of qualified laboratories for sample analysis. Independent chemical composition verification and integration with neutron diagnostics are also necessary for complete materials traceability.

11.1.6: Fluid activation

Validation of activation models for fluids, specifically the cooling water and liquid lithium-lead (LiPb) used in the BEST facility, will be performed under reactor-relevant conditions. The objective is to determine the C/E ratios and uncertainties associated with predicting fluid activation levels, which are crucial for design and safety assessments in future reactors. The experimental approach includes sampling from coolant loops during and after operations to measure activity. Following JET experience [1], gamma spectrometry stations will be installed near selected outlet pipes, complemented by dose rate detectors and neutron spectrometers. Measurement systems will be placed in pre-defined positions according to operational scenarios, with appropriate space, supports, magnetic/radiation shielding, and collimators as needed. These active systems will be fully integrated into the BEST CODAS for correlation with plasma operations and neutron diagnostic data. A neutronics model based on detailed CAD representations of flow channels and pipe geometries will be developed and linked with computational fluid dynamics (CFD) simulations. Multiphysics tools described in Annex 1 will be employed to simulate the coupled behaviour of fluid dynamics, neutronics, and activation processes. These simulations will be validated using experimental data collected during both close to steady-state and pulsed plasma operation, with special focus on long-duration DT pulses. System requirements depend on detector sensitivity, loop layout, coolant parameters, and access points. While no specific plasma scenario is strictly necessary, the main interest lies in understanding how activation evolves as a function of plasma performance, particularly during long pulses in the DT phase. Preparatory steps include pre-selection of loop segments and detectors, neutron yield estimates, and dose rate predictions. A complete set of performance, safety, and reliability specifications must be defined. Calibration procedures, installation logistics, and cost assessments will also be carried out. Interface needs include adequate space for detectors and auxiliary systems, electronics installation, cable routing, CODAS integration, and fluid diagnostics, including flow rate and condition monitoring.

11.1.7: Activated corrosion products

The generation and transport of activated corrosion products (ACPs) is a critical contribution to occupational radiation exposure (ORE), safety and waste management procedures and classifications, and accident scenarios of future machines. To support validation of ACP assessment, measurements and analysis will be performed in BEST, in particular in high-performance DT operation phases to capture ACP evolution under realistic reactor-relevant conditions. A dedicated ACP cooling loop will be designed or existing loop exploited and implemented integrating proper passive and active detection systems for gamma spectrometry outside the torus hall. These detection systems will monitor activity deposited in pipe walls, coolant, filters, and resins. Additional dose rate systems will be installed close to water loop outlet pipes to measure gamma dose resulting from ACPs generated during normal operations and baking. Sufficient space will be required for the installation of this loop, including shelves, radiation shields, and auxiliary systems for pressure, temperature, and oxygen control. The system will also include holders for candidate structural materials such as stainless steel and copper alloys, which will be retrieved post-irradiation for detailed analysis of corrosion rate, composition of ACPs, and radioactive isotope content. Endoscopic tools will allow internal pipe inspections before and after extended operational periods. The CODAS system will handle data acquisition and correlation with neutron diagnostics. A corresponding neutronics model will be developed from CAD geometry, incorporating pipe flow channels and materials data. Simulations will be carried out using ACP codes identified in Annex 1, with input parameters such as material properties, water chemistry, and operational flow conditions, combined with irradiation histories from neutron diagnostics. The implementation of the system will depend on various factors, including BEST operational performances, detector type, cooling loop configuration, water chemistry, and operating parameters such as flow rate and temperature. Circuit operation must ensure sufficient corrosion to enable quantifiable measurements. Preparatory work involves selecting appropriate cooling loops and detectors, estimating activity and dose rate levels, and defining all performance and design constraints. Full risk and cost assessments will guide system specification. Interfaces must include space for all detectors and auxiliary equipment, cubicles and cable access, integration with CODAS, and systems for monitoring flow rate, oxygen, and temperature.

11.2: Nuclear Safety

As a tokamak operating with a DT fuel mixture, BEST will provide useful data in support of the design, nuclear safety and licensing of future fusion nuclear facilities. In particular, the following topics represent domains of interest that will substantially benefit from a better evaluation of existing uncertainties:

- Tritium contamination, measurement and removal
- Dust contamination
- Incident analysis

- Waste management
- Collective and individual radiation doses with a special focus on internal exposure in the context of Occupational Radiation Exposure assessment

11.2.1: Tritium measurement, contamination and removal

Control of the radioactive inventory, the basis of a license, is an important safety activity. Achieving this safety objective in a DT fusion environment necessitates mastering, in particular, tritium accountancy. Tritium accountancy shall be ensured through the implementation of Mass Balance Areas in operation (including at the bottom of the stack). BEST is suited to provide an excellent opportunity to explore different strategies for controlling the tritium inventory.

In a closed fuel cycle, tritium is bred in a blanket, managed through the fuel cycle and injected inside the vacuum vessel. In this section, focus is put on the quantification of the in-vessel tritium inventory, in complement to tritium inventory in the Fuel Cycle covered in Section 3.3.4 and the detritiation techniques proposed to be developed in Section 3.3.3. The objective is to demonstrate that it is possible to control tritium inventory in the vacuum vessel (safety limit to be respected) and that tritium can be recovered from waste (to facilitate waste storage, transport and final disposal acceptance). This will also allow tritium retention factors in the different materials to be clarified. In the context of BEST, this quantification of the in-vessel tritium inventory shall be done both in-situ, in order to assess how much tritium is trapped in the in-vessel components, and via postmortem analysis. Obviously, the development of means to control and recover these inventories is an additional necessary task. Once components are removed from the vacuum vessel and ready to be treated as waste, further detritiation may be performed, if required (by heating or melting). These in-vessel tritium quantification activities (in-situ or post-mortem) will provide data for the Mass Balance Areas in the context of the overall plant tritium inventory (linked with the fuel cycle). Means to estimate the tritium content in casks and in selected rooms of the hot cells will be also put in place to support the justification of the requirement on leak-tightness necessary for contamination control. More generally, the control of the tritium inventory covers the first and second confinement systems.

The strategy for in-vessel tritium quantification will rely on diagnostics such as Laser Induced Breakdown Spectrometry (LIBS) and dedicated remote handling (RH) tools for tritium retention inspection. Hence, provision shall be made in BEST for some space required for the installation of dedicated diagnostics and RH tools.

In support of BEST licensing and prior to nuclear operation, tritium retention and the efficiency of tritium removal from in-vessel components after plasma and baking operations will need to be evaluated. This will also enable benchmarking of numerical analysis with experimental data. Needed diagnostics, even if not credited in the safety analysis, will need to be qualified and calibrated before being used in the machine. Safety management and cost assessments are required before this experimental plan. It should also be highlighted that BEST operation will contribute to adding more clarity to the quantification of tritium retention factors in different materials.

11.2.2: Dust contamination

Dust is expected to be produced by interactions between the plasma and the plasma facing components during normal and abnormal events such as disruption. BEST operation will enable linking dust production in a tungsten machine with plasma operation by observation via fast cameras during operation. However, the strategy for the quantification of dust that could be produced is currently based on an assessment of erosion inside the vacuum vessel to establish an envelope value of the quantity of dust for the safety case. In addition to erosion measurements, it is proposed to collect dust inside the machine in Dust Collection Boxes installed in the lower part of the vacuum vessel, and to remove them from the machine during maintenance. It is also proposed to collect dust during maintenance operations by vacuum cleaning, metallic taps or other techniques to reduce dust inventory inside the vacuum vessel and enable dust characterization. The feasibility of the various techniques will need to be further assessed. Means to estimate the dust content in the cask and in selected rooms of the hot cells will be also put in place to support the justification of the requirement on the leak-tightness.

The objective is to quantify and characterize dust in BEST: morphology, size repartition, specific surface area, chemical composition, activation, fuel trapping in order to better define the inventories and their control, and their mobilization during pressurization events occurring in the vacuum vessel. BEST will also contribute to validating the methodology and tools used for dust inventory assessment and prediction for fusion machine analysis. It is thus suggested implementing in BEST in-vessel erosion and dust diagnostics as well as corresponding RH tools, and a vacuum cleaner to enable dust RH removal. The RH transfer of dust to the hot cells will be then required for characterization or shipping preparation for outsourced analyses.

To achieve these objectives, D-T plasma operation is required, ideally composed of a good number of pulses with high fusion power, or pulses with longer duration of flat-top plasma with lower fusion power.

In support to BEST licensing and prior to nuclear operation, the dust amount and characteristics will need to be evaluated. This will also enable to correlate numerical analysis with experimental data. The diagnostics and tools will need to be qualified and calibrated before being used in the machine. Safety management and cost assessments are required before this experimental plan.

11.2.3: Incident analysis

Nuclear facility design is fundamentally shaped by the defense in depth principle: prevent, detect and mitigate incidents. In fusion, because of the lack of relevant return on experience, the safety case is mostly based on a deterministic approach to ensure that reactors can handle a wide range of scenarios – from routine disturbances to rare, severe accidents. It is proposed to collect any type of information (scenario, component failure rate, mitigation, consequences) in case of off normal operation (incident) that may occur in BEST. BEST will then be suited to provide useful data for future fusion machine design and safety analyses regarding the prevention, detection and mitigation

of such events. It will also enable validating models and codes such as MELCOR used for incident analysis and enrich the fusion failure rate data base.

The analysis of incident sequences and postulated initiating events will be necessary for the BEST safety case, including the reliability of some devices that potentially serve as initiating events. To collect as much information as possible during operation, detectors will be installed to monitor the key parameters that will be integrated into a database. Safety management and cost assessments are required before this experimental plan.

11.2.4: Radioactive waste characterization

A coherent strategy for a management scheme for wastes arising from operation and decommissioning needs to be part of the design justification. It includes an assessment of wastes that will be produced. The collection of BEST data related to liquid effluents and solid waste arising from operation (including maintenance), incidents and decommissioning will enable reducing the uncertainties on the requirements on the design of waste management areas (hot cells) of future fusion plants and anticipate the final disposal needs.

For BEST licensing, a pre-analysis is required to predict waste categorization and tritium retention. The objective of the experimental plan is to collect useful data enabling the estimation of process and housekeeping waste production for a given future fusion machine, as such data are based on return on experience, and to analyze waste actually produced vs prediction. The analysis of the segregation of components (type of materials, levels of activity…) will enable optimizing waste classification.

Collected data shall cover the various waste types, mass, volume, activity and chemical composition, including tritium content and radioactive isotopes from activation and contamination. Data would cover the various areas of production: in-vessel (in-vessel component), ex-vessel (pumps, valves, filters…) and process and housekeeping waste. Dedicated facilities and measurement devices will need to be supplied into the hot cell or in an off-site lab qualified for such measurement and analysis.

For such analysis, neutron irradiation will be necessary but without specific operational requirements. This work is linked with Section 11.1.5 (material activation, tritium content in materials…) and will enable comparison between coupons put in place for neutronic assessment and data at component scale.

Waste management routes from production area to processing will be established for each type of waste. RH tools will be required to remove the activated components and transfer them to the hot cell, and a detritiation system will be employed in the hot cell (as seen in Section 11.2.1).

11.2.5: Collective and individual radiation dose with special focus on internal exposition for occupational radiation exposure assessment (data collection)

Protecting workers from radiation is a cornerstone of nuclear safety design. A combination of technical measures, design principles, and regulatory frameworks is applied to ensure that occupational radiation exposure (ORE) remains as low as reasonably achievable (ALARA). ORE assessment takes into account the maintenance scenario and the environmental conditions of the areas where hands-on maintenance is performed. The relevance of the ORE analysis depends on the data available; these being limited and unprecise at the present stage.

The objective is to collect data from BEST to reduce the uncertainties on ORE assessment for future facilities and provide input to DEMO/CFETR design and safety analyses. BEST will also contribute to validating the methodology and tools used for the ORE assessment.

A special focus on the individual internal dose of the workers shall be brought to the attention of the BEST operation.

The atmospheric contamination measurement would help as well to confirm the radiological and ventilation zonings.

For each hands-on maintenance in radiological areas where the ALARA approach should be applied, data shall cover in particular the measured external and internal dose rate, the time required for the hands-on activity, the number of persons involved, the use of Personal Protection Equipment. Health Physics records will be required to populate the database. The measurement tools will need to be qualified and calibrated before being used in the maintenance areas. Safety management and cost assessments are required before this experimental plan.

There are no specific operational requirements for the purpose of collecting data on ORE assessment. Any maintenance scenario will be useful.

11.3: References

[1] R. Villari et al., *Fusion Eng. Des.* **217**, 115133 (2025)
[2] P. Batistoni et al., *Nucl. Fusion* **58**, 026012 (2018)
[3] P. Batistoni et al., *Nucl. Fusion* **56**, 106016 (2018)
[4] R. Villari et al., *Fusion Eng. Des.* **107**, 171 (2017)
[5] P. Batistoni et al., *Nucl. Fusion* **52**, 083014 (2012)
[6] R. Villari et al., *Fusion Eng. Des.* **87**, 1095 (2012)
[7] R. Villari et al., *Fusion Eng. Des.* **136**, 1545 (2018)
[8] L.W. Packer et al., *Nucl. Fusion* **58**, 096013 (2018)
[9] L.W. Packer et al., *Nucl. Fusion* **64**, 10 (2024)

Chapter 12: BEST Diagnostics

Coordinators: H.Q. Liu (ASIPP), S. Zoletnik (CER-Budapest, Hungary)

With contributions from:
ASIPP Team: H. Lian, Y. Yang, Y. Zhang, S.Z. Yuan, S.X. Wang, B. Shen, T. Zhang, L. Zhang, S.Y. Lin, G.Q. Zhong, R.J. Zhou, Y.M. Duan, R. Yan, Q. Hu, H. Cao, Y. Liu, Z. Yip
EUROfusion Team: D. Mazon
External Expert: A. Costley

12.1: Diagnostics requirements and overview

The diagnostic system is an essential and critical component of BEST, as well as future ITER [1], CFEDR [2] and DEMO [3], serving as a vital means to achieve basic operation, plasma control, machine protection and physics studies. As with other large tokamaks, BEST diagnostics have evolved into a complex and diverse system, encompassing electromagnetic measurements, laser aided, microwaves, spectroscopy, radiation detection, neutron and fusion production diagnostics, and other common technologies, including nuclear electronics, first mirrors, synthetic diagnostics, and port integration. These diagnostic systems can actively or passively measure numerous physical parameters inside or near the BEST device. The diagnostics for BEST will combine state of the art and mature technology as appropriate to ensure robust operation and maximize scientific output. The redundant diagnostics systems (~28 subsystems) have been designed for BEST to guarantee the ~43 measurements to cope with harsh environmental conditions, as shown in Fig. 12.1 and Table 12.1. The list of the acronyms for the BEST diagnostics is given in Table A2 (Annex 2).

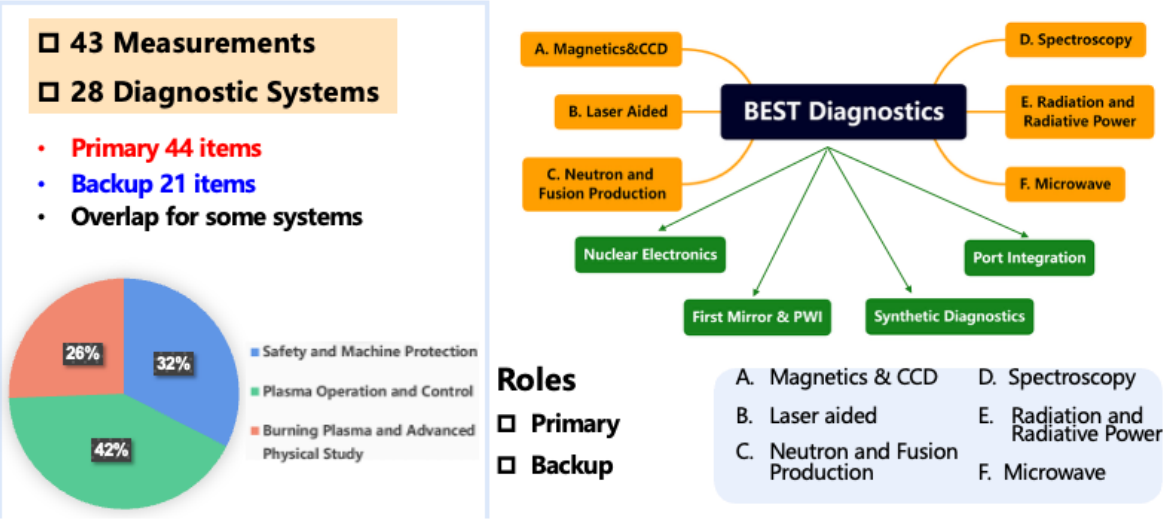

Figure 12.1: Schematic diagram of measurements and diagnostic systems.

Table 12.1: Measurements and diagnostic systems in BEST. Diagnostics categories (column #3): SP – Safety and protection; OC – Operation and control; AD – Advanced operation and physics understanding. Roles (column #5): P – primary; B – backup.

Measurement	**Parameter**	**Cat.**	**Diagnostics**	**Role**
Plasma current / halo current	I_p / current in machine structure	SP	Rogowski coils / Fiber optic sensor	P
Plasma shape and position	Plasma gaps, Δ_{sep}, dZ/dt	SP	Magnetic sensors	P
			CCD camera / SXRC	B
Loop voltage / Plasma energy	V_{loop} / β_p	SP	Magnetic sensors	P
Radiation power	Main plasma, divertor P_{rad}	OC	Bolometer	P
Radiation power profile	P_{rad}	AD	Bolometer	P
Divertor detachment	Detachment state	SP	VIS	P
Divertor and wall temperature	Infrared radiation	SP	Infrared cameras	P
DD/DT Y_n and P_{fus}	Neutron yield	SP	Neutron flux monitor	P
Absolute DD/DT Y_n and P_{fus}	Y_{DD}, Y_{DT}	SP	NAS	P
Runaway electrons	E_{max}, I_{RE}	SP	RGRS, HXR	P
Ion temperature profile	Core and edge T_i	OC	XCS, NES / CTS	P
			IAS-CXRS*	B
Disruption precursors	Locked mode	SP	SXR / Magnetics	P
			Bolometer	B
Tritium retention and deposition	First wall and divertor tritium retention	SP	DDMS-Material Probe	P
Wall erosion	First wall erosion			
Divertor erosion	Divertor surface morphology	SP	DAMS	P
Low-n MHD	B_r(mode)/B_p	OC	SXRC	P
			Magnetic sensor	B
Electron density and temperature	Line-integrated plasma density and profile	OC	POINT / CO_2 DI / TS	P
			MR	B
Plasma current profile	Poloidal magnetic field	OC	POINT	P
			IAS-MSE	B

* *The availability of active spectroscopy on heating beams depends on NBI energy.*

† *Refer to Table A2 (Annex 2) for the acronyms of the diagnostic systems.*

Table 12.1 (continuation): Measurements and diagnostic systems in BEST. Diagnostics categories (column #3): SP – Safety and protection; OC – Operation and control; AD – Advanced operation and physics understanding. Roles (column #5): P – primary; B – backup.

Measurement	Parameter	Cat.	Diagnostics	Role
Electron temperature profile	T_e	OC	TS	P
			ECE	B
Helium ash	Helium density and temperature in divertor	OC	LIF	P
			IAS-CXRS	B
Neutron emission	Neutron emission profile	OC	VNC, RNC	P
Core n_D/n_T	Core D:T isotope ratio and T_i	OC	NES	P
			IAS-CXRS*	B
Edge/divertor n_D/n_T	Edge/divertor isotope ratio	OC	VIS	P
Alpha-particle birth profile	Profile of the alpha-particle source	AD	NES	P
Confined alpha-particles	Density and energy profiles of alphas	AD	RGRS, CTS	P
ELMs and H/L-mode	f_{ELM}, divertor D_α	OC	VIS	P
Effective ion charge	Z_{eff}	OC		
Impurity species, influx, profile	Intensity of lines, full spectra, Γ_{imp}, n_{imp}	OC	EUV / VUV / XCS	P
			IAS-CXRS / BES	
LHW deposition profile	HXR emission	OC	HXR	P
Energetic neutral particle emission	High-energy neutral particle flux	AD	Diamond detector	P
Lost alpha-particles and fast ions	Flux and energy at selected locations / Intensity, energy, pitch	AD	Faraday cups	P
Rotation velocity profile	v_{tor}, v_{pol}	AD	IAS-CXRS, XCS	P
Turbulence rotation, radial electric field	v_{pol}, E_r	AD	MR / DBS	P
Magnetic turbulence	δB	AD	CPS	P
Density fluctuations	δn	AD	MR / DBS	P
			CTS	B
Dust	Total quantity and dust size	AD	DDMS	P
MHD	High- and intermediate-n modes	AD	Magnetic sensors	P

* *The availability of active spectroscopy on heating beams depends on NBI energy.*

† *Refer to Table A2 (Annex 2) for the acronyms of the diagnostic systems.*

Some measurements are primarily for machine protection, operation and control, these diagnostics must be available for every pulse of BEST operation and should be designed accordingly. Other diagnostics required for the evaluation of burning plasma advanced operation and physics understanding are essential for the output of BEST, but can be considered as a different class. Depending on the requirements of each phase of BEST operation, different strategies for the required plasma diagnostics are proposed.

For BEST, the diagnostic system should not only meet the scientific requirements but also be robust enough to survive in harsh nuclear environment. Additionally, it should be compact enough to minimize the occupation of the first wall area, thereby supporting the tritium self-sufficiency for future reactor devices. The rapid development of new technologies, such as Artificial Intelligence (AI) [4], also presents opportunities to develop comprehensive data analysis capabilities and develop real-time versions of synthetic diagnostics. These new technologies should be considered in the process of BEST diagnostic development but balanced against the requirement to ensure safe operation in a nuclear environment.

The measurement needs, parameters to be measured and the category (safety and protection, operation and control, advanced physics) are summarized in Table 12.1. The category is an indication of the importance of the measurement for machine operation and this will have an impact on the detail design of the diagnostic as well as how it will be treated during operations. For each measurement diagnostics are listed together with their roles: i) primary; ii) backup. In some cases, multiple diagnostics will provide information on the same parameters and some diagnostics will provide data on more than one parameter, to manage this an integrate data analysis (IDA) system will be used to ensure accurate and valid data.

12.2: Strategies for plasma diagnostics in different phases of BEST

For the first part of the D-D phase, the basic plasma measurements including adequate magnetic measurement (Hall sensors not included in the design), machine protection, plasma breakdown, density and neutron measurements (even if un-calibrated at first) must be available while other diagnostics may not be available yet. In the second part of the D-D phase the operating space of the machine will be increased, requiring a more extensive set of diagnostics. The calibration of neutron measurements should be demonstrated both to support the scenario development in D-D and in preparation for D-T operation.

During the D-T operation of BEST all of the standard diagnostic systems must work as usual but in addition there will be additional diagnostics required either related to D-T safe operation or to the additional physics that can be exploited in high fusion power, D-T operations. A strategy will be developed in the coming period to prepare the diagnostic systems in D-D such that they will be ready in D-T, including the requirement to operate in the harsh nuclear environment. This can be guided by the JET experience in the build up to DTE2 [5] and should include a strategy to accurately calibrate the 14 MeV neutron rate as this will be used to define the success of the three BEST missions.

12.3: Measurement parameters and diagnostics for specific topics

There are some plasma parameters that are globally required while others are specific to particular topics within the Research Plan. As part of this first phase of discussions the requirements of the different topics have been gathered and are included below. This should be considered a work in progress that will be added to as necessary.

12.3.1: Magnetic diagnostics for machine control

BEST has a comprehensive set of magnetic diagnostics – including multiple arrays of Rogowski coils, fiber-optic current sensors, magnetic and MHD probes, flux loops, diamagnetic compensation coils, saddle coils, and correction-coil probes. Together, these provide measurements of plasma shape and position, MHD activity, and currents in structures close to the plasma. No Hall sensors are installed on the vacuum vessel; however, long pulse operation with similar sensors has been demonstrated on EAST. Although equilibrium reconstruction has been validated in modelling, it has also been observed that incorporating q-profile data from POINT or MSE diagnostics would significantly enhance equilibrium reconstruction capabilities.

12.3.2: Key parameter profile measurement diagnostics

Some basic plasma parameters are considered as essential by all topics and are standard across international tokamak experiments. Such parameters are shown in Table 12.2 where the diagnostic systems foreseen for parameter profile measurements are listed according to the measured quantities (first column) and their corresponding diagnostic techniques (right columns). 'Primary' denotes techniques that will meet the measurement requirements, while 'Backup' denotes techniques that can provide similar measurements but with certain limitations. In the IDAP technique all diagnostics will contribute to the parameter measurement.

Table 12.2: Key parameter profile measurement diagnostics.
Refer to Table A2 (Annex 2) for the acronyms of the diagnostic systems.

Measured parameters	**Primary diagnostics**	**Backup diagnostics**
n_e profile	TS, POINT	MR
T_e profile	TS	ECE
T_i profile	XCS, NES	CTS, IAS-CXRS
Rotation profile	IAS-CXRS	XCS
q-profile / j_p	POINT	IAS-MSE
Radiation profile	Bolometer	SXRC
Impurities	EUV /VUV (for n_{imp} and Γ_{imp}) VIS (for Z_{eff})	IAS-CXRS (for selected n_{imp})
Birth / lost alpha-particle profile	VGC / RGRS / FC	CTS

12.3.3: Energetic-particle and fusion-product related diagnostics

In Table 12.3, the diagnostic systems required for energetic-particle and fusion-product studies are listed. These are key for the physics program of BEST in support of burning plasma physics studies.

Table 12.3: Energetic-particle and fusion-product related diagnostics. Refer to Table A2 (Annex 2) for the acronyms of the diagnostic systems.

Measurement	Parameters	Diagnostics
Core D/T ratio and fusion power	DD/DT Y_n and P_{fus}	NFM
	Absolute DD/DT Y_n and P_{fus}	NAS
	Core n_D/n_T	NES, IAS-CXRS
	Neutron emission profiles	VNC, RNC
Fast ions	Energetic neutral particles	Diamond detector, CTS
Fast electrons	Hard X-ray emission	HXR
		VGC / RGRC
Alpha-particles	Confined alphas	VGC / RGRS
	Lost alphas	FC
Helium ash	Helium concentration in the divertor	LIF

12.3.4: Diagnostics for transport and turbulence studies

BEST will have the unique opportunity to study plasma transport in the presence of significant alpha particle heating. As it was seen on JET, alpha particles may interact with plasma turbulence system, it is unclear whether this would be a positive or negative effect in this parameter domain and will also be of key interest to future burning plasma devices. In Table 12.4, the diagnostic systems foreseen for transport and confinement studies are listed according to the measured parameters (first column) and their corresponding diagnostic techniques.

Table 12.4: Diagnostics related to transport and turbulence studies. Refer to Table A2 (Annex 2) for the acronyms of the diagnostic systems.

Measured parameters	Primary diagnostics	Backup diagnostics
n_e profile	TS, POINT	MR
T_e profile	TS	ECE
T_i profile	XCS, NES	CTS, IAS-CXRS
Rotation profile	IAS-CXRS	XCS
Safety factor	POINT	MSE
Isotope ratio and helium ash	NES (for n_D/n_T), LIF (for n_{He})	

Table 12.4 (continuation): Diagnostics related to transport and turbulence studies. Refer to Table A2 (Annex 2) for the acronyms of the diagnostic systems.

Measured parameters	Primary diagnostics	Backup diagnostics
Impurities and radiation	IAS-CXRS / BES (for n_{imp}), EUV / VUV (for n_{imp} and Γ_{imp}), Bolometer (for radiation)	SXRC
Density fluctuations	Correlation reflectometry, DBS	CTS
T_e fluctuations	ECE (limited)	
Turbulence rotation, E_r	MR (for rotation)	DBS (for E_r)
Magnetic turbulence	CPS	

12.3.5: Diagnostics for disruption mitigation and avoidance

The disruption mitigation and avoidance system for BEST will rely on a comprehensive suite of diagnostics, integrated and interpreted through a central synthetic diagnostics platform. Key real-time inputs include signals from multi-point Thomson scattering for n_e and T_e profiles; magnetic pick-up coils and flux loops for tracking MHD instability growth and vertical displacement events; high-speed visible/IR cameras for thermal monitoring and runaway electron synchrotron radiation; bolometer arrays for radiation collapse; and VUV spectrometers for impurity behaviour. Rogowski coils on the divertor and passive plates will measure disruption-induced halo currents. Electromagnetic forces are incorporated into the vacuum vessel and divertor design, and measured halo currents will provide corresponding force estimates.

The synthetic diagnostics system will not simply display raw data but will fuse these signals to generate a unified, real-time plasma state assessment. It will run physics-based models to predict the evolution of instabilities and the approach to operational limits, providing the Plasma Control System (PCS) with validated, model-based warnings. This enables proactive disruption avoidance through pre-emptive actuator control. When mitigation is unavoidable, the system provides the precise timing and physics justification for triggering the Disruption Mitigation System (DMS), ensuring optimal deployment of shattered pellets and other mitigation actuators to protect device integrity.

12.4: Diagnostic modelling and data analysis

This section describes the core components for diagnostic modelling, data analysis, data processing and usage. The Synthetic Diagnostic Platform (SDP) is a cornerstone of the modern fusion data science ecosystem, particularly for next-step devices like BEST. Its data analysis component is designed to bridge the gap between raw diagnostic signals and physically meaningful, validated information required for machine protection, plasma control, and advanced physics studies. By integrating forward modelling, inverse methods, and robust uncertainty quantification, it transforms heterogeneous diagnostic data into self-consistent, reliable plasma profiles and derived parameters.

12.4.1: Synthetic diagnostics for forward modelling and simulation

Forward models are central to synthetic diagnostics. Each diagnostic model (e.g., POINT for interferometry, ECE for electron cyclotron emission, REF for reflectometry) encapsulates the complete physical principle of the measurement, the hardware response, and the data processing chain. These models simulate the raw signals (e.g., phase shift, radiometer temperature) that a real diagnostic would produce for a given plasma state, providing essential benchmarks for design and validation. Synthetic diagnostics are implemented in the Integrated Modelling & Analysis Suite (IMAS) framework so that the physics core can be transported to other devices (EAST, ITER, etc.), enabling validation on existing experiments and predictions for future devices. IMAS [3], developed by the ITER Organization, meets our requirements and serves as the core infrastructure for building the Synthetic Diagnostic Platform (SDP). IMAS defines a set of Interface Data Structures (IDS) for commonly used engineering, experimental, and simulation data in tokamaks, forming the standard protocol layer (data dictionary, DD) for data exchange. Based on the DD, IMAS encapsulates a low-level layer, implementing a unified data reading and writing interface to MDSplus, HDF5, ASCII, and memory as its database backends. On top of this, the access layer (AL), which supports C++, Fortran, Java, MATLAB™, and Python, provides the open application programming interface for users. Once simulation codes and diagnostic models are adapted to IMAS, workflows can chain or iterate the models to perform the required analysis. With native support for MDSplus and HDF5, IMAS functions both as an integration tool and a convenient database interface, supplemented by auxiliary tools developed by ITER. IMAS-based synthetic diagnostic models and workflows are developed in close collaboration with ITER.

Synthetic diagnostics also underpin real-time models for plasma control, using either simplified physics or AI-based mappings from plasma state to measurements. Neural networks are trained on synthetic-diagnostic data and continuously updated using real measurements as experiments progress. Massive simulations must be run with input and free parameters covering plasma parameters in typical BEST operation scenarios to generate sufficient data for training and this provides a challenge for the early stages of plasma development. For each surrogate model, the input and output data are randomly split into training, validation, and test datasets. Data-driven AI methods are highly dependent on data; the surrogate models should be updated as new data becomes available. Besides the acceleration of data analysis workflows, AI can also be used to automatically monitor the working state of BEST diagnostics, detect fault conditions, which is very important before sending the measured signals to process.

12.4.2: Integrated data analysis and inverse methods

The true power of synthetic diagnostics is realized in its application in Integrated Data Analysis (IDA), which employ sophisticated backward inference techniques. The primary goal is to optimally extract physical quantities (e.g., $n_e(r)$, $T_e(r)$, $T_i(r)$, $j(r)$) from often incomplete, noisy, and sometimes conflicting diagnostic measurements. In this scheme primary and backup diagnostic data are used in a uniform framework

so as all of the contribute to the final result. The Core Profiles Integrated Data Analysis (CPIDA) model is a quintessential example. It uses a Bayesian probabilistic approach to combine measurements from multiple diagnostics (Interferometer, ECE, Thomson Scattering, X-ray spectroscopy, etc.). This method not only provides a best-estimate profile but also quantitatively assesses its uncertainty by combining the error estimates from each individual diagnostic.

12.4.3: Implementation and workflow

The data analysis process is built upon the ITER Integrated Modelling & Analysis Suite (IMAS) infrastructure, ensuring standardization and interoperability. IMAS has a standardized data interface: all data, both experimental and simulated, are stored in Interface Data Structures (IDS), which serve as a common language for all codes regardless of the programming language (Python, MATLAB, C++, Fortran). At present IMAS is not capable of working with large datasets like image streams, turbulence data. Therefore, a native data storage and access infrastructure has to be implemented for these systems. Suitable data can automatically transferred to IMAS.

Automated workflows will be implemented to process data driven by the scientific requirements. A typical workflow for profile reconstruction might: (1) fetch equilibrium and raw diagnostic data from the IMAS database; (2) call the CPIDA module to perform Bayesian inference; (3) store the final self-consistent profiles and their uncertainties back into the database. This automation is crucial for batch processing long-pulse discharge data and for future real-time application.

The analysis is deployed on a dedicated HPC cluster. The computationally intensive tasks – like ray-tracing, Bayesian sampling, and MHD stability calculations – are optimized through parallelization (using CPUs/GPUs) and algorithmic acceleration (e.g., using AI-based surrogate models) to meet the time constraints for inter-pulse (minutes) and eventually real-time (milliseconds) analysis.

12.4.4: Data communication

Synthetic diagnostics generate highly reliable multi-source diagnostic data, which is critical for real-time plasma control and high-fidelity physical simulations. The quality of this data directly influences the stability and accuracy of both control systems and simulation outcomes. To meet the demanding requirements of fast and reliable data exchange between distributed servers in fusion research environments, conventional network protocols have become a significant bottleneck.

The BEST system employs a hardware-accelerated solution based on RDMA over Converged Ethernet (RoCEv2) technology. We design integrated RDMA hardware acceleration with a specialized multi-channel user space architecture, creating an ultra-low latency transmission system based on zero-copy and kernel bypass principles. The system provides critical communication infrastructure for fusion research applications, particularly enhancing real-time plasma control systems and high-speed diagnostic data acquisition. The architecture demonstrates significant potential for improving the reliability and performance of distributed fusion computing environments.

12.5: Further preparations for BEST operations

This chapter has outlined the basic diagnostic requirements for BEST, the rationale behind them, and the associated data workflows. Further work is required now to more completely define each diagnostic requirement through close interaction with other teams to ensure that the unique results from BEST will be accurately measured. The diagnostic requirements for D-T must also be further developed such that they satisfy the team responsible for the safe operation of BEST.

The diagnostic commissioning and calibration will follow a structured two-stage approach. Prior to integrated commissioning, system-level preparation will be conducted, including the calibration of neutron diagnostics and functional checks of magnetic sensors, spectroscopic systems, and visible/IR cameras. In-situ calibration during commissioning will use a portable neutron source to calibrate diamond detectors and neutron flux monitors under vacuum, along with calibration of pressure gauges and interferometers using the gas-injection system.

This phased approach ensures that all critical diagnostics – such as neutron activation systems, Thomson scattering for n_e and T_e, and divertor neutron flux monitors – are accurately calibrated and validated before plasma operations. Key steps include the absolute calibration of the plasma current monitor, cross-illumination checks for imaging systems, and the calibration of bolometers and X-ray spectrometers using reference methods. This comprehensive commissioning strategy guarantees measurement accuracy and supports the reliable operation of neutron and plasma diagnostics during the experimental campaign.

BEST diagnostic experts have also developed a strategy for calibrating all required diagnostics, including the 14 MeV neutron rate. For future in-situ neutron calibration, the use of a D-T neutron source, yielding 14.1 MeV neutrons at intensities above 10^{11} s^{-1}, is envisioned to complement the standard D-D neutron source. While preliminary calculations confirm that D-D neutrons are only practical for calibrating highly sensitive detectors like diamond sensors, the higher flux from D-T neutrons would significantly expand this capability. It promises to enable the calibration of a broader range of neutron diagnostics with greater efficiency and improved counting statistics. Finalizing this strategy will require extensive neutronics modelling to optimize the source placement and fully assess the calibration coverage for all key diagnostic systems. In the next edition of the BEST Research Plan, the commissioning strategy and the calibration strategy will be outlined in detail.

12.6: References

[1] D. Mazon et al., *Nucl. Fusion* **65**, 113001 (2025)
[2] H. Liu et al., *Plasma Sci. Technol.* **27**, 104004 (2025)
[3] J. H. Donné et al., *Nucl. Fusion* **47**, S337 (2007)
[4] F. Imbeaux et al., *Nucl. Fusion* **55**, 123006 (2015)
[5] E. Joffrin et al., *Nucl. Fusion* **59**, 112021 (2019)

Annexes

Annex 1: Nuclear codes and methodology for design and safety assessment

Internationally, several different codes and methodologies are adopted in nuclear design and safety assessments. The importance of the calculated nuclear responses warrants rigorous validation using fusion relevant data – this is sparse and BEST represents a unique opportunity for providing data as described in Section 11.1. Many of the codes are generally primarily adopted in the nuclear fission community, with fusion representing a small percentage of their user base. Approaches for shut down dose rate are either direct patches to the particle transport code or rely on coupling of an activation solver. Underpinning these codes is the physics captured in nuclear data files. Again, numerous international efforts have led to different libraries which are used for different applications.

Where fluids are concerned, the activation of water leading to a short-term decay gamma field and the activation of mobilized corrosion products. Both these phenomena rely on a complex coupling between computational fluid dynamics and neutron transport/activation. Here the need for validation is extremely important with many of the codes nascent in their application/development for fusion application. Note that there a two primary approaches to particle transport- translation to constructive solid geometry (CSG) or transport directly on a mesh version of the geometry. There is value in benchmarking these different workflows. DAGMC is an interface to the different Monte Carlo code that allows for mesh-based tracking.

Table A1 lists the codes identified for potential validation using BEST data. Many of these will be adopted by participants from China, EU and UK.

Table A1: List of nuclear codes and data.

Code	**Distributor/ main developer**	**Open source**
Neutron / Photon transport	Neutron/Photon heating, flux, dpa, tritium production, dpa, He production	
MCNP	RSICC / LANL, US	No
OpenMC	Open source / ANL, US	Yes
Tripoli-4	NEA / CEA, France	No
Serpent 2	NEA / VTT, Finland	No [Yes for academic]
cosRMC	China	No
Shutdown dose rate codes	Dose rate after shutdown (mode 1 + mode 2), waste inventories, nuclide contribution maps	
Shutdown dose rates: R2S		
MCR2S	UKAEA, UK	No
R2SUNED	UNED, Spain	No
R2Smesh	KIT, Germany	No
OpenMC- R2S	Open source / ANL, US	Yes
PyNE R2S	Open source	Yes
NASCA	China	No

Table A1 (continuation): List of nuclear codes and data.

Shutdown dose rates: D1S		
D1SUNED	UNED, Spain	No
AdvancedD1S	ENEA, Italy	No
OpenMC-D1S	Open source / ANL, US	Yes
Shutdown dose rates: N1S		
N1S	UKAEA, UK	No
Activation solvers	Nuclide inventories/activities/decay heat	
FISPACT	UKAEA, UK	No
ORIGEN	RSICC / ORNL, US	No
ALARA	open source	Yes
Fluid activation	Decay gamma source term based on irradiation and flow field for decay time of interest	
RTSM	F4E, Spain	No
FLUNED	open source / UNED,Spain	Yes
GammaFlow	UKAEA, UK	No
ActiFlow	UKAEA, UK	No
Activated corrosion products	Mobilised radiospecies inventory, decay gamma source term	
OSCAR-Fusion	CEA, France	No
CATE	NCEPU	No
TBC	UKAEA, UK	No

Nuclear data		
FENDL	IAEA	Yes
JEFF	NEA / JEFF community	No
ENDF/B	NNDC / CSEWG	Yes
CENDL	CNDC/ CNDCN	Yes
TENDL	IAEA	Yes
JENDL	Japan	Yes

Annex 2: BEST diagnostics acronyms

Table A2: The list of acronyms for BEST diagnostics.

Index Number	Name	Abbreviation
DIAG - 0	**Diagnostic Overview**	
DIAG - 1	**Magnetics & CCD**	
DIAG - 1.1	Magnetics	Mag.
DIAG - 1.2	CCD Camera	CCD
DIAG - 2	**LAPD**	
DIAG - 2.1	Polarimter-Interferometer	POINT
DIAG - 2.2	Laser Induced Fluorescence	LIF
DIAG - 2.3	CO2 Dispersion & Heterodyne Interferometer	CO2 DHI
DIAG - 2.4	Thomson Scattering	TS
DIAG - 3	**Neutron and Fusion Production**	
DIAG - 3.1	Neutron Fluence Monitor	NFM
DIAG - 3.2	Neutron Active System	NAS
DIAG - 3.3	Neutron Camera	RNC, VNC
DIAG - 3.4	Neutron Energy Spectrum	NES
DIAG - 3.5	Gamma Ray Camera	VGC,RGRS
DIAG - 4	**Spectroscopy**	
DIAG - 4.1	Visible Spectroscopy	VIS
DIAG - 4.2	Extreme/Vacuum Ultraviolet Spectroscopy	EUV/VUV
DIAG - 4.3	X-ray Crystal Spectrometer	XCS
DIAG - 4.4	Integrated CXRS-BES-MSE diagnostic	IAS (Integrated Active Spectroscopy)

Index Number	Name	Abbreviation
DIAG - 5	**Radiation and Radiative Power**	
DIAG - 5.1	Bolometer diagnostics	Bolometer
DIAG - 5.2	Soft X-Ray Camera	SXRC
DIAG - 5.3	Hard X-ray diagnostics	HXR
DIAG - 5.4	Faraday Cup	FC
DIAG - 5.5	Diamond Spectrometer	Diamond
DIAG - 6	**Microwave**	
DIAG - 6.1	Microwave Reflectometer	MR
DIAG - 6.2	Doppler BackScattering and Cross Polarization Scattering	DBS-CPS
DIAG - 6.3	Electron Cyclotron Emission	ECE
DIAG - 6.4	Collective Thomson Scattering	CTS
DIAG - 7	**First Mirror & PWI**	
DIAG - 7.1	First mirror and shutter	FM&Shutter
DIAG - 7.2	Divertor laser-induced spectroscopy	DILIS
DIAG - 7.3	Divertor ablation monitor system	DAMS
DIAG - 7.4	Divertor shadow area Dust Monitor System and Material Probe	DDMS
DIAG - 8	**Nuclear Electronics**	
DIAG - 9	**Synthetic Diagnostics**	
DIAG - 10	**Port Integration**	

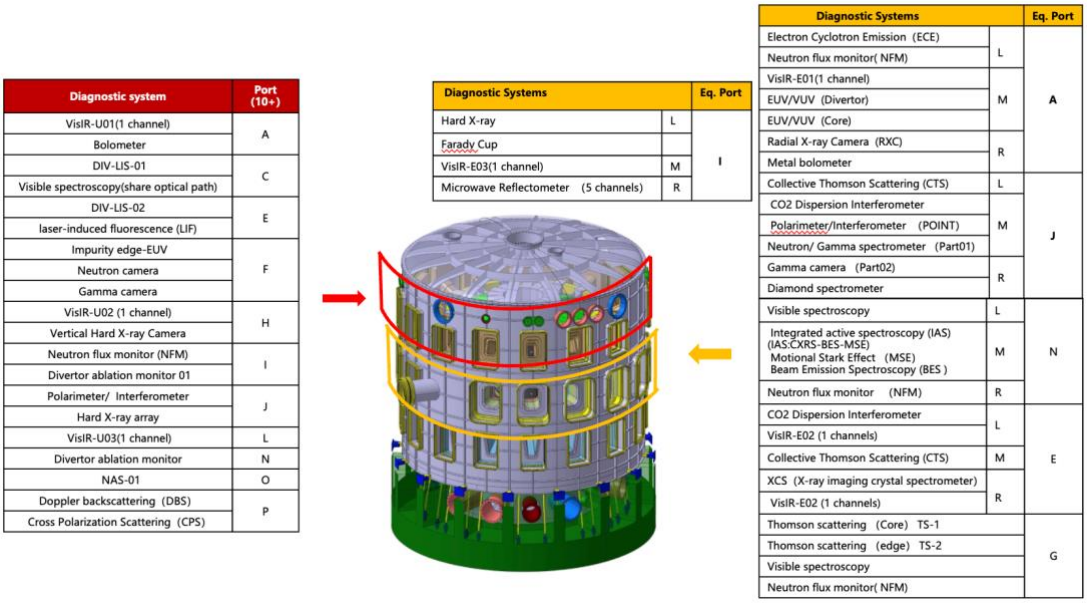

Figure A2: Port allocation for the various diagnostics in BEST.

Topical Group Coordinators for the BEST Research Plan

Jinping Qian
ASIPP
Lead Coordinator

Yevgen Kazakov
LPP-ERM/KMS, Belgium
Lead Coordinator

Bin Zhang
ASIPP
Plasma Scenarios
H&CD and Fuelling

Emmanuel Joffrin
CEA-Cadarache, France
Plasma Scenarios

Xuebing Peng
ASIPP
Fusion Technology

Richard Kamendje
EUROfusion
Fusion Technology

Shanliang Zheng
ASIPP
Fusion Technology

Rosaria Villari
ENEA, Italy
Fusion Technology

Jiale Chen
ASIPP
Transport Physics and Integrated Modelling

Paola Mantica
CNR-Milan, Italy
Transport Physics and Integrated Modelling

Xiaojie Wang
ASIPP
H&CD and Fuelling

Julien Hillairet
CEA-Cadarache, France
H&CD and Fuelling

Topical Group Coordinators for the BEST Research Plan

Rui Ding
ASIPP
Divertor, SOL and PWI

Ou Pan
IPP-Garching, Germany
Divertor, SOL and PWI

Shuai Gu
ASIPP
MHD, Control and Disruptions

Jonathan Graves
EPFL, Switzerland
MHD, Control and Disruptions

Guoqiang Li
ASIPP
Energetic Particles

Rui Coelho
IST-Lisbon, Portugal
Energetic Particles

Tianyang Xia
ASIPP
Theory and Simulations

Matteo Falessi
ENEA, Italy
Theory and Simulations

Haiqing Liu
ASIPP
Plasma Diagnostics

Sándor Zoletnik
CER-Budapest, Hungary
Plasma Diagnostics

UKAEA Contributors

Damian King
Plasma Scenarios (Coordinator)

Luca Garzotti
Transport Physics and Integrated Modelling

Alex Valentine
Fusion Technology

Scientific and Technical Leadership for the BEST Research Plan

Yuntao Song
ASIPP
Director-General

Jiangang Li
ASIPP
Academician

Kun Lu
ASIPP
Deputy Director

Baonian Wan
ASIPP
Academician

Jinping Qian
ASIPP
Deputy Director

Youwen Sun
ASIPP
Head of Theory Division

Jinggang Qin
ASIPP
Deputy Director

Vincent Chan
Senior Visiting Scientist

Guosheng Xu
ASIPP
Deputy Director

Zhiyong Qiu
ASIPP
Director
CAS Key Laboratory

Gianfranco Federici
EUROfusion
Programme Manager

Marco Wischmeier
EUROfusion
Department Head
Plasma Science

Richard Kamendje
EUROfusion
Head of Office
International Collaborations

Joelle Elbez-Uzan
EUROfusion
Department Head
Design and Fusion Technology

List of Contributors

Chapter 1	**Affiliation**
J.P. Qian	ASIPP
Ye.O. Kazakov	LPP-ERM/KMS, Brussels, Belgium
Y.T. Song	ASIPP
J.G. Li	ASIPP
K. Lu	ASIPP
G.S. Xu	ASIPP
B. Zhang	ASIPP
S.L. Zheng	ASIPP
G.Q. Li	ASIPP
X.B. Peng	ASIPP
J.G. Qin	ASIPP
X.J. Wang	ASIPP
V. Chan	ASIPP
R. Ding	ASIPP
Z.H. Liu	ASIPP
S.Z. Huang	ASIPP
J.X. Zheng	ASIPP
Y.Y. Huang	ASIPP
B.J. Xiao	ASIPP
X.Z. Gong	ASIPP
B.N. Wan	ASIPP
G. Federici	EUROfusion
M. Wischmeier	EUROfusion
R. Kamendje	EUROfusion
J. Elbez-Uzan	EUROfusion
E. Joffrin	CEA-Cadarache, France
P. Mantica	CNR-Milan, Italy
A. Loarte	ITER Organization
D. King	UKAEA
L. Garzotti	UKAEA

Chapter 2	**Affiliation**
E. Joffrin	CEA-Cadarache, France
B. Zhang	ASIPP
D. King	UKAEA
M.H. Li	ASIPP
W.B. Liu	ASIPP
D.H. Chen	ASIPP

Chapter 2 (continuation)	**Affiliation**
H.L. Wang	ASIPP
K.D. Li	ASIPP
J.R. Wu	ASIPP
Z.F. Guan	ASIPP
W.Y. Lu	ASIPP
C.B. Wu	ASIPP
Y.H. Wang	ASIPP
P. Li	ASIPP
X.M. Zhong	ASIPP
T. Tang	ASIPP
X.D. Yang	ASIPP
Y. Tao	ASIPP
W. Zhang	ASIPP
K. Wu	ASIPP
R. Ambrosino	Consorzio CREATE, Italy
E. Acampora	Consorzio CREATE, Italy

Chapter 3	**Affiliation**
R. Kamendje	EUROfusion
R. Villari	ENEA, Italy
S.L. Zheng	ASIPP
L. Chen	ASIPP
H.S. Zhou	ASIPP
S.L. Liu	ASIPP
K.C. Jiang	ASIPP
Q.J. Zhu	ASIPP
W.B. Li	ASIPP
X.K. Zhang	ASIPP
K. Xu	ASIPP
J. Wu	ASIPP
X.M. Ren	ASIPP
Y. Lan	ASIPP
S. D'Amico	KIT, Germany
G. Aiello	EUROfusion
J. Elbez-Uzan	EUROfusion

Chapter 4	**Affiliation**
P. Mantica	CNR-Milan, Italy
J.L. Chen	ASIPP
V.S. Chan	ASIPP
H.C. Fan	ASIPP
Y.J. Hu	ASIPP
X. Jian	ASIPP
G.Q. Li	ASIPP
H.L. Wang	ASIPP
C.B. Wu	ASIPP
J.R. Wu	ASIPP
G.S. Xu	ASIPP
X.Y. Xu	ASIPP
X.M. Zhai	ASIPP
C. Angioni	IPP-Garching, Germany
L. Frassinetti	KTH, Sweden
A. Mariani	CNR-Milan, Italy
I. Casiraghi	CNR-Milan, Italy
L. Figini	CNR-Milan, Italy
T. Johnson	KTH, Sweden
F. Auriemma	Consorzio RFX, Italy
J. Lombardo	Consorzio RFX, Italy
L. Garzotti	UKAEA
D. King	UKAEA

Chapter 5	**Affiliation**
J. Hillairet	CEA-Cadarache, France
X.J. Wang	ASIPP
B. Zhang	ASIPP
B. Cao	ASIPP
M.H. Li	ASIPP
J.L. Hou	ASIPP
Y.Y. Tang	ASIPP
J. Wang	ASIPP
H.L. Wang	ASIPP
J.H. Wu	ASIPP
Y.L. Xie	ASIPP
X.Y. Xu	ASIPP
Y. Ye	ASIPP
J.S. Yuan	ASIPP
C.M. Qin	ASIPP
X.J. Zhang	ASIPP
W. Zhang	ASIPP
B.J. Ding	ASIPP
C.B. Wu	ASIPP
H.D. Zhuang	ASIPP
Y.H. Xie	ASIPP
H.D. Xu	ASIPP

Chapter 5 (continuation)	**Affiliation**
F.K. Liu	ASIPP
G.Z. Zuo	ASIPP
L.Z. Liang	ASIPP
Y.Y. Huang	ASIPP
J.S. Hu	ASIPP
Ye.O. Kazakov	LPP-ERM/KMS, Brussels, Belgium

Chapter 6	**Affiliation**
R. Ding	ASIPP
O. Pan	IPP-Garching, Germany
G.Z. Jia	ASIPP
X.J. Liu	ASIPP
T.Y. Xia	ASIPP
G.L. Xu	ASIPP
J.L. Chen	ASIPP
B.F. Gao	ASIPP
C.J. Li	ASIPP
H. Wang	ASIPP
M. Wischmeier	IPP-Garching, Germany
M. Faitsch	IPP-Garching, Germany
P. Mantica	CNR-Milan, Italy
S. Brezinsek	FZJ-Jülich, Germany

Chapter 7	**Affiliation**
X.B. Peng	ASIPP
R. Kamendje	EUROfusion
R. Villari	ENEA, Italy
Y. Cheng	ASIPP
S.L. Zheng	ASIPP
H. Jin	ASIPP
X.Y. Qian	ASIPP
W. Wen	ASIPP
G. Shen	ASIPP
F. Liu	ASIPP
Z.Z. Song	ASIPP
Z.Z. Zhu	ASIPP
Q.X. Yang	ASIPP
C. Bachmann	EUROfusion
V. Corato	ENEA, Italy
P. Bruzzone	EPFL, Switzerland
G. De Marzi	ENEA, Italy

Chapter 8	**Affiliation**
S. Gu	ASIPP
J.P. Graves	EPFL, Switzerland
H.H. Wang	ASIPP
Y. Zhang	ASIPP
X.J. Wang	ASIPP
M.H. Li	ASIPP
Y.H. Wang	ASIPP
D.L. Chen	ASIPP
Y.W. Sun	ASIPP
S. Van Mulders	EPFL, Switzerland
C.Z. Wang	EPFL, Switzerland
O. Sauter	EPFL, Switzerland
M.D. Kong	EPFL, Switzerland
L. Zeng	Tsinghua University
D. Hu	Beihang University
X.M. Li	Tsinghua University

Chapter 9	**Affiliation**
R. Coelho	IST-Lisbon, Portugal
G.Q. Li	ASIPP
T.Y. Xia	ASIPP
Z.Y. Qiu	ASIPP
Y.J. Hu	ASIPP
W. Shen	ASIPP
Y.F. Zheng	ASIPP
W. Zhang	ASIPP
J. Huang	ASIPP
M. Xu	ASIPP
M. Falessi	ENEA, Italy

Chapter 10	**Affiliation**
M. Falessi	ENEA, Italy
T.Y. Xia	ASIPP
Z.Y. Qiu	ASIPP
L. Ye	ASIPP
H.H. Wang	ASIPP
S. Gu	ASIPP
Y.L. Li	ASIPP
H.M. Qi	ASIPP
F. Zonca	ENEA, Italy

Chapter 11	**Affiliation**
S.L. Zheng	ASIPP
R. Villari	ENEA, Italy
R. Kamendje	EUROfusion
X.B. Peng	ASIPP
B. Guo	ASIPP
X.K. Zhang	ASIPP
Q.J. Zhu	ASIPP
G.Q. Zhong	ASIPP
J. Elbez-Uzan	EUROfusion
S. Rosanvallon	CEA-Cadarache, France
P. Pereslavtsev	EUROfusion
A. Valentine	UKAEA

Chapter 12	**Affiliation**
H.Q. Liu	ASIPP
S. Zoletnik	CER-Budapest, Hungary
H. Lian	ASIPP
Y. Yang	ASIPP
Y. Zhang	ASIPP
S.Z. Yuan	ASIPP
S.X. Wang	ASIPP
B. Shen	ASIPP
T. Zhang	ASIPP
L. Zhang	ASIPP
S.Y. Lin	ASIPP
G.Q. Zhong	ASIPP
R.J. Zhou	ASIPP
Y.M. Duan	ASIPP
R. Yan	ASIPP
Q. Hu	ASIPP
H. Cao	ASIPP
Y. Liu	ASIPP
Z. Yip	ASIPP
D. Mazon	CEA-Cadarache, France
A. Costley	Independent expert